Numerical Simulations of Undrained Granular Media

by

Roberto R. Olivera Bonilla

A thesis
presented to the University of Waterloo
in fulfillment of the
thesis requirement for the degree of
Doctor of Philosophy
in
Civil Engineering

Waterloo, Ontario, Canada, 2004

I hereby declare that I am the sole author of this thesis. This is a true copy of the thesis, including any required final revisions, as accepted by my examiners.
I understand that my thesis may be made electronically available to the public.

Roberto R. Olivera Bonilla.

Abstract

The objective of the present study was to develop a fluid flow-coupled distinct element model capable of capturing the undrained behaviour of granular soils by considering fundamental physical mechanisms that involve fluid flow and particle interaction. The method considers granular media as assemblies of ellipsoidal particles arranged on a plane and interacting by means of contact forces. Saturation effects are incorporated by assuming that particles are immersed in fluid, the flow of which is simulated as occurring through a network of conduits. The flow through conduits is according to a Hagen-Poiseuille relation; a transient solution is obtained by solving a system of differential equations. The developed fluid-flow coupled distinct element was used to conduct various numerical simulations and the mechanisms of undrained deformations were examined from a micromechanical point of view.

The dissertation begins with a literature review on the undrained behaviour of granular materials as observed in laboratory experiments. A review of previous attempts to simulate undrained tests micromechanically is also presented, and the advantages and disadvantages of various methods are examined.

The capability of the developed model to simulate two-dimensional fluid-flow and pressure dissipation problems is demonstrated by means of comparisons with analytical solutions. Fluid pressure dissipation problems are qualitatively compared with Terzaghi's one-dimension theory of consolidation. It is shown that transient flow problems are accurately modelled by the fluid flow network approach.

Simulated compression tests were carried out to examine the effects of different confining pressures and initial densities on the macroscopic response. The results compare favorably with those commonly observed in undrained laboratory experiments. Simulated tests are analyzed from a micromechanical point of view. It is shown that macroscopic behaviour can be traced to changes in micromechanical fabric descriptors.

The effects of the interparticle friction angle on the undrained behaviour of the assemblies are investigated. The undrained strength is considerably increased by increasing interparticle friction. The main mechanism found to be responsible for the development of higher strength is the tendency of the specimens to dilate during shear distortion.

The effects of the principal stress direction on the macroscopic response are examined. The behaviour of initially anisotropic samples is significantly altered by the direction of the principal stresses relative to the anisotropy direction.

It is demonstrated that macroscopic permeability of the media has a considerable effect on the strength. This behaviour is attributed to the inhomogeneity of pore pressure distributions which increases with decreased permeability.

The results presented are generally in agreement with observations previously reported from laboratory experiments. The possible applications of the model for future research are also discussed.

Acknowledgements

The author is indebted to many persons and institutions in many different ways. Firstly, the author would like to thank Dr. Leo Rothenburg for his ongoing support and guidance throughout these years.

Appreciation is extend to Dr. Giovanni Cascante, Dr. Mark Knight and Dr. Maurice Desseault for their valuable comments, advises and friendship during all this time at the University of Waterloo. Very special thanks to Dr. Sitharam Thallak, for his valuable advice and friendship.

Heartfelt thanks to my parents Roberto and Ana Rosa and my siblings Ana Rosa and Alejandro for supporting me in all possible ways. To my dearest friends in Waterloo: Adedamola Adadepo, Liu Bingsheng, Shayne Giles, Zahid Khan, Ali Nasseri Mahaddam, Anwar Majid, Gabrijela Mecki, Luis Miranda, Hamza Ouadfel and Francisco Zaragoza for their affection and continuous support.

The financial support provided by CONACYT (Consejo Nacional de Ciencia y Tecnología) is gratefully acknowledged.

Finally, the author would like to thank his wife Gabriela, for her endless support and encouragement. The present work is dedicated to her.

Contents

List of Tables

List of Figures

Chapter 1

Introduction

1.1 General Background

The increasing awareness of liquefaction hazards during earthquakes has aroused the need for understanding the mechanism by which loss of ground shear strength occurs. Liquefaction of sands may arise when saturated soils are shaken and a limiting state of stress is reached. Soils that are prone to liquefaction are generally Holocene alluvial sediments at shallow depths [107]. Perturbations in these saturated materials trigger particle movements that may result in pore water pressure increase. When the rate of pressure generation is higher than the rate of pressure dissipation, pressures start to build up, causing a reduction in the effective stresses. Thus, depending on the ability of the material to dissipate the generated pressures, an eventual loss of effective stresses may occur. The process of gradual pore pressure generation until the effective stress is totally lost is referred to as liquefaction. Liquefaction can cause settlement or tipping of buildings, sand boiling, ground cracking, landslides, dam instability, and highway embankment failures, among other hazards. Such damages are generally of great concern to public safety and are economically significant [47].

The term liquefaction was originally coined by Hazen [37]. He explained the failure of Calaveras dam as follows:

> *"When a granular material has its pores completely filled with water and it's under pressure, two conditions may be recognized. In the first or normal case, the whole of the pressure is communicated through the material from particle*

> *to particle by bearings of the edges and points of the particles on each other. The water in the pores is under no pressure that interferes with these bearings. Under such conditions the frictional resistance of the material against sliding on itself may be assumed to be the same, or nearly the same, as it would be if the pore where not filled with water. In the second case, the water in the pores of the material is under pressure. The pressure of the water on the particles tends to hold them apart; and part of the pressure is transmitted through the water. To whatever extent this happens, the pressure transmitted by the edges and points of the particles is reduced. As water pressure is increased, the pressure on the edges is reduced and the friction resistance of the material becomes less. If the pressure of the water is enough to carry all the load, it will have the effect of holding the particles apart and of producing a condition that is practically equivalent to that of quick sand...".*

Since that dam failure, the term liquefaction has been used when loss of effective stress in static or dynamic laboratory tests occurs. Liquefaction phenomena have been extensively studied over the last several decades, normally using the triaxial apparatus. Results from laboratory experiments conducted over the past several decades indicate that liquefaction resistance of granular materials depends primarily on their relative density and the initial state of stress. [13, 14, 7, 82, 40]. Recently however, the undrained response has been found to be dependent on other factors, such as stress or strain path directions [100, 106, 93, 80], and initial fabric anisotropy[106]. The results of these experiments show the importance of including additional parameters, such as particle arrangement and fabric anisotropy, in the study of undrained deformations. However, quantifying fabric information is a complex, time-consuming and expensive procedure.

Computer modelling of soil liquefaction using continuum approaches has also been used to study the response of soil to a given loading situation [65]. Continuum models cannot explore the physical microscopic mechanisms that lead to liquefaction; they can only simulate the macroscopic response provided that the behaviour is adequately emulated by the adopted constitutive law.

An alternative approach to studying soil behaviour takes into consideration the discrete nature of the particles. Early attempts to observe force distributions and particle behaviour at microscopic levels were made by Dantu and Wakabayashi [24] using optically sensitive materials. Later, De Josselin de Jong and Verruijt [26] analyzed force distribution in such assemblies, studying individual particles. The results of these experiments provided a qualitative understanding of the mechanisms of load transfer and the deformation characteristics of granular materials. New experimental techniques [27] using computer tomography also provide important information about the evolution of the fabric. The Distinct Element Method (DEM) initially proposed by Strack and Cundall [23] is an attractive computation technique that treats a granular system as a collection of discrete granules. The method allows the extraction of all the required information at the particle level at any stage during the deformation process. Although the technique was originally developed to consider assemblies of idealized particles sheared in a dry environment, it has been extended to account for the effects of pore fluid [36, 35, 53, 50].

1.2 Statement of the Problem

The need to fully comprehend the process of liquefaction has arisen from catastrophic failures that occurred in the past. Physical processes involved in undrained deformations are complicated and are dependent on the type of soil, which, in turn, can exhibit great variability. Results from laboratory experiments have shown that void ratio and initial state of stresses are necessary, but are not sufficient parameters to describe the response of a soil specimen when sheared in undrained conditions. Undrained soil response has been found to be dependent on other parameters, such as stress and strain paths and the method of sample preparation. Such dependency would not be surprising if the soil were analyzed from a micromechanical frame of reference, where it is recognized that macroscopic observations are just the result of microscopic processes occurring at the grain scale level [68]. These processes include the evolution of the orientation of inter-particle contacts and forces.

A study of this nature in the laboratory is complicated if not impossible to conduct, yet an adequate analysis requires the quantification of this information. Therefore, alternative procedures, such as computer simulations, have to be employed.

A granular material like sand is composed of distinct particles that interact with their neighbours through complex contact mechanisms. A system of several particles under the loading and unloading action of dynamical forces is complicated to model. Moreover, in undrained deformations, the effects of the fluid on the individual grains should also be simulated, adding complexity to the model. Thus, assumptions must be made in an attempt to reproduce the system's behaviour.

The continuum approach lacks some of the required characteristics, since it does not provide information about grains and contact orientations. In contrast, the DEM meets all these characteristics by providing information at the contact-to-contact level that can be extracted and analyzed at any time during the deformation process.

There is perhaps no perfect scheme to simulate liquefaction of granular materials, but an attempt was made by the author to select a simple system capable of capturing the fundamental features of undrained deformations. The result of this attempt is a fluid-coupled DEM which is used to explore the microscopic processes of undrained experiments on idealized systems of elliptical particles.

1.3 Objectives and Scope of Study

The main objective of this study was to develop a fluid-coupled DEM algorithm that incorporates fundamental physical processes involved in liquefaction. Specifically, these processes include:

1. The generation of pore pressures at the microscopic level as response to particle movement.
2. The flow of fluid between pores considering explicitly the microstructure and particle arrangement at all times during deformation.
3. The transient movement of fluid using pore pressure generation-dissipation scheme.
4. The effects of pore pressure forces on the particles.

A comprehensive analysis was undertaken to study the effects of different parameters on the global response of an idealized system of elliptical particles. The compressibility of the fluid, hydraulic conductivity of the system, interparticle friction angle, and initial particle arrangement are some aspects that were examined.

One of the features of the model is that it allows extraction of information from the contacts with a level of detail that is impossible to obtain in laboratory experiments. Contact information includes orientation of normal vectors to the contacts and orientation and magnitude of contact forces, the latter being a direct measurement of the effective state of stresses present in the assembly. It is shown that this information is essential for conducting a comprehensive analysis of the deformation mechanisms. One of the objectives of this work was to study the evolution of these parameters to gain insight into the mechanics of undrained deformations.

The new model was used to simulate biaxial tests under different initial confining pressures and different densities. The results have shown that the implemented algorithms realistically emulate undrained characteristics as reported in the literature.

Another objective of this research was to study the effects particle orientations on the undrained response of the assemblies. Simulations were conducted on assemblies with particles preferably oriented horizontally. The assemblies were loaded along different paths and the direction of the major principal stress with respect to preferred particle orientation was examined.

The scope of the study was to introduce this novel approach as a research tool to study liquefaction phenomena. The DEM model provides an insight to guide future numerical and laboratory experiments. Furthermore, it provides valuable information that may be used to develop micromechanical-based constitutive models by studying the evolution of the parameters that control the deformation process.

1.4 Organization of the Thesis

The remainder of this thesis is organized as follows:

Chapter 2 presents a literature review of liquefaction of granular materials behaviour and discusses the factors affecting liquefaction susceptibility of laboratory specimens. A brief introduction to micromechanical concepts is provided as a preamble for the use of the concepts in later chapters. Different approaches to modelling soil liquefaction using DEM are reviewed and their limitations discussed.

Chapter 3 introduces the equations of motion used in the DEM and details the flow-coupled discrete element model. The flow-coupled algorithms used in the model assume that fluid flows between neighbouring pores through small passages of circular cross section. Pore pressure is generated microscopically using pore strains and assuming an elastic fluid. The individual pores in the system are identified using an algorithm that searches for group of particles that are continuously in contact enclosing discrete spaces and constructing a network of polygons, the vertices of which are the centres of particles forming the pores. The combined effects of pore pressure generation and dissipation at the pore level result in the emergence of a system of ordinary differential equations that effectively capture the transient nature of the problem.

Chapter 4 presents the results of the verification of the algorithms employed in the computations.

Chapter 5 reports the results of a series of simulations in which the effect of initial density and confining pressure was examined. Parameters necessary to describe the fabric evolution were analyzed to gain insight into the mechanisms of undrained deformations of idealized systems. The results showed that the implemented algorithms are capable of reproducing undrained tests. The effects of the interparticle friction angle on the response of the assemblies were also examined. A comparison of results from volume-controlled tests and simulations conducted using the proposed implementation is presented at the end of the chapter.

Chapter 6 presents the results of a series of tests conducted on initially anisotropic assemblies where the direction of the major principal stresses was rotated. The results show that density and initial state of stresses are not sufficient parameters to describe the behaviour of two-dimensional systems of elliptical particles. Finally, the effects of intrinsic permeability on the assembly's response is studied. Statistical analysis of the pore pressure distribution in the assembly at different deformation stages is also presented.

Chapter 7 summarizes the major conclusions drawn from the present research, presents some recommendations for future research and discusses the limitations of the model.

Chapter 2

Literature Review

2.1 Introduction

This chapter presents a review of literature covering two broad topics: First, the fundamentals of drained and undrained behaviour of granular materials observed in the laboratory are reviewed and discussed. Despite the vast amount of experimental data, it is shown that discrepancies regarding the possible differences between the ultimate drained and undrained states of sands are still found in the literature. Second, a brief review of micromechanical descriptors that are most commonly used when modelling discrete granular systems is presented here as a prelude to a more detailed discussion in Chapters 5 and 6. The existing approaches to simulating liquefaction using the DEM are also presented.

2.2 Drained Behaviour of Sand

In his pioneering work on shear strength of soils, Casagrande [12] conducted direct shear tests on initially loose and dense sand samples. The results showed that specimens tested at the same confining effective stress ended up having the same residual resistance at large deformations and that the final void ratio was also the same. Initially loose samples tended to contract and initially dense samples tended to contract, but suddenly began to dilate as shear deformation continued.

Figure 2.1 presents a schematic showing the fundamental results obtained by Casagrande [12]. Both the loose and the dense specimens show a tendency to reach the same void ratio and same residual strength. Based on his results, Casagrande postulated that a given specimen would always reach the same void ratio at relatively large deformations independent of the void ratio at the time of consolidation. The limiting value of the void ratio was termed the *critical void ratio* or *critical density* and was found to be a function of the initial confining effective stress. When the critical void ratio is reached, the volumetric changes cease and the strength provided by the sheared particles is practically constant. The condition at which the soil is deforming at constant stress and constant volume has been termed *critical state* [78].

Critical void ratio line

The soil strength at the critical state is mainly defined by the the initial confining effective stress and the initial void ratio. It thus becomes possible to graphically represent a relationship between void ratio and confining stress at the critical state using the so called *critical void ratio line* (CVR). The void ratio versus confining stress space is usually referred to as the *state diagram*. The critical void ratio line is shown on the state diagram in Figure 2.1. If a sand specimen initially at point A is sheared, it will reach the CVR line at constant confining stress. Consequently, the sample will contract, reducing its void ratio until it becomes equal to the critical void ratio. Similarly, if the initial state of the soil is at point B, the specimen will dilate under constant effective confining stress upon shearing until it eventually reaches the critical void ratio on the critical state line.

In general, three different tendencies of volume change can be identified: tendency to contract, to dilate, and to preserve volume, that is, no volume change.

If the initial conditions of the specimen are such that they plot on the CVR line, the specimen will deform under constant volume, that is, at a constant void ratio. Thus, if the CVR is known for a given soil, it becomes possible to predict what the volumetric tendencies will be during shear. This observation led Casagrande to hypothesize that sand samples, when sheared undrained under an equal initial confining pressure, would exhibit the same volume change tendency. This hypothesis implied that dense samples when sheared, generate negative pore water pressures as a result of the tendency to increase their volume, whereas the contractile characteristics of loose samples would enhance the development of positive pore water pressure. As a result, Casagrande believed that the CVR line in the state diagram would mark a boundary, separating specimens that are susceptible to liquefaction from those that are not.

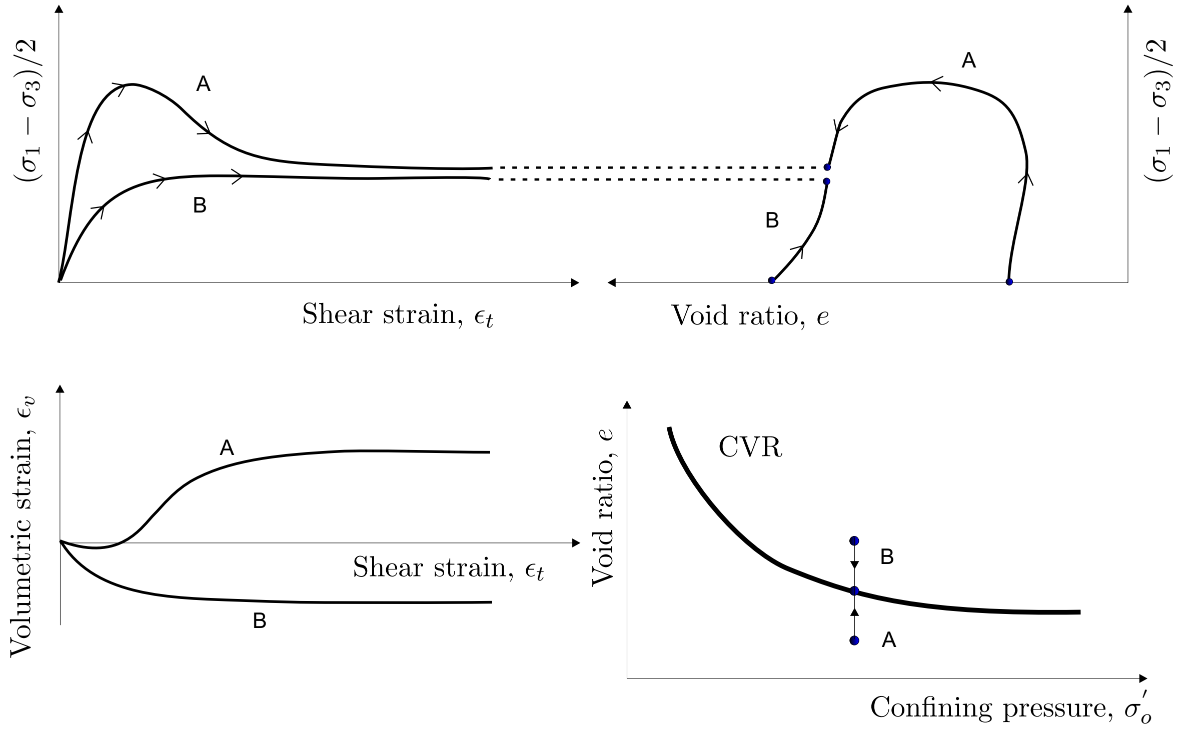

Figure 2.1: Typical stress-strain, stress-void ratio, volumetric strain-shear strain and void ratio-confining pressure curves

2.3 Undrained Sand Behaviour

The results from tests conducted in dry sands indicate that dilative or contractive characteristics are governed by the initial void ratio and state of stresses. These initial conditions can be identified by their location in the state diagram with respect to the critical state line. According to this concept, initial states above the CVR will exhibit contractive behaviour, whereas initial states below it will dilate upon shearing. A similar relationship has been found to exist for undrained tests when sheared under particular conditions. These concepts are introduced in the present section, along with some of the common findings observed in the laboratory.

2.3.1 Undrained Behaviour under Monotonic Loading

Static or monotonic undrained tests are usually conducted in the triaxial apparatus under stress or strain-controlled conditions. The discussion in the present work will be limited to the behaviour of soil samples tested statically in the triaxial chamber.

Figure 2.2 shows results of stress-controlled experiments conducted by Castro [13] on Banding sand. The specimens were at different initial densities but were consolidated under the same effective confining stress ($\bar{\sigma}_c = 4.0$ kg/cm^2). Specimen A exhibits strain-softening behaviour, reaching a maximum deviatoric stress at a relatively small deformation ($\epsilon \approx 1\%$). As deformation is continued, the specimen starts to lose strength markedly until it reaches a minimum value and stabilizes. The strength at large strains remains constant, similar to the behaviour observed in drained tests at the critical state. This stage of deformation has been termed *steady state*. The steady state of residual resistance envisaged for sand is essentially the same as the critical state for clay [78], where the soil is continuously deforming at constant volume, constant normal effective stress, constant shear stress, and constant velocity. According to Poulos [64], such steady state is achieved only after all particles orientations have reached a statistically steady-state condition and after all particle breakage, if any, is complete, so that the shear stress needed to continue deformation and velocity of deformation remains constant.

It is also observed that for specimen A, the pore pressure initially increases and continues to grow at a decreasing rate during the strain-softening stage until it gradually stabilizes at a value almost equal to the initial confining pressure.

The deformation of specimen B shown in Figure 2.2 is also characterized by a strain-

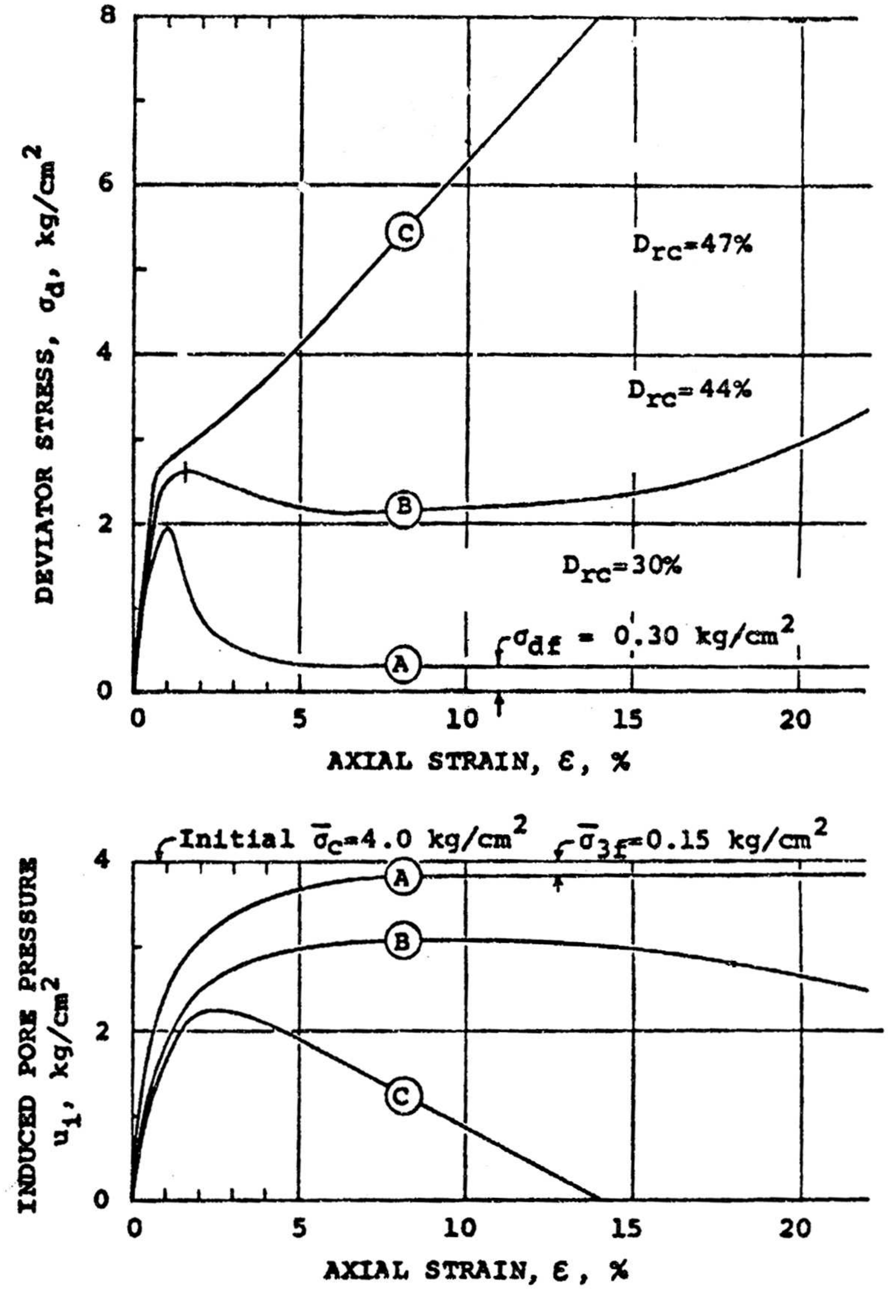

Figure 2.2: Typical undrained behaviour. Adapted from [11]

softening type of response. The imposed stress reaches a maximum value, after which the specimen begins to lose strength. However, the strength reduction occurs only over a limited range of deformation, reaching a minimum value, after which the specimen begins to regain strength when further strained. The pore pressure for specimen B increases at the beginning of the test until it reaches a maximum value that appears to coincide with the occurrence of the minimum strength. After the maximum value of pore pressure has been reached, the specimen begins to dilate, generating reduction in the pore pressure. One of the important aspects of the minimum strength state is that the mobilized shear strength is smaller than the strength mobilized at large strains. Therefore, when residual strength becomes a mayor concern in relation to some practical problem, most researchers have adopted this minimum mobilized strength as a design parameter [40]. This state of minimum strength coincides with what is called the point of phase transformation (PT) [41], to imply a temporary state of transition from contractive to dilative behaviour. A similar drop in shear stress has been reported by other researchers [8, 14, 51]. The stage at which the specimen experiences the minimum strength has been named *quasi-steady state* (QSS) of deformation by Alarcón-Guzmán *et al.* [4] as opposed to the steady state, which is the ultimate strength reached only at large strains.

Specimen C presents a strain-hardening response. As soon as the loading is initiated the specimen gains a considerable amount of strength when compared to tests A and B. The development of the pore water pressure shows that initially the sample exhibits contractive characteristics; however, at an axial strain of $\epsilon \approx 3$ % the sample begins to dilate.

The results of the three tests show that a change of relative density from 30% to 47% was responsible for the different types of behaviour. Sample A reached the steady state of deformation, that is, a state of deformation under constant volume conditions, whereas specimens B and C continue gaining strength without showing any tendency to stabilize at a steady strength. For some sands, very large strains (axial strain $\epsilon > 20\%$) are required to reach the steady state condition, and in some cases conventional triaxial equipment may not reach these large strains [66].

The tests conducted by Castro [13], were conducted in an undrained environment where water is not allowed to leave or enter the sample. Since the compressibilities of both the fluid and the particles are small, it assumed that the volume (and consequently void ratio) of the specimen remains constant during the tests. Accordingly, the path in the state diagram transverses horizontally at a constant void ratio until the change in effective

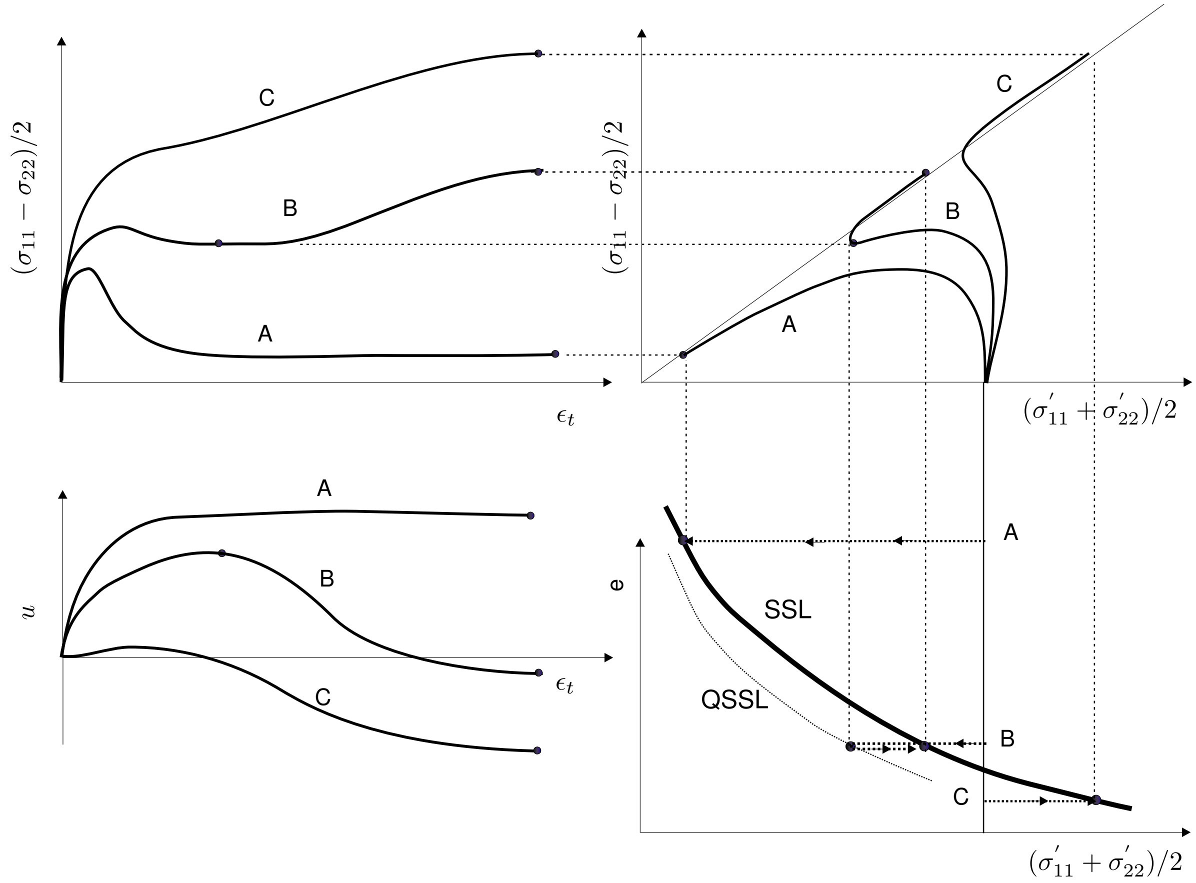

Figure 2.3: Steady state line concept. Behaviour of initially loose, medium and dense specimens sheared under undrained conditions

confining stress and the internal arrangement of the particles bring the specimen to a steady state of deformation. The idealized response of the three specimens is schematically shown in Figure 2.3. As in drained tests, the loci of all points in the state diagram at which the soil specimen deforms under conditions of constant effective stress, constant void ratio, and constant velocity define what is called the *steady state line* (SSL) [7]. The steady state line can be envisaged as a space curve in the $e - q - p'$ coordinate system, projected unto the state diagram. The existence of such a boundary surface has been confirmed by the extensive work of several investigators [41, 48, 79, 82, 95, 7, 51, 4, 3] following the work by Castro [13].

Figure 2.3 shows that the specimen initially at point A will display strain-softening characteristics. The pore pressure will increase until it reaches a steady state value and the effective confining stress will be reduced accordingly. The initial condition at the state diagram will transverse horizontally to the left until it reaches the steady state line.

Specimen B exhibits initially strain-softening response until it reaches the quasi-steady state of deformation. After the state of minimum strength is reached, the pore pressure begins to decrease, resulting in an increase of the deviatoric strength and confining stress. This behaviour will cause the initial state to move horizontally to the left, to a value corresponding to the effective quasi-steady state strength, where it then reverses towards the right, until reaching the steady state line. If the occurrence of the QSS , as well as the value of the minimum post-peak strength, are of interest in a certain situation, it is also possible to plot the effective confining stresses at these stages in the state diagram. The average line through all these points is called the *Quasi-Steady State Line* (QSSL) [96, 40].

Specimen C, whose initial condition plots below the steady state line exhibits dilative characteristics and the initial state will move towards the right, indicating that some effective confining strength will be gained in addition to the initial strength at the time of consolidation.

In principle, the CVR line obtained from drained tests should be reached at the steady state of deformation, since the tendency of a drained specimen to deform at a constant volume would correspond to a tendency of an undrained sample to deform at a constant pore pressure, and hence the process of continuous deformation under constant shear stress is expected to develop at large strains in both the drained and the undrained environment. However, there exist experimental evidence that suggests that the CVR and the SSL may not be the same [2, 103] and thus the undrained behaviour of sand can not be predicted from drained tests as Casagrande initially hypothesized.

2.3.2 State Parameter

As with the CVR concepts in the drained case, observations regarding the steady state of deformation suggest that, given the initial relative density, the initial confining stress and the SSL of a given sandy soil, it should be possible to predict the potential to pore pressure generation. Initial states plotting above the SSL would exhibit a strain-softening type of response, whereas those states below the SSL should present strain-hardening behaviour. This concept further suggests that dense granular structures can be susceptible to liquefaction when initially confined under sufficiently large stresses. Accordingly, the state of stress at the steady state would be determined solely by the initial void ratio [16].

When the relationship between void ratio and confining stress at steady state is plotted in the $e - \log \sigma_3^{'}$ diagram, it has been observed that the loci of points define a straight line [96, 40]. In order to predict the deformation characteristics of a soil sample under loading conditions, it is necessary to know the location of the initial state prior to loading in the $e - \log \sigma_3'$ plane with respect to the steady state line, an observation made by Roscoe and Pooroshasb [67]. They stated that the behaviour of a cohesionless soil should be more closely related to the proximity of its initial state to the steady-sate line than to absolute measures of density. In other words, soils located at the same vertical distance from the steady-state line should exhibit similar behaviour. This vertical distance was taken up later by Been and Jeffries [7], defining it as the *state parameter* ψ . The state parameter can be defined as the difference between the void ratio in an initial state e_i and the void ratio of the steady state e_{ss} line for the same initial effective first stress invariant I_1 . The first stress invariant is defined as $I_1 = \sigma_1^{'} + \sigma_2^{'} + \sigma_3^{'}$.

$$\psi = e_i - e_{ss} \tag{2.1}$$

Such a definition is shown in Figure 2.4. According to the information depicted, when the state parameter is positive, the soil will exhibit contractile behaviour; when negative, it will dilate under loading, exhibiting stable characteristics at high strains. The state parameter ψ, as defined by Been and Jeffries [7], implies that similar behaviour should be expected for similar ψ values, independent of the initial effective confining stress.

2.3.3 Conditions for Strain Softening Development

The onset of strain softening depends on a combination of different factors, including, void ratio, effective confining stress, initial static shear and the inherent anisotropy. Evaluation of these parameters is one of the most critical parts in liquefaction hazard evaluation.

A problem of great importance concerning sand liquefaction is the identification of conditions at which the specimen begins to lose its strength. Such conditions are usually studied by observing the state of stresses at which strain softening begins on the $p' - q$ plane (stress state diagram).

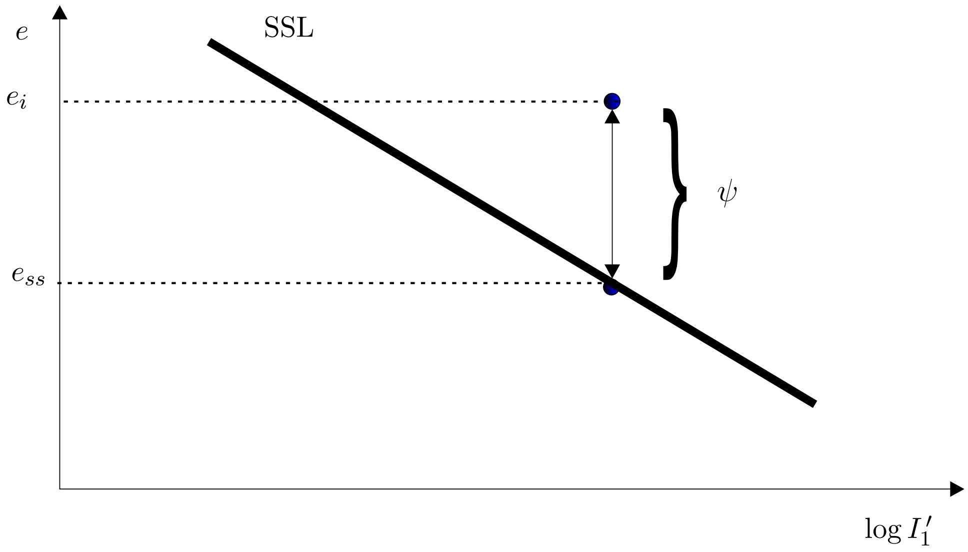

Figure 2.4: Definition of the State Parameter according to Been, *et al.* [7]

Vaid *et al.* [95] conducted both monotonic and cyclic strain-controlled triaxial tests on Ottawa sand . Specimens were prepared using the water pluviation technique. They identified a locus of points on the p' -q plane at which strain softening of the specimens initiated. They concluded that the contractile response is initiated at a constant value of the effective stress ratio (q/p'). Such a stress ratio is referred to as a *critical stress ratio* (CSR). Dobry *et al.* [28] reported similar results.

Figure 2.5 depicts idealized stress paths of three samples initially consolidated under different pressures along with their respective projections on the $p' - q$ plane. The samples all had the same initial void ratio, and the residual strength reached is the same, in agreement with the steady state concepts. The specimens consolidated under higher confining stress will reach a higher peak strength. Therefore, peak shear strength is a function of the initial confining stress. The initiation of strain softening which coincides with the maximum shear strength $(dq/dp' = 0)$ has been marked by crosses. The locus of peak stresses forms a line whose slope has been identified by M_L . Sladen *et al.* (1985) noticed that the slope of the line described by the peak strengths loci were the same, independent of the initial void ratio. Then, hypothetically, there exist an infinite number of such lines. The observation that peak strength falls in a straight line and that this line only changes position but not slope with void ratio has given rise to the concept of *collapse surface* in

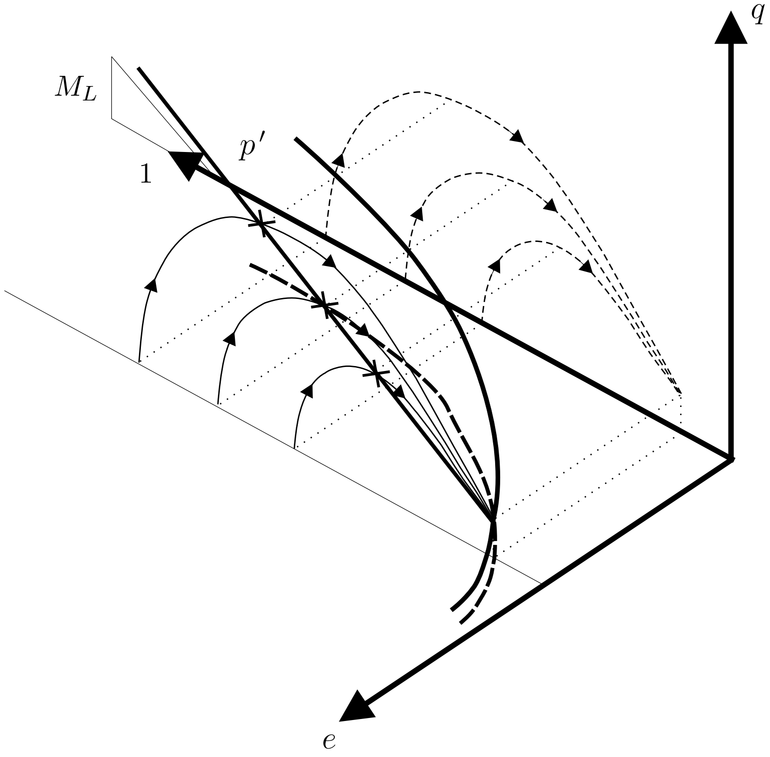

Figure 2.5: Triggering of unstable behaviour according to Sladen *et al.* [82]

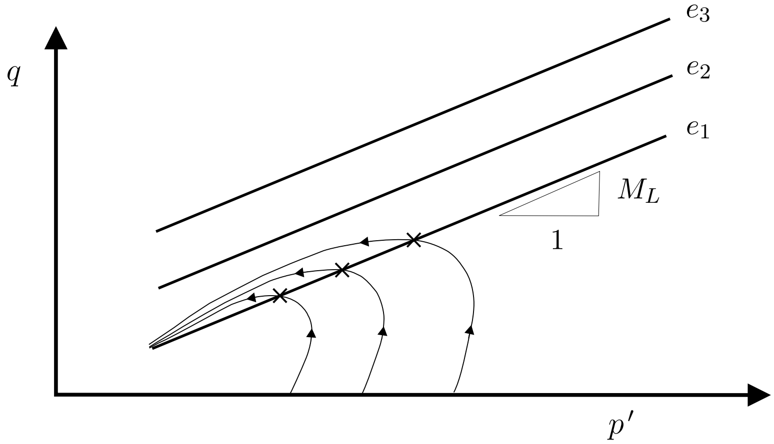

Figure 2.6: Idealized collapse surface according to Sladen *et al.* [82]. Different void ratios generate different collapse lines with the same slope.

the three dimensional $(e - q - p')$ space [82]. For strain softening to initiate, the soil state has to reach the collapse surface and the shear stress has to exceed the steady state shear strength. This collapse surface can be represented by a line in the stress path plane that corresponds to the critical stress ratio observed by Vaid and Chern [94]. An illustration of the collapse surface is given in Figure 2.6.

According to the concept introduced by Sladen, the so-called critical stress ratio line originates at the quasi-steady-state line.

The concept of the collapse surface presented is a complementary approach to that of the steady state concept. The steady state concept omits any consideration of the stress magnitude required to trigger instability. Further, no comment is made on the *in situ* stress state on strain softening potential [82].

From the previous discussion of results, it is concluded that specimens tested undrained in the triaxial cell at particular initial conditions reach a hypothetical limit at large deformations, at which the strength provided by the individual particles remains constant. The limiting shear strength permits the definition of a boundary in the state diagram called the steady state line that separates strain-softening from strain-hardening type of responses. The existence of the steady state line on the state diagram gives rise to the concept of the state parameter.

Hypothetically, there exists a surface in the $e-q-p^{'}$ diagram above which the behaviour of volumetrically contractive samples becomes unstable. However, these concepts only hold valid for specimens sheared under the same boundary conditions prepared by the same technique and presenting approximately the same initial degree of saturation. A number of parameters known to have an important influence in undrained deformations are discussed in the next section.

2.4 Factors Affecting Deformation Characteristics

The vast amount of research done concerning the behaviour of sands tested in an undrained environment has lead to the recognition of different parameters that govern the mechanical response. Density and initial state of stresses were previously introduced as parameters controlling the undrained behaviour of granular materials. However, other factors are known to influence the stress-deformation mechanisms. Stress or strain paths [100, 106, 93, 80], initial anisotropy[106], degree of saturation[46, 99], fines content [102, 103], intermediate principal stress [92, 106], particle shape [95], strain rates [9], and boundary conditions [32, 105] are among other factors known to have an important effect on the undrained response of sands. The effects of some of these parameters on the undrained behaviour of granular materials are reviewed in the present section.

2.4.1 Type and Rate of Loading

Among the factors known to have an effect on the deformation characteristics of an undrained specimen is the type of loading. Stress or strain-controlled experiments are conducted depending on the field condition that needs to be mimicked. Although the great majority of experimental results are reported from strain controlled tests, there exists evidence that indicates that both loading patterns produce different ultimate states [48, 4, 103]. To examine the effects of type of loading and the effects of strain rate, Yamamuro and Lade (1998) conducted stress-controlled tests and strain-controlled tests with different strain rates on Nevada sand with 20 % fines. The results of these experiments are reproduced in Figure 2.7. It is observed that increasing the strain rate produces a significant effect in steepening the effective stress paths. This behaviour has also been reported for undrained tests at high pressures by Yamamuro and Lade [101].

In contrast, from a limited study (three strain-controlled tests), Castro *et al.* [15] reported “no significant difference between results from load-controlled and strain-controlled

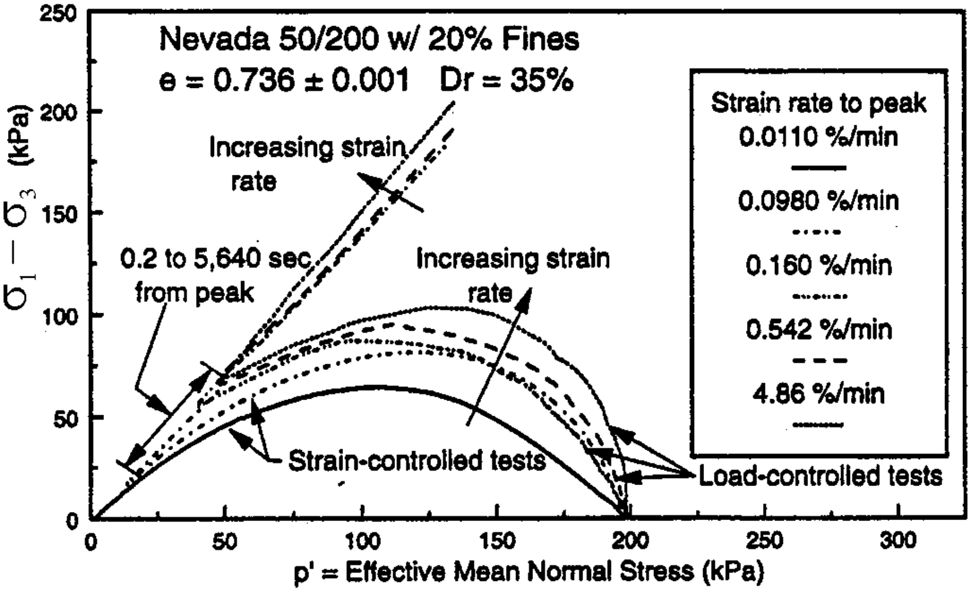

Figure 2.7: Effect of type and rate of loading on Nevada sand (adapted from Yamamuro *et al.* 1998)

tests". This same behaviour was later observed by Sladen *et al.* [82]. They reported "no significant differences are apparent between steady state parameters determined by the two methods".

Although the results of these investigations are contradictory, the ability of a specimen to withstand a deviatoric load should be affected by the imposed loading rate when a sufficiently high percentage of fines are present. The addition of fine particles may cause various effects in the structure, mainly, the ability of the medium to allow fluid flow is reduced, increasing the interaction between the fluid and the particles.

The results presented in Figure 2.7 suggest that the position of the SSL can depend on the loading rate. Further, stress or strain controlled type of loading can also influence the response of the specimen.

There are various practical implications of this behaviour. The transient deformation mechanisms occurring in a soil deposit during an earthquake are neither load nor strain controlled. If a given deposit contains enough fines so that its behaviour is affected by the loading rate, the concept of steady state line breaks down because its position may be influenced by the type and rate of loading, and the prediction of liquefaction susceptibility becomes more complex.

2.4.2 Mode of Shear

Another factor that has been identified as influencing the undrained deformation characteristics is the shape of the boundary. When a drained direct shear test is conducted in a sand specimen a failure plane is induced by the apparatus (*i.e.*, the horizontal plane) which does not necessarily corresponds to the weakest plane [25]. The stress is also higher at the boundaries than at the centre. This condition results in progressive failure. Thus, the mode of shearing highly influences the overall behaviour of a given specimen. Finno *et al.* [32] presented results of masonry sand tested undrained under plain-strain and triaxial conditions. The results of the tests show that different steady state lines are obtained for the two types of tests. A specimen can exhibit either strain softening or strain hardening characteristics even though confined under the same stress and having the same void ratio, just by being sheared under different boundary conditions.

2.4.3 Principal Stresses Direction and Fabric Anisotropy

The direction of the principal stresses with respect to the bedding plane has been found to have a considerable influence on the response of granular materials when sheared under consolidated undrained conditions.

Yoshimine *et al.* [106] conducted hollow cylinder torsional tests on Toyura sand using the dry deposition method for the construction of the sample. The hollow cylinder device allows the control of the principal stress direction and the intermediate principal stress. The angle of the maximum principal stress to the normal of the bedding plane is denoted as α whereas the intermediate principal stress coefficient is b. The results of some of these experiments are summarized in Figure 2.8, which indicates that significantly different stress-strain responses are obtained from tests approaching axial compression ($\alpha = 15°$) to tests where the mayor principal stress is parallel to the bedding plane ($\alpha = 90°$).

Similar results were reported by Uthayakumar and Vaid [92]; they conducted tests using a hollow cylinder torsional shear device. For a given initial stress and density state, the behaviour of the sand was found to be influenced by both b and α during shear. An increase in α from 0° to 90° at constant b enhanced the contractive behaviour. In fact, it was found that the behaviour may change from dilative when $\alpha = 0°$ to strongly contractive

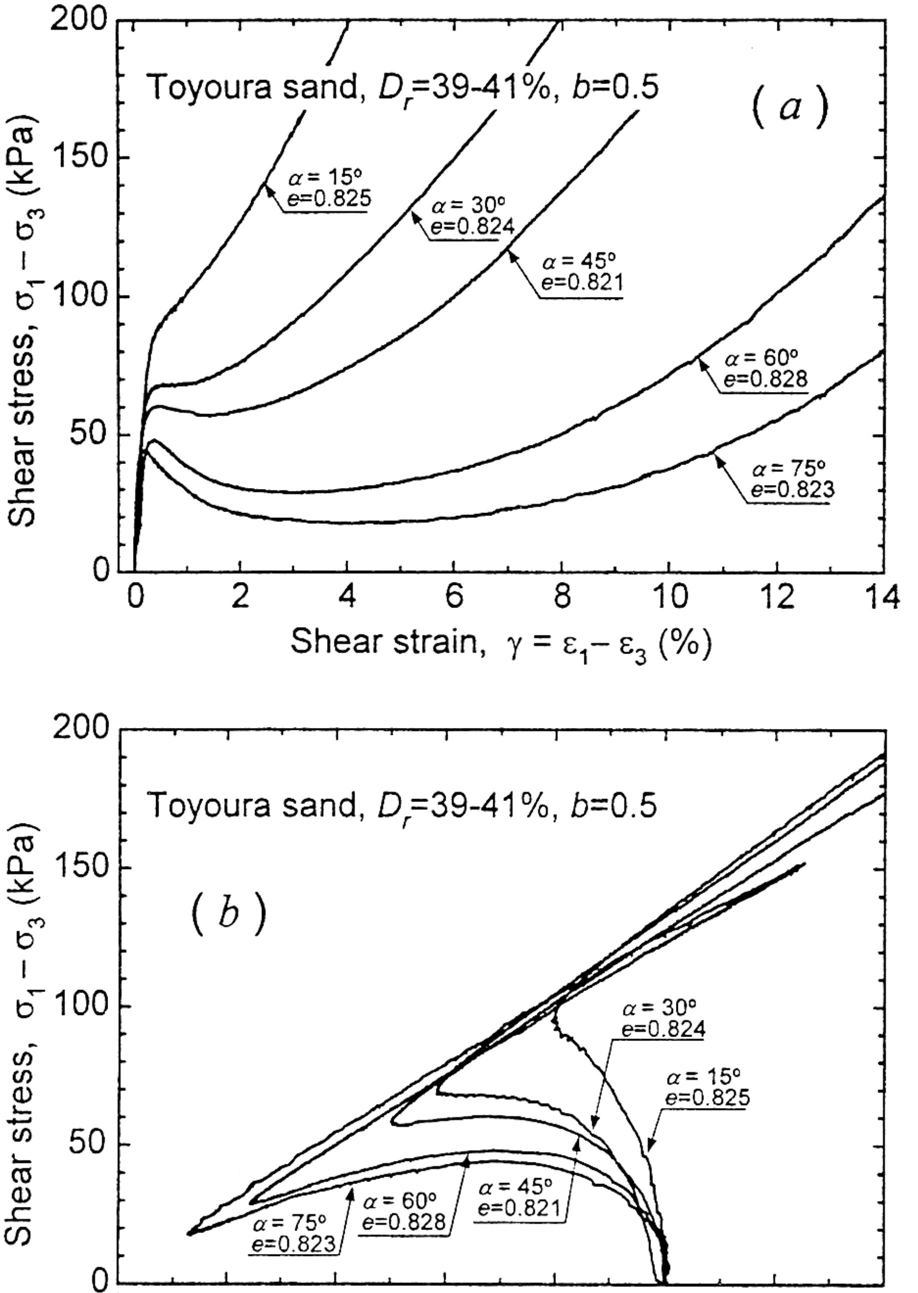

Figure 2.8: Hollow cylinder torsional shear tests on Toyura sand showing the effect of mode of shear (from Yoshimine *et al.* 1998)

when $\alpha = 90°$. Thus, the residual strength depends not only on void ratio, but also on loading direction and intermediate principal stress when the arrangement of the particles is initially anisotropic. Since the principal stress direction in soil elements along potential failure surface varies substantially, the use of a single residual strength value for a given void ratio estimated from triaxial compression tests ($\alpha_\sigma = 0°$, $b = 0$) alone can overestimate the factor of safety against a flow failure, considering that this loading mode is most resistant to contractive deformation, and in fact may not even be contractive [92].

The results show the importance of mode of shear on the response of undrained samples. Further, they highlight the existing relationship between liquefaction susceptibility and the initial arrangement of the grains. The observed anisotropic behaviour previously reported is a consequence of the method of sample preparation. It has been shown that contacts between particles can increase in the direction of loading [26]; hence, it is expected that resistance to loading would be reduced if loading is applied in a direction where fewer contacts exist.

2.4.4 Degree of Saturation

Lade and Pradel [46] investigated the validity of Drucker's stability criteria by conducting undrained experiments in which the degree of saturation was varied. Their conclusion was that contractile sands become unstable if the degree of saturation is sufficiently high. The results indicate that unstable behaviour is enhanced by higher saturation degrees. Reducing the fraction of air present in a given soil causes a considerable reduction of the compressibility of the air-liquid phase.

2.4.5 Grain Crushing

Depending on the mechanical and morphological characteristics of the particles, crushing can occur during shear [8, 45]. Grain crushing typically occurs at effective stresses greater than 1 to 2 MPa. However, grain crushing can occur at lower effective confining stresses in some silty sands or clean sands composed of relatively weak minerals. For example, grain crushing has been reported to occur at a mean effective stress of approximately 220 kPa in Mai-Liao silty sand [38]. As a consequence of crushing at higher stresses, the grain size distribution and the number of contacts carrying load can be affected. For example, It has been found that at high confining stresses the slope of the steady state line significantly increases [8]; thus, samples with the same state parameter (ψ) may exhibit different behaviour as a consequence of the higher confining forces.

2.5 Micromechanics of Granular Media

2.5.1 Microscopic Descriptors of Granular Assemblies

Micromechanics can be defined as a branch of geo-mechanics that deals with the study of the behaviour of granular structures considering physical processes at the particle level.

Granular materials can be envisaged as a collection of discrete elements with particular morphology and mechanical properties interacting with their neighbours by means of contacts. The macroscopic properties of granular materials are intimately related to the particle characteristics and their mode of interaction. It was shown in the previous sections that information about the porosity of a given specimen is insufficient to adequately describe its behaviour upon the application of a load. The description of a granular assembly from a micromechanical perspective uses average quantities obtained at the inter-particle level. The average particle coordination number is the most fundamental of such quantities, and it is defined as the average number of contacts per particle. Given the number of particles N in a given assembly, the average coordination number γ of the assembly is calculated from

$$\gamma = \frac{M}{N} \tag{2.2}$$

where M is twice the number of physical contacts in the assembly. The importance of the coordination number can easily be understood if it is considered that a given assembly with higher coordination number is more stable that the same assembly with a lower γ. The average coordination number by itself does not reflect the density of contacts in a given of volume. A more adequate descriptor that overcomes this hurdle is the average contact density defined as follows:

$$m_v = \frac{M}{V} \tag{2.3}$$

where V is the volume of the assembly. The previous descriptors are fundamental in micromechanics; it will be shown that their evolution during the deformation process, relates to the state of stresses observed at the boundary and to the static stability of the granular structure. These average descriptors, however, do not provide information about the spatial orientation of contacts and the magnitude and direction of forces transmitted through them. Additional tensorial descriptors that overcome this difficulty are therefore needed.

2.5.2 Contact Normal Distribution

Pioneering studies in the field of micromechanics were conducted on idealized assemblies of particles molded from photo-elastic sensitive material [24, 26]. Loading tests were conducted from which the magnitude and direction of the forces between contacting particles could be studied. It was observed that forces were transmitted through chains of particles aligned in the direction of loading. In this way, the evolution of forces and their microscopic distribution were recognized as processes resulting from the imposition of loads.

The stresses imposed at the boundary of a granular assembly are carried by inter-particle contacts. However, it is only during the last decades that contact orientation and their evolution during loading have been quantified. Oda [59] conducted interesting experiments where samples of sands were impregnated with water-resin mixture at different stages during drained triaxial compression. Meticulous analysis of thin sections showed that the distribution of contacts readjusted during deviatoric loading to maximize contact alignment along the direction of the maximum principal stress. From a number of similar studies [52] it is now recognized that during a biaxial experiment, the contact orientation is maximized along the direction of the mayor principal stress.

The gradual redistribution of contacts during loading into an anisotropic state is known as the creation of *contact anisotropy*. A convenient way of representing the distribution of contacts in plane assemblies is to plot a polar histogram of the portion of contacts with normal falling inside an angle $\Delta\theta$. The definition of a contact normal *i.e.*, a unit vector $\boldsymbol{n}^c$ normal to a tangential plane to the point of contact, is depicted in Figure 2.9. A polar histogram showing such a distribution is presented in Figure 2.10. From a number of experimental and numerical studies it has been recognized that when distributions of contact normals are plotted using polar histograms, characteristic statistical arrangements emerge. The distribution depicted in Figure 2.10 was created using an small assembly consisting of 1000 particles and it has the shape of a *peanut*.

It is expected that the histogram, when taken over a sufficiently large specimen, will become smooth so it can be represented by a continuous function $E(\theta)$. A convenient way

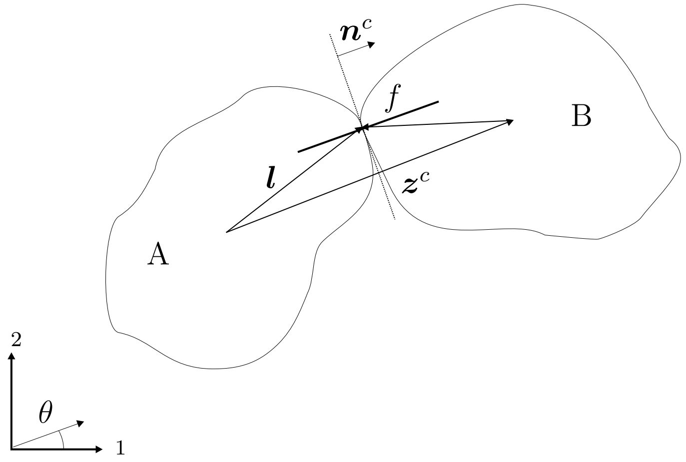

Figure 2.9: Definition of the particle contact normal, contact vector, branch vector and contact force

of describing the distribution of contact normals in plane systems by a continuous function has been suggested by Rothenburg [68].

A contact formed by two particles will contain two contact normals with the same orientation, but different direction. Each contact vector will correspond to one particle. This observation indicates that the proposed function should have the property $E(-\theta) = E(\theta)$. Because of this symmetry, the function $E(\theta)$ can be represented by an infinite Fourier series of even order terms as follows:

$$E(\theta) = \frac{1}{2\pi}\left(1 + a\cos 2(\theta - \theta_a) + b\cos 4(\theta - \theta_b) + \dots\right) \tag{2.4}$$

The limit of the expansion can be limited to the second order terms, although for systems comprising particles other than disc-shaped, truncation up to the fourth term might be necessary for a more accurate representation. The terms a and b are known as *coefficients of contact normal anisotropy* and are related to the intensity of contact normals in principal directions, coincident with unit vectors 1 and 2. The constant terms θ_a and θ_b represent the principal directions of anisotropy for contact normals. Analysis of (2.4) indicates that the terms a and b describe deviations from the isotropic state. For the case where $a = b = 0$, $E(\theta)$ describes the unit circle, *i.e.*, the isotropic condition.

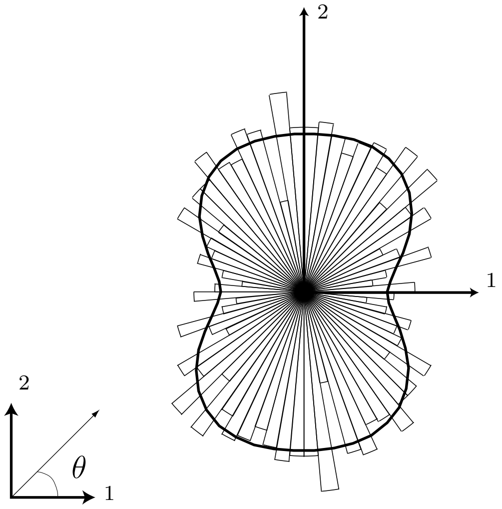

$$a = 0.282$$
$$b = 0.092$$
$$\theta_a = 1.542$$
$$\theta_b = 0.778$$

$$2\pi\, E(\theta) = 1 + a\cos 2(\theta - \theta_a) + b\cos 4(\theta - \theta_b)$$

Figure 2.10: Measured contact normal directions and approximation to the distribution by a continuous function

The function $E(\theta)$ is normalized by the term $(1/2\pi)$ and it has the following property:

$$\int E(\theta) d\theta = 1 \tag{2.5}$$

2.5.3 Contact Forces Distribution

The parameters of contact normal anisotropy are adequate descriptors of the evolution of contacts during a biaxial test. Since forces are transmitted by inter-granular contacts, it should be expected that similar descriptions could be obtained to represent the distribution of forces. The force at a contact (f^c) has a magnitude and a direction (Figure 2.9) and can be described in vectorial form. The average contact force acting on contacts with orientation θ in a given assembly can be further decomposed into two orthogonal components, one average normal force component $\bar{f}^c_n(\theta)$, and one average tangential component $\bar{f}^c_t(\theta)$. Letting $\boldsymbol{n}^c = \{\cos\theta, \sin\theta\}$ and $\boldsymbol{t}^c = \{-\sin\theta, \cos\theta\}$, the following average contact force distribution $\bar{f}^c_i(\theta)$ can be obtained:

$$\bar{f}^c_i(\theta) = \bar{f}^c_n(\theta)\boldsymbol{n}^c + \bar{f}^c_t(\theta)\boldsymbol{t}^c \qquad i, j = 1, 2 \tag{2.6}$$

The form of the average distributions $\bar{f}^c_n(\theta)$ and $\bar{f}^c_t(\theta)$ were first proposed by Rothenburg [68] based solely on physical considerations and have been verified using numerical

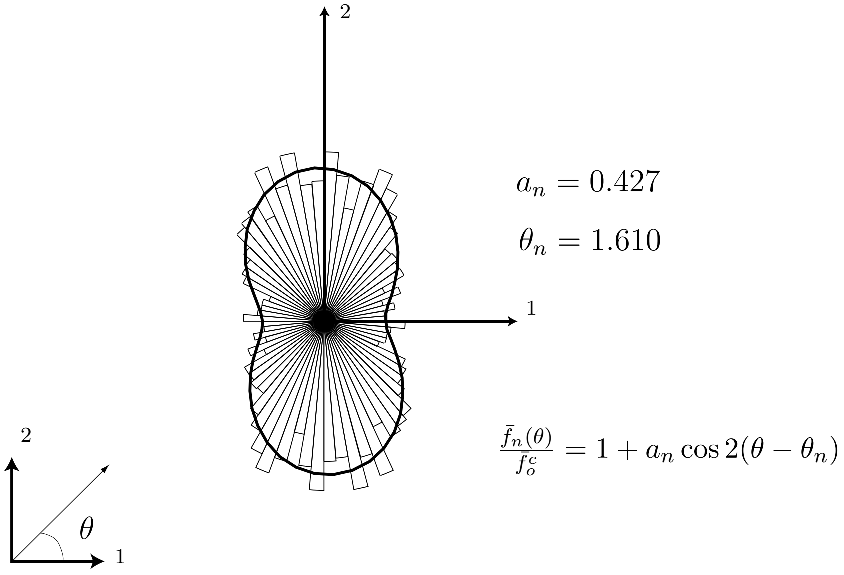

Figure 2.11: Measured average normal contact force and approximation to the distribution by a continuous function

simulations of two- and three-dimensional assemblies [6, 19, 63].

Average Contact Normal Force Distribution

The distribution of the average normal contact forces $\bar{f}^c_n(\theta)$ can be represented by a truncated Fourier series of even orders. This expansion up to the second order is given as:

$$\bar{f}^c_n(\theta) = \bar{f}^c_o \left\{1 + a_n \cos 2(\theta - \theta_n)\right\} \tag{2.7}$$

As in the case of the contact vector distribution, the parameter a_n represents the deviation of the distribution from an isotropic state and is known as the *coefficient of contact normal force anisotropy*. The parameter θ_n is the principal direction of anisotropy. The parameter $\bar{f}^c_o$ represents the normal average contact force over different orientation groups and may differ from the average normal contact force ($\sum f^c_n/V$) if the contact normal orientation distribution is anisotropic.

Figure 2.11 shows a polar histogram of contact normal force distribution measured from an assembly of 1000 particles, along with the continuous approximation using relation (2.7).

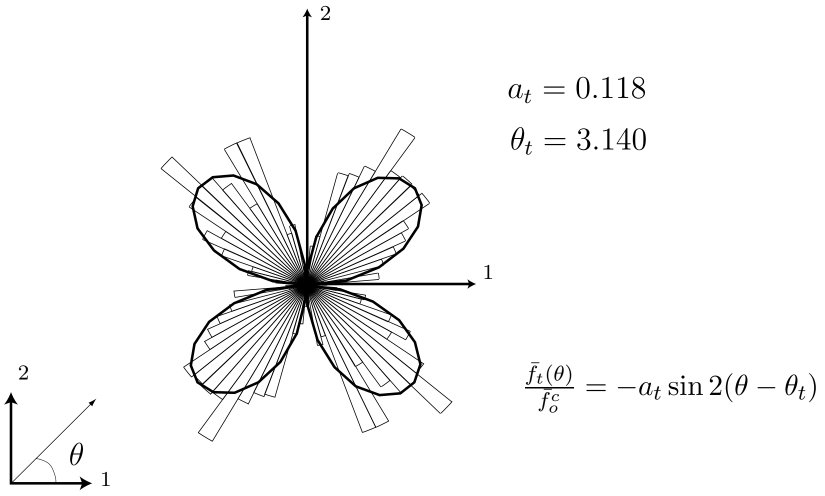

Figure 2.12: Measured average shear contact force and approximation to the distribution by a continuous function

Average Tangential Contact Forces Distribution

The distribution of tangential contact forces $\bar{f}_t^c(\theta)$ can also be represented by a truncated Fourier series, this time of odd numbers.

$$\bar{f}_t^c(\theta) = -\bar{f}_o^c \left\{ a_t \sin 2(\theta - \theta_t) \right\} \tag{2.8}$$

The parameter a_t is known as the *coefficient of tangential (shear) force anisotropy*, and the angle θ_t represents the mayor direction of anisotropy.

Figure 2.12 shows a measured polar histogram of contact tangential force distribution along with the continuous approximation using relation (2.8).

Tangential contact forces are considered positive if they induce a counter-clockwise rotation.

2.6 Stress Tensor

Understanding the macroscopic behaviour of granular material requires a comprehensive examination of mechanisms acting at the inter-particle level. Of special importance is the relation existing between the state of stresses acting at the boundary of a granular assembly and the inter-particle forces. Consider the system depicted in Figure 2.13 where a granular system is being subjected to a certain state of stresses imposed at the boundary. The equilibrium condition must be satisfied at each point at the surface of the stressed body. This condition implies that if $\mathbf{T}^\beta$ is the surface force applied on the boundary of the solid, and $\mathbf{n}^\beta$ represents the external normal to its surface, the stress tensor can be envisaged as a linear transformation between the two, that is:

$$\mathbf{T}_i^\beta = \sigma_{ij}^\beta \, \mathbf{n}_j^\beta \qquad i, j = 1, 2, 3 \tag{2.9}$$

The above relation applies when tractions are applied to a continuous surface. The stress tensor in a discrete system will also involve tractions applied to the surface of a body. Rothenburg [68] showed that the boundary stress tensor σ_{ij}^β can be related to the forces applied at discrete points on the surface (x^β) by the following expression:

$$\sigma_{ij}^\beta = \frac{1}{V} \sum_{\beta \in S} f_i^\beta \, x_j^\beta \qquad i, j = 1, 2, 3 \tag{2.10}$$

Another form of this expression which makes no reference to the shape of the surface can be obtained by relating internal contact forces f^c and contact vectors l^c with boundary forces as:

$$\sum_{\beta \in S} f_i^\beta \, x_j^\beta = \sum_{c \in V} f_i^c \, l_j^c \tag{2.11}$$

The above equation relates internal inter-particle forces with the state of forces applied at the boundary (Figure 2.13). Using the relation between discrete forces applied at the boundary and internal contact forces, the stress tensor can be calculated in terms of interparticle forces as follows:

$$\sigma_{ij}^\beta = \frac{1}{V} \sum_{c \in V} f_i^c \, l_j^c \qquad i, j = 1, 2, 3 \tag{2.12}$$

The terms f_i and l_j refer to scalar components of a contact force vector $\boldsymbol{f}^c$ and a contact vector $\boldsymbol{l}^c$ at a contact location. The above expression shows that the macroscopic stress tensor can be obtained from consideration of contact forces and microstructure described by contact vectors. This relation is equally valid for plane and three-dimensional systems. For plane systems, V is the area A occupied by the assembly, and the indices are restricted to $i, j = 1, 2$.

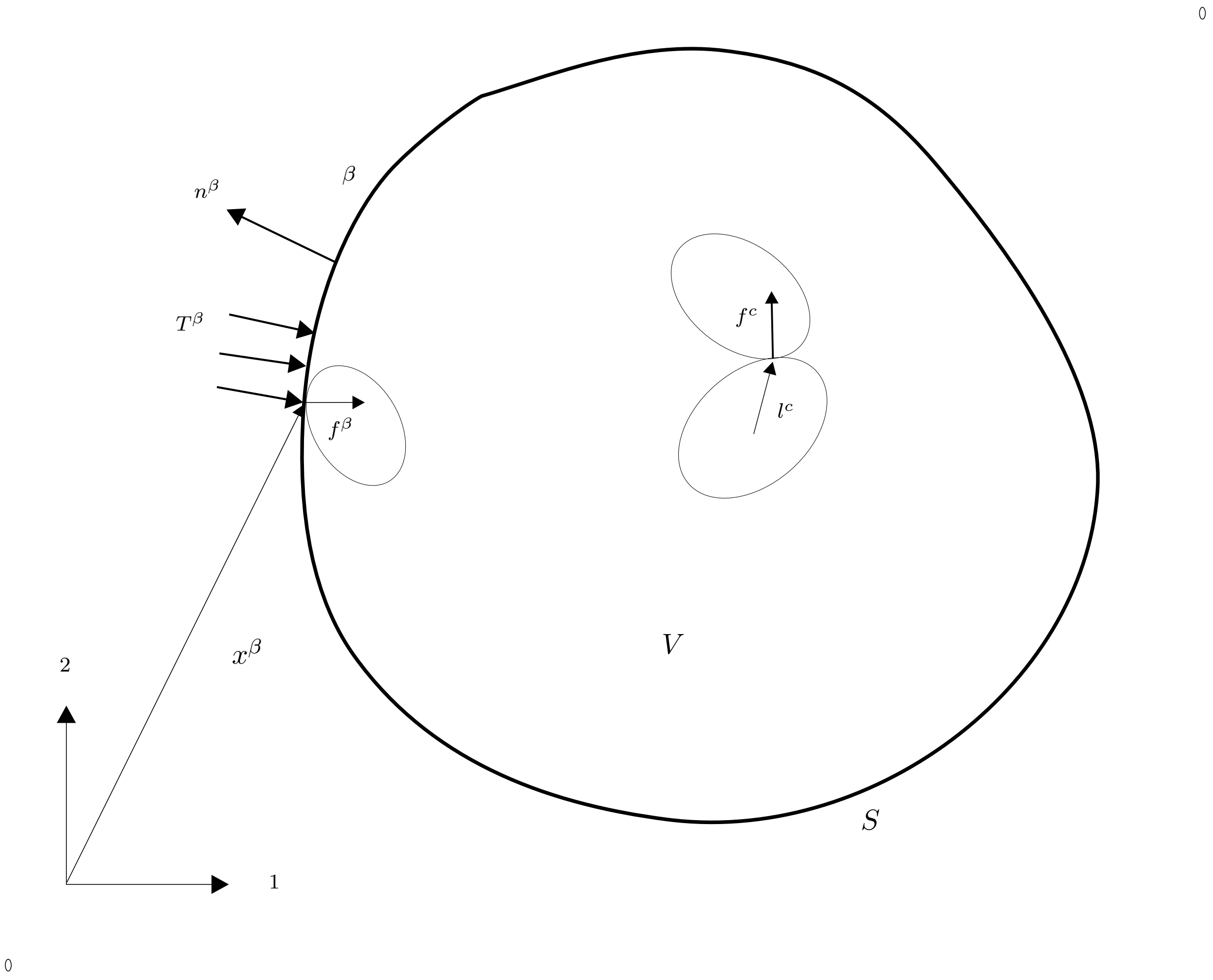

Figure 2.13: Stress tensor components

The stress tensor can be viewed as a contribution of the contact-force vector to many subregions in the assembly volume. Contributions of different subregions are expected to be different. However, as the number of particles increases, and thus also the number of sub-regions, the overall differences are expected to become smaller. The average tensor from a discrete assembly is an accurate analog to the stress tensor in continuum mechanics when sufficiently large systems are considered.

Expression (2.12) was derived under different forms by several authors [68, 20].

Static equilibrium requires that the resulting moment around each coordinate axis in any point of the solid be nil. This condition is satisfied if and only if:

$$\sigma_{ij}^{\beta} = \sigma_{ji}^{\beta} \qquad i, j = 1, 2, 3 \tag{2.13}$$

this shows that σ_{ij}^{β} is a symmetric tensor.

2.6.1 Average Stress Tensor from Fabric Descriptors

Although the average stress tensor can be calculated considering the interparticle forces according to relation (2.12), it has been shown that the product $f_i^c\, l_j^c$ can be approximated by the use of averages of contact and force vectors over finite, but large volumes of particle assemblies [68]. Description of contact vectors are made in a cartesian frame of reference using spherical coordinates (*i.e.*, $0 \leq \beta < \pi$ and $0 \leq \theta < 2\pi$).

Average values of the contact term $f_i^c\, l_j^c$ are calculated for all contacts whose normals fall within the elementary solid angle $\Delta\Omega = \sin\beta\, \Delta\beta\, \Delta\theta$. Product terms corresponding to a group orientation Ω_g can be expressed by their average as $\overline{f_i^c\, l_j^c}(\Omega_g)$. If group averages are used, it is necessary to introduce a discontinuous function $E(\Omega)$ that describes the fraction of the total number of contact normals falling in $\Delta\Omega$. This function is normalized in the sense that:

$$\sum_{\Omega_g} E(\Omega)\; \Delta\Omega = 1 \tag{2.14}$$

The average stress tensor can be now approximated by

$$\sigma_{ij}^{\beta} = m_v \sum_{\Omega_g} \overline{f_i^c\, l_j^c}(\Omega)\, E(\Omega)\, \Delta\Omega \qquad i, j = 1, 2, 3 \tag{2.15}$$

where m_v is the contact density defined in (2.3). If it is further assumed that there is no statistical bias between f^c and l^c, then $\overline{f_i^c\, l_j^c} = \bar{f}_i^c \bar{l}_j^c$. For a volume comprising a large number of particles, the discontinuous functions involved in expression (2.15) can be considered continuous, and the average stress tensor can be now approximated by:

$$\sigma_{ij}^{\beta} = m_v \int_{\Omega} \bar{f}_i^c(\Omega)\, \bar{l}_j^c(\Omega)\, E(\Omega) d\Omega \qquad i, j = 1, 2, 3 \tag{2.16}$$

The developments thus far presented are equally applicable to two dimensional systems, for which case the solid angle Ω becomes θ and the continuous functions will be given by (2.4), (2.6). For two dimensional systems, relation (2.16) becomes:

$$\sigma_{ij}^{\beta} = m_v \int_0^{2\pi} \{\bar{f}_n^c(\theta) \boldsymbol{n}_i^c + \bar{f}_t^c(\theta) \boldsymbol{t}_i^c\}\, \bar{l}_j^c(\theta)\, E(\theta) d\theta \qquad i, j = 1, 2 \tag{2.17}$$

Relation (2.17) can be simplified for the case of assemblies of discs, where the direction of the contact vector is coincident with that of the contact normal. If it is further assumed that the average contact length of all discs is independent of the contact vector orientation (*i.e.*, $\bar{l}^c(\theta) = \bar{l}^c_o \boldsymbol{n}^c_j$) over the range of diameters present in the system, relation (2.17) simplifies to:

$$\sigma^{\beta}_{ij} = m_v \bar{l}^c_o \int_0^{2\pi} \{\bar{f}^c_n(\theta)\boldsymbol{n}^c_i\boldsymbol{n}^c_j + \bar{f}^c_t(\theta)\boldsymbol{t}^c_i\boldsymbol{n}^c_j\}\, E(\theta)d\theta \qquad i,j=1,2 \tag{2.18}$$

Although (2.18) was derived assuming disc-shaped particles, Rothenburg and Bathurst (1993) have shown that it can be applicable to assemblies of elliptical particles without introducing a considerable error.

2.7 Stress-Force-Fabric Relationship

It has been shown in the previous sections that discrete information at the inter-particle level can be adequately represented using continuous distributions for the distributions of average contact forces and average contact vectors. These are substituted in relation (2.18) and the result from integration is an approximation to the stress tensor. For the case of biaxial compression tests, numerical simulations indicate that principal directions of anisotropy are almost coincident with the direction of loading, that is $\theta_a \approx \theta_n \approx \theta_t \approx \pi/2$. The direction of the fourth order contact anisotropy is very close to 45^o ($\theta_b \approx \pi/4$). Considering these observations, a number of relations commonly use to describe the strength of a soil specimen can be derived by integrating the relation (2.18).

The mobilized friction angle is found to be:

$$\sin\phi_{\text{mob}} = \frac{\sigma^{\beta}_{11} - \sigma^{\beta}_{22}}{\sigma^{\beta}_{11} + \sigma^{\beta}_{22}} = \frac{a + a_n + a_t + \frac{a_t b}{2} - \frac{a_n b}{2}}{2 + a\,a_n} \tag{2.19}$$

The anisotropy coefficients are always less than 1, thus, neglecting their products will not induce a considerable error. When anisotropy products are neglected, the previous relation simplifies to the following:

$$\sin\phi_{\text{mob}} \approx \frac{a + a_n + a_t}{2} \tag{2.20}$$

The above relation for the mobilized friction angle was originally derived by Rothenburg [68], and it is only a function of the parameters of anisotropy, that is, the spatial arrangement of contacts and forces.

The following invariant quantities associated with Mohr circle may also obtained:

$$p = \frac{\sigma_{11}^{\beta} + \sigma_{22}^{\beta}}{2} = \frac{m_v\, \bar{l}_o^c\, \bar{f}_o^c}{2} \left\{1 + a\, a_n\right\} \tag{2.21a}$$

$$q = \frac{\sigma_{11}^{\beta} - \sigma_{22}^{\beta}}{2} = \frac{m_v\, \bar{l}_o^c\, \bar{f}_o^c}{4} \left\{a + a_n + a_t + \frac{a_t b}{2} - \frac{a_n b}{2}\right\} \tag{2.21b}$$

2.8 Liquefaction Simulations using DEM

Previous simulations using the Distinct Element Method (DEM) have considered the effects of pore pressure to simulate liquefaction [36, 35, 53, 50]. These methods have been applied to assemblies of disc-shaped particles subjected to dynamic and cyclic loadings.

Hakuno [36] was the first to propose a technique to numerically couple fluid flow with the DEM considering individual pores. The volume change of each pore was used to calculate pore pressure generation by assigning elastic properties to the fluid. The technique incorporates the effects of the fluid based on four assumptions:

- pore volume changes are the result of particle movements
- pore pressure develops by change of pore volume
- forces act on the particles due to excess pore pressures
- flow occurs between pores due to gradients produced by discrete pore pressures

The second assumption implies that the fluid contained in a pore space behaves as a perfectly elastic material and therefore any change in volume in the pore will produce a force in the section of the particle that limits the pore space. The excess pore pressure U for pore K was obtained from:

$$U_K = B_w \frac{\Delta V_K}{V_K} \tag{2.22}$$

where B_w is the volumetric stiffness of the water and V_K is the volume of pore K. Possible buoyancy effects were not considered.

In an attempt to optimize Hakuno's technique, Nakase *et al.* (1999) used an alternative approach where pore pressure generation was not considered at the pore level, but in square-cell elements. The dimensions of the cells dx and dy are chosen such that there are about

15 discs whose centres are located inside the cell. The total volume change $\Delta V^{(i,j)}$ of the pores in the cell (i,j) are calculated using weighted average displacements of the particles in the four neighbouring cells $(i-1,j)$, $(i+1,j)$, $(i,j-1)$ and $(i,j+1)$. To compute the excess pore pressure, the method employs the same approach as Hakuno's. Once the volume change of cell (i,j) is computed, the pore pressure change is obtained from

$$\Delta u_w^{(i,j)} = \gamma_w \Delta V^{(i,j)} \frac{1}{dx\, dy \kappa^{(i,j)}} \tag{2.23}$$

where γ_w is the unit weight of the water and $\kappa^{(i,j)}$ is the storage coefficient.

The volume change in cell (i,j) is computed by considering particle displacements in the neighbouring cells.

The pressure difference among cells generates a gradient that drives water flow. A finite difference scheme has been used by Nakase *et al.* [53] to solve the equations describing pore pressure dissipation. Once pressure dissipation has occurred after a time increment Δt, the remaining pressures are converted into forces acting on particles.

To obtain high internal friction angles corresponding to natural granular soils, no rolling was allowed at the contacts during the simulation.

2.8.1 Indirect Methods

Undrained tests are generally known as constant volume tests as a consequence of the low compressibility of particles and fluid. In principle, it will seem that drained strain-controlled constant volume test is equivalent to an undrained test. This idea have lead some researchers to conduct dry simulations at a constant volume and assume that the results are representative of undrained tests [56, 29]. The former assumption however, nullifies the possibility of studying pore pressure generation at the microscopic scale.

2.8.2 Summary

The method proposed by Hakuno [36] and Hakuno *et al.* [35] considers pressures to be equal at the end of the time step to solve for the equation of fluid flow. This assumption is overcome in the method proposed by Nakase *et al.* by employing a finite difference scheme of integration and solving for pressures at the end of each calculation cycle. The solution of flow equations, however, is particular to each cell and does not consider the interaction of the assembly as a system. Further, the method proposed by Nakase *et al.* to generate pore pressures considering weighted averages of incremental displacements cannot be directly extended to the case of assemblies comprised of elliptical particles, where the effect of incremental rotational displacement may be considerable.

Nevertheless, a review of the methods available in the literature provides important information regarding the different assumptions involved in the methodologies, to delineate a point of departure for the present research. Table 2.1 summarizes the fundamental assumptions of each method.

Effect	**Reference** [36]	**Reference** [35]	**Reference** [53]
Elastic fluid	✓	✓	✓
Pore pressure considering volumetric changes at pore level	✓	✓	-
Approximation of volumetric changes by considering weighted averages of incremental displacements	-	-	✓
Body forces	-	✓	✓
Buoyancy forces	-	-	-
Pore pressure equalization	✓	✓	-
Pressure using finite difference	-	-	✓
Elliptical particles	-	-	-
Non-linear contact law	-	-	-

Table 2.1: Assumptions involved in previous fluid-flow coupled distinct element methods

2.9 General Comments

General comments on the three different topics reviewed in this Chapter are presented below.

Undrained Laboratory Tests

The results of some undrained experiments considered relevant to the present dissertation have been reviewed. The purpose of the present research is to develop a novel technique that will contribute to a better understanding of the mechanics of undrained deformations.

The following points summarize the reviewed works regarding undrained experiments to study liquefaction phenomena:

1. The steady state line concepts originally proposed by Casagrande (1936) [12] hold valid for a particular mode of shearing, particular boundary conditions, and a particular initial structure. The undrained behaviour in this case can be characterized by the void ratio and initial confining stress at the start of shear.
2. Other parameters different from the void ratio and the initial state of stresses are known to have an effect on the deformation of undrained granular samples. Among these parameters are the stress or strain paths, initial anisotropy, degree of saturation, fines contents, strain rates, grain crushing, and boundary conditions.
3. The initial fabric of a given specimen is the result of the sample preparation method. The direction of the principal stresses with respect to the bedding plane has a significant effect on the response of the sample when sheared.
4. A number of contradictory conclusions exist. These contradictions may be partly attributed to the lack of an adequate study of the microstructure evolution imposed by the inherent limitations of the laboratory equipment.

Micromechanics of Granular Materials

The micromechanical parameters introduced are adequate descriptors of the macroscopic state of stresses and provide valuable information that can be difficult to obtain from real experiments.

The stress tensor is the result in which the interparticle forces are arranged. Using statistical averages of the number of contacts, the spatial distribution of contacts and interparticle forces, a general expression for the stress tensor can be obtained.

Simulations of Undrained Tests Using DEM

The DEM technique has been used in the past to simulate the behaviour of granular assemblies in an undrained environment. The results of previous research shown that it is feasible to simulate pore pressure generation. The simulations, however, were conducted by applying a dynamic or cyclic load to the assembly, and direct comparisons with biaxial laboratory tests is not feasible.

The techniques developed to incorporate fluid effects have been used in assemblies of perfectly circular particles. Disc-shaped particles present little resistance to rotation, and internal friction angles obtained from such simulations are usually lower than those measured in natural granular soils. This observation led Nakase *et al.* [53] to inhibit rolling at the contacts. Another disappointing aspect of studies with simulated assemblies of discs is the difficulty of controlling the density in these systems [71]. Plane assemblies of discs have an average coordination number (γ) very close to 4 [71], and the study of "loose" systems with coordination numbers close to 3, becomes more difficult.

These difficulties are overcome when elliptical particles are employed. Rothenburg and Bathurst [70] have shown that peak friction angles obtained using elliptical elements are closer to those of natural sands. Furthermore, the average coordination number of these systems can be very close to 3, allowing a higher control on the range of densities that can be achieved. Therefore, the use of elliptical-shaped particles is more appropriate for studying the mechanisms of undrained deformations.

Chapter 3

Development of the Fluid-Flow Coupled Distinct Element Algorithm

3.1 Introduction

Granular materials such as sand and clay are complex materials that exhibit both solid and fluid properties. There are three reasons for this [60]. The first is that geo-materials such as soils are three-phase mixtures of solid, liquid, and gas. The second is that granular materials are not continuous at the microscopic scale, but consist of discrete particles that interact through complex mechanisms. The third is that natural soil is not homogeneous.

Computer simulations are powerful methods that can be used to analyze the behaviour of granular materials. There are two fundamental approaches to simulate soil behaviour under loading. The first approach is based on the principles of mechanics of solids and continua. The soil is treated as a continuum whose behaviour can be described by a set of constitutive relationships. The constitutive relations are mathematical formulae that relate the stress tensor σ_{ij} to the strain tensor ϵ_{ij} . As new testing methods and techniques become available, the dependency of the mechanical behaviour of soils on other parameters not previously considered has become clearer. This has led to the development of more complex constitutive relations that consider a greater number of independent variables and constants, which sometimes have no clear physical meaning.

The second approach to simulating soil behaviour consists of treating the specimen as a collection of discrete elements which behave according to a set of physical laws. This method is usually referred to as particulate mechanics or micromechanics, from which recent developments in theoretical, experimental and computational research have been made. The theoretical approach generally assumes that the medium is made up of granules of idealized shapes or arranged in regular patterns. Regardless of the nature of the assumptions, the micromechanical approach has proven valuable in understanding the behaviour of granular structures in a way that cannot be achieved by continuum approaches.

Experimental studies of particle assemblies have made use of photoelastic sensitive material. In their pioneering study of granular media, Dantu and Wakabayashi [24] observed force distributions and particle behaviour at microscopic levels by using optically sensitive materials. Later, De Josselin de Jong and Verruijt [26] used the same technique to analyze the evolution of forces during the application of a load at the boundaries of a sample. These experimental techniques are of special importance in the field of micromechanics, but are expensive to conduct, and the size of the assembly that can be used is bounded by physical restrictions.

Over the past four decades, theoretical micromechanics has been a subject of study. In this area, the work presented by Rothenburg [68] is of special importance since it provides a link between microscopic force distributions at the particle level and the macroscopic state of stresses at the boundary. Moreover, stress-force-fabric relationships that explained the observed state of stresses were developed. Other research efforts have derived models that considered isotropic [18, 17] and anisotropic [104] fabrics based on theoretical considerations. Although these models have proven useful to gain insight into the dependency of the macroscopic response based on fabric characteristics, some specific assumptions were made: the granules are bounded or that strains are sufficiently small so that contacts are neither created nor lost.

Recent computational micromechanical approaches started with the development of the Distinct Element Method (DEM) by Strack and Cundall [84] and Cundall and Strack [23]. The method was originally developed to simulate interactions of rigid blocks to model rock mechanics problems, but it was later extended to soil mechanics by assuming disc-shaped elements [23] and three-dimensional spheres [21]. The intention of extending the capabilities of the technique to simulate undrained tests was mentioned by Cundall and Stack [23], but it was not until 1988 that fluid interaction effects were incorporated into the DEM by Hakuno and Tamiri [36]. Their technique was successful in simulating pore pressure generation when an assembly of disc-shaped elements was subjected to seismic excitation.

An outline to the DEM is presented in this chapter. Physical and mathematical theories behind the method are introduced in Section 3.2, along with non-linear contact law developments that are based on the theory developed by Hertz.

The approach adopted to couple fluid flow to the DEM is presented in Section 3.3. In this work, fluid flow has been simulated by constructing a network of small pipes or conduits, termed the flow network. The theory and method employed in the construction of the flow network are presented in Section 3.5. The coupling of fluid flow with the system was achieved by solving a system of ordinary homogeneous differential equations.

The procedures adopted to convert pore pressure into forces acting on the particles are described in Section 3.6.

3.2 Distinct Element Method

The Distinct Element Method (DEM) employs a finite difference scheme in which the position of the particles is obtained by integration of Newton's Second Law of motion over a small increment of time Δt. The forces and moments acting on the elements are obtained from force-displacement laws applied at the contacts. Slippage between contacting particles occurs if the frictional resistance at the contact is overcome according to Coulomb's law.

The DEM models a dynamic transient mechanical system which can be envisaged as a network of lumped-mass-dashpot elements in which springs connect masses that represent particles. Although the system is dynamic, the transient state approaches equilibrium if loading at the boundary is sufficiently small that inertial forces are a small fraction of the contact forces acting in the assembly. Kinetic energy is dissipated by introducing numerical damping, without which static equilibrium could not be achieved.

The present Section describes the techniques used to calculate the displacement between elements based on the original work presented by Cundall and Strack [23] extended to the case of elliptical elements, and assuming a non-linear contact law.

3.2.1 Equations of Motion

Consider the two contacting particles A and B whose position is referenced to a cartesian set of coordinates depicted in Figure 3.1. Newton's Second Law applied to the particles can be written as:

$$m(\ddot{\boldsymbol{x}}_i)_N = (\boldsymbol{F}_i)_N \qquad i = 1, 2 \tag{3.1}$$

$$I\,(\ddot{\theta})_N = (M)_N \tag{3.2}$$

where m and I represent the mass and moment of inertia of the particle, and $(\boldsymbol{F}_i)_N$ and $(M)_N$, the net force components and moment acting at the particle centroid at the beginning of the time-step corresponding to t_N. Assuming particle acceleration $\ddot{\boldsymbol{x}}_i$ and $\ddot{\theta}$ to be constant over the interval $t_{N-1/2}$ to $t_{N+1/2}$, using a finite difference technique, particle velocities can be calculated from:

$$\begin{aligned} (\dot{\boldsymbol{x}}_i)_{N+1/2} &= (\dot{\boldsymbol{x}}_i)_{N-1/2} + \frac{(\boldsymbol{F}_i)_N \Delta t}{m} \qquad i = 1, 2 \\ (\dot{\theta})_{N+1/2} &= (\dot{\theta})_{N-1/2} + \frac{(M)_N \Delta t}{I} \end{aligned} \tag{3.3}$$

The coordinates of the particle centroid and the corresponding rotation are calculated at the end of the time step t_{N+1} according to:

$$\begin{aligned} (\boldsymbol{x}_i)_{N+1} &= (\boldsymbol{x}_i)_N + \left[(\dot{\boldsymbol{x}}_i)_{N+1/2}\right] \Delta t \qquad i = 1, 2 \\ (\theta)_{N+1} &= (\theta)_N + \left[(\dot{\theta})_{N+1/2}\right] \Delta t \end{aligned} \tag{3.4}$$

Elliptical Particles

The geometry of circular or disc-shaped particles is readily characterized by its radius R or corresponding diameter D. In the case of elliptical particles, it becomes necessary to introduce two additional parameters to describe their geometry [70]: particle eccentricity and principal axis orientation.

Consider the ellipse shown in Figure 3.2. The geometrical properties of elliptical particles are described using three variables: the angle θ of the mayor axis with respect to the horizontal, an average radius $\bar{R}$ or average diameter $\bar{D}$, and the eccentricity, defined as follows:

$$e_c = \frac{a - b}{a + b} \tag{3.5}$$

where a and b are the mayor and minor axis respectively.

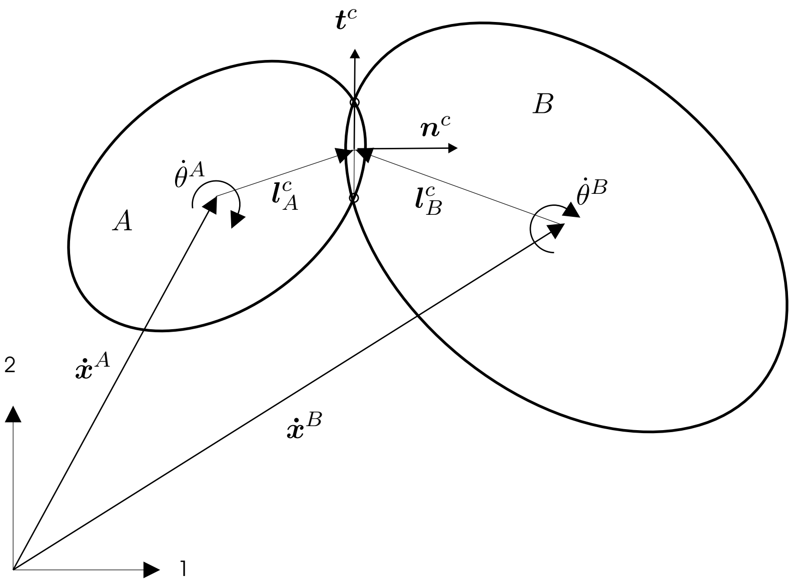

Figure 3.1: Description of particles' position

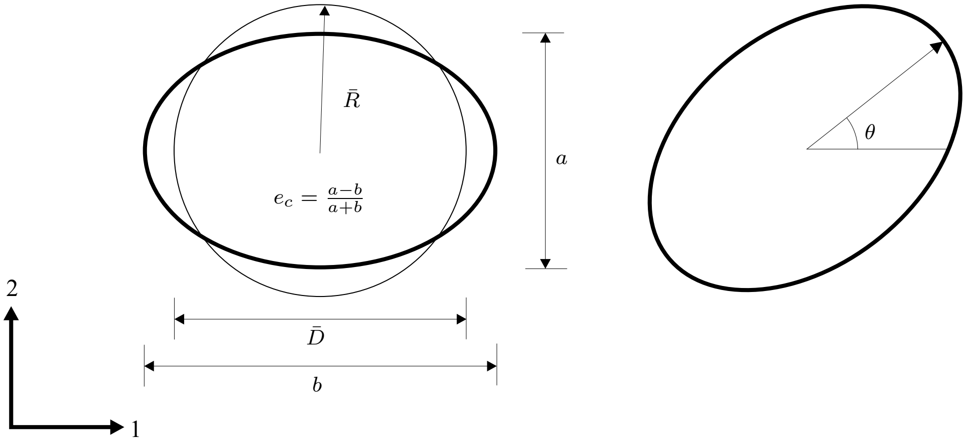

Figure 3.2: Ellipse nomenclature

3.2.2 Force-displacement laws

Following Cundall and Strack [23], interaction between particles is assumed to occur by means of contact forces if the contact area is negligible compared with the dimension of the particles. After application of Newton's Second Law, the centre of mass of a particle A and B moves with velocities $\dot{\boldsymbol{x}}^A$, $\dot{\boldsymbol{x}}^B$ and rotates with angular velocities $\dot{\theta}^A$ and $\dot{\theta}^B$.

Contact displacements can be calculated using the following finite-difference equations:

$$\begin{aligned}(\Delta_n)_{N+1/2} &= [(\dot{\boldsymbol{x}}_i^B - \dot{\boldsymbol{x}}_i^A)_{N+1/2}]\, \boldsymbol{n}_i^c\, \Delta t \qquad i = 1, 2 \\ (\Delta_s)_{N+1/2} &= \{[(\dot{\boldsymbol{x}}_i^B - \dot{\boldsymbol{x}}_i^A)_{N+1/2}]\, \boldsymbol{t}_i^c - (\dot{\theta}^A |\boldsymbol{l}_c^A| + \dot{\theta}^B |\boldsymbol{l}_B^c|)_{N+1/2}\}\, \Delta t \end{aligned} \tag{3.6}$$

Having obtained the incremental displacements at the point of contact, contact force components are updated using:

$$\begin{aligned}(F_n)_{N+1} &= (F_n)_N + (\Delta F_n)_N = (F_n)_N + k_n (\Delta_n)_{N+1/2} \\ (F_s)_{N+1} &= (F_s)_N + (\Delta F_s)_N = (F_s)_N + k_s (\Delta_t)_{N+1/2}\end{aligned} \tag{3.7}$$

where k_n and k_s refer to normal and tangential stiffness.

The final step in the calculation cycle is updating particle forces $\boldsymbol{F}_i$ and moments M, which is done by adding all contact force components and moments in the following manner:

$$\begin{aligned}(\boldsymbol{F}_i)_{N+1}^k &= \sum_{n=1}^{n_k} [(F_n)_{N+1}\, \boldsymbol{n}_i^c + (F_s)_{N+1}\, \boldsymbol{t}_i^c] \quad i = 1, 2 \\ (M)_{N+1}^k &= |\boldsymbol{l}^k| \sum_{n=1}^{n_k} [(F_s)_{N+1}]\end{aligned} \tag{3.8}$$

When simulations of cohesionless particles are conducted, the contacting particles are not allowed to take any tensile force, that is, $F_n > 0$. For the case $F_n \leq 0$, the contact disintegrates, and particles are not considered to be in contact. Disrupted contacts can reform again with further deformation of the assembly.

A Coulomb frictional type of law is employed and slippage between particles is initiated once a threshold tangential force is reached. The criteria for commencement of slippage is expressed as:

$$\begin{cases} F_s < \mu\, F_n & \text{No slippage} \\ F_s \geq \mu\, F_n & \text{Slippage} \end{cases} \tag{3.9}$$

3.2.3 Non-Linear Stiffness

To compute contact forces in (3.7), it is necessary to assign a stiffness to the contact in both the normal k_n and tangential k_t directions. Computer simulations of solid particle systems are usually performed using the method proposed by Cundall and Strack [23], where linear elastic laws for normal and tangential stiffness are assumed. A more realistic contact law based on established theories of contact mechanics has been implemented by some authors [22, 90, 55, 19]. Usually the classical theory developed by Hertz for two elliptical bodies in contact is implemented. It has been shown that the effect of a non-linear contact law does not have a significant effect on the macroscopic strength of dense assemblies of spheres [22, 19]. In the present work however, a non-linear contact law was implemented in order to avoid high interparticle penetrations that alter the volumetric response of the pores, which, in turn, is used to calculate pore pressure generation.

Normal Stiffness

In general, for particle shapes other than circular, stiffness contact properties are dependent on the location of the contact point on the particle's surface. This conclusion follows from Hertz's solution of the contact problem between two elliptical elastic bodies. The latter implies that contact stiffness will be dependent on radii of curvature of the contacting particles. For elliptical particles, radii of curvature vary depending on the location of the contact point on the particle exterior. However, it has been proposed [69] that for plane elliptical particles, the contact-force-displacement relationship is independent of the location of a contact point, so long as displacements are understood as relative displacements between centres of curvature of two particles in contact.

There are at least two definitions of point of contact for the case of plane systems of elliptical particles [69, 91]. The definition presented by Rothenburg and Bathurst [69] was adopted in this work. Accordingly, the point of contact is defined as the midpoint of the line segment $\overline{ab}$, where a and b are the intersecting points formed by the overlapping ellipses as depicted in Figure 3.3. The radii of curvatures and their corresponding centres are computed at the location indicated by the contact vectors $\boldsymbol{l}_A^c$ and $\boldsymbol{l}_B^c$, respectively (Figure 3.1).

A plot of the curvature (the inverse of the radius of curvature) of an ellipse of eccentricity $e_c = 0.2$ with respect to the angle α is shown in Figure 3.4. Depending on the position of

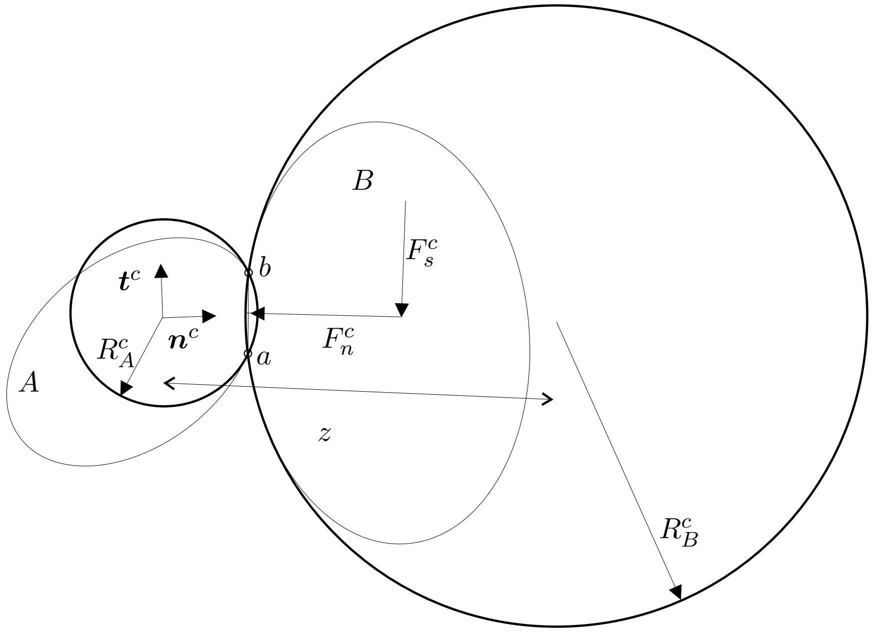

Figure 3.3: Radii of curvature at the contact point

the contacting point with respect to the ellipse's major axis, the change of curvature may be considerable.

If the assumption is made that displacement takes place in the normal direction, then F_n can be estimated from:

$$F_n = \frac{4}{3} E^* \sqrt{R^* u_n^3} \tag{3.10}$$

where R^* is computed from:

$$\frac{1}{R^*} = \frac{1}{R_A^c} + \frac{1}{R_B^c} \tag{3.11}$$

and:

$$\frac{1}{E^*} = 2\frac{1-\nu^2}{E} \tag{3.12}$$

where R_A^c and R_B^c are the radii of curvature at the point of contact for particles A and B respectively, E is Young's modulus of the particles and ν is Poisson's ratio and u_n is the compliance of the two bodies. The value of u_n in the normal direction is computed using the relative distance between both centres of curvature z , and the corresponding radii of curvature, that is, $(R_A^c + R_B^c - z)$. The normal force F_n is found directly from the normal displacement according to (3.10).

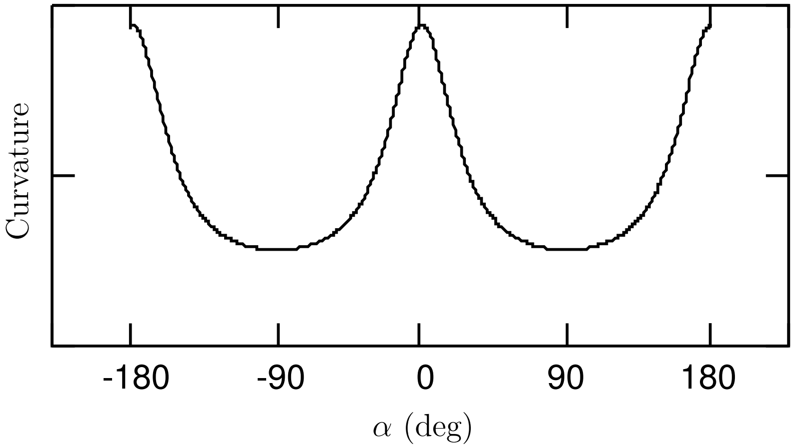

Figure 3.4: Variation of the curvature of and ellipse as a function of the angle α

Tangential Stiffness

The tangential stiffness for the case of Hertzian contacts is history-dependent, and its implementation requires storage of all load reversal points. Since the number of stress reversal points is not known a priori, memory storage becomes impractical [**?**]. To simplify these difficulties, shear forces are estimated using the method proposed by Cundall [22]. Accordingly, the shear stiffness is a function of the normal force, and it is equal to the initial loading stiffness:

$$k_s = \frac{2G^{2/3}\left[3(1-\nu)R^* F_n\right]^{1/3}}{2-\nu} \tag{3.13}$$

where G is the shear modulus of the particles. The incremental shear force ΔF_s is calculated using relation (3.7).

3.2.4 Damping

The DEM method must include a provision for damping so that the assembly can approach a state of static equilibrium under all conditions [6]. Damping is incorporated in the system through a series of dashpots assumed to be located at different positions (Figure 3.5). Three forms of damping have been introduced by Strack and Cundall [84]:

1. Contact damping, which acts on the relative velocities at disc contacts in both normal

and tangential direction. Contact damping may be envisaged as dashpots which act in parallel with the linear springs describing contact stiffness.

2. Global damping, which acts on the absolute velocities of the discs and can be envisaged as dashpots connected to each particle to a fixed frame of reference.
3. Friction damping, in which tangential contact forces are restricted according to the interparticle friction criteria. Consequently, whenever this value is substituted into the force-displacement expressions, it represents a damping mechanism on interparticle tangential displacements. To prevent excessive tangential damping when $\|(F_s)\|_{max}$ is achieved, the tangential contact damping is not applied during sliding.

Normal and tangential contact damping forces are calculated from:

$$\begin{aligned}(D_n)_N &= c_n \left[\left(\left(\dot{\boldsymbol{x}}_i^B - \dot{\boldsymbol{x}}_i^A \right)_{N-1/2} \right) \boldsymbol{n}_i^c \right] \\ (D_s)_N &= c_s \left[\left(\left(\dot{\boldsymbol{x}}_i^B - \dot{\boldsymbol{x}}_i^A \right)_{N-1/2} \right) \boldsymbol{t}_i^c - \left(\dot{\theta}^A |\boldsymbol{l}_A^c| + \dot{\theta}^B |\boldsymbol{l}_B^c| \right)_{N-1/2} \right] \quad i = 1,2 \end{aligned} \tag{3.14}$$

where c_n and c_s are contact damping coefficients.

Contributions of contact damping are resolved into components $\boldsymbol{D}_i$ and added to the force term in (3.3) leading to:

$$\begin{aligned}(\dot{\boldsymbol{x}}_i)_{N+1/2} &= (\dot{\boldsymbol{x}}_i)_{N-1/2} + \left[\left(\frac{\boldsymbol{F}_i + \boldsymbol{D}_i}{m} \right)_N \right] \Delta t \quad i = 1,2 \\ \left(\dot{\theta} \right)_{N+1/2} &= \left(\dot{\theta} \right)_{N-1/2} + \left[\left(\frac{M}{I} \right)_N \right] \Delta t \end{aligned} \tag{3.15}$$

Strack and Cundall [84] noted that there is a half-time step error between the force and moment sums in (3.15) and terms $(D_n)_N$ and $(D_s)_N$, however, they considered this error to be negligible. Global or mass damping coefficients are related to the mass and moment of inertia of each particle through a coefficient of proportionality α:

$$\begin{aligned} c_m &= \alpha m \\ c_I &= \omega \alpha I \end{aligned} \tag{3.16}$$

where ω is yet another coefficient that amplifies the effect of α in the rotational component. The original equations of motion can now be rewritten to include both contact and global damping contributions:

$$\begin{aligned} m(\ddot{\boldsymbol{x}}_i)_N &= (\boldsymbol{F}_i + \boldsymbol{D}_i)_N - c_m(\dot{\boldsymbol{x}}_i)_N \quad i = 1,2 \\ I(\ddot{\theta})_N &= (M_n)_N - c_I(\dot{\theta})_N \end{aligned} \tag{3.17}$$

Letting:

$$\begin{aligned} (\dot{\boldsymbol{x}}_i)_N &= \frac{1}{2}\Big((\dot{\boldsymbol{x}}_i)_{N+1/2} + (\dot{\boldsymbol{x}}_i)_{N-1/2}\Big) \qquad i = 1,2 \\ \Big(\dot{\theta}\Big)_N &= \frac{1}{2}\Big((\dot{\theta})_{N+1/2} + (\dot{\theta})_{N-1/2}\Big) \end{aligned} \tag{3.18}$$

and:

$$\begin{aligned} (\ddot{\boldsymbol{x}}_i)_N &= \frac{(\dot{\boldsymbol{x}}_i)_{N+1/2} - (\dot{\boldsymbol{x}}_i)_{N-1/2}}{\Delta t} \quad i = 1,2 \\ (\ddot{\theta})_N &= \frac{(\dot{\theta})_{N+1/2} - (\dot{\theta})_{N-1/2}}{\Delta t} \end{aligned} \tag{3.19}$$

leads to the revised equations of motions in the form:

$$\begin{aligned} (\dot{\boldsymbol{x}}_i)_{N+1/2} &= \frac{(\dot{\boldsymbol{x}}_i)_{N-1/2}\,(1 - \alpha\,\Delta t/2) + (\boldsymbol{F}_i + \boldsymbol{D}_i)_N\,\Delta t/m}{1 + \alpha\,\Delta t/2} \quad i = 1,2 \\ (\dot{\theta})_{N+1/2} &= \frac{(\dot{\theta})_{N-1/2}\,(1 - \alpha\,\Delta t/2) + (M)_N\,\Delta t/m}{1 + \alpha\,\Delta t/2} \end{aligned} \tag{3.20}$$

It is easily seen that setting $\alpha = 0$ and $\beta = 0$ leads to the original equations of motion (3.3) without the option of damping.

The lumped-mass non-linear spring and dashpot systems are schematically depicted in Figure 3.5.

3.2.5 Critical Time Step

The discrete nature of the employed technique requires the selection of a time step small enough to assure equilibrium of particles. Equilibrium can only be achieved if the time step Δt is taken as a fraction of a certain critical time step. The critical time step is estimated

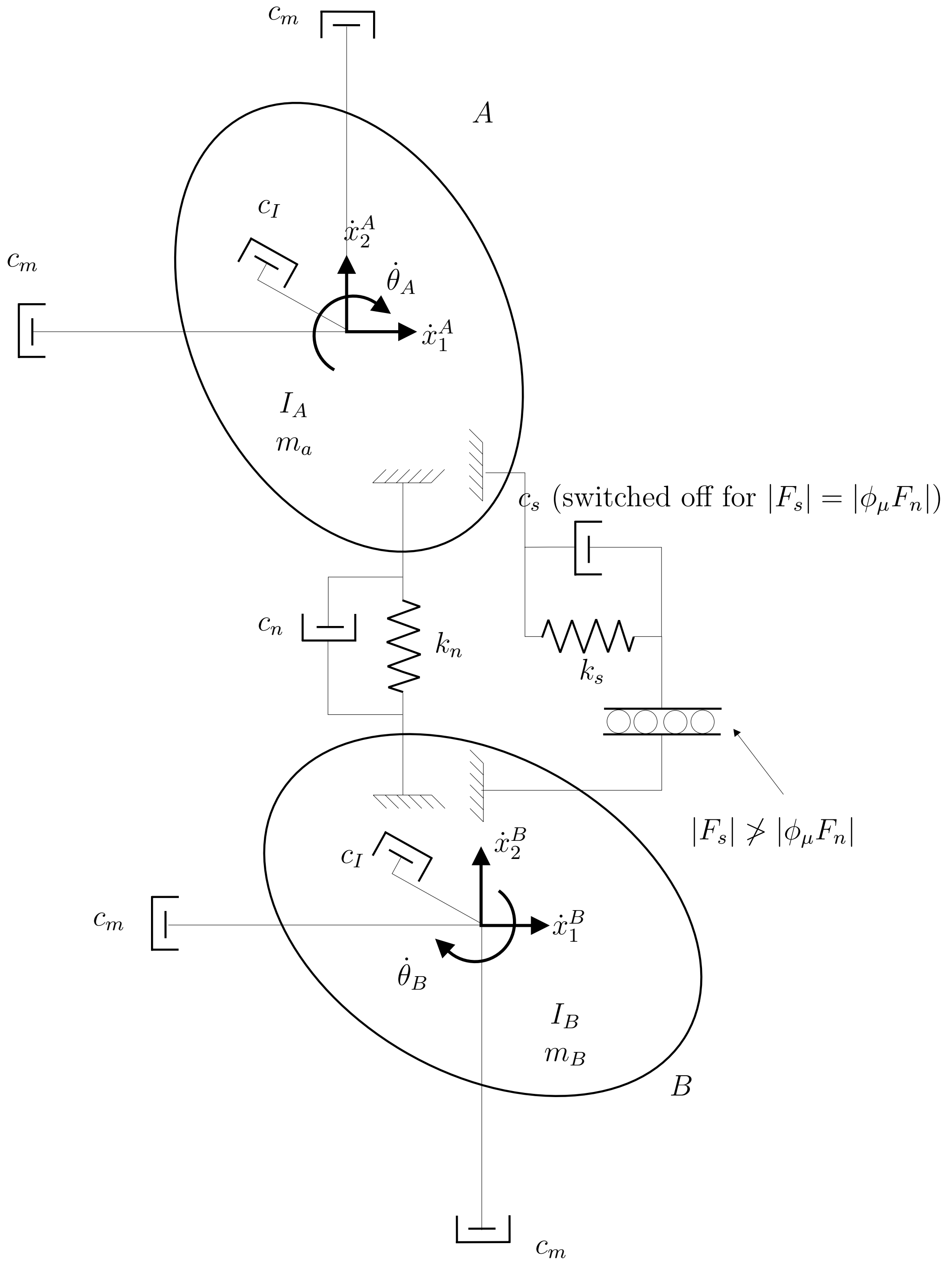

Figure 3.5: Principal rheological elements in the DEM

on the basis of a single degree-of-freedom system of mass m connected to ground by a spring of stiffness k [23]. The critical time step equals

$$\Delta t_c = \Delta t = 2\,\mathrm{FRAC}\sqrt{\frac{m_{\min}}{k_{\max}}} \tag{3.21}$$

where $k_{\max}$ and $m_{\min}$ represent the largest normal or shear contact stiffness and the mass of the smallest particle in the assembly respectively. FRAC represents a constant that accounts for the fact that each particle is acted on by several springs. Strack and Cundall (1978) suggest that a value equal to 0.1 is small enough to assure numerical stability. The value of Δt_c is equal to Δt, which is the global time step appearing in equations (3.3), (3.4), (3.6), (3.15), (3.7), (3.19), (3.20).

The term Δt appearing in relation (3.20) controls the influence of inertial (unbalanced) forces. In the present study, a non-linear contact law was introduced to counteract the effect of high interparticle penetrations. The maximum stiffness in the normal or tangential directions required to compute the critical time step are not constant parameters, but change during deformation. To assure the convenient selection of an adequate time step, the maximum stiffness employed $k_{\max}$ is computed at the beginning of the simulation. Additionally, the numerical stability is monitored at all times during the simulation by computing the ratio of the average inertial forces to the average contact forces generated in the assembly.

3.2.6 Contact Detection Algorithm

Real particles are almost rigid and they deform only at the contacting points by small amounts that depend on the contact-force magnitude and the mechanical properties of the grains, among other factors. The idealized elliptical particles are also deformed at contact points without changing shape. The particle deformation is simulated by allowing particles to geometrically inter-penetrate each other by small amounts at the contact location. The amount of overlapping is a measure of contact deformation, and it is usually a small fraction of the particle diameter. The major problem of DEM for elliptical particles is to detect the particle contact with the neighbouring particles, and calculate intersection and contact points as well as the normal and tangential contact vectors.

The overlapping between elliptical surfaces is calculated by considering the general second-order nature of the elliptical curves and detecting the points of intersection. The problem of detecting the intersection is reduced to a simultaneous solution of two second-order equations, or alternatively, by determining the roots of a fourth-order equation.

A major difficulty with finding intersections of two ellipses relates to small interparticle penetration that can result in two numerically close roots of the fourth-order polynomial. This may lead to degradation of numerical accuracy that depends on the relative orientations of the two ellipses [69]. Rothenburg *et al.* [69] proposed to rotationally transform the curves to a coordinate system that gives the largest separation between roots. Their method is employed in the present work.

To obtain the intersection points, the quadric polynomial is solved iteratively using Laguerres's method, as described by Acton [1]. The method uses complex arithmetic, but will always converge to the solution with the desired accuracy. Even though the roots of a quadric polynomial can be found analytically, this method may be ill-conditioned for the case when principal axes of ellipses are aligned to each other [31].

3.3 Particle-Fluid-Flow Interaction

A number of algorithms have been programmed to account for the fluid-particle interactions during undrained deformations in idealized assemblies of elliptical-shaped particles.

The additional micro-mechanisms incorporated in the DEM, can be better understood considering the system of particles illustrated in Figure 3.6. The particles are enclosing a space assumed to be filled by a fluid. The enclosed space will be referred to as pore or void. At an initial static equilibrium, pore i has an initial volume V_i and the fluid effect on the particles are only buoyancy forces. It has been assumed that the system of particles represents a horizontal cross section, so the initial hydrostatic pressure will be the same throughout the assembly and forces resulting from integrating pressures around the particles' surfaces will be nil. As deformation is initiated, the granules re-arrange into a different configuration altering the morphology of the void. Depending on the velocities at which the particles are moving and hydraulic conductivity of the medium, pressures in excess of hydrostatic may start developing at the pore. During deformation, the fluid escaping the pore and the built-up pressure can induce additional forces on the particles that may affect the mechanical response of the particles.

The aforementioned mechanisms can be separated into three main processes and applied to an assembly composed of a higher number of particles and pores in the following manner:

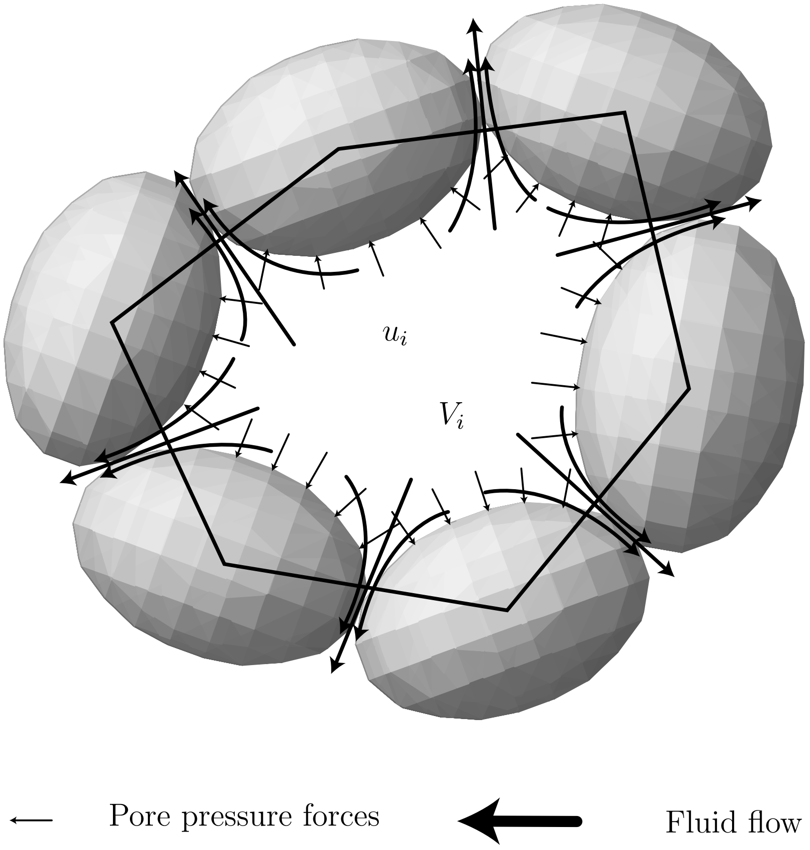

Figure 3.6: Pore pressure generation scheme

1. Excess pore water pressure develops as a result of particle rearrangement,
2. Differences in pore pressures at each pore create micro-gradients that generate fluid flow among pores, and,
3. Excess pore pressures act on the particles, resulting in pore pressure forces that may affect the effective state of stresses.

The identification of the processes listed above was the first step towards adopting a suitable physical model; they are considered to be major contributors to the mechanics of undrained deformation. The effect of buoyancy forces has not been considered in the calculations.

The method employed to simulate these processes and the employed coupling technique are described in the following sections.

3.4 Pore Pressure Generation

The procedure adopted to simulate pore pressure generation is similar to the one proposed by Hakuno *et al.* [36] and Hakuno [35]. The technique relates pore deformations to pressures by assigning elastic properties to the fluid. Implementing this procedure requires the identification of all individual voids and computation of their volume-change rates. A major part of the present work was devoted to developing a set of subroutines capable of performing these tasks. The logic employed in developing these subroutines is explained in the present section.

3.4.1 Algorithm for Voids Identification

The algorithm used to identify voids searches for groups or clusters of particles that are continuously in contact in such a way that they form a loop. If such a condition is encountered, the space enclosed by the group of particles is identified as a pore or void. The same definition of pore for plane systems has been presented elsewhere [30].

First, contacting particles carrying a normal compressive force ($F_n > 0$) are identified (Figure 3.7). The algorithm creates a list of all particles and their contacting neighbours, named the contact array. It then modifies the order in which the neighbouring particles are stored in the contact array according to the angle formed by the branch vector ($\boldsymbol{z}^c$) with respect to the horizontal in the counter-clockwise direction (Figure 2.9). The process of polygon construction starts by considering an initial particle i and the contact particle j which was firstly positioned in the contact array. The neighbouring particle j is thus identified. The contact array of particle j is further analyzed, and the position of i is located. The particle located in the previous position to that of i in the j array is selected as a possible particle conforming the loop. This process is repeated until the followed path comes back to the initial starting particle or until it has exceeded a certain number of loops defined by the user. The path followed during the search is registered by the program. If the loop is closed, the path is saved by storing the particles' number in the order they were encountered. A polygon that joins the centres of particles enclosing a void is in this way

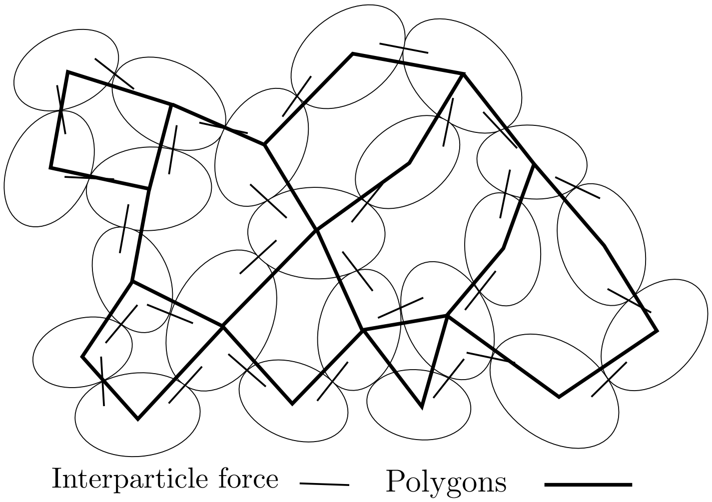

Figure 3.7: Calculation of polygons enclosing the assembly's voids

created. The subroutine returns a list of all polygons created. The polygons define the groups of particles enclosing the assembly's pores.

As will be explained in Section 4.1, the assembly used for the simulations is bounded by a "membrane" composed of the plane elliptical particles with eccentricity $e_c = 1.0$. The polygon generation algorithm locates particles that are continuously in contact identifying the pores in the system, and creates a network of polygons whose vertices are the centroid of particles. When the polygon construction algorithm is directly applied to identified boundary pores, the shape of the polygons is dependant on the position of the centre of the boundary particle with respect to the boundary contact point. Thus, it was observed that the shape of these pores may not always be adequately described. To overcome this problem, additional particles of zero size are considered to exist at the contact points between particles and the boundary. Introducing these fake particles allows the use of only one algorithm to identify internal as well as boundary polygons. In this way, an edge of the polygon originally going from the centre of an internal particle to the centre of a boundary particle will now pass through the centre of the fake particle located at the contact point, resulting in a polygon that adequately describes the shape of the pore. The algorithm to construct polygons is called in the program whenever a new contact is created or and existing contact disintegrates.

The employed subroutine was originally created by Thallak [88] to simulate hydraulic fracturing. This subroutine has been further modified and optimized to analyze the present problem.

Maximum Number of Polygons

The problem of constructing polygons is commonly encountered in graph theory. It consists of identifying the minimum number of faces (polygons), given the edges (branch vectors) of a given set of vertices (particle centres).

The polygons comprising the voids of the system can be envisaged as a graph whose properties can be studied at a given instant during the deformation.

Graph theory concepts were initially used to describe assemblies of granular materials by Satake [77]. Some of these concepts were used in the initial programming stages to dimension the arrays in order to optimize memory storage. Let F , E, and V be a number of faces, edges and vertices in a particular graph. Then, the following relation applies:

$$F - E = 1 - V \tag{3.22}$$

which is known as *Euler's relation.*

Relation (3.22) can be used to find an upper bound for the maximum number of polygons or faces expected in any particular assembly. Consider a system of N elliptical particles in a dense state, so the average particle coordination number expected is approximately $\gamma = 6$. Using relation (2.2), the number of contacts in the assembly N_c is equal to $3N$. Assume $E = N_c$ in (3.22), then the maximum number of polygons expected for a dense system of elliptical particles is:

$$F = 2N + 1 \tag{3.23}$$

or approximately two times the number of particles.

3.4.2 Pore Pressure Generation

To simulate saturation effects, the pore space is treated as filled by a fluid. The fluid is assumed to be an elastic material that possesses a certain stiffness. The stiffness relates the amount of deformation that the medium will experience to a given spherical state of stresses. Volumetric pore changes experienced due to particle rearrangement under external

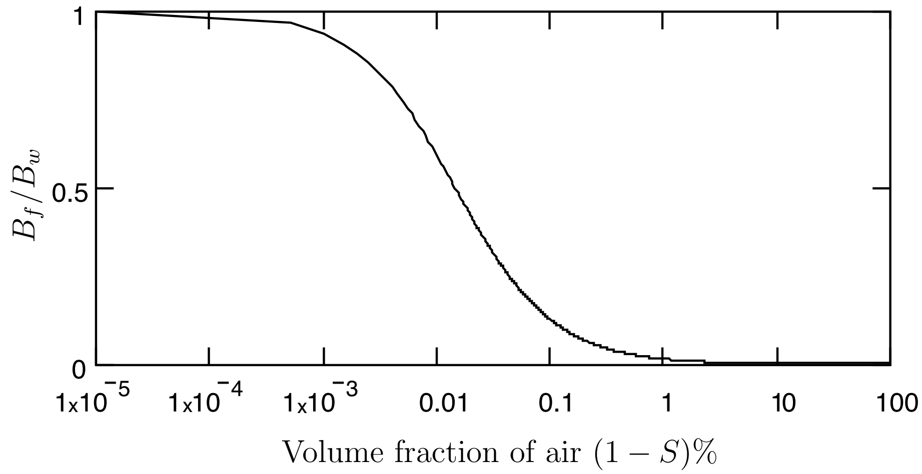

Figure 3.8: Variation of normalized fluid modulus with air content

forces are assumed to be the same as those of the fluid. In this manner, the change in volume ΔV_i of the fluid in a given pore i is considered to provoke a change in the pressure Δu of the fluid according to:

$$\Delta u_i = B_f \frac{\Delta V_i}{V_i} \tag{3.24}$$

where V_i is the original volume of pore i and B_f is the bulk modulus of the fluid. By varying the value of B_f, the effect of a different fluid compressibility may be evaluated.

A fully saturated medium can be replaced by a partly-saturated one whose fluid compressibility depends on the degree of saturation. It has been shown [76] that the bulk modulus of a fluid mixture of air and water is:

$$B_f = \frac{1}{\frac{S}{B_w} + \frac{1-S}{B_a}} \tag{3.25}$$

where B_f, B_w , and B_a are the bulk moduli of the fluid, water and air, respectively and S is the degree of saturation of the mixture. The values of the bulk moduli of water and air are approximately equal to 2.9 GPa and 142 kPa at one atmosphere [76].

Figure 3.8 shows the variation of the normalized fluid modulus with air content. It is observed that a small volume of air results in a large decrease in the modulus of the fluid. Since compressibility of the fluid becomes small for degrees of saturation near unity,

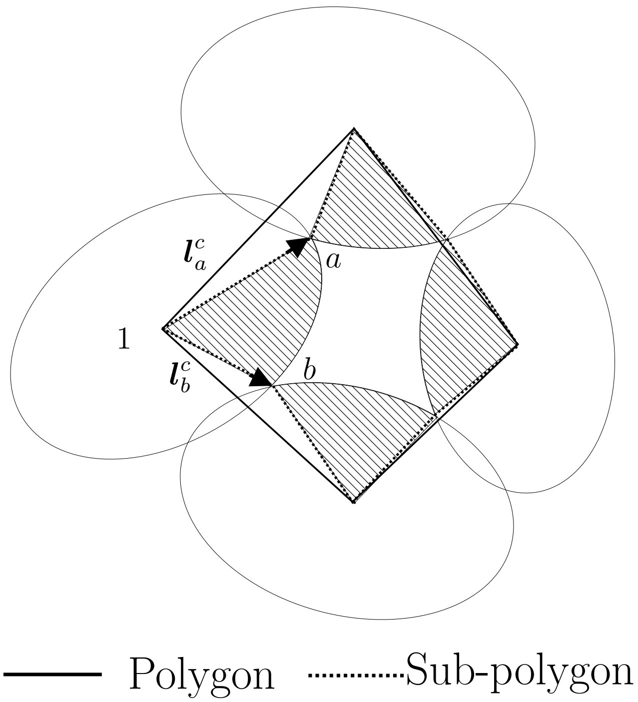

Figure 3.9: Definition of contact vectors for pore volume computation

a small volumetric fluid strain results in large pressures; therefore, precise pore volume computation becomes necessary.

The geometrical intersection between elliptical particles is used to compute the void volume with the required accuracy. To illustrate pore volume computation, consider the set of particles depicted in Figure 3.9, where particle interpenetrations have been exaggerated for illustration purposes.

Additional polygons or sub-polygons are constructed by joining the intersection points with the particles' centre. The area defined by the sub-polygon and the shaded areas of the ellipses are then calculated, and the sum of the later is subtracted from the former. The result of this operation is the desired pore area.

The shaded regions are computed as follows. Consider the ellipse depicted in Figure 3.10 in which a cartesian frame of reference is located at its centre. The normalized area of a region of the ellipse (A_n) delimited by the major axis and a given vector $\boldsymbol{l}_p^c$ directed to a point p is given by the next relation:

$$A_n = \frac{1-e_c^2}{2}\left\{\arctan\left[\frac{1+e_c}{1-e_c}\tan(\alpha)\right]\right\} \qquad 0 \leq \alpha < \pi/2 \tag{3.26}$$

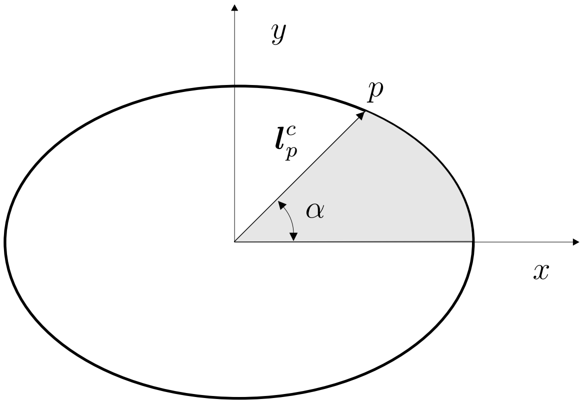

Figure 3.10: Computation of area of a region on the ellipse

or alternatively:

$$A_n = \frac{1-e_c^2}{2}\left\{\arctan\left[\beta\tan\left(\frac{\alpha}{2}\right)\right] + \arctan\left[\frac{1}{\beta}\tan\left(\frac{\alpha}{2}\right)\right]\right\} \qquad 0 \le \alpha < \pi \tag{3.27}$$

where β is the solution to:

$$\frac{\beta}{2} + \frac{1}{2\beta} = \frac{1+e_c}{1-e_c}$$

e_c is the eccentricity of the ellipse, α is the angle defining the region of interest measured from the ellipse's major axis. The area computed from the previous relations is normalized by $\bar{R}^2$. Relation (3.27) is plotted in Figure 3.11 for eccentricity values of 0, 0.2 and 0.4.

The former relations assume collinearity between the ellipse's major axis and the abscissa, so the elliptical curve and the vectors delimiting the region of interest have to be rotationally transformed.

3.5 Coupling of the Flow-DEM Particle System

Liquefaction is a transient phenomenon occurring as a result of particle re-adjustment and subsequent loss of effective stresses. A micromechanical approach to the problem should consider the unsteady-flow nature of the fluid and the consequent pore-pressure forces exert on the particles' surfaces. An important part of this work consisted of proposing and developing a model capable of describing the unsteady-flow among pores satisfactorily and at the same time computationally efficient. The resulting model has been coupled with the

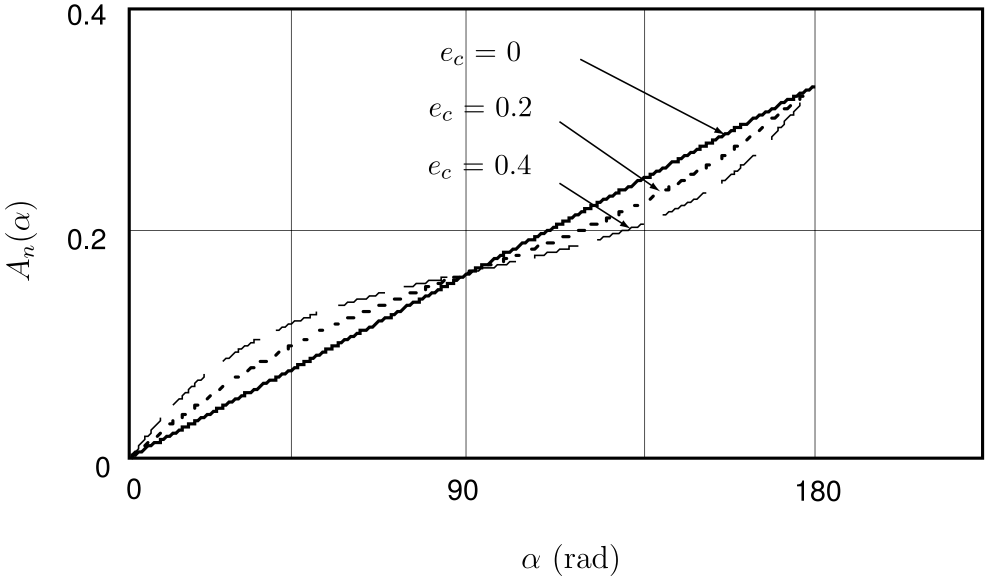

Figure 3.11: Normalized area of a region on the ellipse as a function of the angle θ for Three Different Eccentricities

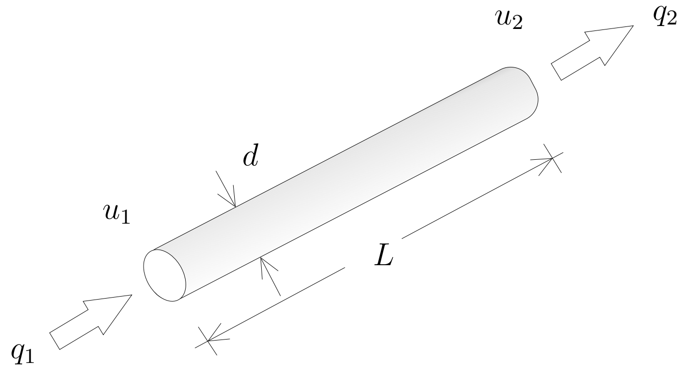

Figure 3.12: Conduit diameter and macro-permeability

mechanism of particle movement. The proposed scheme for flow-coupled DEM is described in the present section.

3.5.1 Fluid Flow Description

A porous medium is formed by a collection of grains of different mineralogy and morphology. Flow of water in porous media is basically three-dimensional and mechanisms that participate in energy losses are multiple and variate. The space between grains can be imagined as a complex structure of channels and reservoirs when the medium is fully saturated and the shape of pores can be highly irregular. These complexities are usually overcome using continuous approaches; these are adequate for the phenomenological description of macroscopic transport processes [34].

The discrete nature of the DEM makes the use of the continuous approach unsuitable, and alternative methodologies have to be considered.

Network models are difficult to generate as models of porous media because of the lack of accurate information on the details of pore structure. Furthermore, the passageway through the pore is not straight but has many bends and the actual length of the flow path cannot be calculated. Additionally, the pores in the soil mass are interconnected, and for a water particle starting at a given point, many possible flow paths exist. The complete description of a porous medium is impossible to accomplish precisely, although one can overcome this difficulty by considering simplified models through which fundamental mechanisms can be understood by examining the connectivity of the pores.

Different techniques to simulate single-phase flow considering pore structure are reported in the literature [73, 88, 39]. Two fundamentally different approaches can be found: in one, the flow inside assumed conduits is analyzed; in the other, the flow around solid objects immersed in the fluid is considered. For low and intermediate porosities, the conduit flow approach is more suitable [30].

To simulate fluid exchange among pores, the medium has been envisaged as composed of a collection of flow channels. It has been further assumed that the passage between voids can be described by conduits having a circular cross section and that velocity of flow through the passages is small enough to be described by the Hagen-Poiseuille theory. According to the Hagen-Poiseuille relation, the volumetric flow rate q that passes through a pipe or conduit of diameter d and length L is given by:

$$q = \frac{\pi d^4}{128\bar{\mu}} \frac{(u_1 - u_2)}{L} \tag{3.28}$$

in which u_1 and u_2 are the pressures at the entrance and exit of the pipe, respectively (Figure 3.12). The properties of the fluid are integrated in the process through the fluid's viscosity $\bar{\mu}$. The above relation considers volumetric flow rates to be proportional to the gradients generated.

Flow Network

When all the voids in the systems are connected by means of pipes or conduits, a network of nodes and pipes, termed the flow network, arises. The flow network is used to model flow through the particulate medium.

The algorithm to generate the network of conduits makes use of information about pore connectivity as captured by the neighbouring polygons. During the process of polygon construction, pores adjacent to contacts are identified and stored in array form. The contacts in the assembly must have at the most two adjacent pores.

The first step consists in the creation of the flow network; it consists of computing the centre of gravity of all the polygons. A given polygon is surrounded by n neighbouring polygons. For each polygon, conduits that emerge from the centre of the mass of the polygon i to the centre of the neighbouring polygons are generated.

The higher the number of neighbouring voids, the higher the conduit confluence. Accordingly, a given polygon is assumed to be connected with its surrounding neighbours, and a network is created by locating the ends of the straight cylindrical capillaries at the

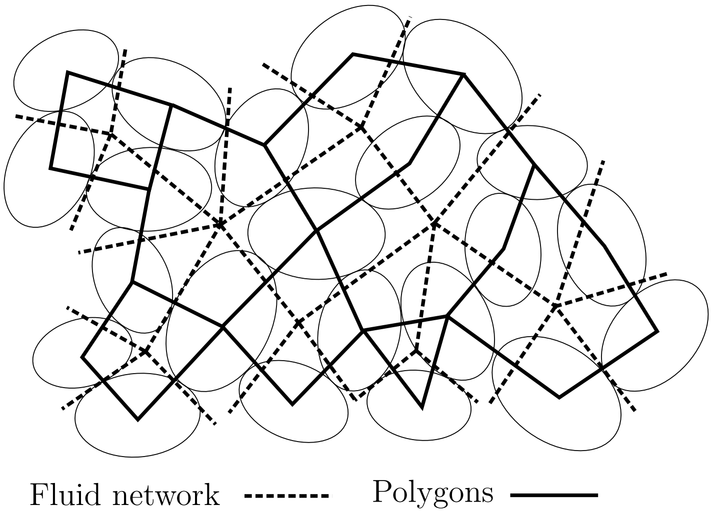

Figure 3.13: Flow network construction for a set of polygons

centres of gravity of the polygons. The lengths L required in (3.28) are computed by considering the end points of each individual conduit which correspond to the centre of gravity of corresponding polygons. A detail of a flow network is depicted in Figure 3.13 for a given set of polygons.

Reformulation of the network is necessary only if an existing contact is lost or when a new contact is created.

After pressures develop in all pores during a time increment, local gradients are generated which induce flow among neighbouring pores through the conduits. The resulting pressures will dissipate and may exert a pore-pressure force on the surface of the particles.

3.5.2 Transient Fluid Flow

Consider a numerical simulation conducted on a *saturated* assembly. At the beginning of each time step, the system is conformed by N_p number of pores containing fluid under pressures u_i (these pressures being zero for the first time step). The volume change ΔV_i of the fluid contained in pore i during a time increment will be equal to the change of the pore volume ΔV_i^β plus the volume of fluid injected or extracted from the pore through the converging conduits. Considering conservation of mass, the following relation is obtained:

$$\Delta V_i = \Delta V_i^{\beta} + \sum_{j=1}^{n} \Delta q_j \Delta t \quad i = 1 \ldots N_p \tag{3.29}$$

where Δq is the total volume entering or leaving the pore i, Δt is an increment of time and n is the number of conduits converging to pore i . Substituting (3.28) into (3.29) and considering the entire system of pores-conduits in the assembly leads to:

$$\frac{du_i}{dt} = \left\{ \frac{dV_i^{\beta}}{dt} - \sum_{j=1}^{n} \kappa_j \left(u_i - u_j \right) \right\} \frac{B_f}{V_i} \quad i = 1 \ldots N_p \tag{3.30}$$

where

$$\kappa_j = \frac{\pi \, d_j^4}{128 \, \bar{\mu} \, L_j}$$

Relation (3.30) is a system of ordinary differential equations; it combines the mechanism of particle movement with effects of fluid flow through the flow network.

Integration is carried out numerically over an increment of time Δt which corresponds to the time increment employed for the solution of the particle's motion.

The volumetric change rate dV_i^{β}/dt is directly obtained from pore volumes at the beginning and end of the global time step and it is assumed constant when solving (3.30).

The resulting pressures after integration are converted to forces acting on the particles. The following section presents the methodology and equations necessary to convert the pore fluid pressures into forces.

3.6 Pore Pressure Forces on Particles

The pressure difference between two adjacent pores represents in discrete form a local pressure gradient in the system. Integration of the local pressures around the particles result in discrete forces directed along the direction of the local pressure gradient. This effect defines pore pressure forces that must be included in the force-displacement solution of the particles. The present section introduces the proposed computational scheme for decomposing pore pressure into forces.

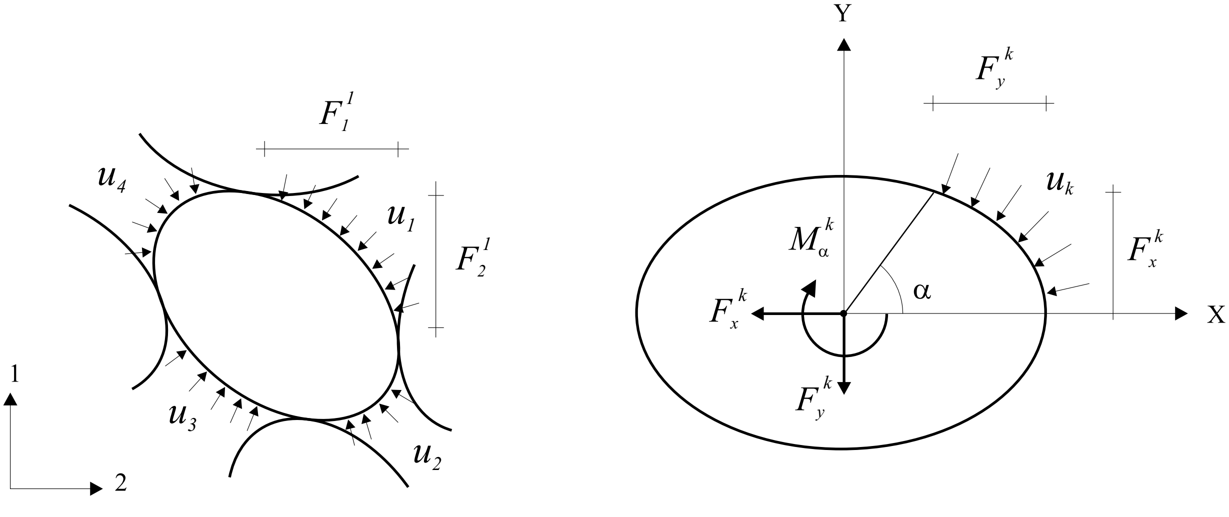

a) b)

Figure 3.14: Computation of pore pressure forces

Horizontal and Vertical Components

Consider the particle depicted in Figure 3.14a, surrounded by four pores presenting different pressures u_i acting normal to its surface. For the case of elliptical surfaces, the individual pressures can be decomposed into a horizontal, vertical and rotational force components acting on the particle's centre. In the case of disc-shaped particles, the rotational component becomes zero and only the horizontal and vertical components remain. The horizontal and vertical force components denoted as F_1^i and F_2^i resulting from the pressure u_i in pore i can readily be computed by considering the projected areas as shown in Figure 3.14a.

In order to implement this procedure in the program, it becomes necessary to compute the contact vectors bounding the region of interest. Consider the section of an ellipse bounded by vectors $\boldsymbol{l}_a^c$ and $\boldsymbol{l}_b^c$ depicted in Figure 3.15. The horizontal and vertical components of the pore pressure in pore n are computed as

$$F_1^n = -u_n(a_2 - b_2)\Delta \tag{3.31a}$$

$$F_2^n = u_n(a_1 - b_1)\Delta \tag{3.31b}$$

where Δ is the thickness of the particle.

The set of vectors $\boldsymbol{l}_a^c$ and $\boldsymbol{l}_b^c$ are properly assigned by considering the direction of the paths followed by polygon loops. For example, pore n in Figure 3.15a corresponds to a polygon path directed in the clockwise direction. Similarly, the path followed by the polygon delimiting pore n in Figure 3.15b is directed counterclockwise. For both cases, contact vectors are computed and the vector first encountered along the path is identified as $\boldsymbol{l}_b^c$. The second contact vector is $\boldsymbol{l}_a^c$. This definition was adopted in the program.

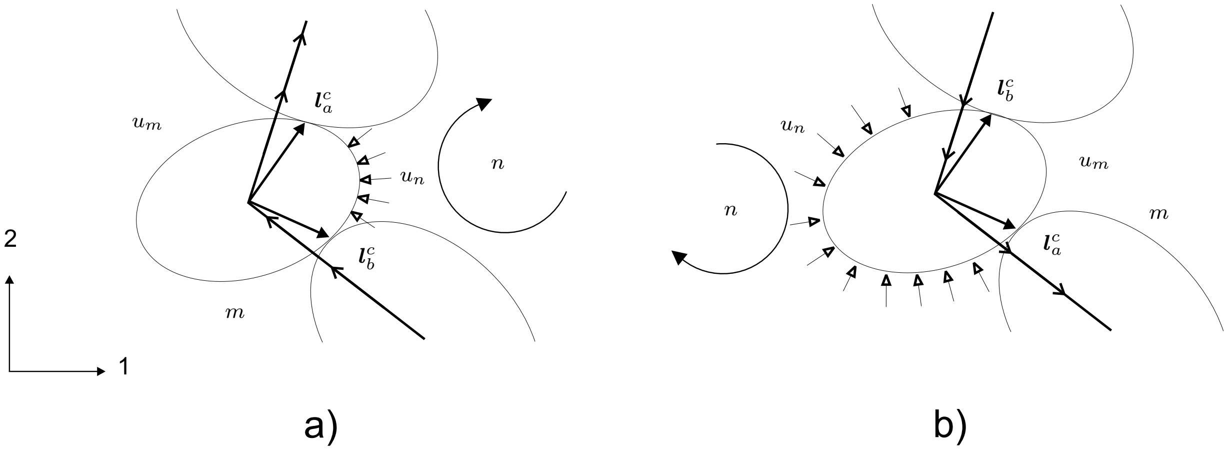

Figure 3.15: Definition of contact vectors for pore pressure force computation

Rotational Component

Computation of the rotational force component of the pore pressure requires a transformation of the particles such that the ellipse's major axis coincides with the horizontal. Consider the region delimited by a vector forming an angle α with respect to the horizontal (Figure 3.14b). The normalized rotational force component of pressure u_k is obtained by integrating the pressure from 0 to α, leading to the following relation:

$$M^k(\alpha) = u_k\,\Delta\left[\sqrt{1+e_c^2-2e_c\cos 2s}+e_c-1\right] \tag{3.32}$$

where s is a parameter computed from:

$$s = \arctan\left\{\frac{1+e_c}{1-e_c}\tan\alpha\right\} \qquad 0 \le \alpha < \pi$$

The resulting rotational force component computed from relation (3.32) is normalized by the average radius $\bar{R}$ of the ellipse and is defined as positive in the clockwise direction.

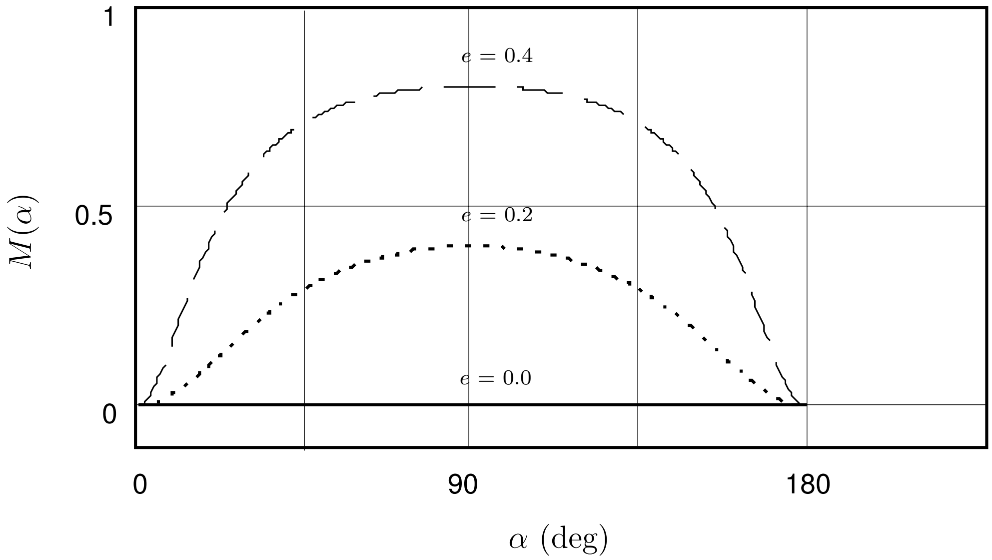

Figure 3.16: Variation of normalized moment for different eccentricities

Relation (3.32) is shown in Figure 3.16 for three different eccentricity values of e_c equal to 0, 0.2 and 0.4 respectively. Analysis of the plots reveals that the rotational component of the pore pressure vanishes when eccentricity is zero; *i.e.*, when the particle is a perfect circle. The rotational component, however, increases with particle eccentricity, and becomes maximum when $\alpha = \pi/2$.

Equation (3.32) is limited in the sense that one can only compute the moment component for a region bounded by the abscissa and a given contact vector. More general regions however, are obtained in the program by over-imposing the rotational effects.

The final step in the calculation cycle is obtaining the particle pore pressure forces $\boldsymbol{F}_i^u$ and moments M^u, which is done by summing all pore water force components and moments in the following manner:

$$\begin{aligned} (\boldsymbol{F}_i)^u &= \sum_{n=1}^{n_p} F_i^n \qquad i = 1,2 \\ (M)^u &= \sum_{n=1}^{n_p} M^n \end{aligned} \tag{3.33}$$

where n_p is the number of pores surrounding a given particle. The total force components are included in the force-displacement solution in Equation (3.20). Incorporating these additional forces has an important effect on the overall behaviour of the assembly.

3.7 Macroscopic Pressure

Undrained experiments conducted in the laboratory generally involve measurements of pore pressure. Such measurements are necessary to compute the effective state of stresses, which are known to govern the deformation process.

The model thus far adopted is able to simulate micro-pressure generation according to the deformation of voids originating from disturbances provoked at the boundary. It is desirable to adequately average the discrete pressures in order to define a representative pore pressure for the assembly.

The increase in macro-pore pressure is computed over a time increment by averaging all discrete pressures at the pore level and assigning a weight to each of them. To maintain consistency with the manner in which discrete pressures are computed, the volumes of the voids are taken as averaging weights. Accordingly, the average macroscopic pore pressure increment ($\Delta\bar{u}$) is computed at the end of each time step as:

$$\Delta\bar{u} = \frac{\sum \Delta u_i V_i}{\sum V_i} \tag{3.34}$$

The macro-pore pressure is an important variable as the tendencies to change volume (contractile or dilatant) of a given assembly are directly capture in its evolution.

The following section presents the general organization of the program and introduces some of the subroutines incorporated in the DEM algorithm. An explicit calculation cycle of the flow-coupled DEM is presented if Figure 3.17, where the solution of the flow equations and the effect pore pressure forces have been integrated in the calculation process.

3.8 Calculation of Stresses and Strains

The average stress in the assembly is obtained considering the internal distribution of contact forces using expression (2.12). The volume V in (2.12) corresponding to the entire assembly is approximated by the area formed by connecting the centres of adjoining boundary particles.

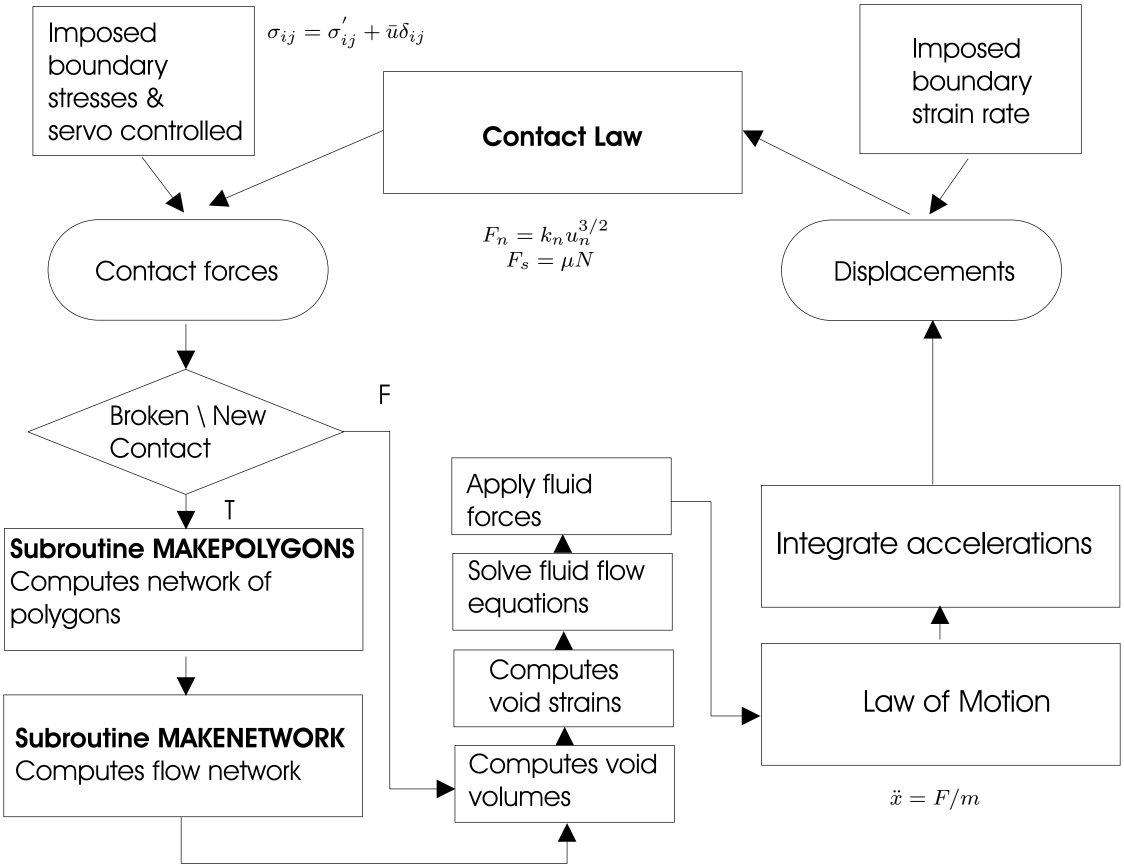

Figure 3.17: Calculation cycle in flow-coupled DEM

3.8.1 Total and Effective Stress Tensors

Knowledge of the total and effective state of stresses at any stage during a simulation is important when conducting undrained simulations. It has been shown in relation (2.12) that the stress tensor in a given domain can be obtained by considering spatial averages of forces and contacts according to:

$$\sigma_{ij}^{\beta} = \frac{1}{V}\sum f_i^c l_j^c \qquad i,j = 1,2,3 \tag{3.35}$$

(10) where f^c is the interparticle force vector and l^c is a vector from the particles' centre to the point of contact. The above relation is equally valid for two or three dimensional

systems; it makes use of interparticle forces and is therefore an effective stress tensor. In further discussions, the effective stress tensor $\sigma_{ij}^{'}$ is assumed equivalent to relation (3.35) or:

$$\sigma_{ij}^{\beta} = \sigma_{ij}^{'} \tag{3.36}$$

Using the macro pore pressure calculated from (3.34) and the effective stress tensor $\sigma_{ij}^{'}$, the total stress tensor σ_{ij} is computed as:

$$\sigma_{ij} = \sigma_{ij}^{'} + \bar{u}\delta_{ij} \qquad i,j = 1,2 \tag{3.37}$$

where δ_{ij} is Kronecker's delta.

3.8.2 Average Strain

An adequate measure of the strain tensor is required to obtain a macroscopic description of the assembly of particles. The strains are computed at selected intervals during the simulations using the displacements of boundary particles according to the expression proposed by Cundall *et al.* [23].

$$\epsilon_{ij} = \frac{1}{V}\sum_{\beta=1}^{n^{\beta}}\left[\frac{1}{2}\left\{\Delta\boldsymbol{x}_j^{\beta} + \Delta\boldsymbol{x}_j^{\beta+1}\right\}\boldsymbol{e}_i^{\beta}S^{\beta}\right] \qquad i,j = 1,2 \tag{3.38}$$

Quantities involved in (3.38) are defined in Figure 3.18. The term V represents the area contained by the polygon described by the scalar line segment S^{β} connecting boundary particles. Each line segment is defined by the coordinates of adjacent boundary particles β and $\beta+1$ having displacements $\Delta\boldsymbol{x}^{\beta}$ and $\Delta\boldsymbol{x}^{\beta+1}$ respectively. The term $\boldsymbol{e}^{\beta}$ is a unit vector normal to the line segment S^{β}.

Invariant quantities are computed from the strain tensor using the following expressions:

$$\epsilon_n = \epsilon_{11} + \epsilon_{22} \tag{3.39a}$$

$$\epsilon_t = \sqrt{(\epsilon_{11} - \epsilon_{22})^2 + (\epsilon_{12} + \epsilon_{21})^2} \tag{3.39b}$$

$$\epsilon_{\omega} = \epsilon_{21} - \epsilon_{12} \tag{3.39c}$$

here, ϵ_n is the volumetric strain, ϵ_t is the shear strain, and ϵ_{ω} is the rigid body rotation defined positive in the counter-clockwise direction.

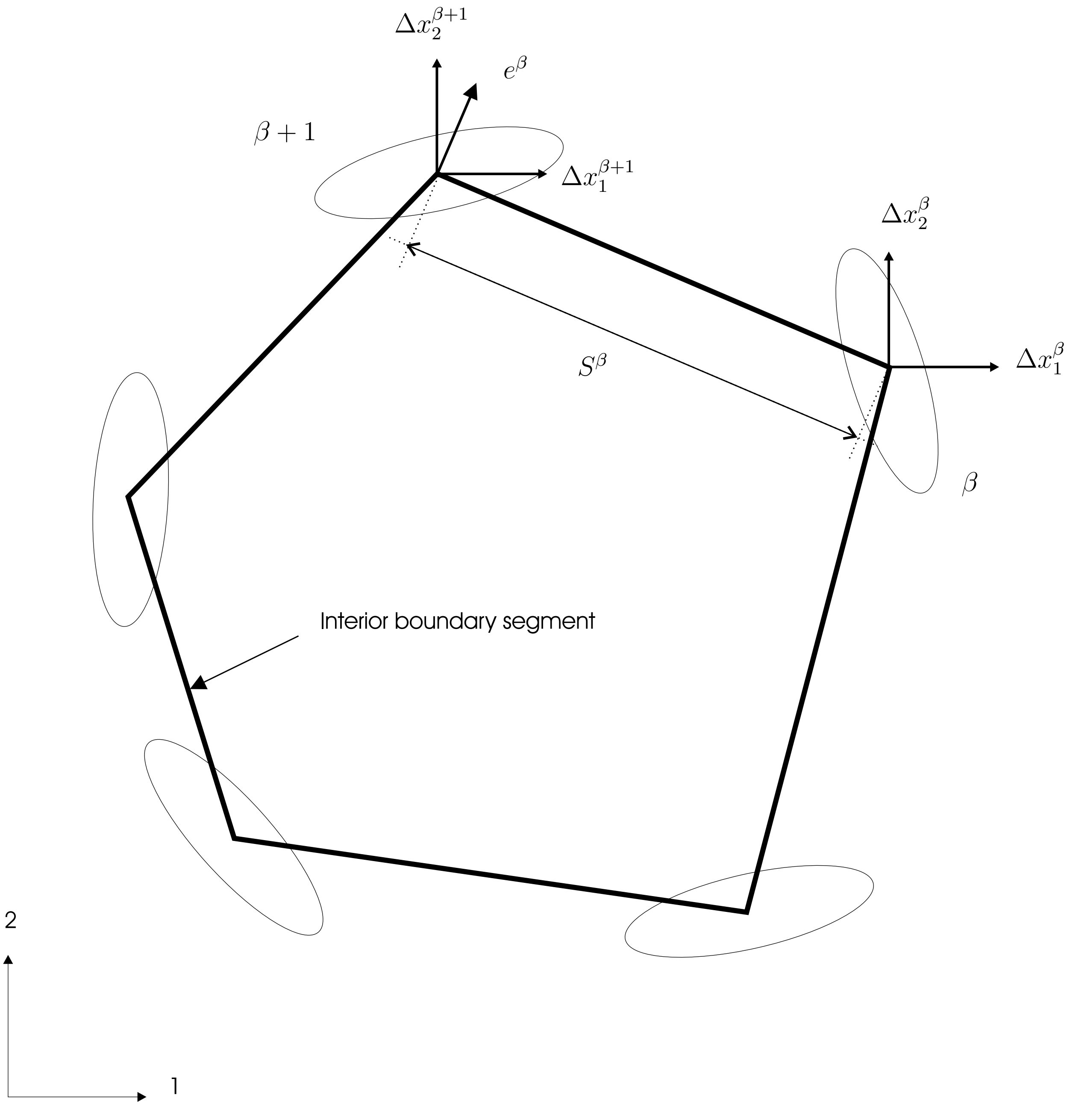

Figure 3.18: Calculation of strain tensor from boundary displacements

Principal strain directions are calculated from

$$\sin 2\theta_\epsilon = \frac{\epsilon_{21} + \epsilon_{12}}{\epsilon_t} \tag{3.40a}$$

$$\cos 2\theta_\epsilon = \frac{\epsilon_{11} - \epsilon_{22}}{\epsilon_t} \tag{3.40b}$$

The term average strain tensor does not imply that strains reflect the displacement fields observed in the interior locations. A continuous deformation is applied to the boundary, but internal deformations are discontinuous and present rotational components that are a result of the movement and rotation of discrete particles.

3.9 Boundary Control

A number of boundary conditions can be simulated using a servo-control mechanism. Only three were used in the present investigation and will be summarized in this section.

Constant Boundary Strain Rate Tests

This shearing mode applies constant velocity components $\dot{\boldsymbol{x}}_i^\beta$ to the centre of each boundary particle according to a prescribed strain-rate tensor $\dot{\epsilon}_{ij}^b$. The velocities of the boundary particles are calculated from

$$\dot{\boldsymbol{x}}_i^\beta = \dot{\epsilon}_{ij}^b(\boldsymbol{x}_j^\beta - \boldsymbol{x}_j^c) \qquad i = j = 1, 2 \tag{3.41}$$

where $\boldsymbol{x}_j^\beta$ is the particle location at the beginning of the calculation cycle and $\boldsymbol{x}_j^c$ represents the centre point of the assembly. This boundary control was employed to compute constant volume ($\dot{\epsilon}_v = 0$) tests by setting $\dot{\epsilon}_{11}^b = -\dot{\epsilon}_{22}^b$.

Constant σ_{11} Test

This mode of deformation models both biaxial compression and extension tests in which a constant vertical velocity $\dot{\epsilon}_{22}^b$ is applied to the boundary while maintaining the total horizontal stress σ_{11} constant. The boundary particle velocity $\dot{\boldsymbol{x}}_2^\beta$ corresponding to the prescribed strain rate is calculated from expression (3.41). The total horizontal stress component is maintained constant by controlling the strain rate in the manner of a servo mechanism. At the end of each calculation cycle the current state of stresses is compared with the prescribed boundary stress component σ^b_{11}. For undrained simulations, it becomes necessary to know the value of the macroscopic pore pressure $\bar{u}$ at all moments. The boundary rate velocity $\dot{\boldsymbol{x}}^\beta_1$ is obtained from

$$\dot{\boldsymbol{x}}^\beta_i = \frac{g(\sigma^b_{ij} - (\sigma'_{ij} + \bar{u}\delta_{ij}))(x^\beta_j - x^c_j)}{\sigma^\beta_{ij}} \qquad i = j = 1 \tag{3.42}$$

where g represents the servo gain that is a user-defined input parameter. Note that if the value of $\bar{u}$ is zero, the conducted simulation becomes a biaxial drained test in which the total horizontal stress is maintained constant.

Servo Strain-Rate Controlled Test

This mode allows a prescribed strain-rate tensor $\dot{\epsilon}^b_{ij}$ to be applied to the boundary simultaneously with a prescribed boundary stress σ^b_{ij}. The resultant boundary velocities are calculated as the sum of the contributions from the strain rate boundary control and the servo-mechanisms boundary control. The contributions of the prescribed strain rate tensor are calculated from relation (3.41). The contributions of the prescribed boundary stress tensor are calculated from equation (3.42) with $i, j = 1, 2$. The resultant boundary particle velocities are calculated from

$$\dot{\boldsymbol{x}}^\beta_i = \dot{\boldsymbol{x}}^\beta_{\epsilon i} + \dot{\boldsymbol{x}}^\beta_{bi} \tag{3.43}$$

This boundary control model was used in the present research to isotropically confine the assemblies to the desired level of stresses.

3.10 Modified Program AQUA

The proposed methodology to simulate undrained tests has been programmed in a series of subroutines, and the obtained program has been named AQUA. Program AQUA was developed from an existing code named *Ellipse*, originally modified by Rothenburg and Bathurst [69] to accommodate elliptical particles and it is in itself a modified version of the program DISC [6]. The programming language originally used was FORTRAN 77 and requires a 32 bit-processor. This same programming language was used in the present implementation.

The program structure has been divided into three parts, specifically pre-processing, processing, and post-processing. The pre-processing stage consists of creating an initial configuration file containing information about the assembly and initiating a number of parameters and variables needed for the computations to be carried out in the processing stage.

The processing part consists of solving the equations of motion described in Section 3.2, coupled with the fluid flow interaction described in the previous sections. The assembly configuration can be stored in a file at any calculation cycle during the simulation. These files can be subsequently analyzed in the post-processing stage.

3.10.1 Pre-Processing

The program AQUA reads the particle information and their distribution data from a configuration file initially created by an independent program named AUTODISC, which generates an assembly of discs located with respect to a fixed, rectangular co-ordinate space. The discs are converted into ellipses and the configuration file is generated.

The first subroutine INITP reads the execution commands from an instruction file called “ellipse.dat.” The input file provides information about the geometric, mechanical and physical properties of the particles such as dimensions, Young’s modulus, Poisson’s ratio, interparticle friction angle cohesion and density. For the case of undrained tests, it provides further information about the fluid viscosity, bulk modulus of the fluid and the average diameter to be used in the conduits comprising the flow-network. The instruction file also provides instructions on the type of test to be conducted. Currently, program AQUA is capable of conducting six different servo modes of shearing mechanism.

The INSTR subroutine reads the binary configuration file containing the information about individual particles as position in space, forces, velocities and increments of motion for three degrees of freedom. One partition of the binary file contains information about contacts, mainly the contacting particles, the normal and tangential forces generated by the contact. It also calculates the critical time step.

3.10.2 Processing

The processing stage is composed of a large number of subroutines, but only seven are of major importance because most of the computations are performed by them. The names of these subroutines are SERVO, MOTION, FORDELLIPSE, MAKEPOLYGONS, MAKENETWORK, POFO, RUNGE.

The number of calculation cycles is initiated according to the information gathered from “ellipse.dat” in subroutine INITP. The first subroutine encountered in the cycle is SERVO. This subroutine applies velocities to the boundary discs according to conditions initially prescribed in the instruction file “ellipse.dat”.

Subroutine MOTION solves the equations of motion (3.17) through (3.20) presented in page 49 to provide the updated particle velocities.

Subroutine FORDELLIPSE applies the force-displacement law according to equations (3.8) to each contact. The contact array is updated according to newly-formed and broken contacts, and the polygons containing such contacts are identified and stored.

Subroutine POFO calls MAKEPOLYGONS and MAKENETWORK if the contact array was modified in FORDELLIPSE, *i.e.*, if a contact was formed or disintegrated. The straining of the voids is also calculated in this subroutine and the corresponding pressures are supplied to RUNGE.

Subroutine MAKEPOLYGONS computes the polygons of the assembly, as explained in Sections 3.4.1. If the contact array was modified in subroutine check, MAKEPOLYGONS re-calculates the network of polygons. The void volumes are computed for the newly updated particle positions.

Subroutine MAKENETWORK calculates the flow network using the information provided by MAKEPOLYGONS as explained in Section 3.5.1.

Subroutine RUNGE implements the Runge-Kutta technique to numerically solve the systems of differential equations (3.30). It returns the values of the pressures after an increment of time Δt.

3.10.3 Post-Processing

The post-processing part includes extraction of any required data saved in the binary configuration files during the processing stage. An additional subroutine named AUTOCAD is used to generate .dxf files, which can later be read in a number of commercial packages such as AutoCad.

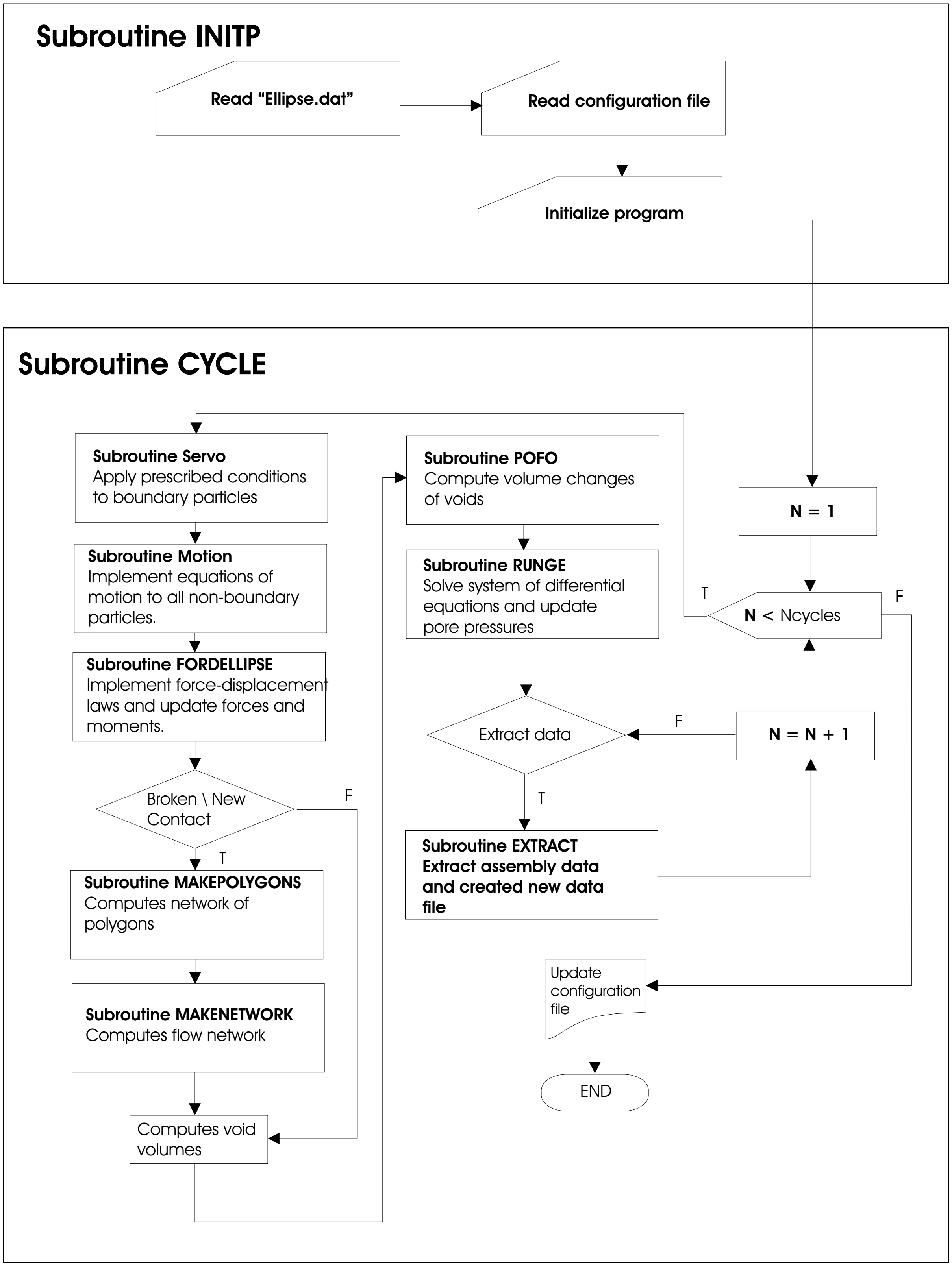

Figure 3.19: Flow Chart of Program AQUA

3.11 Comments

A great amount of work was invested in developing the algorithms to relate the strains of voids from cycle to cycle, especially for the case where new contacts are either formed or broken. Numerous trial runs were performed by the author to verify the correctness of the results provided by the algorithms during the debugging stage. The subroutine AUTOCAD was of great aid in visualizing the geometry of the problem.

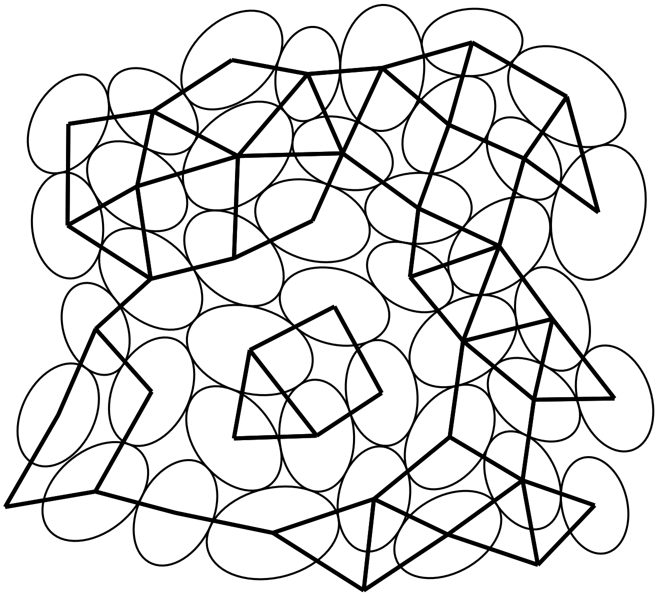

Figure 3.20: Isolated polygons

During the preliminary runs, the situation depicted in Figure 3.20 was encountered a number of times. A number of contacts are lost within separate regions and clusters of particles form creating isolated polygons or *islands* in the assembly. This condition creates a number of possibilities on how to redistribute pressures, and the computation time is considerably affected.

Under the present approach, the fluid is allowed to take an indefinite amount of tension; possible effects caused by cavitation of the fluid are not contemplated. Typically, 4.3E5 cycles are required to reach a shear strain of about 20 %. The execution time to achieve these strain levels fluctuates around fifteen days using an AMD Athlon processor with a frequency of 1.4 GHz. A large amount of CPU time is required for calculating the polygon network and solving the differential equation for fluid flow. Clearly, the current implementation is only suitable for research purposes.

Chapter 4

Verification and Parametric Study of the Program

This chapter presents the results of several calculations performed to verify that the code was working as expected and to study the behaviour of the system after having programmed all the proposed implementations.

The non-linear contact law, the effect of the geometry and frictional characteristics of the boundary contacts on the global response of the assembly were studied. The existing relationship between the macroscopic pore pressure increments and the change in volume of the assembly was used to independently verify the calculations of the individual pore strains. Special emphasis was placed on the evaluation and study of the behaviour of the fluid-flow network under different initial and boundary conditions. It is shown how a particular conduit diameter was assigned to the conduits of the fluid-flow network so that the assembly would present a permeability similar to those found in medium to coarse grained clean sands. Finally, the effects of the compressibility of the fluid on the volumetric changes and global responses of the assembly were studied.

4.1 Mechanical and Physical Characteristics of the Assembly

Elliptical particles have an advantage with respect to disc-shape particles because elliptical ones reproduce better some parameters commonly measured in real sands, such as the interparticle friction angle. Additionally, the undrained behaviour of granular materials has been found to greatly depend on the initial density of the sample. For numerical simulations, it is then desirable to work with a particle shape that allows production of the widest possible range in densities and that better simulates the behaviour of sands.

Results of numerical experiments have shown that the elongation of the elliptical particles as measured by their eccentricity (e_c) has an important effect on the packing characteristics of the assembly and on the peak friction angle [70]. Rothenburg and Bathurst [70] found that the maximum packing density was obtained when the particles presented an eccentricity equal to 0.2. Therefore, elliptical particles with an eccentricity equal to 0.2 were chosen to study the undrained behaviour of the idealized systems.

Numerical simulations are generally conducted on assemblies of particles confined by rectangular boundaries. The use of rectangular boundaries causes stresses to concentrate at the corners of the specimen, an observation made both in laboratory tests [75] and in numerical simulations [61]. In the present work, a circular boundary was used to encourage uniform deformations and lessen localized effects emerging as a consequence of the uneven distribution of stresses. The circular boundary was simulated using 76 flat particles termed the *boundary particles*. The eccentricity of the boundary particles is equal to 1.0, and their average diameter ($\bar{D}$) varies during the tests to maintain a continuous boundary. The boundary particles act rigidly in the sense that they do not penetrate the interstices. The effects of membrane penetration commonly observed in laboratory experiments are nullified by the present approach.

All the assemblies used in the present study are composed of 1000 elliptical particles, a number that ensures a statistically representative assembly of a greater specimen and, at the same time, ensures that computational time is not excessive [6]. An initially loose assembly, and the particles forming the boundary, are depicted in Figure 4.1.

4.1.1 Properties of the Particles

The static elastic parameters assigned to the particles were those of quartzite [33]; namely, Young's modulus E=80 GPa, and Poisson's ratio μ=0.25. The interparticle sliding criterion is calculated according to the Mohr-Coulomb law:

$$F_t = F_n \tan \phi_\mu \tag{4.1}$$

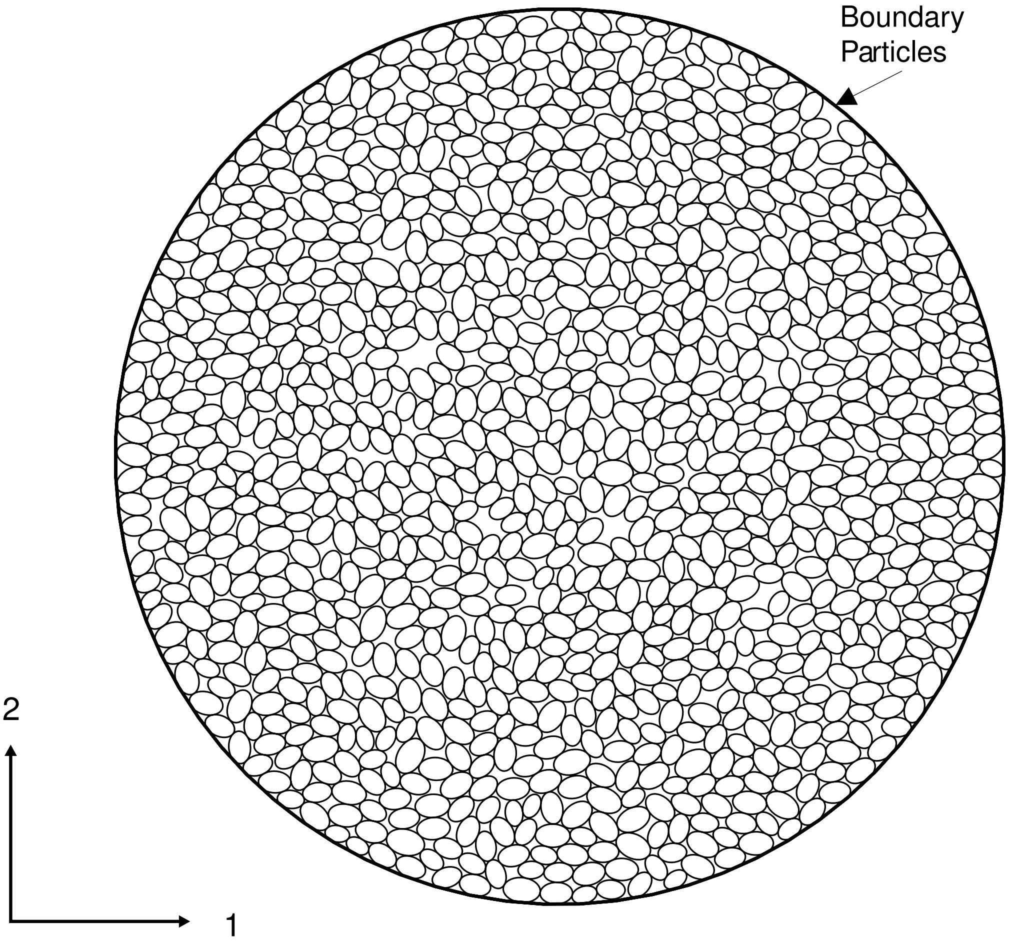

Figure 4.1: Initial loose assembly formed by 1000 internal particles ($e_c = 0.2$) and 76 boundary particles ($e_c = 1.0$)

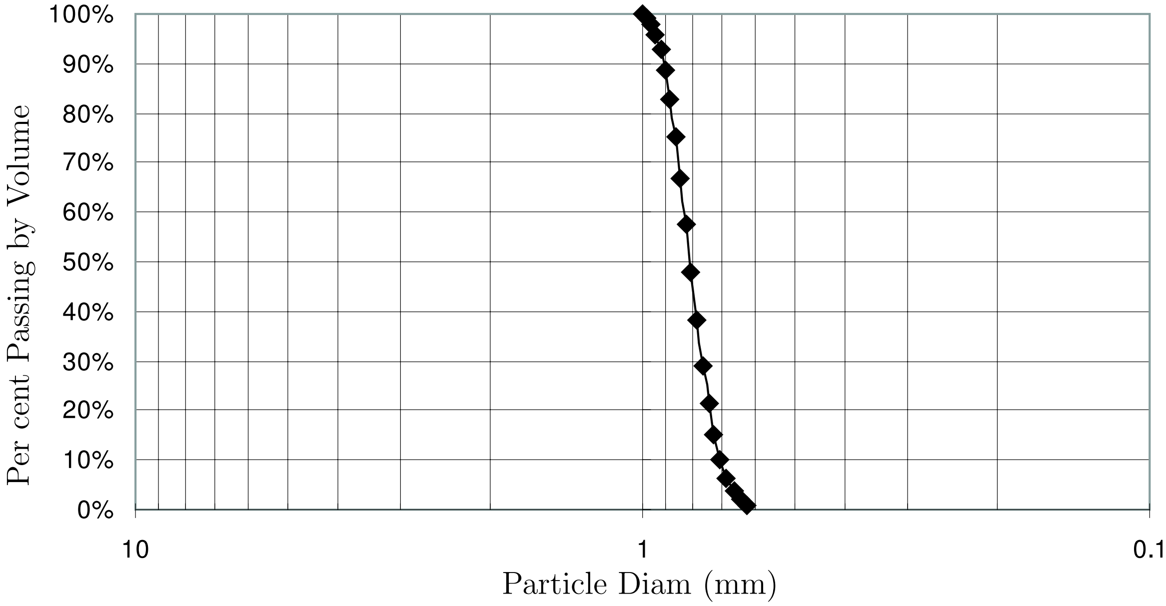

Figure 4.2: Grain size distribution

where F_t and F_n are the tangential and normal contact force respectively, and ϕ_μ is the interparticle friction angle. A value of 0.55 was assigned as an interparticle friction coefficient tan ϕ_μ and the density of the particles was assumed equal to 2700 kg/m^3. The assembly shown in Figure 4.1 is assumed to have a thickness Δ of 1.0 mm.

The elliptical particles display 20 different equivalent diameter sizes that are log-normal distributed. The grain size distribution shown in Figure 4.2 is considered typical for well-graded medium to coarse-grained sands.

Time Step

The discrete nature of the DEM requires the selection of a time step small enough to assure static equilibrium of particles at all times, but as large as possible to optimize computational time. The critical time step can be calculated according to (3.21) for the case of a linear contact law. For the case of a non-linear contact law, however, an optimal selection of the time step must be sought to maintain the inertial forces (ratio of the average particle force to the average normal contact force) to their minimum possible value. The percentage of inertial forces are an adequate measurement of the static particle equilibrium and it has to be kept to a minimum value as a consequence of the explicit nature of the discrete element method. Following a number of trial tests, it was found that a time step $\Delta t = 4.781 \times 10^{-3}$ was sufficiently small to maintain the ratio of inertial forces to a value less than 0.1 according to the recommendation of Strack and Cundall [84]. All the numerical simulations of the fluid-flow coupled DEM in this dissertation were performed using this time step, unless otherwise stated.

Damping Coefficients

The DEM employs an artificial damping mechanism using a system of dashpots that dissipate energy and bring the particles to a state of static equilibrium. Program AQUA incorporates four different mechanisms of energy dissipation. For every particle, it considers the existence of two dashpots affecting the translational and rotational movement, as well as two additional dashpots acting at every contact in the normal and tangential directions. The amount of damping in the translational and rotational directions is controlled through coefficients α and ω respectively. The coefficient β controls the amount of damping at the contacts. These coefficients have been incorporated in the equations of motion, *e.g.*, relation (3.16).

Property	Nomenclature	Value
Global damping	α	0.0 1/sec
Contact damping	β	2500 1/sec
Rotational damping	ω	10.0

Table 4.1: Optimum damping coefficients

Values for the damping coefficients α, β and ω that produced the least unbalanced forces were chosen after a number of trial runs. These values are presented in Table 4.1.

4.2 Contact Law

A non-linear contact law based on the theory developed by Hertz was implemented in the algorithms. The purpose of this implementation was twofold: to compute interparticle force-displacement in a more realistic manner; and, to restrict high interparticle penetrations that arises when using a linear-contact law model. Particle inter-penetrations have a direct effect on the mechanical response of the assembly since higher pore pressures are generated, resulting in a greater stiffness degradation.

The effects of the adopted slippage criteria were verified by tracking the force-displacement evolution of several contacts during a drained simulation.

Different types of contact geometries and interparticle friction coefficients for boundary contacts were examined. Additionally, free vibration tests were carried out to demonstrate the behaviour of the elliptical non-linear response and the effects on the final response at equilibrium. A description of these tests, and the results, are summarized below.

4.2.1 Slippage Criterion

Biaxial drained tests were carried out to verify the interparticle slippage mechanism. The magnitudes of the normal $|\mathbf{f}_n^c|$ and tangential $|\mathbf{f}_t^c|$ contact forces at several contacts were extracted during a simulation, and the slippage criterion was verified. The coefficient of interparticle friction μ was set at 0.5.

Figure 4.3 shows the measured variation between normal and tangential forces at one selected contact during a test. This particular contact point was chosen because it did not disrupt during the test.

The contact constitutive relation involves non-linear springs both in the normal and tangential directions. Coulomb friction criterion imposes the condition at the contact $|\mathbf{f}_t^c| \leq \mu|\mathbf{f}_n^c|$. For cohesionless contacts, the region of admissible forces should be bounded by the lines $|\mathbf{f}_t^c| = \pm\mu|\mathbf{f}_n^c|$ according to Coulomb's principle. For the case $|\mathbf{f}_t^c| = 0.5\,|\mathbf{f}_n^c|$, data presented in Figure 4.3 indicate that, as expected, slippage occurs along the boundary imposed by the friction coefficient.

4.2.2 Contact Criteria Between Boundary and Internal Particles

The assembly employed for the simulations is bounded by a group of elliptical particles of eccentricity e_c= 1, termed the *boundary particles.* Drained simulations were carried out to examine the effects of different contact geometries and friction coefficients of contacts between internal and boundary particles. More specifically, the force-displacement calculation of internal and boundary particles was carried out assuming the following:

1. The internal particles (particles identified as number two) are treated as spheres whose radii of curvature are defined by the point of contact. The boundary particles

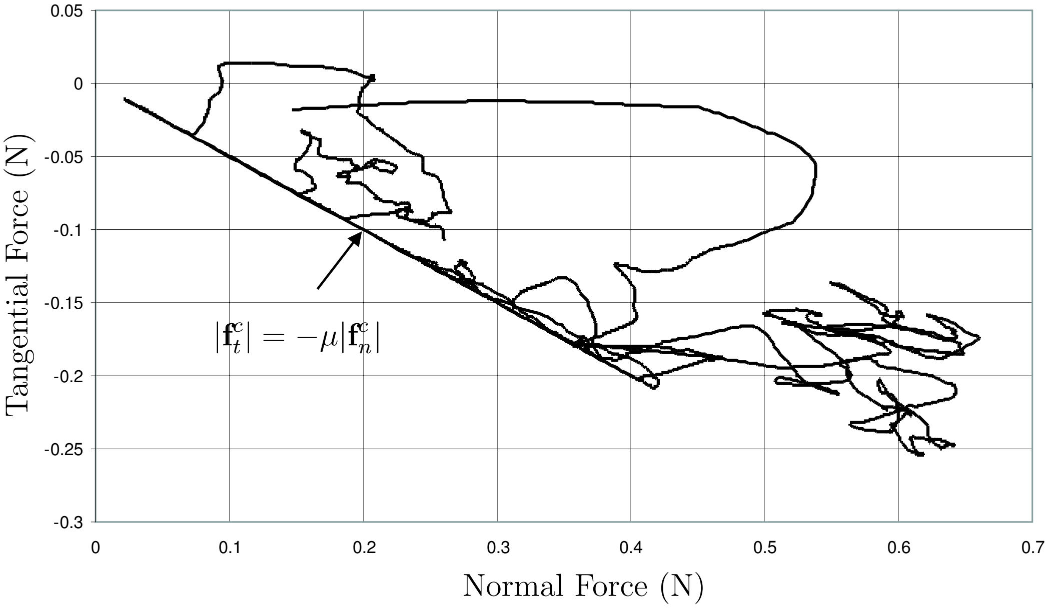

Figure 4.3: Verification of the interparticle slippage criterion

(particles identified as number one) are assumed to be frictionless plane surfaces,

$$\begin{cases} R_1 = R_1' = \infty \\ R_2 = R_2' > 0 \\ \mu = 0.0 \end{cases}$$

where R_i and R_i' are the radii of curvature of particle i at orthogonal directions.

2. The internal particles are treated as spheres whose radii of curvature are defined at the point of contact. Boundary particles are assumed to be plane surfaces with a friction coefficient,

$$\begin{cases} R_1 = R_1' = \infty \\ R_2 = R_2' > 0 \\ \mu = 0.5 \end{cases}$$

3. Both internal and boundary particles are treated as spheres. The radii of the boundary particles are assumed to be equal to the radii of the internal particles. The radii of the internal particles are given by the radius of curvature at the point of contact. The contact is assumed frictional as follows:

$$\begin{cases} R_1 = R_1' > 0 \\ R_2 = R_2' > 0 \\ \mu = 0.5 \end{cases}$$

The results of the drained simulations for the three different cases considered are presented in Figure 4.4. The curves show the change of the quantity $\sin\phi_{\text{mob}} = (\sigma_{22} - \sigma_{11})/(\sigma_{22} + \sigma_{11})$ with the level of deviatoric strains ϵ_t.

The first observation that can be made from Figure 4.4 is that the resistance is considerably increased when friction is assigned to the boundary contacts. The data also suggest that considering a sphere-sphere contact or sphere-plane contact in the frictional case produces very similar results. A higher frictional resistance is mobilized by considering frictional boundary contacts.

A detailed analysis of the results shows additional differences between the different scenarios, mainly, the displacement fields and the internal force distribution were not uniform in the frictionless case. The displacement fields showed that internal deformations of particles near the boundary, due to the lack of friction, did not follow the deformation of the

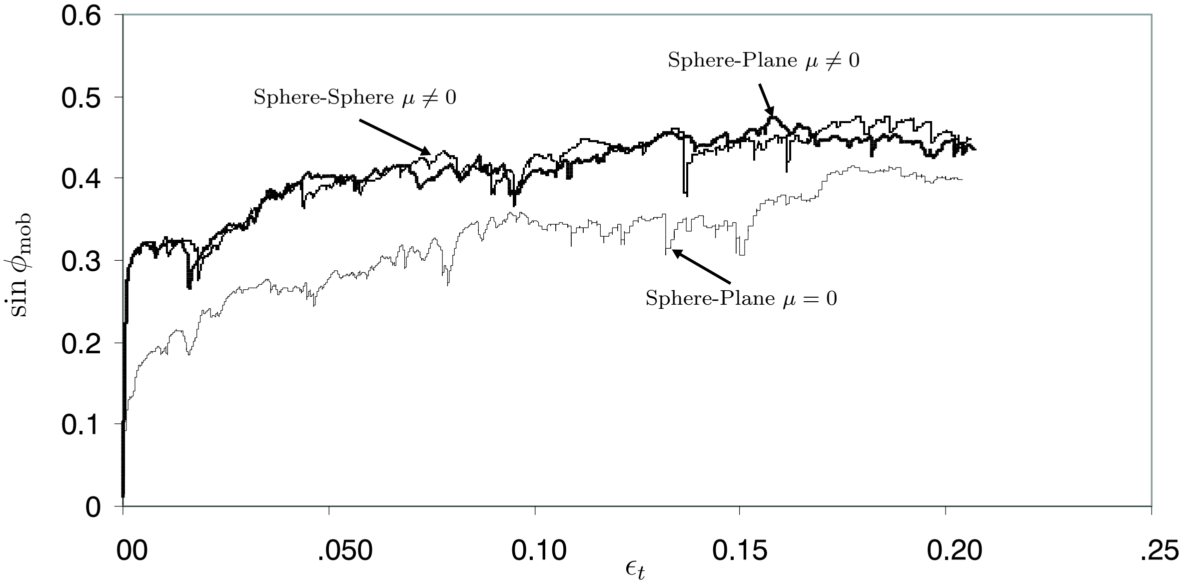

Figure 4.4: Effect of boundary type of contact on the drained strength of an initially loose assembly

boundary particles. As observed in Figure 4.5a, this condition lead to the development of chains of forces which aligned in the loading direction, and concentrated in the middle third of the assembly. For the case of frictional contacts however, a more uniform distribution of forces is obtained. The force distribution for the frictional case is depicted in Figure 4.5b.

From the results of the above study, it was considered appropriate to assign a friction coefficient to the boundary contacts equal to the friction of the internal contacts. Additionally, forces at the boundary were calculated by assuming a spherical-planar contact. Even though this assumption has no practical implications in the final resistance of the assembly (see Figure 4.4), it conforms to the geometry of the problem.

Free-Vibration Response

The effects of damping coefficients on the free response of a particle were evaluated using a procedure similar to the one presented by Cundall and Strack [23]. A particle was initially disturbed from its equilibrium position by applying translational and rotational forces to its centre. The movement of the neighboring particles was inhibited, and the change of a contact force with the number of cycles for a given contact was monitored. The application

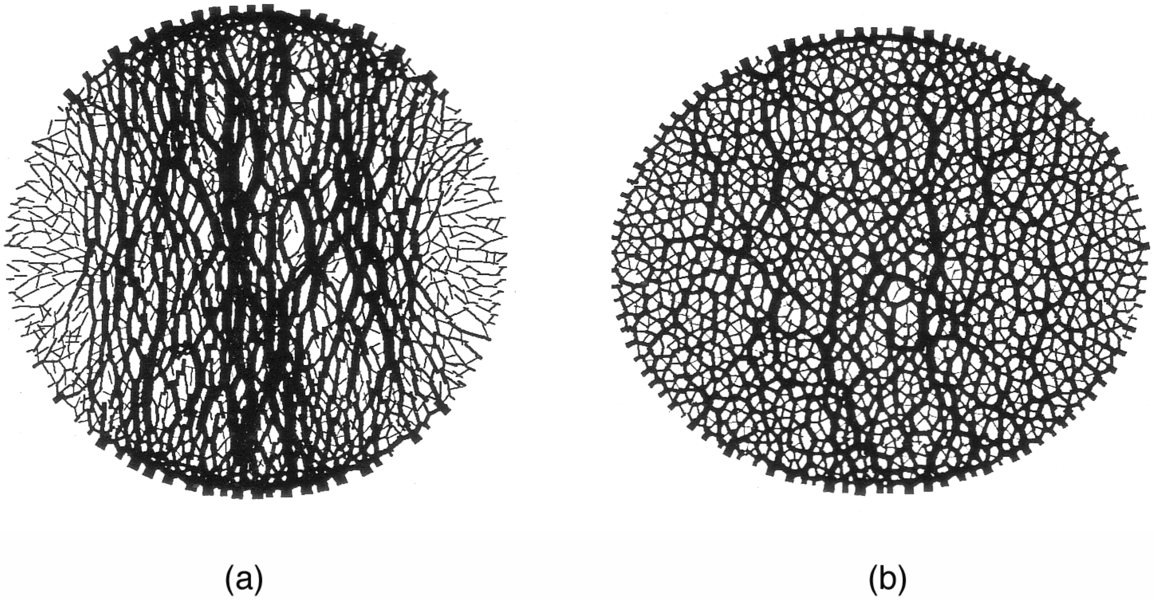

Figure 4.5: Interparticle force distribution for a) frictionless and b) frictional boundary contacts

of a rotational disturbance permitted the observation of how the contact stiffness changes with the radii of curvature at the contact point.

Three different values of α were evaluated (5, 500 and 1000 1/sec) while maintaining β and ω constant ($\beta = 0$ and $\omega = 1$). The results of the free vibration test are depicted in Figure 4.6.

The curve corresponding to $\alpha = 5$ oscillates around an equilibrium position and, even after 1000 cycles, equilibrium is not reached. The curve corresponding to $\alpha = 500$ reaches equilibrium in about 300 cycles, while the curve corresponding to $\alpha = 1000$ reaches equilibrium in fewer cycles. The results demonstrate the effects of the non-linear contact law for the case of elliptical particles. The ultimate force at equilibrium changes with the amount of damping. As the particle oscillates around the equilibrium position, the radii of curvature at the contact change, modifying the contact stiffness. The change of curvature is a function of the position of the contact vector with respect to the ellipse's major axis as shown by the plot in Figure 3.4. This effect is also reflected in the change of frequency of the curves.

The effect of the mass-rotational damping coefficient ω on the free response of the particle is presented in Figure 4.7. Three different coefficients were used, ω= 1, 10 and 20, while maintaining $\alpha = 1000$ constant. The data show that the coefficient ω affects the frequency of the response curve but does not considerably change the amplitude nor the final force at equilibrium.

The results of these numerical experiments demonstrate the implication of considering non-linear effects in elliptical particles, mainly, that the force at static equilibrium depends on the location of the contact point along the perimeter of the contacting ellipses. For the particular cases examined, the contacting point, and hence the stiffness, changed during the free vibration, affecting the final force. This behaviour differs from that reported by Cundall and Strack [23], where the equilibrium force of two contacting disc-shaped particles was the same.

4.3 Testing the Void-Strain Calculations

Undrained simulations in the laboratory are assumed to evolve under constant volume, an assumption arising from the fact that the compressibility of the fluid and grains is sufficiently small that any possible deformation can be disregarded. In program AQUA,

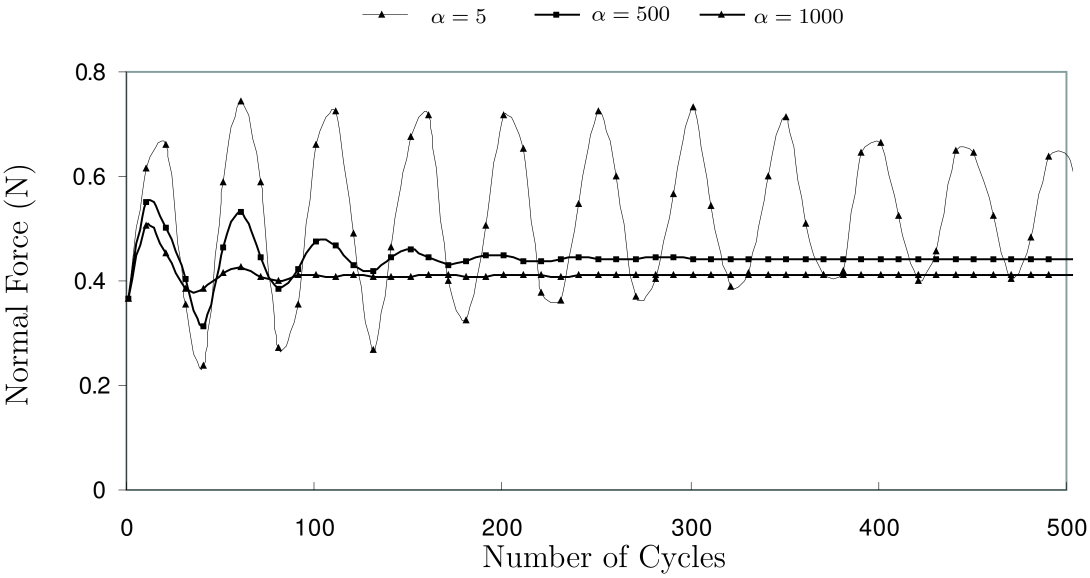

Figure 4.6: Effects of mass damping coefficient; ω=1,$\beta = 0$

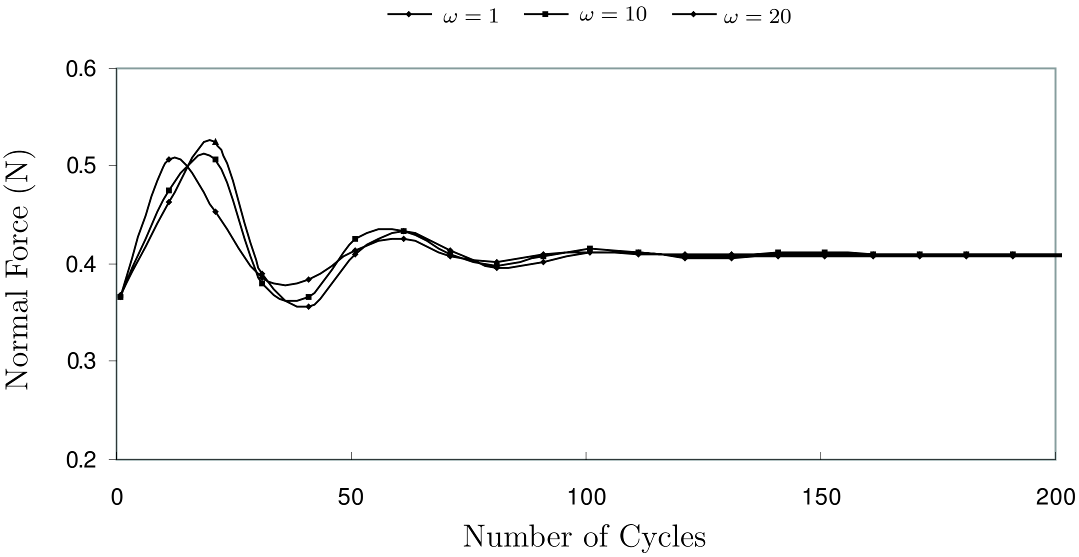

Figure 4.7: Effects of mass-rotational damping coefficient; α=1000, $\beta = 0$

small deformations occur both at the contacts and the voids. Deformations of voids are used to compute pore pressure increments according to a stiffness initially assigned to the fluid.

Computing the volume of voids is a complex process that involves a vast number of calculations performed by different subroutines. Even though the behaviour of the idealized assemblies may be in agreement with the behaviour of granular materials, it is still desirable to verify that the pore volume computations are correct. This section presents results of simulations carried on to verify the pore pressure computations using independent subroutines. The verification was conducted using the existing relationship between the macroscopic volumetric strain and the pore pressure generation. Details of the computations and the results are provided below.

4.3.1 Volumetric Relationships

The macroscopic deformation of a granular assembly is the result of the deformation of its constituents, that is, particles and pore-fluid. The suggested method in program AQUA uses pore deformations to generate pore pressures through the elastic properties of the fluid. Hence, there exists a relationship between pore pressure generation (pore strains) and volumetric strains.

A comparison between incremental strains measured at the boundary using relation (3.38) and increments of pore pressure generation was conducted as a way of verifying that the pore strain calculations were correct. It was considered that making this comparison was possible because the different quantities are independently computed by different subroutines.

Consider an assembly of volume V composed of saturated pores and particles penetrating one another by small amounts at the contact points. The compatibility conditions relating deformations of the constituents and the boundary is given by the following:

$$\Delta V = \sum_{v \in V} \Delta V_i^p + \sum_{c \in V} V_j^c \qquad i = 1 \dots N_p;\ j = 1 \dots N$$

where V^p and V^c are the volumes of the pores, and overlapping particles respectively, and N_p and N are the number of pores and contacts. Alternatively, the previous relation can be written as:

$$\frac{\Delta V}{V} = \frac{\sum\limits_{v\in V} \Delta V_i^p}{V} + \frac{\sum\limits_{c\in V} \Delta V_j^c}{V} \qquad i = 1 \ldots N_p;\; j = 1 \ldots N \tag{4.2}$$

The above relation may be envisaged as analogous to the volumetric strain in continuum mechanics, where strains are the sum of the elastic and plastic contributions. The first term on the left is related to the plastic or irrecoverable deformations experienced by the voids, while the second term describes the amount of elastic deformations or recoverable deformations at the contacts.

From relation (3.34), the global increment of pressure is computed as:

$$\Delta\bar{u} = B_f \frac{\sum\limits_{v\in V} \Delta V_i^p}{\sum\limits_{v\in V} V_i^p} \qquad i = 1 \ldots N_p \tag{4.3}$$

Substituting (4.3) into (4.2) leads to

$$\frac{\Delta V}{V} = \frac{n}{B_f}\Delta\bar{u} + \frac{\sum\limits_{c\in V} \Delta V_j^c}{V} \qquad j = 1 \ldots N \tag{4.4}$$

where n is the porosity of the assembly. The sum of the overlapping volumes is in general small, since the elastic modulus of the particles is high, hence the contribution of this term can be can be disregarded, leading to

$$\Delta\epsilon_v = \frac{n}{B_f}\Delta\bar{u} \tag{4.5}$$

Equation (4.5) provides a link between increments of volumetric strains and pore pressure [49]. Increments in volumetric strains may be computed at selected intervals during the simulations using the displacements of boundary particles. Relation (4.5) uses a strain tensor computed in relation to the deformation state at the beginning of the increment and not in relation to the initial configuration.

4.3.2 Simulation Results

A simulation was carried out using pore pressure data to compare measures of $\Delta\epsilon_v$ with the values predicted by relation (4.5). The assembly had an initial porosity n=0.173 after

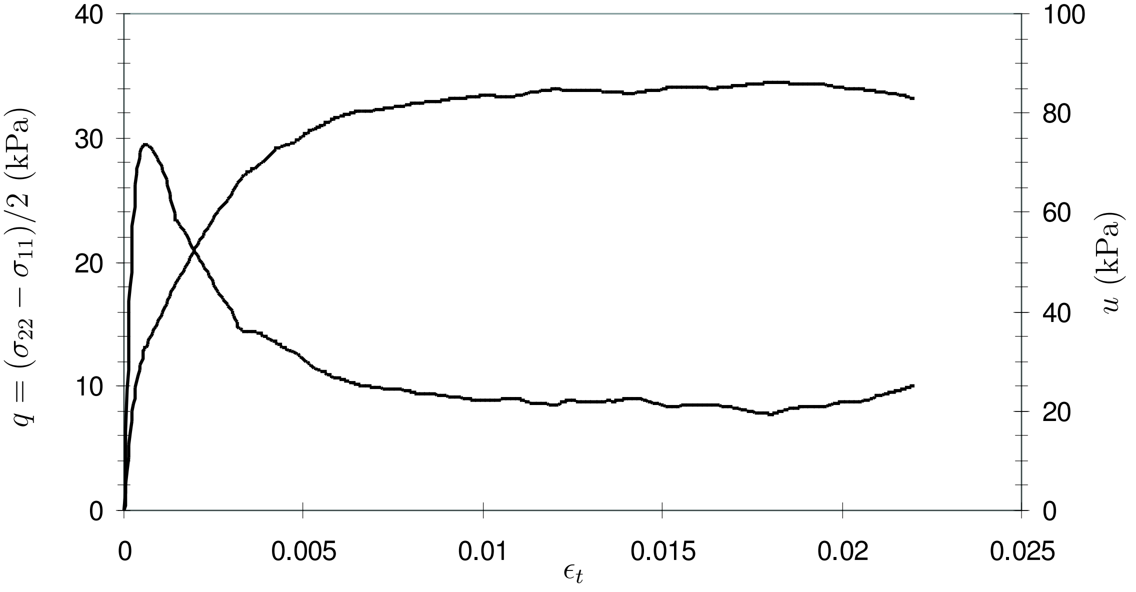

Figure 4.8: Strength of the assembly and evolution of macroscopic pore pressures

consolidated under $\sigma_o^{'} = 100$ kPa. The bulk modulus assigned to the fluid was $B_f = 100$ MPa.

The stress-strain curves and the evolution of the pore pressure are presented in Figure 4.8. The strength reaches a peak at small deformations, and the post-peak strength is characterized by a strain softening behaviour. It is interesting to compare the evolution of $\bar{u}$ with the strength of the assembly q. The assembly generated a positive pore pressure even during the post-peak stage. Additionally, the stage of maximum pore pressure coincides with that of the minimum strength. The measured data is in agreement with previously reported results (Figure 2.2).

During the simulation, 600 strain increments were sampled after 3×10^5 cycles; they are plotted in Figure 4.9 against the predicted increments using pore pressure data.

The resulting plot shows the correlation between different measurements. The data fall within a line of unit slope, which validates the void strain calculations.

The measured points present some scatter, especially near the origin. These increments correspond to the top portion of the volumetric strain curve. The farthest right point in the graph presents the highest deviation from the straight line; this point corresponds to

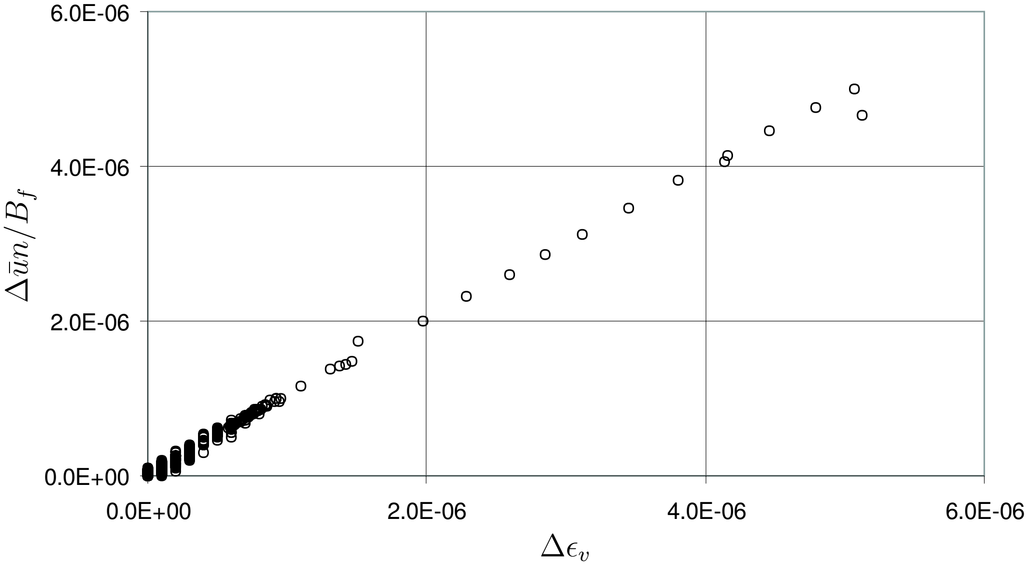

Figure 4.9: Relationship between increments of volumetric strain and macroscopic pore pressure

the first increment. The observed sparsity of the data can be attributed to roundoff errors.

The accuracy of the computations is satisfactory because the relation (4.5) is still satisfied despite the magnitude of the increments considered. The computed volumetric strains are too small to be measured with conventional laboratory equipment. Nevertheless, expression (4.5) suggests that any increment in the macroscopic pore pressure should be accompanied by sample deformations.

4.4 Fluid-Flow Scheme

The evolution of pore pressures in the system was analyzed by conducting two different types of tests. First, initially random pressures were assigned to the pores of an assembly composed of 1000 elliptical particles. The process of pore pressure equalization was monitored with time and the final equilibrium pressure was compared with the theoretical value. Second, boundary and initial conditions were assigned to a given rectangular assembly. The process of pressure dissipation was qualitatively compared with the analytical solution of Terzaghi's one dimensional consolidation theory.

The method employed for the solution of the system of differential equations and the results of the fluid-flow simulations are discussed below.

4.4.1 Numerical Solution of Fluid-Flow Equations

The combined response of the system to generate and dissipate pore pressures is provided by the solution of relation (3.30). Two different numerical techniques were examined to solve equation (3.30). In a first stage, integration was conducted using Euler's scheme according to the following relation:

$$f\,(\,t+\Delta t_f) = f\,(\,t) + [\,\chi f'(t) + (1-\chi) f'(\,t+\Delta t_f)]\,\Delta t_f \tag{4.6}$$

where f and f' denote the set of unknown functions and their time derivatives, respectively, χ is the parameter of the scheme ($0 \leq \chi < 1$), and Δt_f is the time step employed in the solution. Integration was carried out using $\chi = 0.5$.

After several runs, it was found that the time step required to minimize errors was too small, and usually considerably lower than the time step used for the solution of the particle's motion (*i.e.*, $\Delta t_f \ll \Delta t$). The error involved in Euler's technique is of the order of Δt_f^3, that is, $E = O(\Delta t_f^3)$ [83]. Thus, choosing an appropriate time step is critical, because errors can readily be accumulated, leading to incorrect solutions.

Because of limitations in Euler's method, an alternate method using a suite of subroutines named RKSUITE [10] was examined. RKSUITE is a suit of codes based on the Runge-Kutta formulas that solve the initial value problem for a first-order system of ordinary differential equations. One of the advantages of this suite is that it automatically chooses the time step at the beginning of the computations, and constantly readjusts it as the slopes of the solution change. This feature, among others, makes the use of these routines preferable to Euler's method.

RKSUITE was incorporated in program AQUA and after several runs, it was considered adequate to use these algorithms to integrate (3.30).

4.4.2 Pressure Equalization

A simulation was conducted in which only the pressure dissipation process was studied. Consider an assembly initially containing n pores filled with fluid at different pressures u_i at a certain time t. If particles are not allowed to move, the system can be envisaged as composed of n reservoirs inter-connected through pipes. If fluid is neither allowed to enter nor allowed to leave the system, depending on the characteristics of the network, the existing micro-gradients will initialize fluid flow among neighbouring pores. Theoretically, at time $t = \infty$, the pressures in the pores should equalize to a value given by the following relation:

$$u(\infty) = \frac{\sum_{i=1}^{n} u_i V_i}{\sum_{i=1}^{n} V_i} \tag{4.7}$$

where V is the pore volume.

A simulation was conducted in an assembly composed of 1000 elliptical particles. The movement of the particles was inhibited during the simulation; this procedure nullified the pressure generation mechanisms leading to the condition $dV_i^{\beta}/dt = 0$. The flow network was assumed to consist of 10μm diameter conduits and random pressures between 0 and 100 kPa were initially assigned to the pores.

The variation of the fluid pressure with time in four different pores is presented schematically in Figure 4.10. Note that a logarithmic scale was used in the abscissa.

Analysis of the curves reveals that most of the pressure equalization process takes place during a short time. However, the final equilibrium is not reached until after 1.5 sec.

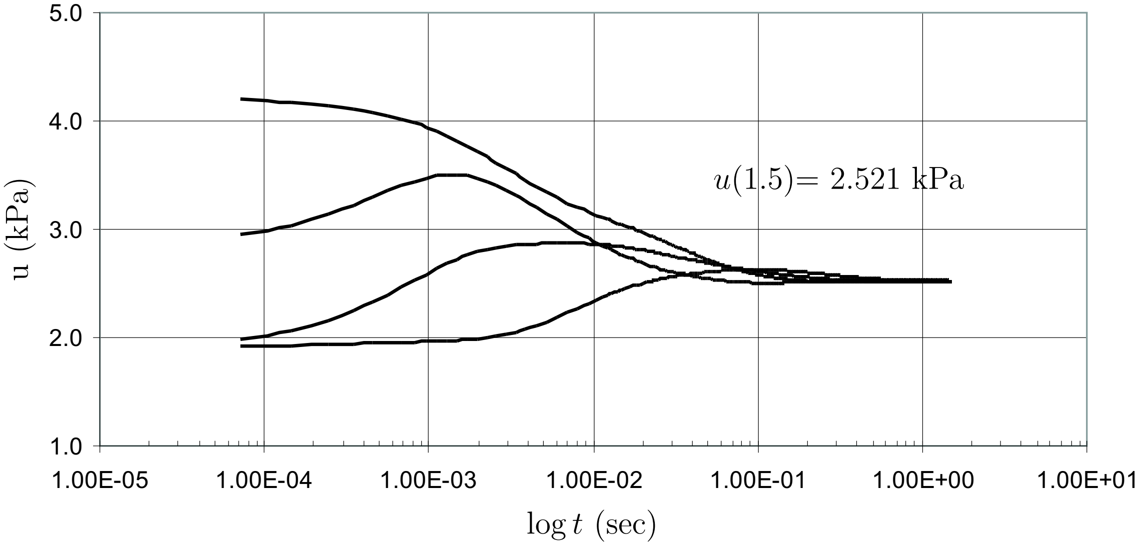

Figure 4.10: Test to monitor the pressure equalization process. The Figure shows the change with time of micro-pressures in four different pores

The results further show that the pressure in the assembly reached an equilibrium value of $u(1.5)$= 2.521 kPa, which is the same as the value predicted by relation (4.7), that is, $u(\infty)$= 2.521 kPa, confirming the accuracy and validity of the results.

4.4.3 Pressure Dissipation

The results of an experiment are presented to demonstrate the applicability of the proposed approach in solving excess pore pressure dissipation problems. The primary objective of the test was to quantitatively compare the numerical solution of (3.30) subjected to particular initial and boundary conditions with the analytical solution of Terzaghi's one-dimensional theory of consolidation.

As in the study of pressure equalization, the particle movement was inhibited throughout the simulations. The test consisted of assigning an initial excess pressure u_o to all the pores of a rectangular assembly (Figure 4.11). The contacts carrying normal forces were initially identified, and the programmed algorithms were used to generate the polygon and flow networks. A detail of the networks thus obtained is depicted in Figure 4.11; the

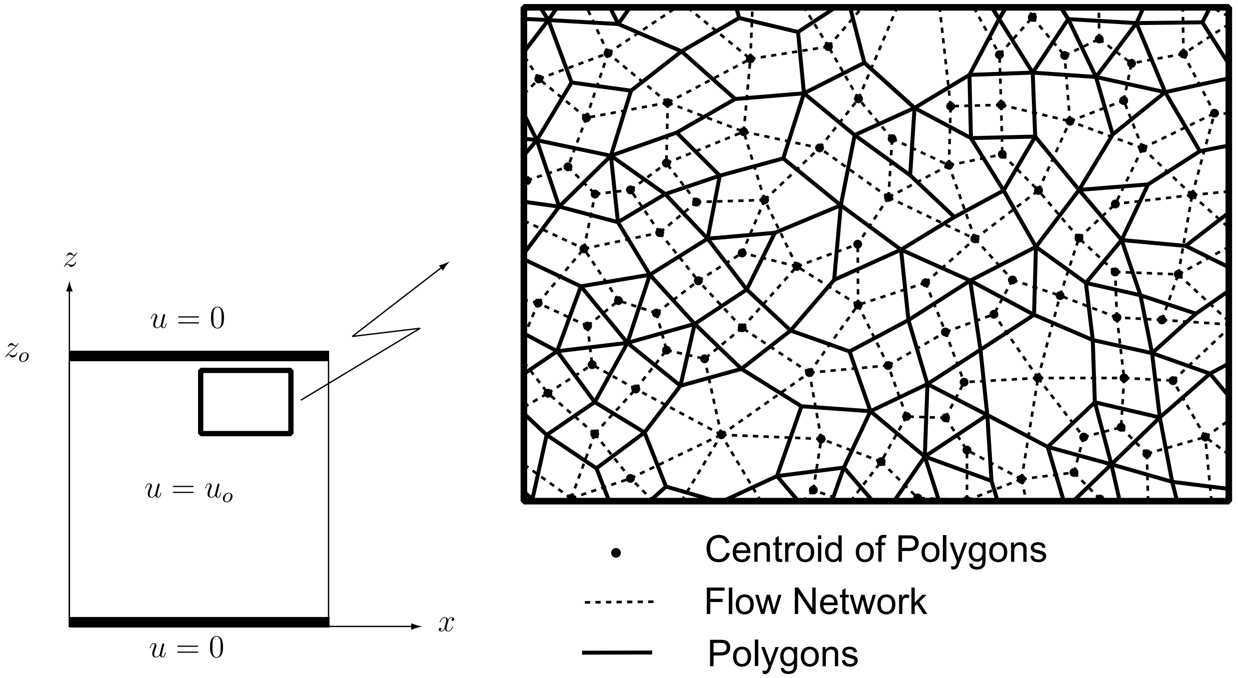

Figure 4.11: Detail of flow network used in a pore pressure dissipation problem

rectangular boundary is referenced to a Cartesian frame. Pores located at the top and bottom boundaries ($z = 0$; $z = z_o$) were identified as boundary pores. Once the simulation was commenced, the pressure in the boundary pores was set to zero and kept at this value throughout the test.

The spatial distribution of pore pressures was extracted at two different times during the test as illustrated schematically in Figure 4.12. The vertical x axis shows the value of the normalized pore pressure u/u_o throughout the assembly. The distributions obtained were qualitatively compared with those derived from Terzaghi's theory of consolidation. Terzaghi's development of a one-dimensional theory of consolidation [87] led to the description of pore pressure dissipation posed by the solution of:

$$\frac{\partial u}{\partial t} = C_v \frac{\partial^2 u}{\partial z^2} \tag{4.8}$$

where C_v is the coefficient of consolidation. Equation (4.8) is a second order linear parabolic partial differential equation used in physical contexts to model heat conduction and diffusion phenomena. The solution of (4.8) under proper initial and boundary conditions de-

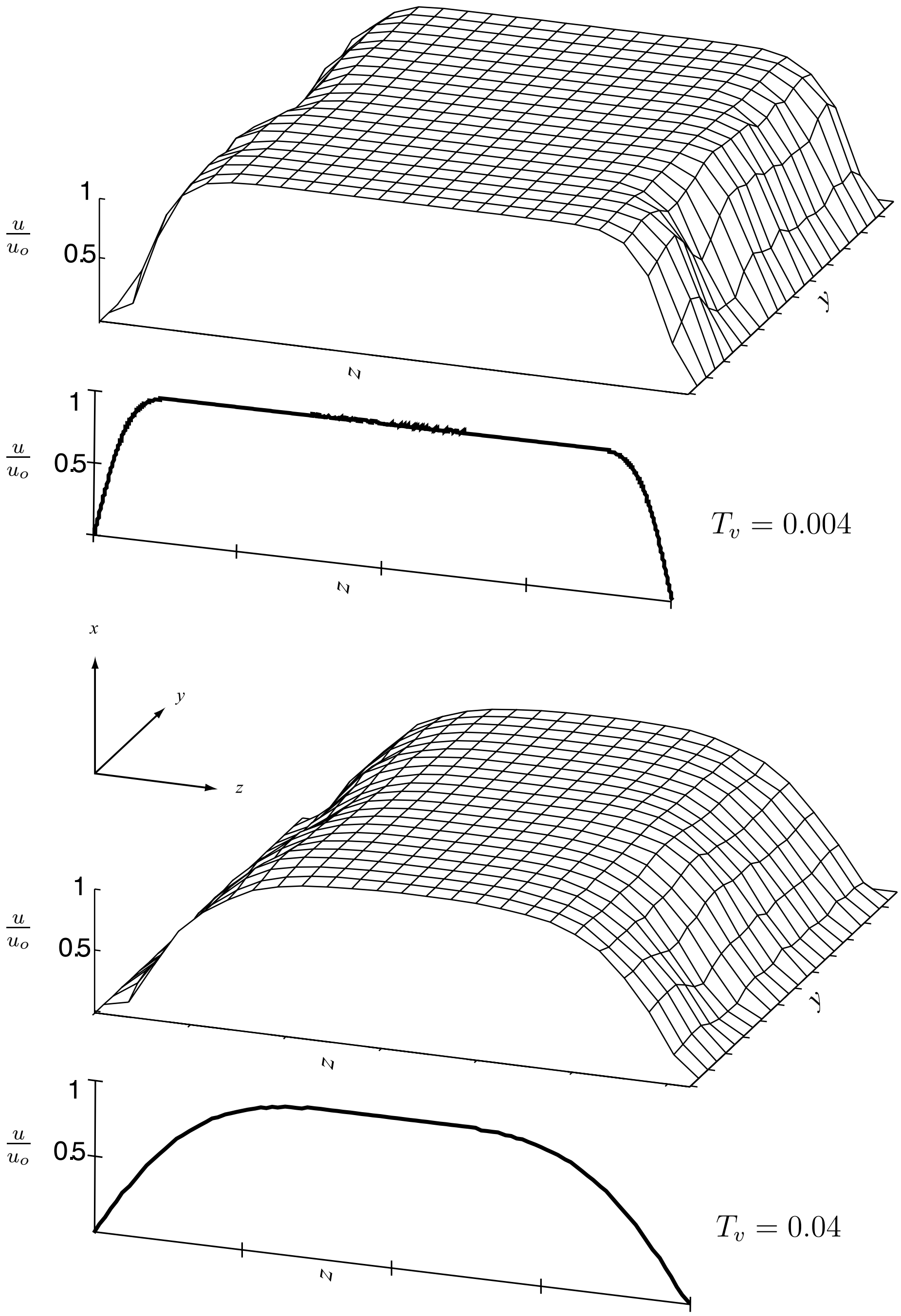

Figure 4.12: Comparison of pore pressure dissipation obtained from proposed scheme with Terzaghi's one-dimensional consolidation theory

scribes the distribution of pore pressure with time, and it is usually expressed as $u(T_v, z)$, where T_v is a non-dimensional coefficient which is a function of time, the coefficient of consolidation, and the length of the drainage path.

The solution of Eq. (4.8) is also presented in Figure 4.12 for $Tv = 0.004$ and $Tv = 0.04$, respectively. A qualitative comparison of the one-dimensional analytical solution with the two-dimensional numerical solution shows that both solutions are remarkably similar. The measured data proves the capability of the conduit network approach in modelling two-dimensional unsteady fluid-flow problems through granular assemblies. Homogeneity and isotropy are some of the assumptions made in the derivation of (4.8). Under the present approach however, the spatial arrangement of the conduits emerges naturally as a consequence of the fabric arrangement; hence, possible anisotropy effects are accounted for in the proposed model.

4.5 Global Hydraulic Conductivity

The volumetric flow rate through each individual conduit is modelled according to the Hagen-Poiseuille's relationship. Hagen-Poiseuille's relation indicates that flow is proportional to the fourth power of the conduit's diameter and inversely proportional to the conduit's length; thus, choosing the proper geometrical characteristics for the conduits prior to conducting any simulation is a critical step.

The length of individual conduits (L) is computed as the distance between centres of mass of the connected pores; therefore, the spatial orientation and the lengths are the result of the arrangement of the particles. Still, an adequate channel diameter remains to be assigned.

To access this problem, a number of flow tests were conducted using a rectangular assembly. A microscopic pressure gradient ∇u was applied to the boundary nodes, as shown in Figure 4.13, until a steady state condition was established, that is, until the pressure in all boundary nodes remained constant. Once steady state flow was established, the total volumetric inflow rate q_{in} was calculated by adding the inflow volumes V_{in}^{β} necessary to maintain the pressure gradient constant during an increment of time Δt as:

$$q_{in} = \frac{1}{\Delta t} \sum_{t}^{t+\Delta t} V_{in}^{\beta} \tag{4.9}$$

From this relation, the hydraulic conductivity of the assembly K in the direction of the applied gradient was calculated as:

$$K = \frac{q_{in}}{A_{cross}\nabla u} \tag{4.10}$$

where A_{cross} is the cross sectional area of the assembly.

Having determined the hydraulic conductivity, the aforementioned procedure was repeated changing the diameter of the conduits. Figure 4.14 shows the relationship between macro-permeability and conduit diameter for the fluid network employed.

The information presented in Figure 4.14 shows that a small variation in the diameter of the channels produces a significant change in the overall permeability of the assembly; such change was expected, since the quantity of the fluid that passes through a given conduit varies as the fourth power of its diameter.

The next step in the study was to select an appropriate diameter for the conduits, considering the geometrical characteristics of the particles. The average diameter of the particles (D_{50} =0.8 mm) falls within ranges commonly found for fine to medium sand; these materials are known to present a hydraulic permeability on the order of 1x10^{-3} cm/s [43]. If this permeability value is accepted as representative of the assembly, a diameter can be assigned to the conduits using the information depicted in Figure 4.14. Analysis of Figure 4.14 shows that $k(80) \approx 1 \times 10^{-3}$; hence, it is assumed that a diameter equal to 80μm will adequately model the conductive properties of the particles' assembly.

It must be stated that the relation shown in Figure 4.14 is exclusive to the network tested. The macro-permeability tensor in network models is known to be a function of the spatial arrangement of the conduits [73]. Furthermore, the anisotropy varies as the positions of the particles change during deformation [88]. Despite these aspects, the relation obtained provides a valuable reference on the possible range of diameters to be employed. Although the program allows use of a variety of diameters that perhaps could follow a predefined distribution, all the simulations reported in this research were conducted by exclusively assigning the same diameter to all the conduits.

4.6 Fluid Compressibility Effects

Fluid compressibility can be related to a certain extent to the degree of saturation of the sample. The higher the degree of saturation, the lower the compressibility of the assembly,

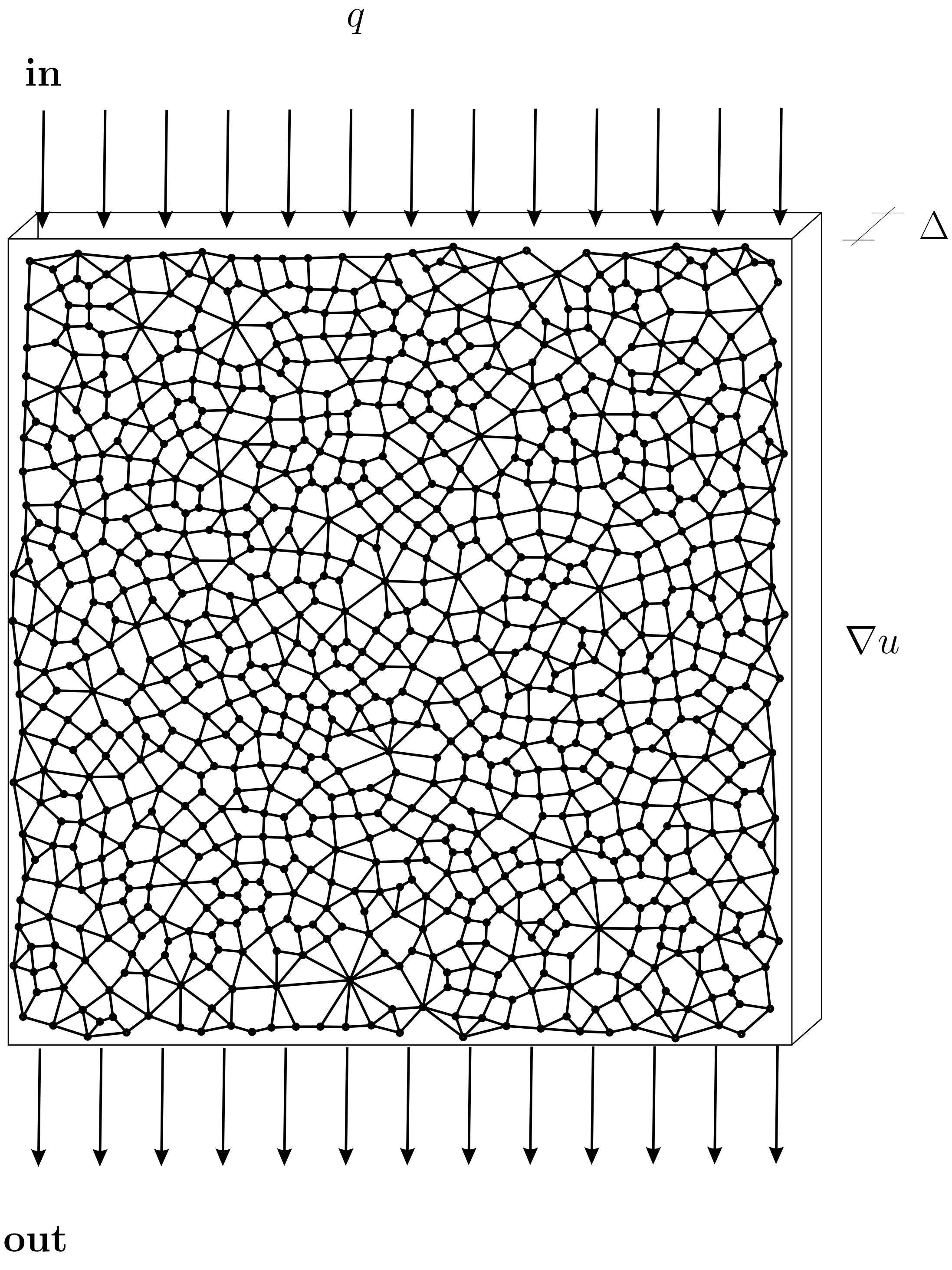

Figure 4.13: Flow network used to relate micro and macro permeability

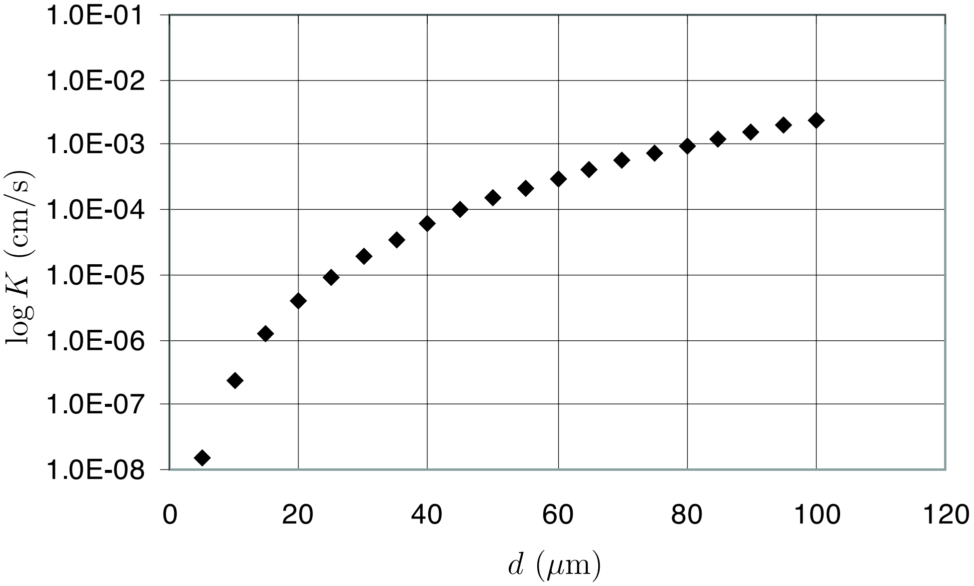

Figure 4.14: Relationship between conduit diameter and macro-permeability

and vice versa.

The effect of saturation degree on the mechanical behaviour of undrained tests in the laboratory has been recognized since the mid 50's. This condition was recognized by Skempton who proposed the application of back pressure to enhance saturation. Different saturation degrees results in responses that can vary considerably.

The model adopted makes use of volumetric changes to compute pore pressure increase according to elastic properties initially assigned to the pore's fluid. Hence, the fluid pressure changes as a response to pore volumetric strains and is directly proportional to the bulk modulus assigned to the fluid. It was previously shown in Section 3.4 that a fraction of undissolved air in the water will dramatically alter the bulk modulus of the air-fluid mixture, which can be evaluated according to (3.25).

The effects of different moduli $B_f(S)$ on the macroscopic behaviour are evaluated assuming that the bulk modulus of the air-water mixture is adequately predicted by relation (3.25). Accordingly, the stiffness of the fluid-mixture can vary from that of water (0 per cent air content) to that of air (0 per cent water content). The amount of water in the mixture has been called the degree of water saturation S and is defined as the ratio of

Test	S	B_f (kPa)
A	1.00	2.9×10^6
B	0.98	2.0×10^4
C	0.90	4.1×10^3
D	0.00	4.1×10^2

Table 4.2: Initial degree of saturation (S) and corresponding bulk moduli

water volume with respect to volume of the pores.

The theory used to describe flow through conduits is that for single-phase fluids. The difficulties involved in adequately modelling a two-phase fluid flow condition are eliminated by further assuming equalization of pressures at the end of each calculation cycle.

4.6.1 Simulation Results

The discussion is based on data obtained from four simulations in which the compressibility of the fluid, B_f, was varied in each test. The assumed degrees of saturation and the corresponding bulk moduli computed according to relation (3.25) are presented in Table 4.2. The letters A, B, C and D will be used as distinctive labels assigned to each test, and reference to them will be made subsequently.

The assembly used presented an initial contact anisotropy $a = 0.16$, and was consolidated under a confining pressure $\sigma_o^{'} = 100$ kPa. The simulations considered the fully *saturated* $S = 1$ and fully *dry* situations as well as two cases in between ($S = 0.90$ and $S = 0.98$). The results of assembly D, that is, $S = 0$ provide a useful comparison between the behavioral characteristics of a fully saturated test and an equivalent drained test departing from the exact same initial fabric.

Marked differences in strength can be observed in the stress-strain curves for different saturation degrees presented in Figure 4.15. Specimen A presented a typical unstable behaviour. After reaching a minimum strength at $\epsilon_t \approx 0.01$, it gradually recovered resistance under further deformation. Specimen B, on the other hand, exhibited higher maximum shear strength, and the rate of the stress-strain curve during the strain softening stage was considerably lower than that of specimen A. At higher levels of deformation, its strength is practically the same as that of specimen A.

Specimen C presented a higher maximum shear strength than those of specimens A

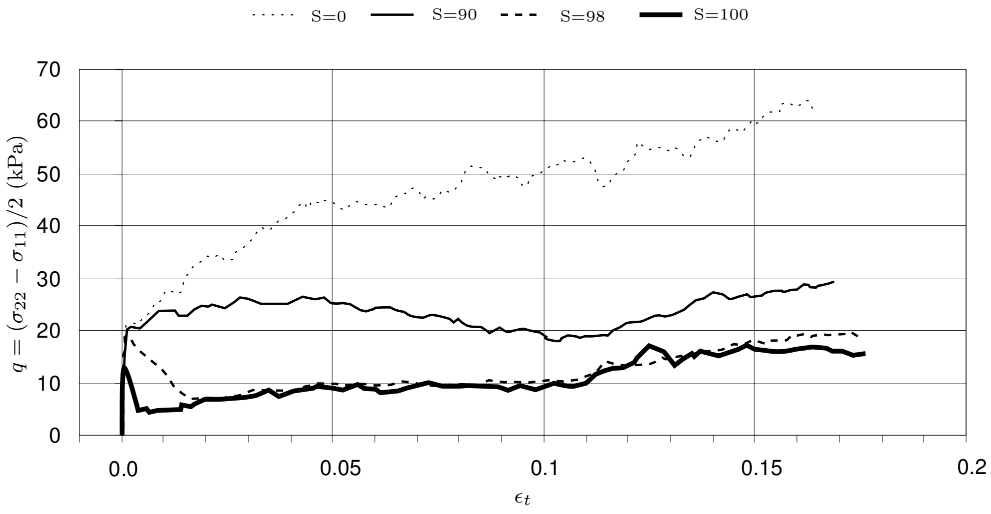

Figure 4.15: Stress-strain curves for varying saturation degrees

and B, the minimum strength being achieved only after $\epsilon_t = 0.1$ had elapsed. Specimen D presents a behaviour characteristic of loose sands, the strength continually grows and shows a tendency to stabilize as it approaches the end of the test.

The stress-paths for varying saturation degrees are presented in Figure 4.16. Specimen A starts to depart from the drained curve from the beginning of the simulation. This not being the case for any of the other specimens. Specimen D deforms under a constant q/p' ratio and the slope of the path is 45°, as expected for the drained case.

4.6.2 Evolution of Void Ratio

The evolution of the void ratio e is presented in Figure 4.15. Analysis of the void ratio provides information about the amount of volume decrease caused by compression of air in the fluid. It is interesting to note that the void ratio was compelled to remain constant in test A by the lateral response of the boundary. Such was not the case for specimens B, C and D, where variations of void ratio occurred at an amount closely related to the fraction of air in the fluid.

The exclusive action of the servo-mechanism is responsible for these differences. The volumetric strain can be calculated at any stage as the sum of the diagonal terms in the

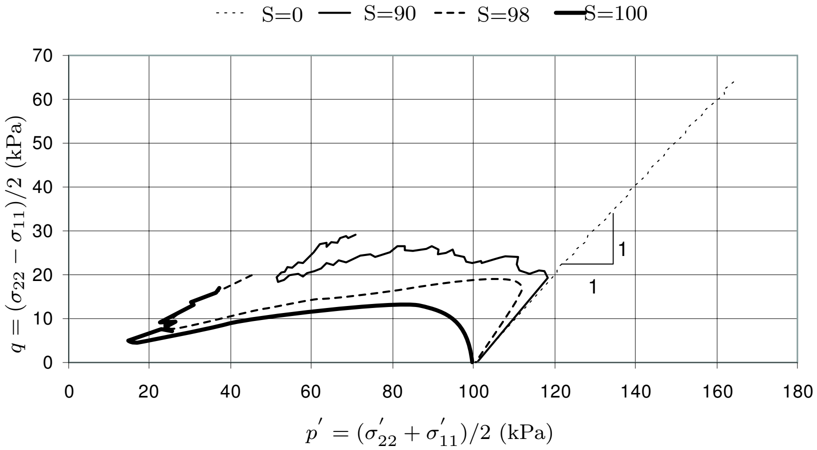

Figure 4.16: Stress paths for varying saturation degrees

strain tensor. Since axial strain rate is a constant $\dot{\epsilon}_{22}$, the deviations from the condition $\dot{\epsilon}_v$=0 originate in the lateral strain rate component $\dot{\epsilon}_{11}$. The lateral stress σ_{11} is automatically maintained using a strain-controlled boundary which functions in the manner of a servo-mechanism for which $\dot{\epsilon}_{11}$ has to vary.

These observations can readily be confirmed by tracking the evolution of the strain ratio (ϵ_{11} / ϵ_{22}), which provides a useful means of evaluating the lateral response of the boundary. This type of plot is presented in Figure 4.18.

The measured deformations at the boundary show that strain ratio $\epsilon_{11}/\epsilon_{22}$ was practically maintained constant for test A. Regardless of the observed similarities between tests A and B, the evolution of the principal strain ratio shows differences in boundary strain rates for these two tests. These curves show the reaction of the lateral boundary as a consequence of the compressibility of the fluid.

4.6.3 Contact Evolution

The evolution of the average coordination number γ is presented in Figure 4.19. The evolution of contact anisotropy coefficient a is presented in Figure 4.20. The evolution of γ for specimen A is characterized by the sudden loss of contacts upon initiation of shearing. The rapid increase of parameter a during the initial stage suggests that most of the contacts

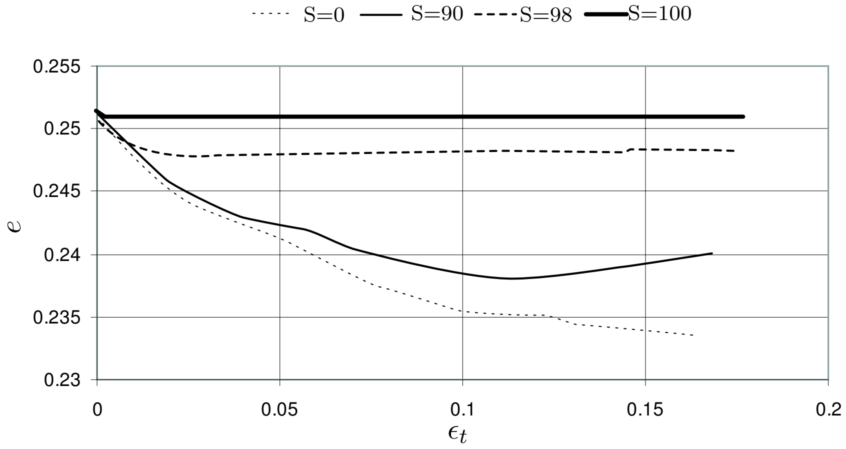

Figure 4.17: Evolution of void ratio for varying saturation degrees

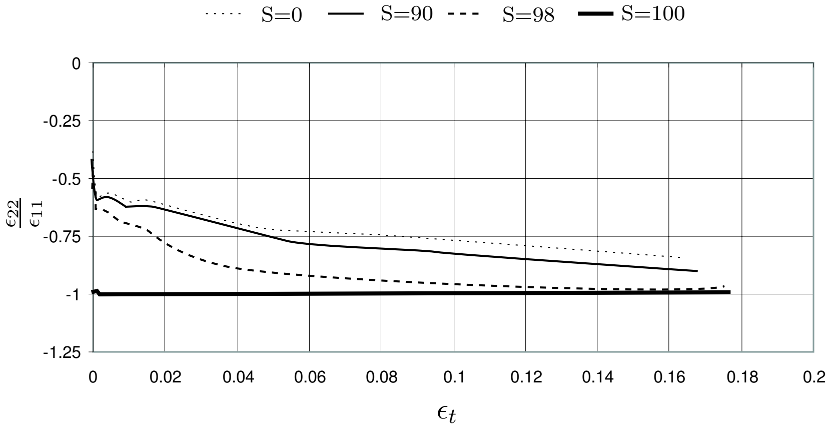

Figure 4.18: Ratio of vertical to horizontal strain for varying saturation degrees

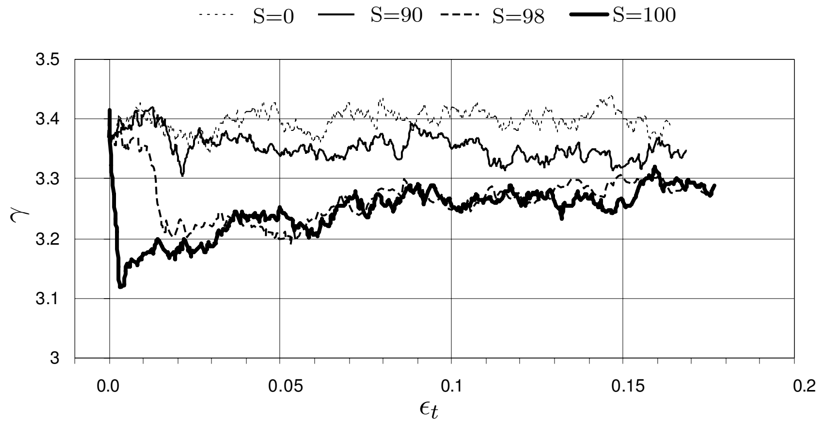

Figure 4.19: Average coordination number for varying saturation degrees

were lost in the horizontal direction. The shear strains at which minimum γ and minimum stress difference q occur are coincident. After the specimen reached a minimum γ, the average number of contacts increases as deformation continued until it reached an average value of 3.3 at the end of the test.

Regarding the behaviour of test B, the process of lateral contact disintegration appears to be delayed by the higher air content of the fluid. This situation also retards the strength loss during the strain softening stage observed in Figure 4.15. Specimen B shows a similar coordination number during a short period of deformation. It is interesting to note that both curves for test A and B converge and are of similar shape during the rest of the test.

The evolution of contacts for specimen C is different from that of the other tests. The coordination number fluctuates between 3.2 and 3.4 throughout the simulation.

The evolution of the average coordination number for specimen D is interesting, since the number of contacts, at least in average, remains practically the same throughout the test, while the contact anisotropy parameter grows, suggesting that the rate of contact disintegration should be similar to the rate of contact creation. A coordination number of 3.4 seems to be required to preserve particle stability regardless of the volume reduction experienced by the assembly.

The results show that the average coordination number at the end of the tests is different for the different degrees of saturation. Even though volume is practically preserved for the 100 per cent saturation case, it is observed that particles are still able to rearrange internally

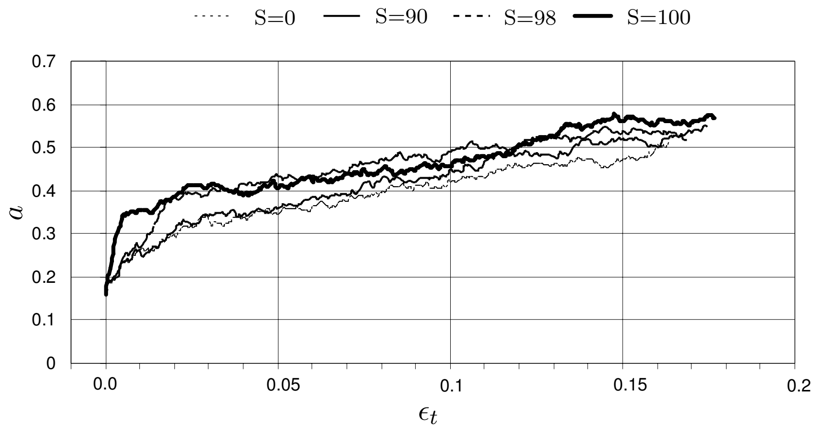

Figure 4.20: Contact anisotropy for varying saturation degrees

and the coordination number increases slightly at the end of the simulations so as to reach a more stable configuration. Additionally, the spatial arrangement of the contact normals for all the tests are quite similar at large strains. Nevertheless, significant differences are observed at the beginning of the tests; mainly, the initial rate of contact normal anisotropy is considerably higher for the 100 per cent saturation case. This observation combined with the acute drop initially experienced by specimen D reflects the higher amount of lateral contact disintegration as a result of the lateral movement of the boundary.

4.6.4 Conclusions

From the previous results, a number of conclusions can be drawn:

- A change in void ratio was observed in specimens B, C and D. Test A however, evolved under constant volume conditions. The results have practical implications since it is most likely that a degree of saturation of 100 per cent cannot be always attained in laboratory experiments; thus, some significant change in volume might occur when conducting biaxial tests. It was confirmed that the program AQUA preserves the volume at the macroscopic scales, and the ratio between axial and lateral strains and the void ratio further supports this conclusion.

- The maximum peak strengths were affected by varying degrees of saturation. However, a change from S = 100 percent to S = 98 percent does not appears to considerably affect the strength at large strains.

- In general, the assembly used could be characterized as loose because the stress-strain curve did not present a clear peak and a tendency for volume reduction was observed. For this particular case, an assembly with contractile characteristics in a drained environment behaved in a strain softening fashion when tested under undrained conditions.

- The evolution of the coordination number shows very different characteristics with different saturation degrees. For the dry case, the number of contacts on average remained practically constant. The observed increase in contact normal anisotropy for this case, however, increased, denoting the gradual disintegration of contact in the lateral direction. Thus, during deformation, a continuous process of contact disruption and contact creation is simultaneously occurring: contacts disintegrate, but are suddenly recovered to maintain a condition of static equilibrium. This is captured by the coordination number curve, as it presents lots of fluctuations of a small magnitude during the deformation. The curve corresponding to 100 percent saturation shows its own particular characteristics, mainly the acute drop in the number of contacts at the beginning of the test and the gradual regain of contacts at greater deformations. Although volume was practically preserved in the saturated case, it was observed that the number of contacts on average changes considerably.

- The simulations showed that the main difference between the responses of test A and test B was the maximum shear resistance, which was 1.5 times higher in test A, but the post-peak strength was practically the same. Hence, a change from $S = 1$ to $S = 0.98$ appears to affect only the peak strength, but the strength at large deformation is not considerably affected.

The results demonstrated that program AQUA handles fluid compressibility effects in a realistic manner. Furthermore, the data shows the capability of the DEM to provide statistical information about contact and interparticle force evolution at any deformation stage. The results were obtained by artificially reducing the bulk modulus of the fluid in the assembly; in reality, at lower degrees of saturation, water menisci form between particles, providing additional capillary strength. These effects were not considered in the simulations.

4.7 Concluding Remarks

The studies presented in this chapter provide useful guidance to the selection of appropriate parameters to model the behaviour of the idealized assembly. These numerical experiments are an important step to comprehending how the proposed model functions. The main conclusions may be summarized as follows:

- Slippage at the contacts follows a Mohr-Coulomb criterion.
- The contact location point along the ellipses may considerably influence the contact stiffness.
- The friction and geometry of the boundary contacts have an important effect on the overall strength of the assembly and influence the displacement field representing the particle movement.
- Pore pressure generation can be related to the assembly's volumetric strain and the algorithms closely follow this relation.
- Euler's method proved to be inefficient in solving the system of ordinary differential equations representing the pore pressure dissipation-generation in the assembly. The Runge-Kutta technique, as programmed in the set of subroutines RKSUITE, is a better method for solving this system of differential equations.
- The development of pore pressures in a system of 1000 elliptical particles was monitored during time by inhibiting the particle movement. The results showed that pressures eventually equalize to the expected value.
- The scheme proposed to model pore pressure dissipation problems generated values in close agreement with those predicted by Terzaghi's one-dimensional consolidation theory. Additionally, the degree of anisotropy in the fabric can be captured by the fluid flow network.
- The degree of saturation may be modelled by selecting different values for the fluid's compressibility. The results show that the volume of the assembly during the simulations is automatically preserved for the 100 per cent saturation case.

Chapter 5

Simulations of Undrained Tests

5.1 General

This chapter presents the results of undrained simulations conducted on idealized systems of elliptical particles using the program AQUA. The main objective of the tests was to investigate the macroscopic and microscopic features of the assemblies when sheared under different initial densities and different confining stresses. The physical and elastic characteristics of the assembly and the flow network are presented in Section 5.2. The results of biaxial simulations are presented in Section 5.3

The theoretical stress-force-fabric relationships presented in Section 2.7 are used in Section 5.3.5 to examine some of the simulation results. The accuracy of these relations has been confirmed on a number of occasions; it is not the purpose of the author to verify them again, but rather to use them to study the results because they are an alternate tool to investigate the contribution of the individual microscopic parameters to the stress tensor.

The effect of the interparticle friction coefficient on the global mobilized angle of friction of the assembly is analyzed in Section 5.5.

Section 5.6 presents a comparative analysis of volume-controlled drained tests and undrained tests using the proposed scheme.

5.1.1 Program Stability

Because of the discrete nature of the DEM and the assumptions involved in the solution of the equations of motion, an adequate time step has to be chosen to ensure that inertial forces and velocities are kept to low values. Optimal time step and boundary strain rates were selected after several trial runs so that the maximum particle force would be less than one percent of the maximum inter-particle force. The individual static equilibrium of the particles was monitored at all times during the simulations; tests not meeting the previous requirement for equilibrium were discarded.

Several attempts were made to test assemblies with low coordination numbers. Although different parameters were varied to seek stable results, the stability criterion was not satisfied in assemblies presenting an initial average coordination number lower than about 3.2. This condition was invariably encountered for different confining pressures.

5.2 Characteristics of the Assembly

All the numerical simulations reported in this work use assemblies composed of 1000 elliptical particles of eccentricity e_c= 0.2.

Numerical simulations of discrete particles have been conducted by a number of researchers using rectangular assemblies. The use of this boundary shape results in stress concentrations at the specimens' corners and the subsequent localization of shear strains. In an attempt to minimize boundary influence on the system and encourage more uniform deformations, a circular boundary was used.

The boundary of the assembly was formed by 76 particles of eccentricity equal to 1.0. Boundary particles act rigidly in the sense that they do not penetrate the interstices, but the program continually readjusts the length of the particles when necessary to maintain continuity. The effect of membrane penetration commonly encountered in laboratory tests is nullified under the present approach.

Assembly Generation

In general, the simulations of undrained tests were carried out in two steps:

1. Generation of the initial assembly

2. The corresponding mechanical test

Different densities and initial conditions were achieved by initially expanding the assembly, applying a constant displacement to particles' centre according to

$$\boldsymbol{x}_i = \boldsymbol{x}_i^c + (\boldsymbol{x}_i - \boldsymbol{x}_i^c)\xi \qquad i = 1, 2 \tag{5.1}$$

were $\boldsymbol{x}^c$ is a vector directed to the centre of the assembly, $\boldsymbol{x}$ is the particle position, and ξ is a coefficient that governs the amount of expansion. After expansion, the orientations of the ellipses were randomized. Subsequently, the assembly was compressed hydrostatically using a high interparticle friction coefficient (μ= 4). Next, the assembly was brought to the desired state of stress using servo-mode 4 (see page 73). Last, the interparticle friction coefficient was gradually reduced and the assembly was slowly brought to equilibrium. Figure 4.1 shows a loose assembly after compaction.

Properties of Particles

The elastic and physical properties of quartzite [33] were assigned to the particles, these are summarized in Table 5.1.

Particle Property	Nomenclature	Value
Young's modulus	E	80 GPa
Poisson's ratio	ν	0.25
Interparticle friction coefficient	μ	0.55
Density	ρ	2700 kg/m^3
Thickness	Δ	1×10^{-3} m

Table 5.1: Properties of the particles.

Although the approach adopted can be envisaged as two-dimensional because particle movement occurs only on the plane (three degrees of freedom), the system is in essence three-dimensional. The particles are assumed to have a certain constant thickness (Δ) in the direction normal to the plane.

Properties of Flow Network

The properties of the conduits forming the flow network are presented in Table 5.2. The diameter of the conduits was selected using the information presented in Figure 4.14, and was kept constant throughout the simulations. The length of the conduits was internally calculated using the distance between centres of gravity of the connected polygons.

Property	Nomenclature	Value
Pipe diameter	d	80 μm
Fluid viscosity	$\bar{\mu}$	1×10^{-3} N·s/m^2
Bulk modulus of the fluid	B_f	2.0 GPa

Table 5.2: Properties of the fluid network

The value of the fluid viscosity is the same as that of water at 20° C.

5.3 Biaxial Compression Tests

5.3.1 Summary of the Test Program

The effects of the initial density and the initial confining pressure on the global response of the idealized assemblies of elliptical particles were studied by two sets of experiments. First, assemblies with approximately the same initial density (e = 0.229) were confined under initial isotropic pressures ($\sigma_o^{'}$) of 50 kPa, 100 kPa and 200 kPa. These assemblies will be referred to as 5a, 5b, and 5c, respectively. Second, two additional tests were conducted on assemblies of density equal to e= 0.245 and e = 0.208, but initially confined under the same isotropic pressure ($\sigma_o^{'} = 200$ kPa). The two additional tests will be called 5d and 5f, respectively; they allowed a comparison of the effects of initial density on the response of the idealized assemblies.

The initial characteristics of the assemblies are presented in Table 5.3. The range of densities chosen permitted a study of both strain-softening and strain-hardening types of behaviour.

All the experiments were conducted by maintaining a constant total lateral stress σ_{11}, while applying a constant axial strain rate $\dot{\epsilon}_{22}$. The parameters used in the simulations are summarized in Table 5.4.

Test	Initial γ	Void ratio	$\sigma_o^{'}$ (kPa)
5a	3.67	0.229	50.0
5b	3.73	0.229	100.0
5c	3.78	0.229	200.0
5d	3.35	0.245	200.0
5f	4.13	0.208	200.0

Table 5.3: Summary of the tests program

Property	Nomenclature	Value
Global damping	α	0.0 1/sec
Contact damping	β	2500 1/sec
Rotational damping	ω	10.0
Time step	Δt	4.78×10^{-3} sec
Vertical strain rate	$\dot{\epsilon}_{22}$	$1.0\ \times10^{-3}$ 1/sec

Table 5.4: Parameters used for the Computations

5.3.2 Effects of Initial Confining Pressure

The stress-strain curves and the corresponding stress paths for tests 5a, 5b, 5c are presented in Figures 5.1 and 5.2 respectively.

The figures show that the initial confining pressure has an important effect on the peak strength of the idealized assemblies. The stress-strain curves show a clear peak at an early stage of deformation; also higher initial confining pressures resulted in higher peak strengths. The post-peak behaviour is characterized by an acute drop in shear strength to a minimum value which is practically the same for the three samples. After this point, the specimens deform steadily up to a shear strain of about $\epsilon_t \approx 0.05$. As deformation continues, the assemblies gradually regain strength.

The deformation characteristics of the idealized assemblies compare favorably with typical undrained responses of loose to medium dense sands.

The stress paths plotted in Figure 5.2 show the samples reaching a point of maximum strength. Upon further shearing, the paths move to the left, denoting a reduction of the effective stress, and after the specimens reach a state of minimum strength, they gradually recover strength. The mobilized friction angle ($\sin \phi_{\text{mob}}$) during the strain softening stage

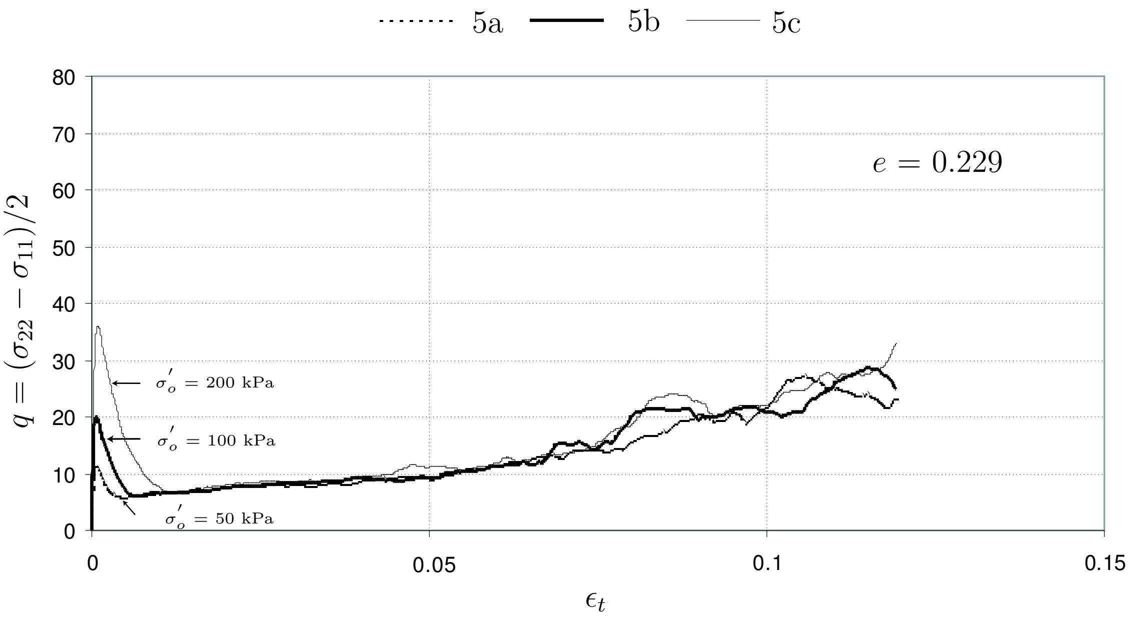

Figure 5.1: Stress-strain curves for assemblies tested under different initial isotropic confining pressures

remains constant and is slightly different for each test. At the end of the tests, $\sin\phi_{\text{mob}}$ remains constant at about 0.45.

The results of the simulations clearly show that the initial confining pressure has a considerable effect on the initial peak strength. However, for the case of the assemblies tested, the post-peak strength does not seem to be significantly affected by the initial confining pressure. Hence, for the same initial density, the assemblies reached a very similar ultimate strength. These observations are in agreement with the steady state line concepts.

5.3.3 Effects of Initial Density

The stress-strain curves and stress paths corresponding to assemblies 5d and 5e are shown in Figure 5.3 and 5.4 respectively. The results of test 5b, previously presented, have also been included for comparison.

It is observed in the figures that the deformation of specimen 5d was limited to a deviatoric strain of about $\epsilon_t > 0.005$, the reason being that unbalanced forces after this

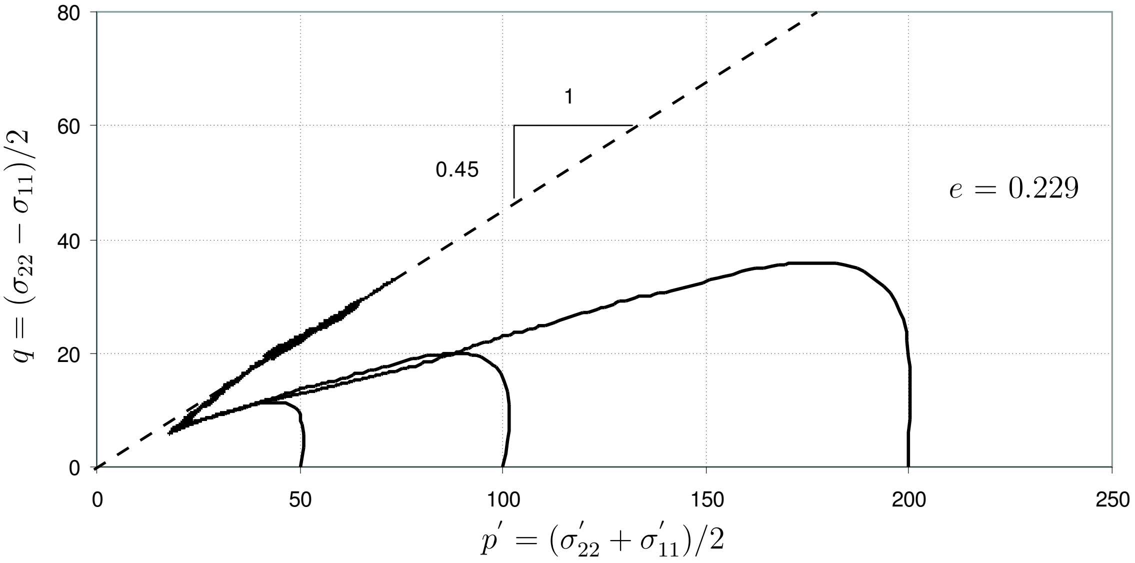

Figure 5.2: Stress paths for assemblies tested under different initial isotropic confining pressures

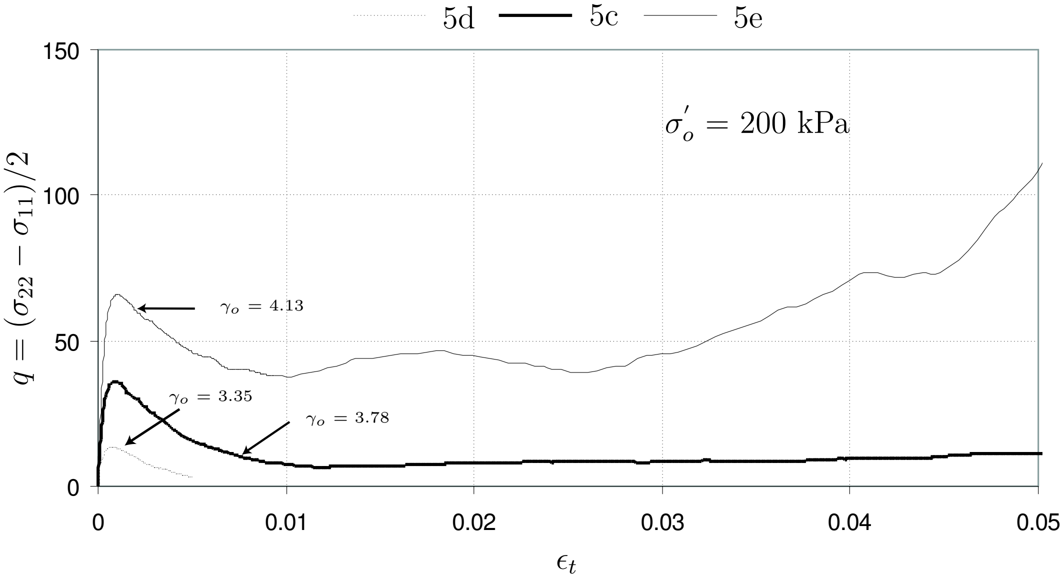

Figure 5.3: Stress-strain curves for assemblies tested under different densities

point increased considerably up to a value where the stability criterion was not satisfied. Accordingly, the results obtained for higher deformations were deemed unreliable. It was assumed that the specimen reached an unstable state similar to that of sands during liquefaction; the reason for this consideration will be explained later.

An analysis of the stress-strain curve corresponding to specimen 5e shows a peak at a shear strain of about 0.0015; thereafter, the shear strength starts to decrease - but only for a short deformation range. Upon further shearing, the characteristics of the specimen changed from contractive to dilative, and the pore pressure began to decrease, resulting in a gradual regain of strength. The ratio of the peak to minimum strength for test 5e is about 1.7.

The stress-strain curve corresponding to assembly 5c exhibits a different behaviour. The resistance reached a peak value at small strains, and after the specimen softened, the post-peak strength remained practically constant during the range of strains presented. The difference between the maximum peak and minimum strength for this specimen is about 5.3, considerably higher than that of specimen 5c.

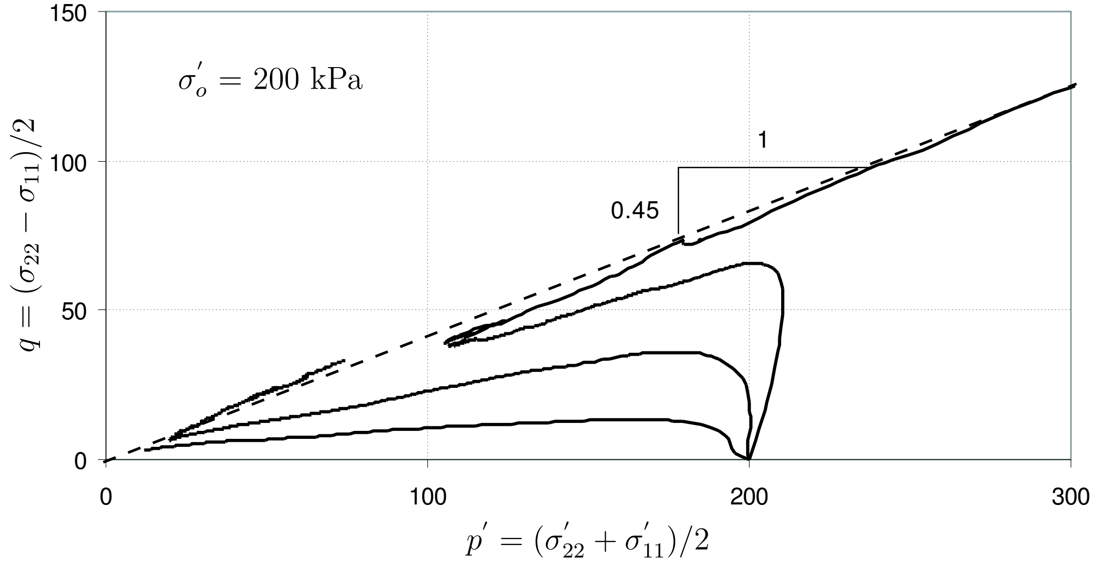

Figure 5.4: Stress paths for assemblies tested under different densities

The stress paths in Figure 5.4 show that the initial slope of the curves increases with a decrease in the density of the assembly, reflecting the higher initial stiffness of the denser specimen. The mobilized friction angle at large deformations is approximately equal to the angle measured in tests 5a and 5b ($\sin \phi_{\mathrm{mob}} = 0.45$).

The results of the simulations clearly show that the initial density affects considerably the initial peak strength and the overall deformation characteristics. For this particular case, denser assemblies behaved in a stiffer manner with a higher resistance to the imposed loads. Additionally, the initial loose assembly exhibited an unstable type of behaviour. Hence, for a given confining pressure, the characteristics changed from strain-softening to strain-hardening as the initial density increases. These observations are in agreement with the steady state line concepts.

5.3.4 Micromechanical Descriptors

Average Coordination Number

An important micromechanical descriptor introduced in chapter 2 is the average coordination number. Figure 5.5 shows the evolution of the average coordination number for tests 5a, 5b and 5c. The initial average coordination numbers were $\gamma_o = 3.67$, 3.73 and 3.78 respectively, while the void ratios remained the same $e = 0.229$. The void ratio has been introduced here as a descriptor of the macroscale behaviour because it is often measured in the laboratory and the steady state concepts are formulated in terms of this parameter.

The data in Figure 5.5 reveals interesting features that partly explain the macroscopic stress-strain behaviour of the samples. The average coordination number of the specimens started to decrease as soon as the simulation was initiated. The initial rate of change was different for the three assemblies, and it appears to be dependent on the initial confining stress. Accordingly, higher initial confining stress decreases the rate of contact disruption. It is interesting to observe that the three assemblies reached approximately the same coordination number at a strain coincident with the occurrence of the minimum strength. At greater deformations the average coordination number remains practically constant until a deviatoric strain of about $\epsilon_t = 0.075$ and increases slightly from this point until the end of the tests.

The initial coordination numbers for tests 5d, 5c and 5e were 3.35, 3.78 and 4.13, respectively. Curves showing the evolution of the coordination number are plotted in Figure 5.6. It can be observed that the initial rate of contact reduction and the shape of the curves corresponding to tests 5c and 5e are similar. Additionally, analysis of the results reveals that the ratio of the initial to the minimum coordination number is the same at $\gamma_o/\gamma_{\min} = 1.18$ for both tests. These observations suggest that the evolution of the number of contacts on average is greatly influenced by the initial confining pressure, while the initial density appears to have little influence.

Of special importance to the present discussion is the decrease in contacts observed in test 5d. This test was stopped at a strain of about $\epsilon_t = 0.005$ because particles became unstable. The average coordination number at this stage was lower than about 3.1, meaning that there were particles with no contacts and others with only one or two contacts; hence, static equilibrium could not be sustained.

Although the computed void ratios were the same and remained practically constant

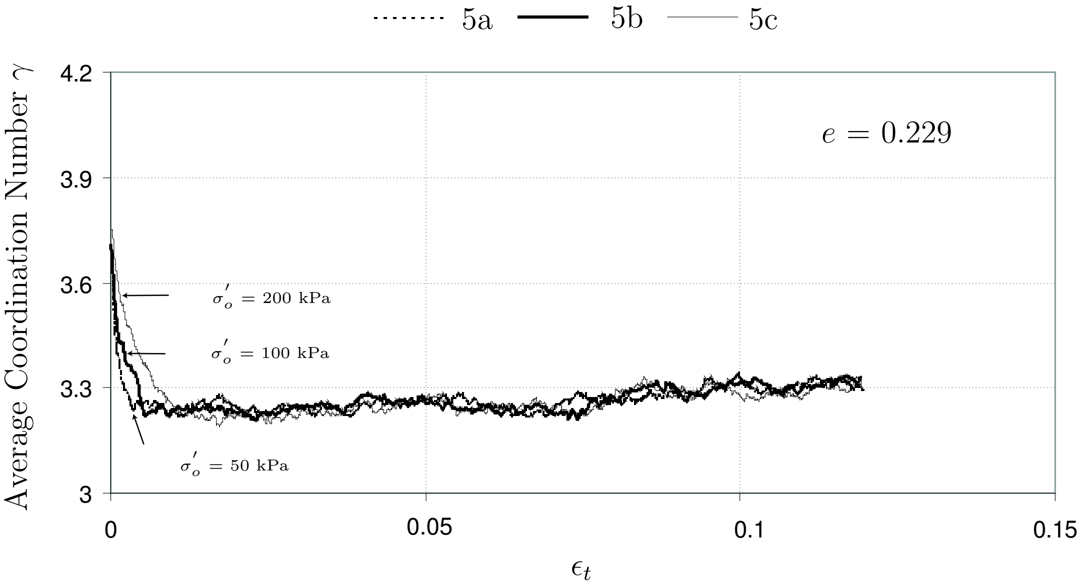

Figure 5.5: Variation of average coordination number (γ)

during the experiments, the simulations show that the number of contacts changed considerably. This observation further suggests that the void ratio alone is not a parameter sensitive enough to capture the internal changes of the fabric.

Development of Contact Normal Anisotropy

Fabric changes can be examined by tracking the evolution of the contact normal anisotropy parameter a introduced in Chapter 2. According to relation (2.4), the distribution of contact normals can be approximated by a fourth order Fourier series $E(\theta)$, where the coefficients a and b are measurements of the deviation from an isotropic state. The evolution parameter a has been plotted in Figure 5.7 for tests 5a, 5b and 5c. Included in the figure are the polar histograms of contact normal orientation at deformation stages of $\epsilon_t = 0.002$ and $\epsilon_t = 0.05$ for the different tests. Additionally, the approximations $E(\theta)$ were calculated and have been superimposed on the computed distributions to demonstrate their accuracy. It is observed that the distribution functions give a reasonable visual approximation to the predominant trends in the computed data.

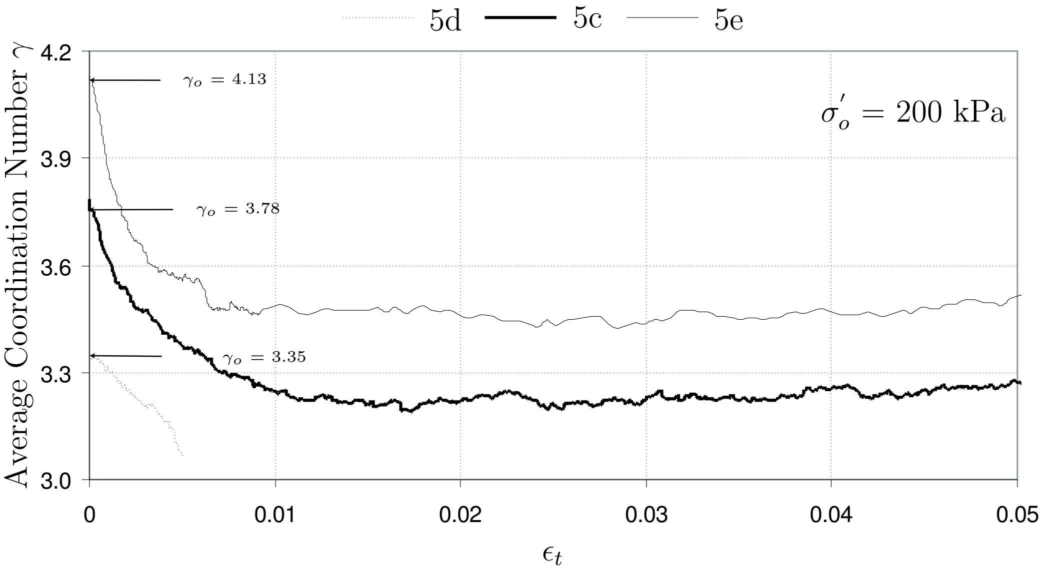

Figure 5.6: Variation of average coordination number (γ)

The information in the plots shows that anisotropy in the contact normal orientations started developing at the beginning of the test and initially the rate of change varied among the curves. For this particular case, the rate of change initially decreased with an increasing confining stress. Contact anisotropy is primarily generated by a reduction in the number of contact normals with orientations close to the direction of maximum extensional strain. These observation suggests that the early reduction in coordination number observed in Figure 5.5 can be attributed principally to a loss of contacts in the lateral direction.

After a level of deformation that coincides with the occurrence of the minimum strength, the shape and magnitude of the curves are very similar, and anisotropy constantly increases until the end of the simulations. While the average number of contacts after the stage of minimum strength increased by an small amount, contact anisotropy continues to increase until the end of the tests, suggesting that the rate of contact disintegration in the lateral direction must be very similar to the rate of contact creation in the axial direction.

Curves showing the development of contact normal anisotropy for tests 5d, 5b and 5e are presented in Figure 5.8. The measurements suggest that the rate of anisotropy development is initially controlled by the initial density. Accordingly, the densest specimen exhibited higher anisotropy at the beginning of the test, while the contact normal anisotropy for the loosest particle arrangement remained almost constant.

The curve corresponding to test 5d shows that parameter a did not change considerably with deformation, even though the average number of contacts decreased significantly, indicating that the amount of contact disintegration in the lateral and axial directions was very similar. Although the boundary was moving vertically towards the centre of the assembly, contacts were lost in this direction suggesting the occurrence of internal instabilities resulting from the initial meta-stable state of the fabric.

The curves corresponding to tests 5b and 5e show that after the minimum strength, corresponding to a shear strain of about 0.01 (Figure 5.3), the contact anisotropy parameter was very similar for both tests over the range of strains examined.

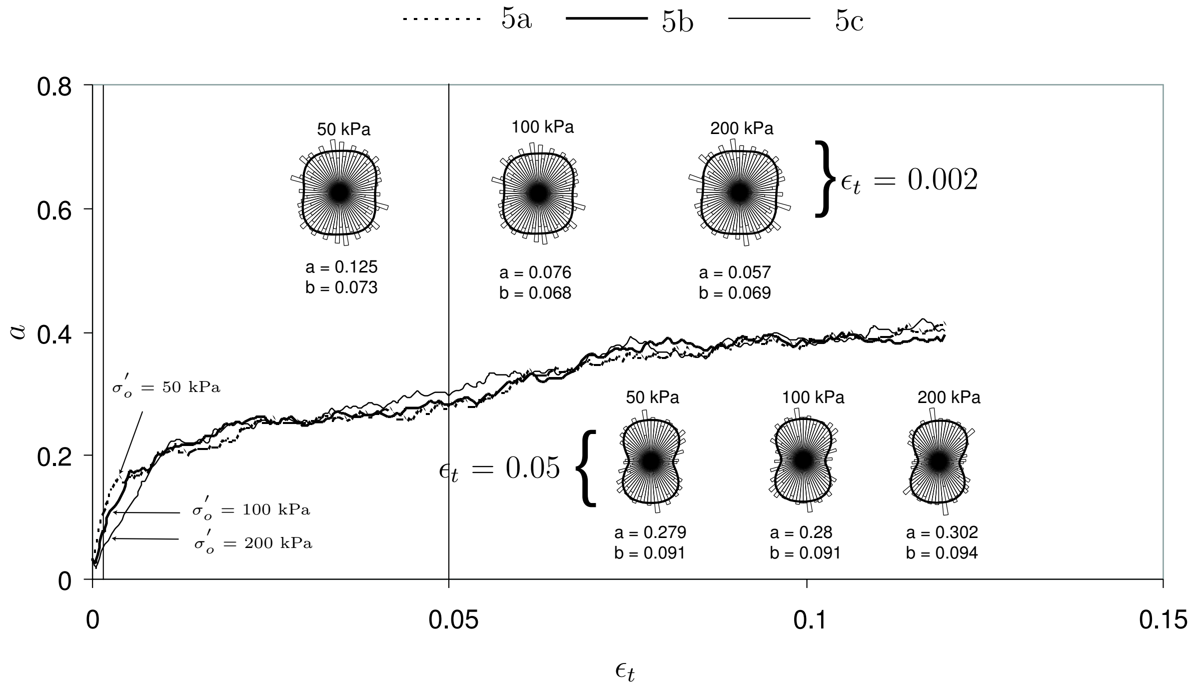

Figure 5.7: Variation of contact normal anisotropy a for tests sheared under the same density

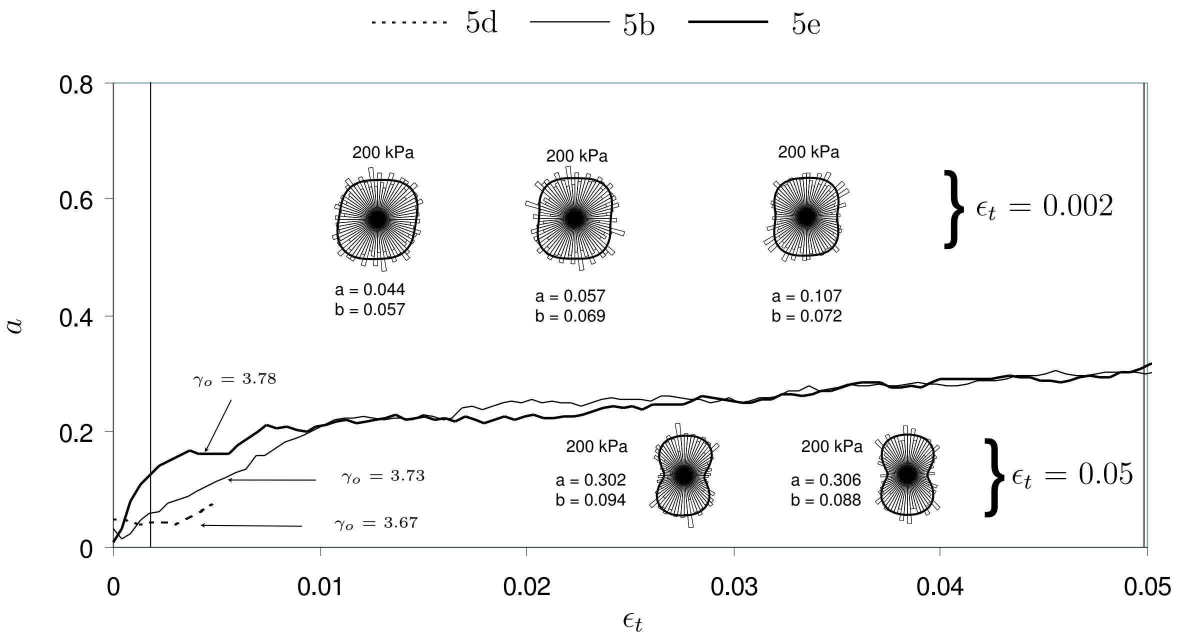

Figure 5.8: Variation of contact normal anisotropy a for tests sheared under the same initial confining pressure

Contact Force Distribution

Figures 5.9 and 5.10 show the development of anisotropy of the normal component of interparticle force (a_n) for the two sets of simulations. The variation of the tangential (shear) component of the contact force (a_t) with different strain levels is presented in Figures 5.11 and 5.12. Polar histograms extracted at deviatoric strain levels of $\epsilon_t = 0.002$ and $\epsilon_t = 0.05$ are also plotted in the figures. Second order Fourier series approximations to the normal $\bar{f}_n^c(\theta)$ and tangential components $\bar{f}_t^c(\theta)$, calculated according to relations (2.7) and (2.8), have been superimposed on the figures.

The first observation derived from the plots is that the computed approximations to the contact force components appear to represent well the computed data.

The behaviour of the curves corresponding to tests 5a, 5b and 5c in Figure 5.9 shows the sudden development of contact normal force anisotropy as soon as the deformation was initiated. After the parameter a_n reached a value of about 0.003 at small strains, the behaviour of the individual curves appears to be governed by the initial state of stress during the strain-softening stage. The rate and magnitude of a_n for the three tests was very similar at higher levels of strain.

The curves corresponding to tests 5b and 5e in Figure 5.10 also show a sudden increase of a_n at the beginning of the simulation. Contrary to the behaviour depicted in Figure 5.9, the parameter evolves toward a limiting value that depends on the initial density. The curve corresponding to assembly 5d shows a drastic increase in the contact normal force component at the stage where instability was initiated.

Figures 5.11 and 5.12 show that the magnitude of anisotropy in the average tangential contact force a_t features a relatively rapid rise at the initiation of the tests. At higher deformations, a_t reaches a limiting value that appears to be independent of the initial confining stress and initial density. The average number of contacts remained constant, the average tangential component of the contact forces kept practically constant.

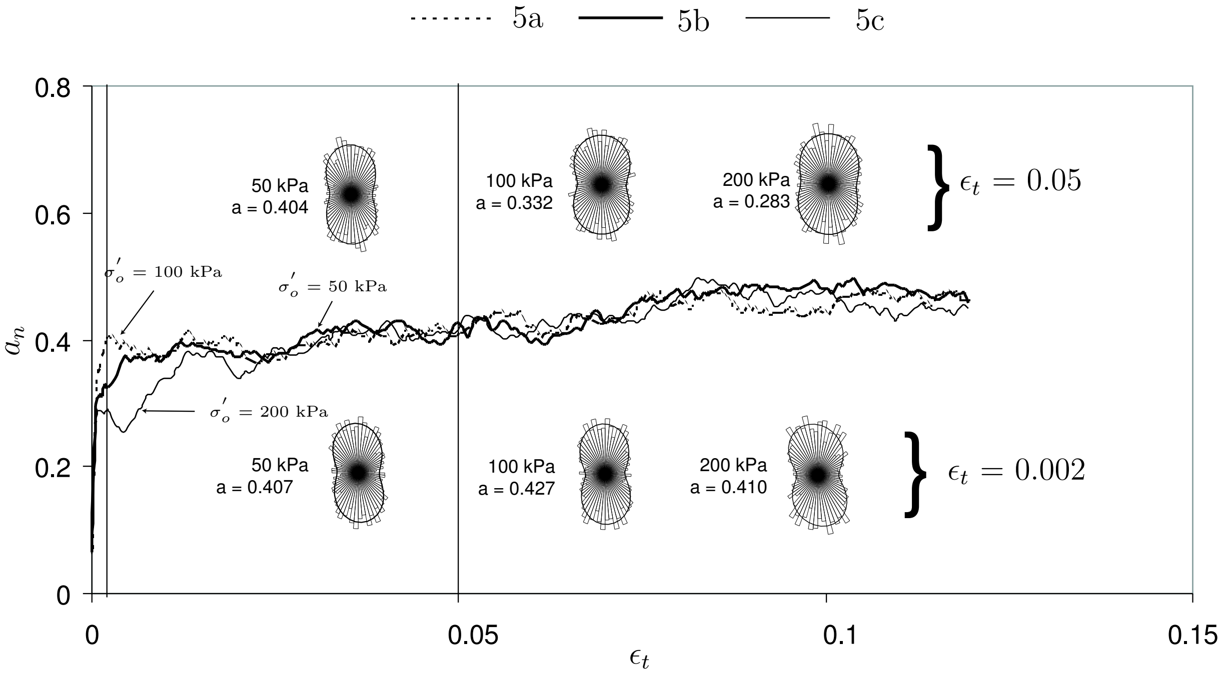

Figure 5.9: Variation of normal force anisotropy parameter (a_n)

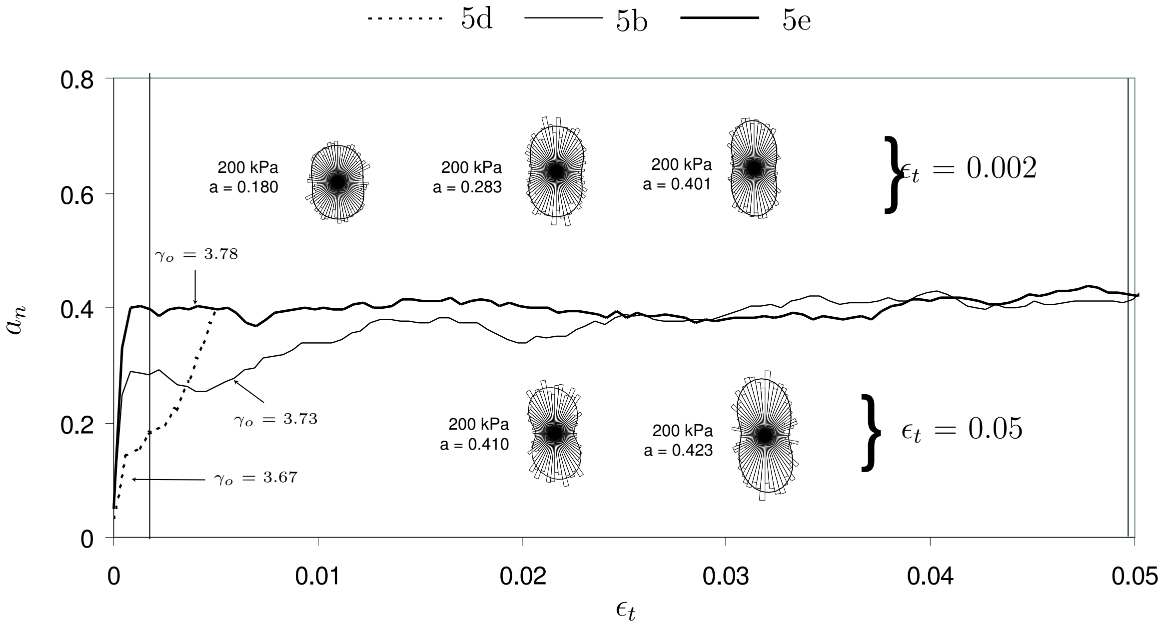

Figure 5.10: Variation of normal force anisotropy parameter (a_n)

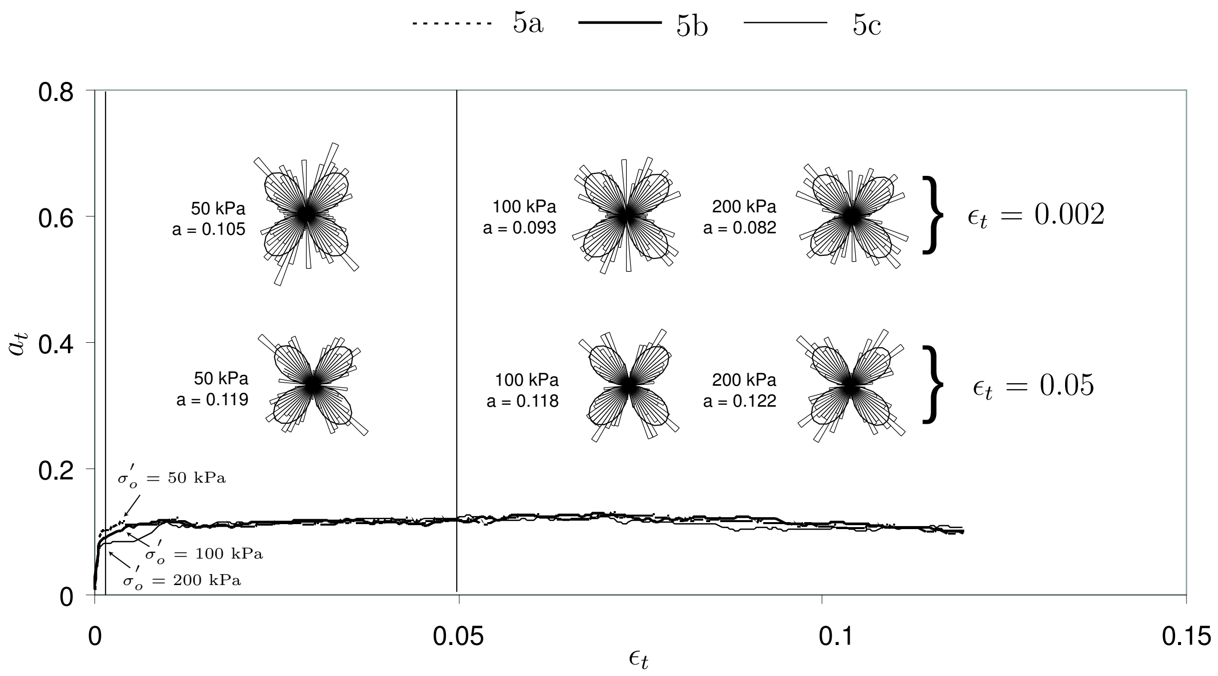

Figure 5.11: Variation of tangential force anisotropy parameter (a_t)

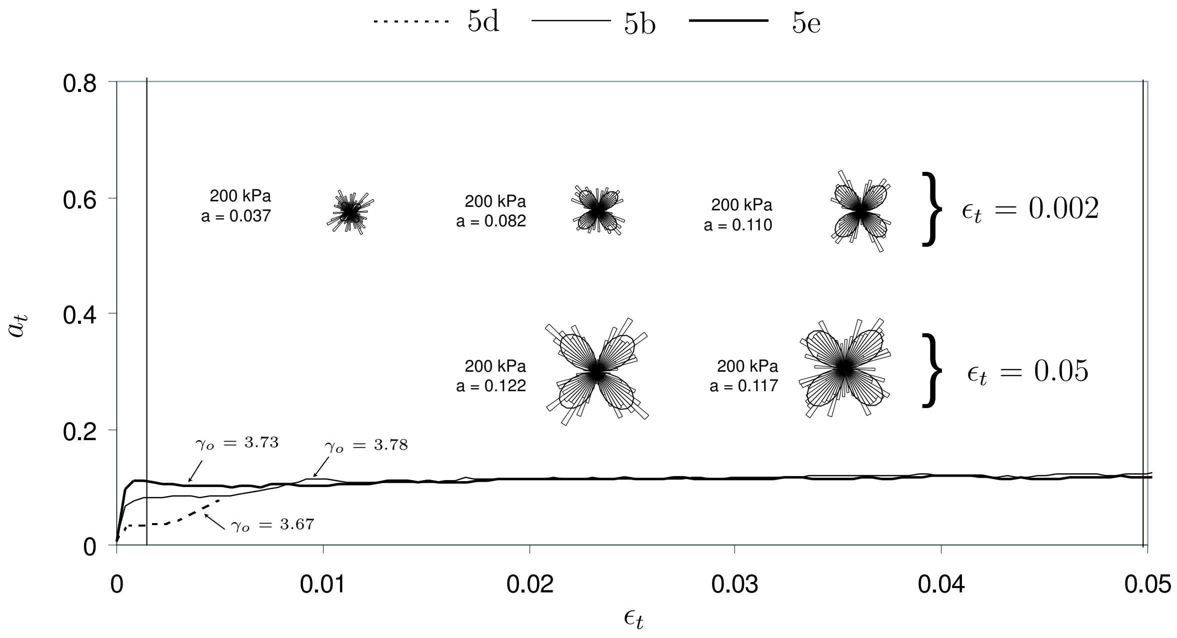

Figure 5.12: Variation of tangential force anisotropy parameter (a_t)

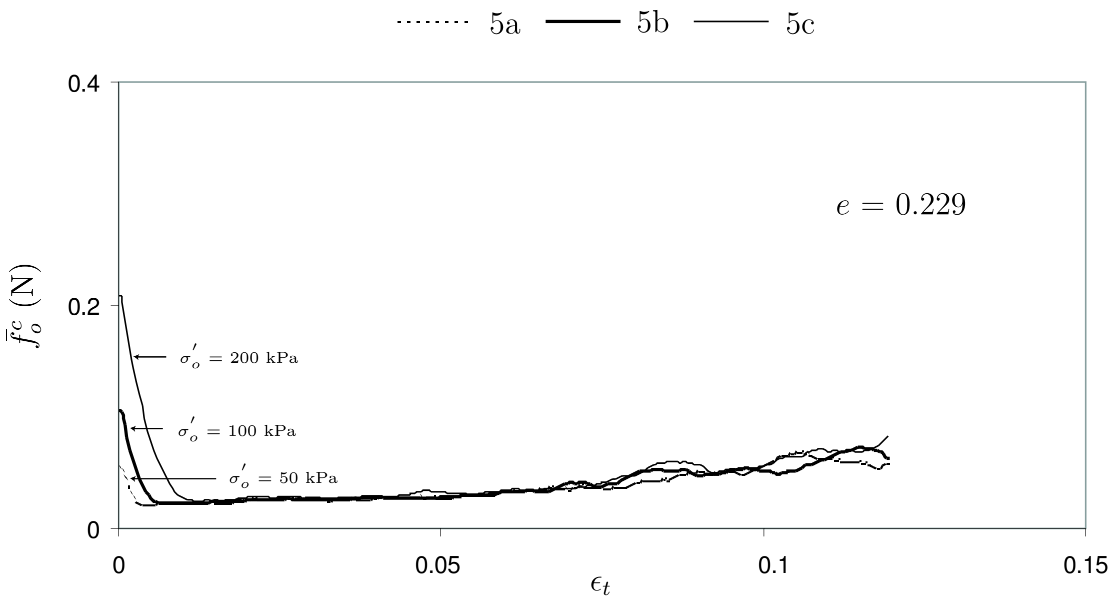

Figure 5.13: Variation of average contact normal force ($\bar{f}_o^c$)

Average Normal Contact Force

The average normal contact forces can be described by the average contact force magnitude $\bar{f}_o^c$ over groups of contact normal orientations. The magnitude of this parameter is a direct measurement of the effective state of stress in the assembly because it represents the effective interparticle contact forces.

Figures 5.13 and 5.14 present the average normal contact force recorded for the two sets of simulations. The influence of the initial confining pressure on the initial values of $\bar{f}_o^c$ can be easily observed in the figures. For the same initial number of contacts and the same initial degrees of anisotropy, relation (2.21a) predicts that $\bar{f}_o^c$ should increase with higher confining stresses. Additionally, for the same initial confining stress but different initial contact density (m_v), $\bar{f}_o^c$ should decrease as the contact density is increased. The computed data agrees with predictions made using relation (2.21a).

The evolution of $\bar{f}_o^c$ with the deviator strain has been plotted to demonstrate the strong correlation with the shape of the stress-strain curves presented in Figures 5.1 and 5.2. The relevance of the parameter $\bar{f}_o^c$ on the macroscopic strength will be highlighted in the

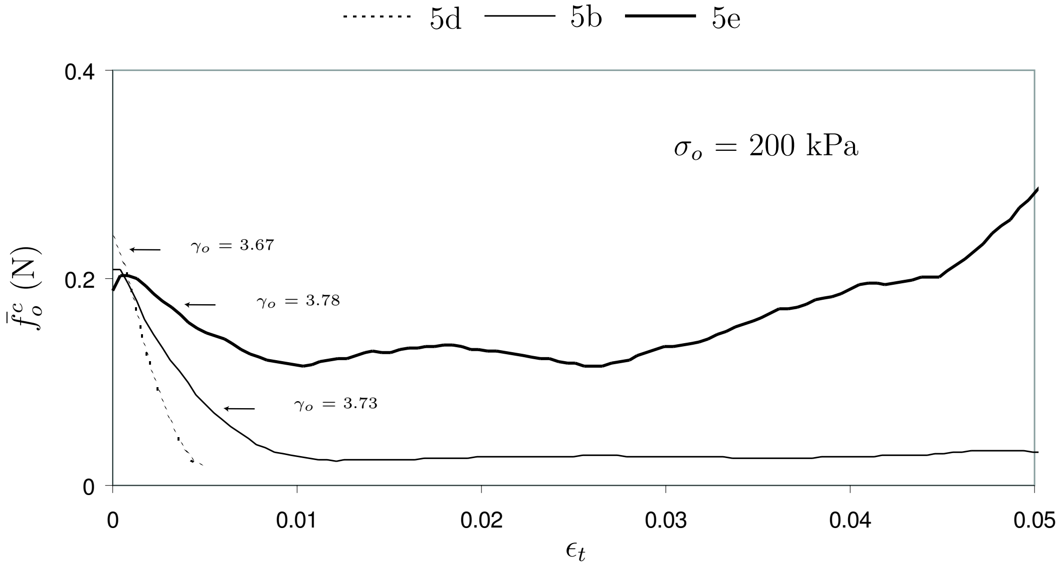

Figure 5.14: Variation of average contact normal force ($\bar{f}_o^c$)

following subsection.

5.3.5 Stress-Force-Fabric Relationships

Relationships which relate the average stress tensor in plane assemblies to average quantities describing the distribution of contact normals and contact force components were introduced in Section 2.7. The shear capacity of the assembly has been described by the following invariant quantity associated with the Mohr circle of stresses:

$$q = \frac{\sigma_{11} - \sigma_{22}}{2}$$

This quantity has been approximated in terms of micromechanical descriptors in equation (2.21b), and it can further be rearranged by neglecting the products of anisotropy coefficients as follows:

$$q = \left[\frac{m_v\,(\bar{l}_o^c)^3}{4}\right]\left[\frac{\bar{f}_o^c}{(\bar{l}_o^c)^2}\right]\{a + a_n + a_t\} \tag{5.2}$$

The relation provides an explicit link between micromechanical features of plane assemblies to macroscopic shear strength computed at the boundary of the system. Further, the decomposition of the deviatoric part of the stress tensor into parts related to contact forces and fabric allows examination of the relation between the fabric descriptors and the state of stresses observed at the boundary.

These micromechanical concepts will be used below to examine the results of numerical simulations conducted on an assembly initially confined under $\sigma_o^{'}$= 100 kPa, with an initial void ratio and coordination number of 0.213 and 3.964 respectively.

Simulation Results

The coefficients of anisotropy (a, a_n, and a_t), contact density (m_v) and the average normal contact force ($\bar{f}_o^c$), were extracted during the simulation and were substituted in relation (5.2). Figure 5.15 shows the stress-strain curve computed along with the approximation obtained, using relation (5.2), were the term $\bar{l}_o^c$ has been assumed constant. The thick line represents the computed data for the test and the circles represent the values predicted from relation (5.2). It is observed that predictions of q compare favorably with the computed data.

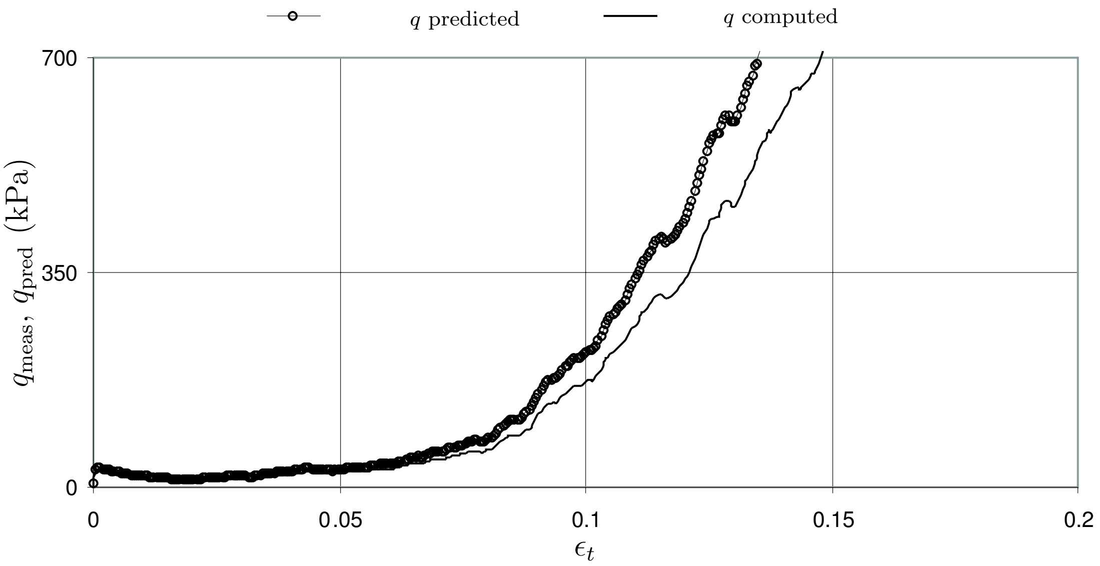

Figure 5.15: Comparison between computed and predicted stress-strain responses. (The prediction was made according to (2.21b))

It has been demonstrated by Nübel *et al.* [58] that the observed deviations of the predicted and the computed values for the case of elliptical particles result from assuming a constant $\bar{l}_o^c$ average contact length, and a better agreement could be achieved when the variation of the average contact length is considered. Nevertheless, the prediction using relation (5.2) is good and shows that the shear capacity of the granular system is due to the creation of fabric anisotropy, number of contacts, and the forces carried by them.

An analysis of the individual contributions of the microscopic descriptors to the shear strength of the system can be made by studying the development of the non-dimensional coefficient $m_v(\bar{l}_o^c)^3 \ / \ 4$, the contribution of the coefficients of anisotropy $(a + a_n + a_t)$ and the interparticle average contact force described by the quantity $\bar{f}_o^c \ / \ (\bar{l}_o^c)^2$. The variation of the modified average normal contact force with deviatoric strain has been plotted in Figure 5.16 along with the global shear strength q. The change of the non-dimensional contact density and the contribution of anisotropy coefficients is presented in Figure 5.17. The following observation can be made from the figures:

1. The curves corresponding to q and $\bar{f}_o^c$ are similar in shape. The average normal contact force closely follows the strain-softening and the strain-hardening exhibited by the assembly.

2. The post-peak strength reduction is associated with the loss of contacts and the consequent reduction in the average contact normal force. The results show that the contact density m_v remains practically constant at relatively large deformations and does not change considerably during the post-peak stage. The undrained environment restricts any attempt of the assembly to contract or dilate.

3. The contribution of the combined microscopic anisotropies constantly increases with the level of deformation, especially at the beginning of the test. At large strains however, the quantity stabilizes, since anisotropy cannot develop indefinitely.

In general, it is observed that the average number of contacts and the anisotropy coefficients reach limiting values at large strains. Since the functions describing the development of anisotropy are essentially geometrical characteristics of the system, there should be a limit in the number of contacts that can be disintegrated with out loss of stability and a limiting amount of anisotropy in the orientations of contact forces. Therefore, there must be a limiting value for the degree of anisotropy. Additionally, the evolution of the contact

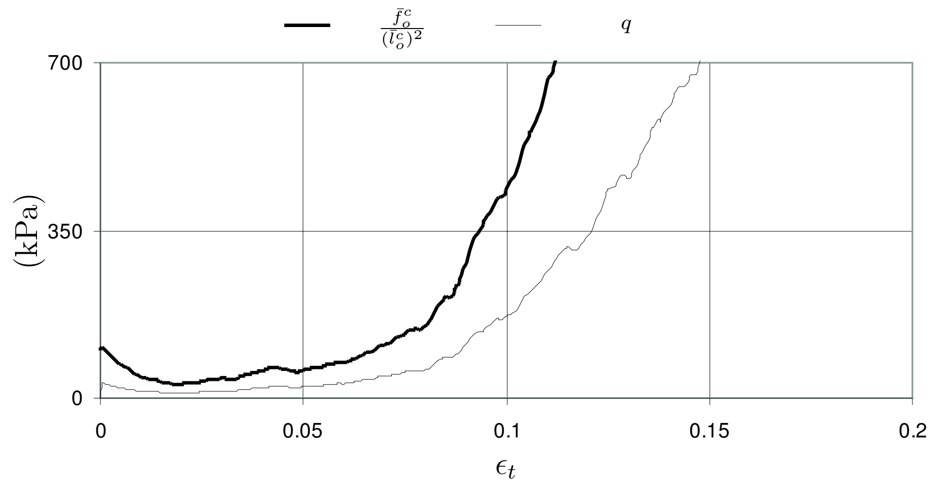

Figure 5.16: Comparison between the deviatoric stress and normalized average contact normal force.

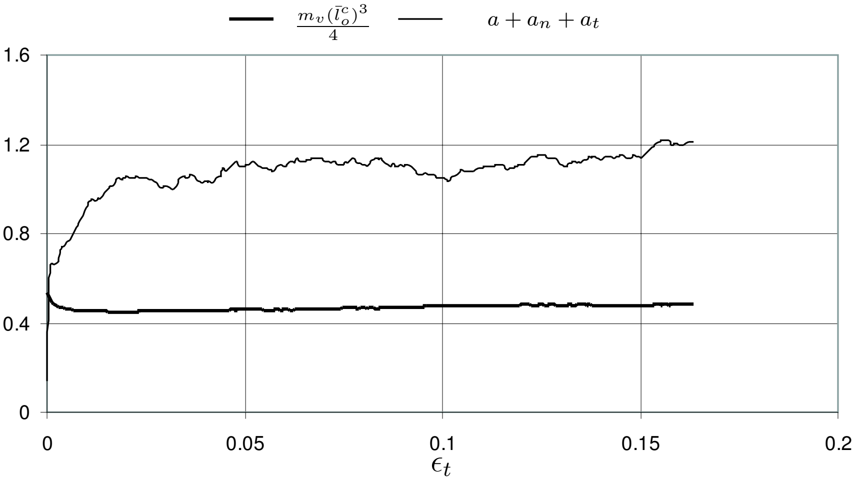

Figure 5.17: Evolution of micromechanical descriptors.

density should be restricted by the constant volume condition, and the maximum and minimum coordination number that can be achieved should be restricted by the initial volume of the assembly. Therefore, at large strains, the increase in the average effective contact forces are principally related to the shear strength computed at the boundary.

The previous observations may be related to dilatant characteristics of the system. It is known that the macroscopic volume change is the result of internal plastic and elastic deformations. For the case of undrained deformations the global volume change is restricted, resulting in the following relation:

$$\Delta V = \Delta V_e + \Delta V_p \approx 0 \tag{5.3}$$

where ΔV, ΔV_e and ΔV_p are increments in the total, elastic and plastic volumetric changes, respectively. Therefore, any tendency of the assembly to dilate or contract reflected as internal plastic deformations should be counteracted by the development of elastic deformations. For the present case, elastic deformations result in higher interparticle forces. Thus, when the assembly tends to dilate, the contact forces increase resulting in the development of higher shear resistance. The opposite is also applicable for contractive characteristics; accordingly, when the assembly tends to contract, the contraction tendencies should be counteracted by a decrease in the elastic deformations, leading to a reduction of interparticle forces.

Hypothetically, at high deformations, the magnitude of the interparticle forces could grow to extremely high values, since the adopted non-linear contact law does not consider plastic deformations of the idealized particles. In real systems however, the increase in contact forces should be restricted initially by plastic deformations and eventually by grain crushing. Grain crushing can result in the development of higher coordination numbers and lower average contact forces, and could lead to a considerable decrease in strength.

5.4 Comments

The results of numerical simulations using the fluid-flow-coupled DEM have shown that fundamental features observed in undrained tests in sands are effectively captured by the model. The effects of the initial confining pressure and initial density on the stress-strain response of the assemblies agree in general with the steady state concepts presented in Chapter 2. Accordingly, a higher initial confining pressure on assemblies with the same density resulted in higher peak strengths and very similar post-peak strengths. Additionally, assemblies with higher initial densities exhibited higher resistance to deformation, and initially loose assemblies exhibited unstable behaviour.

The importance of the micromechanical fabric descriptors on the study of the undrained mechanisms was highlighted. The results from the simulations as well as theoretical considerations indicate that the state of stresses observed at the boundary can be related to the changes in coordination number and anisotropy coefficients.

The post-peak strength reduction has been associated with the decrease in the average number of contacts, principally in the direction of the minor principal stress. Additionally, the coordination number at relatively large deformations was found to be related with the initial packing density. The evolution of anisotropy in the system demonstrates the microscopic readjustment of the particles into more stable configurations, the interparticle forces continuously readjust to sustain the loads imposed at the boundary. It was hypothesized that the development of contact density should be restricted by the initial volume, and that the evolutions of fabric anisotropy should achieve limiting values at relatively large deformations. A great similarity between q and $\bar{f}_o^c$ was observed in all the simulations, the later quantity was found to be closely related to the deviatoric component of the stress tensor.

5.4.1 Initial and Minimum Coordination Number

In an attempt to better understand the results of the undrained tests, reference will be made to drained numerical experiments; the behaviour of these systems has been extensively studied and some concepts previously introduced to explain their behaviour might be extended to the case of undrained experiments. Figure 5.18 shows the results of drained simulations conducted by Rothenburg and Kruyt [72] on assemblies of disc-shaped particles. The curves show the evolution of the coordination number and the packing fraction at different levels of shear strain of two assemblies initially confined under the same pressure. The packing fraction in this case replaces the more traditional volumetric strain ϵ_v and is defined as the total area of the particles divided by the area of the assembly. Their results show that the dense assembly initially contracts, but suddenly begins to dilate until it reaches a steady or *critical coordination number*. The loose assembly, on the other hand, contracts until stabilizing at a constant volume. The significance of the results is that

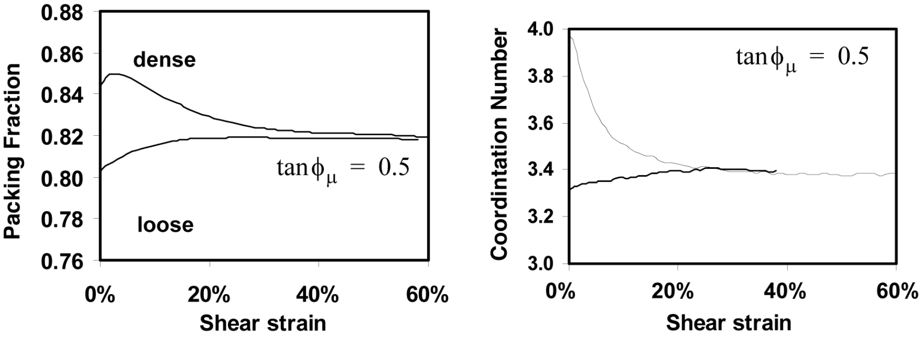

Figure 5.18: Evolution of packing density and coordination number of loose and dense assemblies

both assemblies reached the same critical coordination number regardless of the initial density. Similar observations have been reported by Thornton [89]. The critical coordination number is in connection with the concepts of critical void ratio initially introduced by Casagrande [12]. Thus the granular structure evolves towards an arrangement necessary to achieve a certain coordination number. It has been shown by Rothenburg and Kruyt [72] that the critical coordination number is intimately related with the inter-granular friction coefficient and the minimum number of contacts required to maintain static equilibrium.

Relevant to the present discussion is the existing association between the change in volume with the change in coordination number. Upon shearing, the assembly either expands or contracts depending on the initial density. For the initial dense assembly to reduce its number of contacts, expansion has to occur. The opposite applies to the loose assembly. If the initial coordination number is below the critical value, a certain amount of contraction should occur in order to create additional contacts.

The undrained simulations showed similar characteristics, mainly that the system tends to evolve towards a more or less steady coordination number. For this particular case the results of the undrained experiments showed that the coordination number stabilized at a minimum value ($\gamma_{\min}$) which was found to be dependent on the initial density of the assembly.

If the concept of critical coordination number observed in drained simulations is assumed to hold valid for the undrained case, then it will be expected that the initially dense assembly will try to evolve towards the critical coordination number; however, since volume is preserved, the minimum number of contacts at which the assembly is able to evolve should be restricted by the initial density. Additionally, initially loose meta-stable structures should evolve towards a more stable configuration by increasing the number of contacts. However, this condition is not feasible, since the assembly is not able to reduce its volume, hence the structure reaches a state where static equilibrium cannot be maintained.

Although the previous observations are not conclusive, the results of the numerical experiments showed that during shearing the predominant micromechanical response is related to the reduction of the average number of contacts. In addition, the results provide a catalogue of observations which for the first time give qualitative information of the macroscopic behaviour of these idealized systems sheared in an undrained environment.

5.4.2 Instability Onset

The results show that there exists a limiting coordination number (γ_{lim}) below which instability is initiated. From an intuitive analysis it is expected that a single plane frictional particle cannot remain at static equilibrium with less than 3 supporting points or contacts. Consideration of force and moments acting on the particle also indicates that this is the case. For the special case of plane frictional assemblies the equilibrium condition is satisfied with $3N$ force and moment equations. In general, an assembly with M contacts and $2M$ force components can be at an equilibrium state only when $2M \geq 3N$, which is equivalent to the condition $\gamma > 3$. This means that a plane granular assembly cannot remain in static equilibrium with coordination numbers lower than 3. The simulations showed that instabilities where triggered at $\gamma \approx 3.1$, which is very close to the minimum required to maintain a stable configuration.

The data collected allows construction of the relation plotted in Figure 5.19, which is applicable to the assemblies examined. The figure shows the observed relationship between the initial γ_o and the minimum γ_{min}. The results show that both quantities can be related by a line with a slope of 1.18. In agreement with the observations, the assembly with an initial coordination number of 3.78 exhibited a minimum coordination number of about 3.20. The figure also shows a boundary marked by the limiting coordination number $\gamma_{\text{lim}} \approx 3.5$ below which unstable behaviour is triggered. Hypothetically, if an assembly has an initial coordination number equal to the limiting coordination number ($\gamma_o = \gamma_{\text{lim}}$), it would evolve towards a state where particle equilibrium is not possible, experiencing

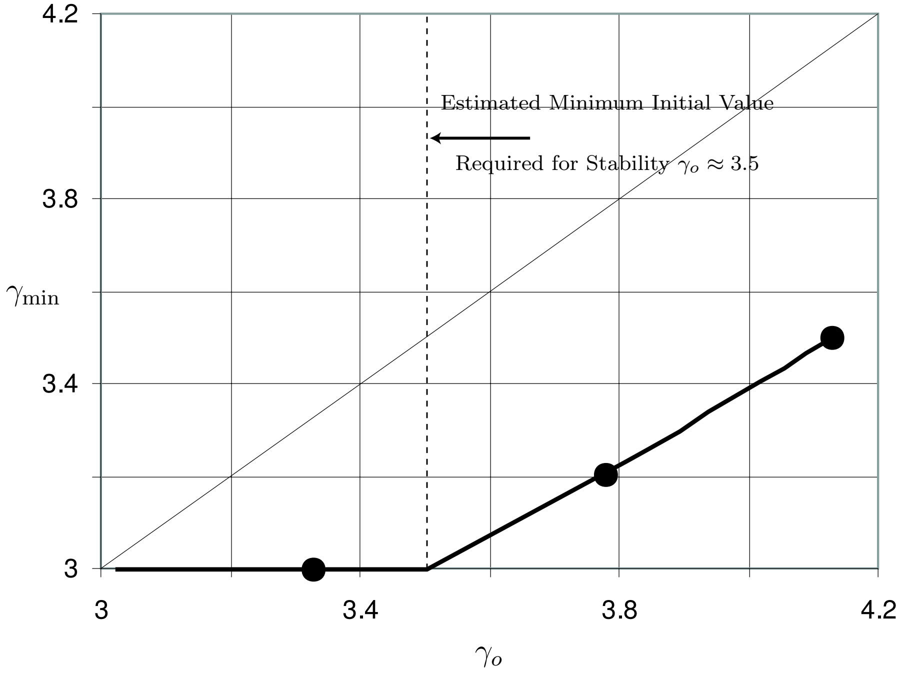

Figure 5.19: Relationship between initial and minimum coordination numbers

unstable behaviour.

From the information collected it appears that a more precise formulation of the steady state concepts can be made in terms of the coordination number. As opposed to void ratio (e), is has been demonstrated that the average coordination number is a better descriptor of the equilibrium state of the structure. Geometrical considerations indicate that both of these parameters should be related to a certain extent. The simulations however indicated that e is not sensible enough to capture the internal deformation mechanisms with the level of detailed offered by the coordination number. Although it is desirable to quantify the average number of contacts during an experiment, this kind of measurement is difficult to perform in real soils.

Laboratory experiments [40] have showed that there exists a limiting value of e_{lim} above which instability occurs. Hence e_{lim} in real systems could be associated with γ_{lim} observed in idealized systems.

5.5 Effects of Interparticle Friction

5.5.1 Introduction

Interparticle friction coefficient is an intrinsic property of the particles known to influence the behaviour of granular materials. A number of researchers have studied the effects of the interparticle friction coefficient both theoretically and experimentally, for example, Taylor [86], Rowe *et al.* [74], Skinner [81].

Following the work by Taylor [86], several attempts have been made to explain the shear strength of a granular sample as consisting of two different components:

1. The strength provided by frictional component between particles, and
2. An additional component provided by particle overriding and interlocking.

The fundament approach has been to use energy considerations and treat both components as independent of each other.

Skinner [81] conducted shear box experiments with glass ballotini having different interparticle friction coefficients. He reported that the effective angle of shearing resistance at constant volume ϕ_{cv} and at peak $\phi_{\max}$ for a given initial porosity do not increase monotonically with increasing the interparticle friction angle ϕ_{μ}. Additionally, the results of

Skinner's experiments showed that a change in interparticle friction angle does not significantly change the effective strength of the specimens.

Numerical simulations with disc-shaped particles [6], elliptical particles [57], and spheres [19] have indicated similar results to the one reported by Skinner [81], mainly that the peak and residual strengths increase in a non-monotonic fashion with increasing the magnitude of the interparticle friction. Bathurst conducted simulations on two dimensional assemblies of disc-shaped particles, finding an increase in the peak friction angle from 10° to 26° by increasing ϕ_μ from 0° to 26°.

Numerical simulations are an attractive tool to study different hypothetical conditions that are not feasible to study in real soils, for example, frictionless contacts. While some research has been directed towards the study of such effects on the drained characteristics, possible effects on the undrained response have been set aside. The convenience offered by the DEM to control ϕ_μ was used to further investigate these concepts.

Biaxial undrained simulations were conducted by setting different interparticle friction coefficients (μ) of 0.55, 0.75, and 0.95, and using the parameters presented in Table 5.4. The assembly was originally confined under 100 kPa and had initial void ratio and coordination number of 0.25 and 3.36, respectively. The results of these simulations are presented in this section.

5.5.2 Simulation Results

The stress-strain and the stress path curves are plotted in Figures 5.20 and 5.21, respectively. The plots show that the macroscopic behaviour of the assembly is significantly affected by the interparticle coefficient. The assembly with interparticle friction coefficient equal to 0.55 presented strain-softening behaviour; the qualitative features of this stress-strain curves are typical to loose sands tested undrained in the laboratory. The response of the assembly changed quite markedly from strain-softening to strain-hardening behaviour by increasing the friction from 0.55 to 0.75 and 0.95. The initial slopes of the stress paths are practically the same in all the experiments; however, the curves start to diverge as loading continues, capturing an important difference in stiffness at higher deformations.

The evolution of the coordination number for the three tests is presented in Figure 5.22. In general, increasing the friction coefficient results in a lower average coordination number. Contacts act as supporting points, providing stability to the particles. The higher

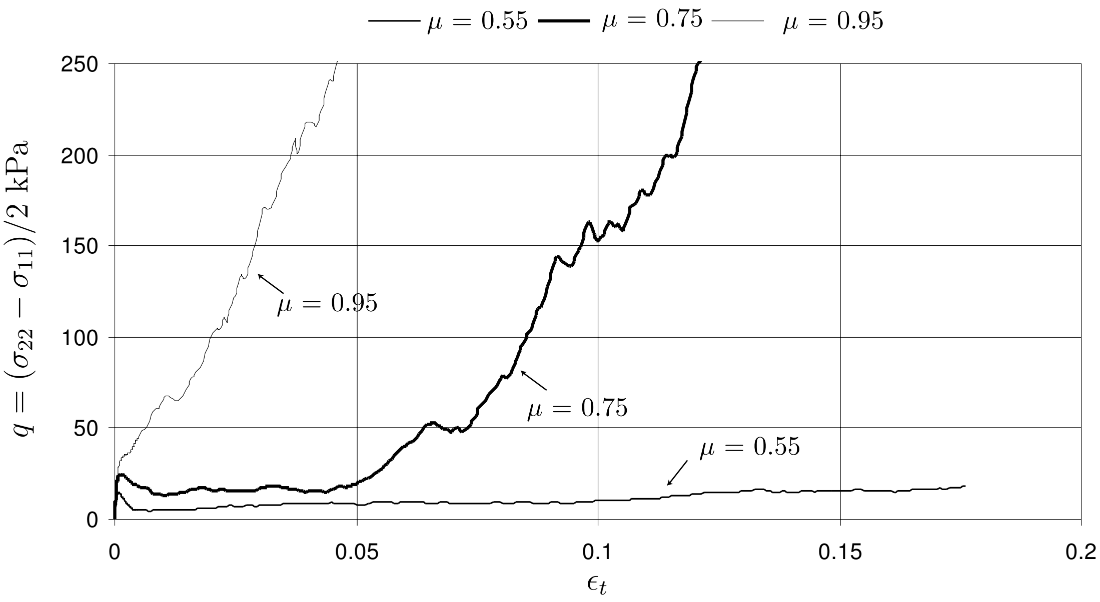

Figure 5.20: Stress-strain curves for varying interparticle friction coefficients

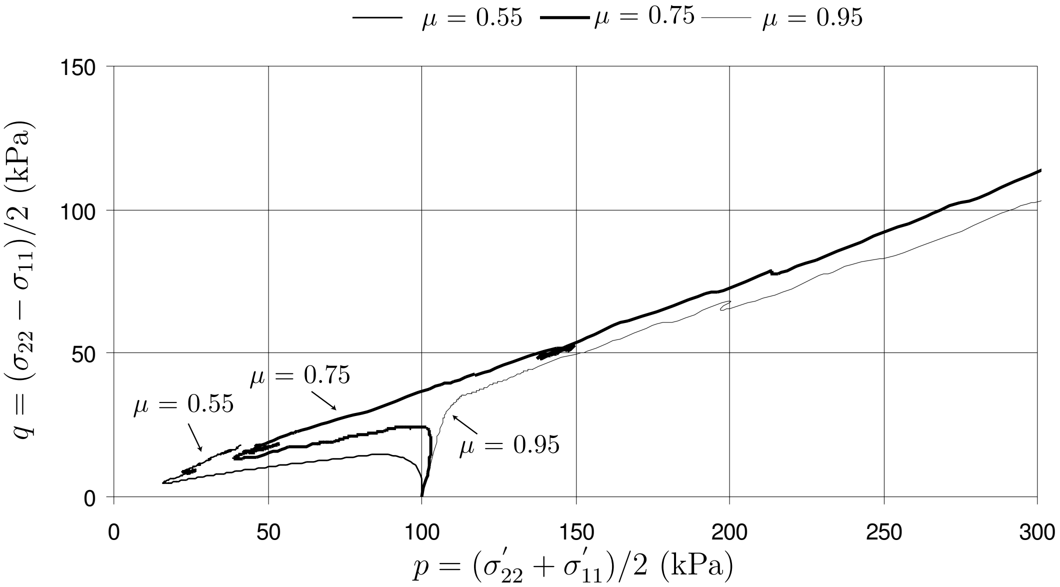

Figure 5.21: Stress paths for for varying interparticle friction coefficients

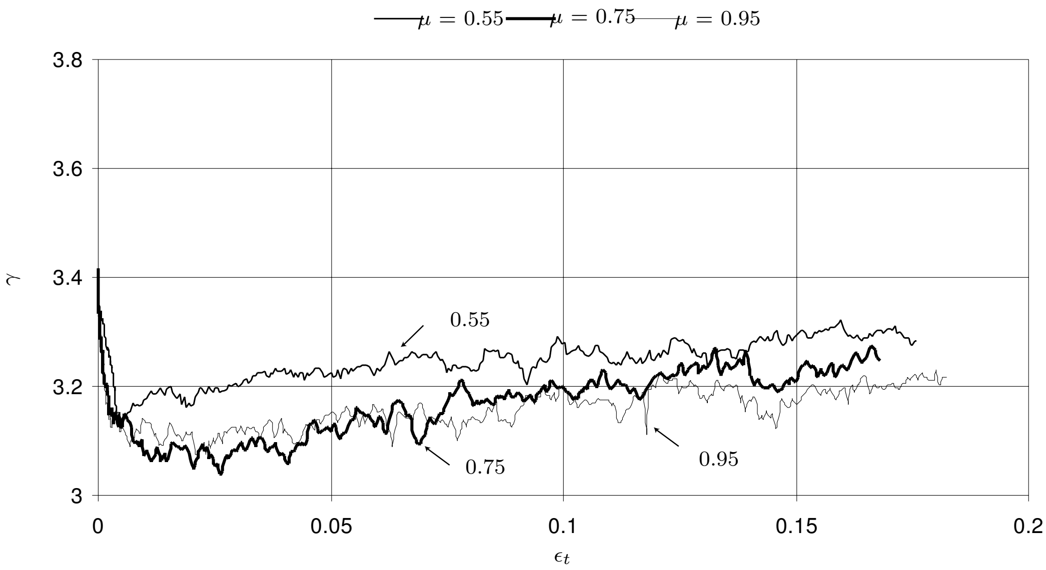

Figure 5.22: Evolution of the coordination number for varying interparticle friction coefficients

shear resistance at the contacts, allows the individual grains to be at static equilibrium with lower coordination numbers. From the data presented, the following conclusion may be drawn:

- The dilatant characteristics of the sample appear to be enhanced with the increase of particle friction; accordingly, the higher friction contributes to the development of lower pore pressures, causing a considerable increase in the strength of the sample.
- The number of contacts initially decreases to a minimum that appears to be controlled by the interparticle friction coefficient. For this particular case greater friction results in lower coordination numbers. The additional frictional resistance allows the individual particles to achieve stable configurations with lower average coordination numbers.

These observations provide important information on the contributions of the interparticle angle of friction to the macroscopic shear strength of the undrained granular structure. An explanation of the possible mechanisms responsible for the dramatic change in

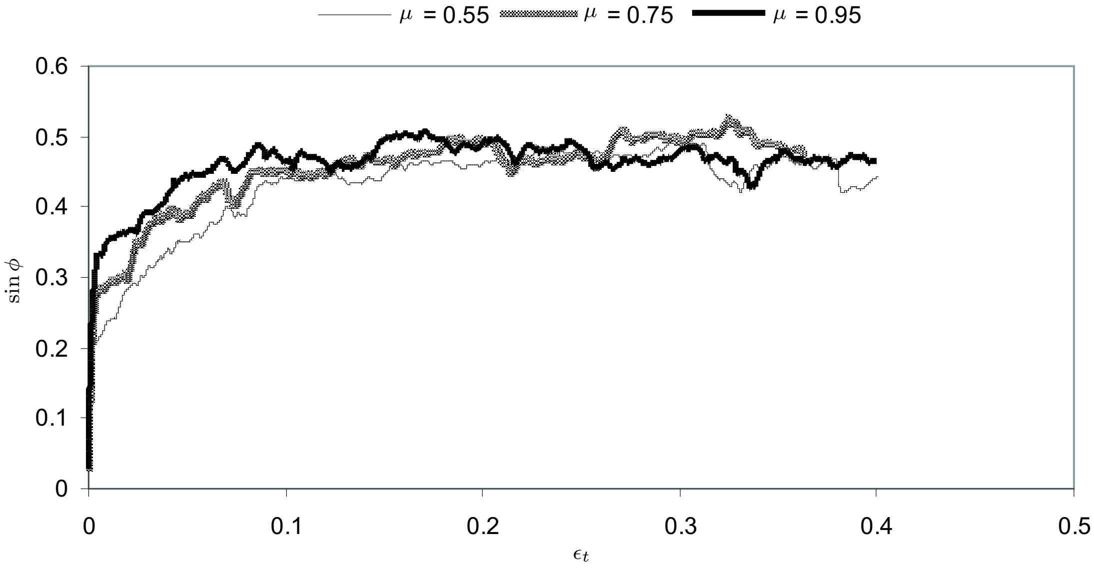

Figure 5.23: Stress-strain behaviour for tests with variable interparticle friction coefficient (μ)

the stress-strain behaviour of the undrained assemblies was sought by conducting three additional drained biaxial simulations on an assembly with similar characteristics to the one used for the undrained tests. The parameters used in these simulations are presented in Table 5.4. The results of these additional simulations are presented below.

5.5.3 Drained Response

The evolution of the mobilized friction angle ($\sin\phi$) for different interparticle frictions coefficients $\mu = 0.55$, 0.75 and 0.95 is shown in the plot of Figure 5.23. The curves show that the peak and ultimate resistance of the assembly is moderately increased when increasing the magnitude of the friction coefficient. The evolution of the average number of contacts is presented in Figure 5.24. The steady state coordination number is considerably affected by the friction at the contacts. In general, increasing μ results in lower coordination numbers. The lower coordination numbers can be directly linked to the higher shear resistance offered by the higher values of μ, since in general the particles can reach stable configurations with fewer contacts.

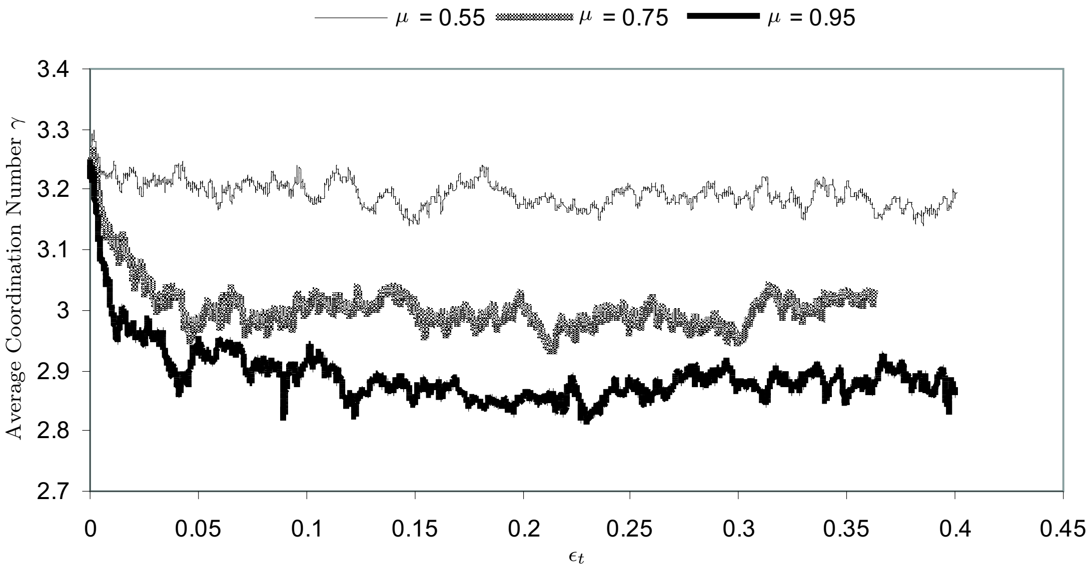

Figure 5.24: Evolution of average coordination number (γ) for tests with variable interparticle friction coefficient (μ)

The features exhibited by the assembly with varying values of μ are in agreement with results of previous numerical experiments on idealized assemblies of disc-shaped particles [6], spherical particles [19] and elliptical particles [57]. These previous investigations have all reported small increases in the effective peak angle of friction $\phi'_{\max}$ and a considerable reduction in steady state coordination numbers induced by μ. For the hypothetical condition of contacts with very low friction $\mu \approx 0$ Bathurst [6], and Rothenburg and Kruyt [72], have showed that assemblies of discs deform with an average coordination number of 4, which is the minimum required for these plane systems to maintain static equilibrium.

Important to the present discussion is the effect that μ has on the dilatant characteristics of the samples. The volumetric strain (ϵ_v) versus deviatoric strain (ϵ_t) for tests with variable interparticle friction coefficients is depicted in Figure 5.25. It is observed that the specimen with $\mu = 0.55$ initially contracts and only at relatively high deformation ($\epsilon_t = 10\%$) starts to dilate, and in general, a higher μ encourages dilatancy. Although the volumetric strains are low (less than about 6 per cent for the range of strains examined), it is evident that the tendency of volumetric change is influenced by the interparticle friction coefficient.

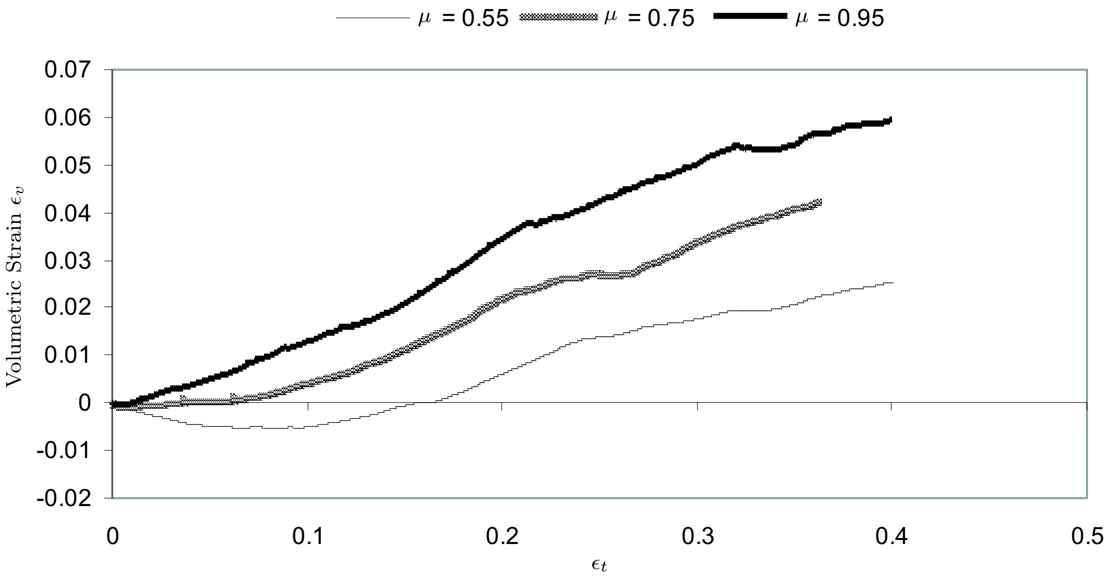

Figure 5.25: Volumetric strain (ϵ_v) versus deviatoric strain (ϵ_t) for tests with variable interparticle friction coefficient (μ)

Dilatancy can be linked with the evolution of the coordination number presented in Figure 5.23; for this particular case, the higher dilatancy is associated with a higher reduction in the number of contacts.

The data thus far examined clearly show that dilatancy in the drained specimen is increased by increasing values of μ. From information collected from the drained tests, it is now possible seek a relation between the effects of particle friction in undrained behaviour.

The increase in strength in the undrained tests can be attributed to the enhancement of dilatancy provoked by the higher interparticle friction coefficients. Strength and dilatancy however, may appear to be disassociated, since while the drained resistance was not considerably affected by the different magnitudes of μ, the undrained strength was drastically altered. In fact, the results showed that the undrained behaviour changed from strain-softening to a highly strain-hardening type of response. Nevertheless, a link between the undrained strength and tendencies to dilate can readily be made.

The dilatancy rate of the sample D is defined as the rate of volumetric change as follows:

$$D = \frac{\Delta\epsilon_v}{\Delta\epsilon_t} \tag{5.4}$$

In reference to Section 4.3, a relation between the global rate in pore pressure $\Delta\bar{u}$ and rate in the macroscopic volumetric strain, as a function of the bulk modulus of the fluid B_f and the porosity n of the sample, can be written as:

$$\Delta\epsilon_v = \frac{n}{B_f}\Delta\bar{u} \tag{5.5}$$

Combining (5.5) with (5.4) a relation between dilatancy rate and the rate of macroscopic pore pressure generation with deviatoric strain can thus be found:

$$\frac{\Delta\bar{u}}{\Delta\epsilon_t} = D\frac{B_f}{n} \tag{5.6}$$

The above relation gives important insight into the dependency of pore pressure changes on the dilatant characteristics of the assembly. Since the compressibility of the fluid is small, small changes in dilatancy would be greatly amplified by the bulk modulus of the fluid. Hence, it can be concluded that the dilatant characteristics enhanced by higher interparticle friction coefficients considerably influenced the development of negative pore pressures, leading to a constant regain of strength with deformation observed in Figure 5.20. The results further show that, assemblies of elliptical particles are highly sensitive to small volume changes, and tendencies to change volume are the dominant mechanisms for undrained behaviour.

The previous experimental findings have a practical value, since they suggest that liquefaction of sands may be inhibited by slightly augmenting the friction between grains, provided that dilatancy is increased. This suggestion however, remains to be verified by means of laboratory experimentation.

5.5.4 Summary

The results of numerical simulations where the interparticle friction angle was varied were presented. It was found that an increase in μ from 0.55 to 0.95 greatly influenced the undrained stress-strain response of the assembly. The behaviour of the specimen changed from strain-softening to strain hardening by changing μ from 0.55 to 0.95.

An explanation of the behaviour was sought by conducting drained simulations in an assembly with similar characteristics. It was found that dilatancy is increased by higher interparticle friction coefficients. A relation between the rate of pore pressure generation and dilatancy was then presented, and it was concluded that the observed increase in undrained resistance could be attributed to the enhancement of dilatancy by higher values of μ.

5.6 Volume Controlled and Undrained Simulations

5.6.1 Introduction

Some authors have considered numerical simulations where volume change is inhibited as representative of undrained tests [44],[56]. The DEM offers the convenience of being able to restrain changes in volume in a relatively easy manner. This approach, however, excludes the effects of fluid-flow interacting with the particles, and thus, the validity of using volume-controlled simulations as representative of undrained tests can be questioned.

The results obtained from program AQUA were compared to those obtained from a drained simulation in which the volume was preserved throughout the test. The constant-volume drained test was carried out by setting the condition $-\dot{\epsilon}_{22} = \dot{\epsilon}_{11}$ using servo-mode 2 (see page 72).

The assembly employed for the simulations was initially consolidated and brought to equilibrium under a confining pressure $\sigma_o^{'}$= 200 kPa. The initial coordination number and void ratio were 3.96 and 0.213, respectively. The parameters used in the computations are presented in Table 5.4.

5.6.2 Comparison of the Results

The stress-strain curves for the different tests are presented in Figure 5.26; a comparison of the curves shows that both methods provide similar results. The initial peak obtained from the undrained test is slightly higher than from the volume-controlled test, but the strengths at the quasi-steady state are practically the same. At large deformations, the strength of the assembly tested under volume-controlled conditions increases at a faster rate than the undrained test; and both curves start to diverge.

The corresponding stress paths presented in Figure 5.27 show that the main difference between both tests is the initial slope of the curves. The undrained assembly behaves in a stiffer fashion, developing lower pore pressures at the beginning of the test, a condition that eventually results in a higher peak strength.

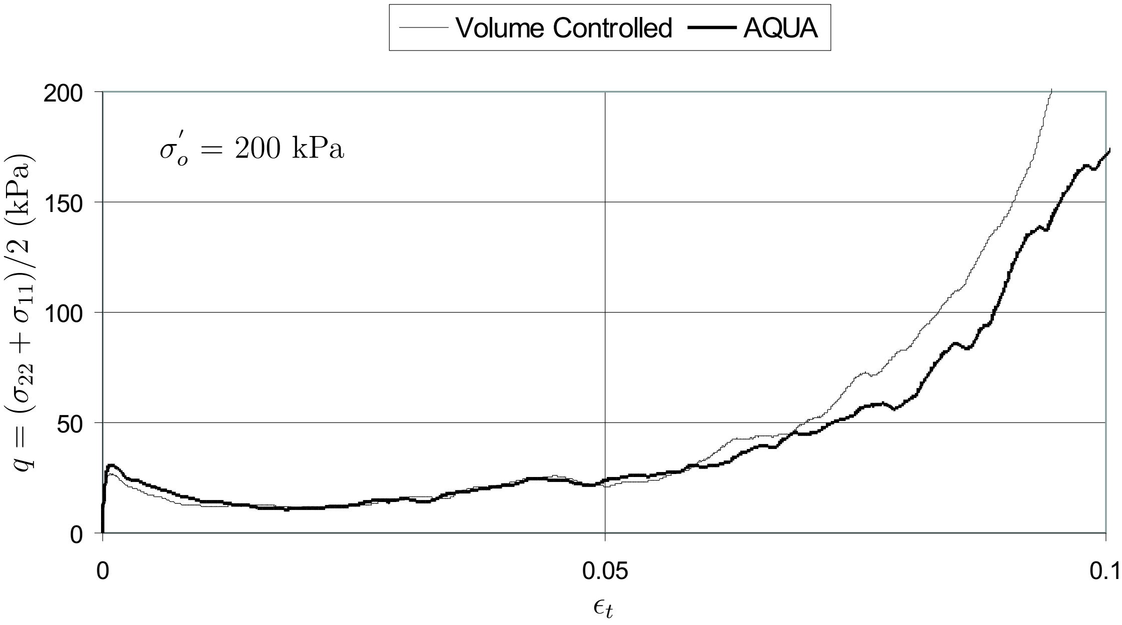

Figure 5.26: Stress-strain curves using the proposed algorithm and preserving the volume at the boundary

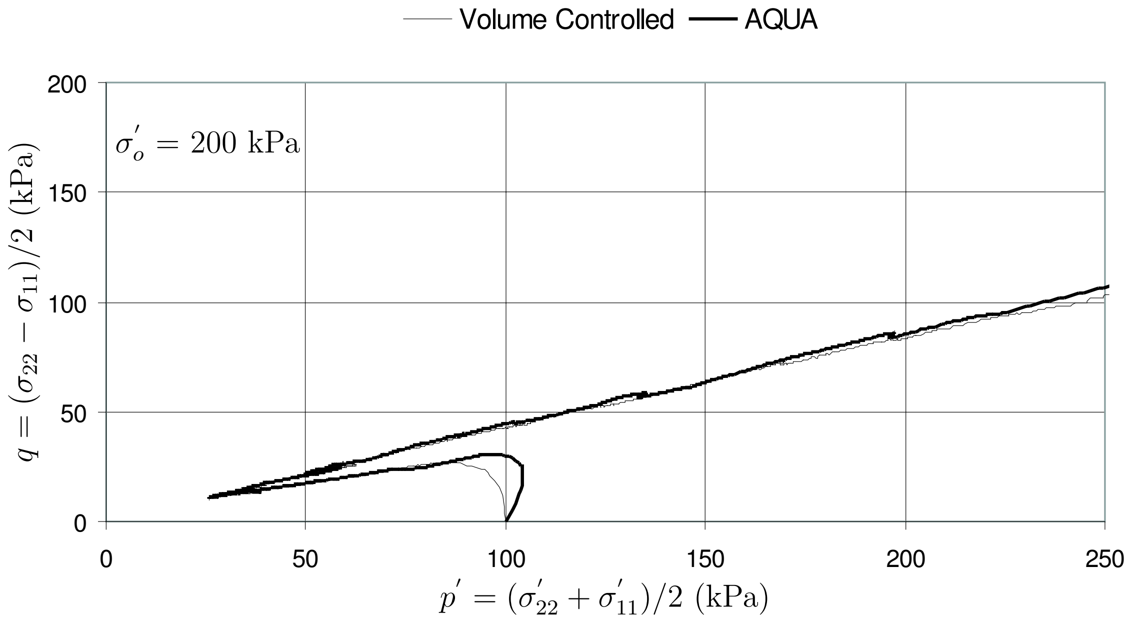

Figure 5.27: Stress paths using the proposed algorithm and preserving the volume at the boundary

The slopes of both tests at greater deformations are very similar. This result agrees with previously reported experimental findings, for example, Negussey *et al.* [54] have shown that ϕ_{ss} is equal to the constant-volume friction angle ϕ_{cv} for the same sand.

5.6.3 Comments

The reason for the development of lower pore water pressures at the beginning of the undrained test can be understood by recalling the averaging technique used in the calculation of the macroscopic pore pressure $\bar{u}$. The program calculates the quantity $\bar{u}$ as a weighted average that takes into account the pore volumes and the individual pressures. The lateral movement of the boundary is in turn controlled by the rate of pore pressure generation. Although microscopic pressures start to built at the commencement of the simulation - most probably at the lower and upper portion of the assembly-, their magnitude does not have a significant influence on the macroscopic average. Therefore, the servo mechanism controlling the lateral movement of the boundary does not react as fast as in the case of a drained test.

The results so far analyzed indicate that for the particular assemblies examined, preserving the volume during a simulation can provide similar results to those obtained using program AQUA. Nevertheless, as shown in Section 6.6, differences between both approaches are expected to emerge when lower conduit diameters are considered. Additional details about the effect of conduit diameter on the macroscopic response of the assemblies are presented in Section 6.6.

In the case of laboratory experiments, volume-controlled tests have been suggested as an alternate method to simulate an undrained environment in the triaxial cell [97]. However, experimental evidence indicates that both tests can provide different results [75].

Chapter 6

Initial Fabric Anisotropy and Permeability

6.1 Introduction to Initial Fabric Anisotropy

The majority of granular materials encountered in civil works possess an initial anisotropy in their fabric and their behaviour is expected to change depending on the direction of the major principal stress with respect to the grain arrangement. Rotation of the principal stress direction is a feature of the stress paths associated with many field and laboratory conditions. It has been shown for example that the cyclic change in shear stress in a soil element in a seabed deposit due to wave-induced loads is characterized by the continuous rotation of principal stresses [42]. Cyclic loading tests also subjects a soil specimen to a state in which the principal stresses are continuously rotating.

The undrained behaviour of sands has been found to be dependent on the orientation of the principal stresses [85, 106, 80]. Such dependency has been attributed to the initial anisotropy present in the structure as a consequence of the deposition mode or specimen preparation method. Soil deposition methods greatly influence the particle arrangement in the samples. For example, water pluviation creates specimens whose fabrics closely mimics those of fluvial and hydraulic-fill sands [62], provoking non-spherical particles to lie along the horizontal plane, also called the bedding plane. The spatial arrangement of particles with long axes oriented horizontally increases the chances for contacts to concentrate in the vertical direction. Thus, a detailed study of the effects of principal stress rotation on the soil response requires an assessment of the anisotropy of the particles and their contacts. An analysis of this nature however, is difficult if not impossible to conduct in the laboratory.

This section presents the results of simulations on initially anisotropic assemblies. The purpose of the tests was to further examine the effects of the direction of principal stresses on the macroscopic response. The evolution of the fabric during deformation was quantified using parameters that indicate the spatial orientation of the particles and their contact normals.

6.2 Assembly Generation and Test Program

6.2.1 Assembly Generation

The assembly used for the simulations was created by initially expanding the particles according to relation (5.1). After expansion, the particles were randomly oriented so that their major axes lay within an angle of ±45° from the horizontal. The assembly was compacted under a confining pressure of $\sigma_o^{'} = 100$ kPa, and brought to equilibrium.

The orientation bias in the principal axes of elliptical particles after compaction is shown in Figure 6.1 by means of a polar histogram. The histogram has the shape of a peanut sitting on the horizontal plane, indicating the dominant orientation of the particles. Similar to the contact orientation distribution, the distribution of the particles' major axis can be approximated by a Fourier series limited to the second order:

$$C(\theta) = \{1 + a_s \cos 2(\theta - \theta_{as}) + \ldots\} \tag{6.1}$$

where the parameter a_s represents the deviation from the isotropic state and θ_{as} indicates the principal anisotropy orientation. The approximation to the measured distribution was computed using relation (6.1) and has been superimposed in Figure 6.1. Although the degree of anisotropy can be visually verified from the figure, the parameter $a_s = 0.769$ additionally shows that the method employed to generate the assembly produced high anisotropy in the orientations of particles. The direction of anisotropy θ_{as} coincides with that of the bedding plane. Mulilis *et al.* [52] have quantified the orientation of sand particles in specimens formed using the water pluviation method by cutting thin sections of samples impregnated with resin. Their measurements revealed distributions similar to the one presented in Figure 6.1.

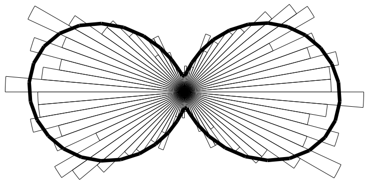

$a_s = 0.769$

$\theta_{as} = 0.011$

$$C(\theta) = \frac{1}{2\pi}\left\{1 + a_s \cos 2(\theta - \theta_{as}) + \ldots\right\}$$

Figure 6.1: Major axis orientation distribution

The method of specimen preparation is expected to affect not only orientation of particles, but also the orientation of contacts and in general, the arrangement and shape of the voids. The degree of anisotropy imposed by the particle arrangement on the contact normal orientation and fluid flow network were examined; the results are presented below.

Initial Contact Normal Anisotropy

The measured histogram of the contact normal orientation is depicted in Figure 6.2 along with the fourth order Fourier series approximation to the distribution. The parameter $a = 0.156$ indicates that a certain degree of anisotropy in the contact normals results from the particle arrangement. Further, the contact normals are preferably oriented in the vertical direction $\theta_a = 1.547$, and perpendicular to the bedding plane $\theta_{as} = 0.011$. Clearly, the contact distribution in assemblies is strongly related to the orientation of the elongated particles.

Initial Flow Network Anisotropy

The particle arrangement also affects the spatial distribution of the pores and, consequently, the conduits orientation in the flow network. Figure 6.3 shows the flow network initially constructed for the assembly as well as a polar histogram of the spatial orientations of the conduits. The conduit orientation distribution was approximated by a truncated Fourier series of the form

$$P(\theta) = \frac{1}{2\pi}\left\{1 + a_p \cos 2(\theta - \theta_{ap}) + b_p \cos 4(\theta - \theta_{bp}) + \ldots\right\} \tag{6.2}$$

where a_p and b_p are the second and fourth order anisotropy coefficients and θ_{ap} and θ_{bp} are the anisotropy orientations. The approximation to the distribution and the computed

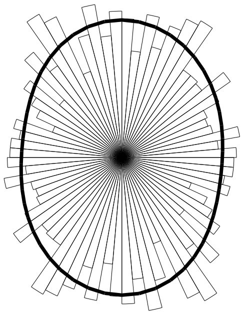

$a = 0.156$

$b = 0.009$

$\theta_a = 1.547$

$\theta_b = 1.377$

$$E(\theta) = \frac{1}{2\pi}\left(1 + a\cos 2(\theta - \theta_a) + b\cos 4(\theta - \theta_b)\right)$$

Figure 6.2: Contact normal distribution

values for the constants in (6.2) are also shown in the figure.

The distribution shows that the conduits are preferentially oriented in the direction parallel to the bedding plane. The resulting arrangement has practical consequences in the hydraulic conductivity of the assembly, mainly that ability of the flow network to conduct fluid is enhanced in the horizontal direction and reduced in the vertical direction.

6.2.2 Summary of the Test Program

The discussion refers to a total of three tests conducted on the initial anisotropic assembly. After compacting the assembly under an initial pressure of $\sigma_o^{'} = 100$ kPa, the coordination number and void ratio were $\gamma = 3.41$ and $e = 0.25$, respectively.

To evaluate the effect of principal stress direction, the assembly was rotated at angles of 90°, 45° and 0°, degrees with respect to the original configuration. The assemblies were tested biaxially by applying a constant axial strain rate ($\dot{\epsilon}_{22}$) and maintaining the total lateral stress (σ_{11}) constant. The tests for 90°, 45° and 0° degrees rotation will be referred to as A, B and C respectively.

A summary of the test program is depicted in Figure 6.4. Assembly A was tested with the principal contact normal anisotropy direction perpendicular to the direction of principal stress. Assembly B was positioned so the direction of contact normal anisotropy

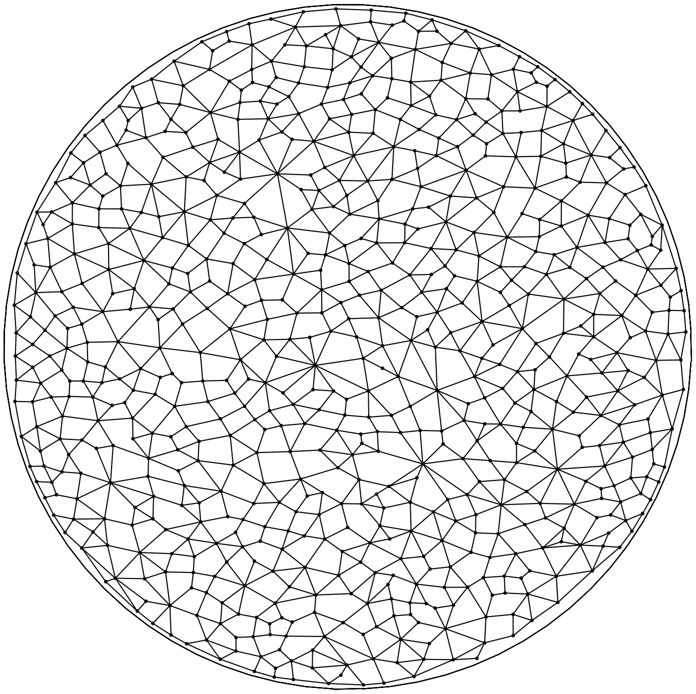

$$P(\theta) = \frac{1}{2\pi}\left\{1 + a_p \cos 2(\theta - \theta_{ap}) + b_p \cos 4(\theta - \theta_{bp}) + \ldots\right\}$$

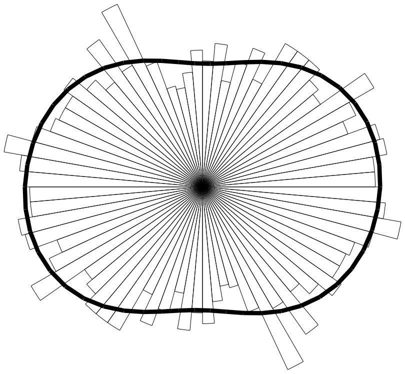

$a_p = 0.175$
$b_p = 0.032$

$\theta_{ap} = 0.015$
$\theta_{bp} = 0.718$

Figure 6.3: Initial network anisotropy

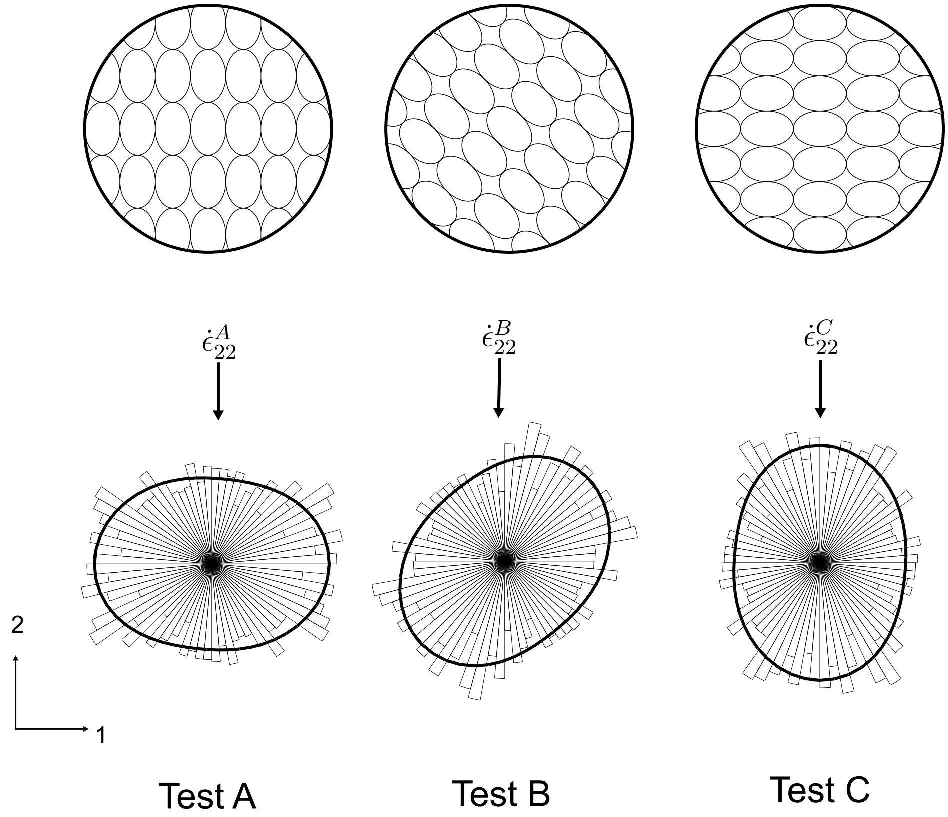

Figure 6.4: Summary of the test program and the initial distribution of the contact normals. The schematics on top of the distributions show the initial arrangement of the particles in the assemblies.

was shifted 45° from that of the principal stress. Both principal stress and contact normal anisotropy directions were coincident in assembly C. Tests B and C were taken to a final deviatoric strain of ϵ_t=0.176, reached after 1.841×10^6 cycles.

The properties assigned to the particles are presented in Table 5.1, while the properties of the flow-network were those shown in Table 5.2.

6.3 Simulation Results

The stress-strain curves for the three tests are plotted in Figure 6.5, while a detail of the initial stage of the deformation is presented in Figure 6.6. The corresponding stress paths are presented in Figure 6.7.

Figure 6.6 notes that test A was halted at a strain $\epsilon_t \approx 0.007$, the reason being that high particle instabilities were detected because the granular structure reached an unstable configuration. The curve however, never shows a tendency to change direction to the right indicating a transition into the steady state of deformation. The response of the three specimens is characterized by the presence of a peak stress difference at a strain $\epsilon_t \approx 0.002$.

The stress-strain curve corresponding to test B is somehow erratic, constantly changing slope after the initial peak. This behaviour is also captured by the stress path as it moves back and forward at a constant $q/p^{'}$ ratio. The post-peak portion of the stress-strain curve shows a general tendency to regain resistance, the tendency increasing considerably as the curve reaches the end of the simulation.

The stress-strain curve corresponding to test C presents a more steady post-peak behaviour than that corresponding to test B. After the minimum stress difference is reached, the strength is gradually recovered as the assembly is further deformed.

The initial slope of the stress paths shows that specimen A presented the higher stiffness, developing lower pore pressures and presenting the highest peak strength. A comparison of specimens B and C reveals that the former reached a higher stress difference, but presented a lower initial stiffness.

The results of the simulations indicate that the undrained response of initially anisotropic assemblies is highly dependent on the direction of the principal stresses. In general, a greater number of contacts perpendicular to the loading direction results in a higher initial stiffness.

Symes *et al.* conducted a series of experiments using a hollow cylinder apparatus [85].

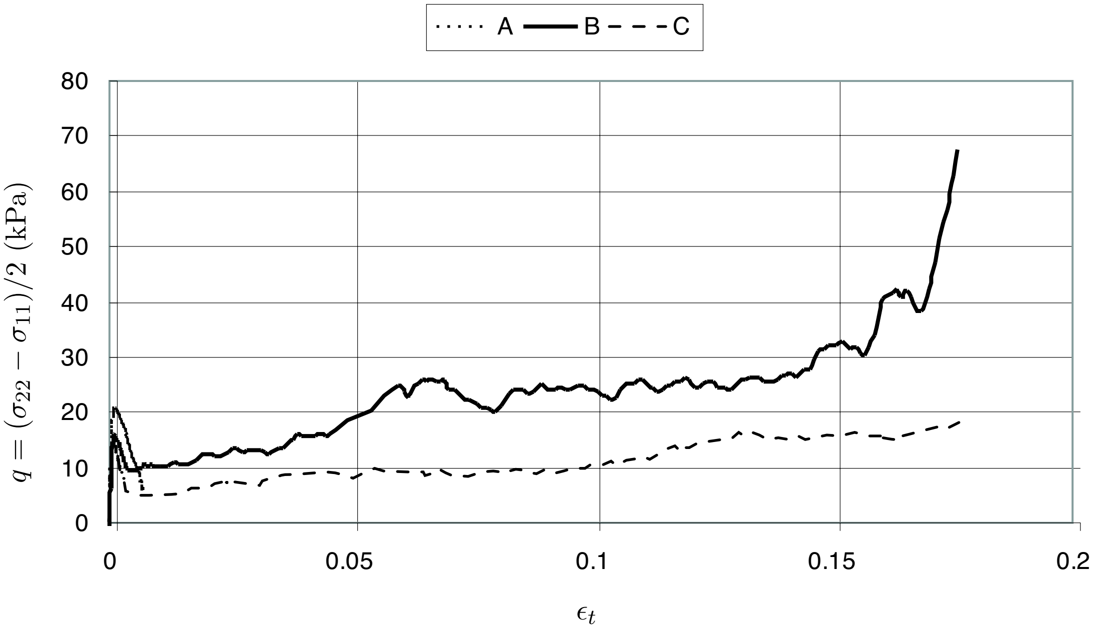

Figure 6.5: Stress-strain curves for initially anisotropic specimens

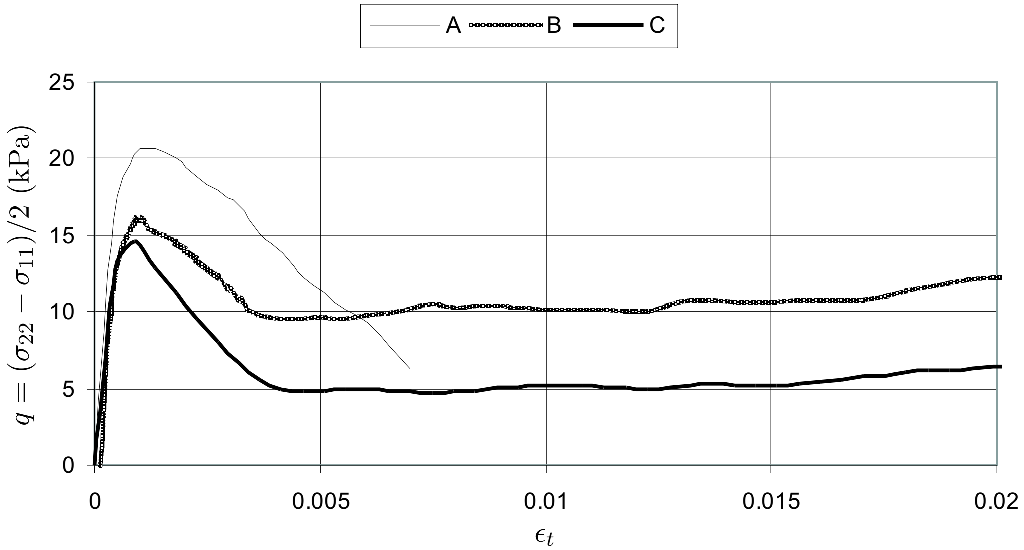

Figure 6.6: Detail of the initial portion of the stress-strain curves for initially anisotropic specimens

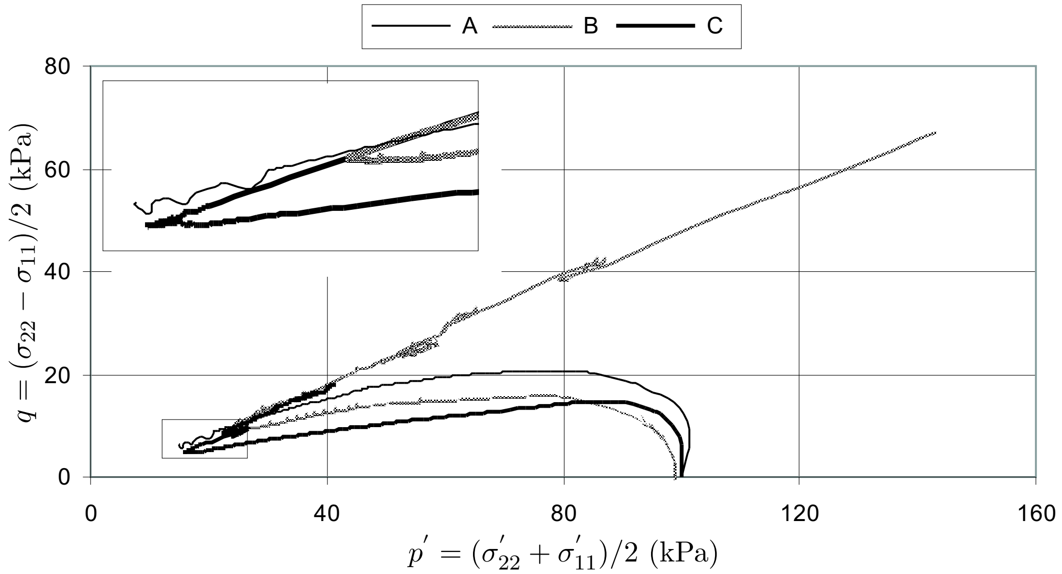

Figure 6.7: Stress paths for initially anisotropic specimens

They reported that samples loaded with the major principal stress perpendicular to the bedding plane were stiffer than those loaded in the perpendicular direction, generating less pore pressure during shear and failing at a higher ratio of q/p'. The results of the numerical simulations are in agreement with the results reported by Symes *et al.* [85].

Initial Slope of the Stress Paths

Consider the slope of the stress path when small incremental stresses are applied to a sand specimen:

$$\theta = \arctan \frac{\delta q}{\delta p'} \tag{6.3}$$

were θ is the direction of the stress path measured counterclockwise from the p' axis. Yimsiri and Soga [104] derived a set of relations to predict the initial slope of the stress paths measured at small strains in the triaxial cell. Their derivations considered a three-dimensional array of mono-sized spheres that behaved non-linearly at the contacts. The results suggest that for the case of an undrained sample presenting an initial degree of contact normal anisotropy oriented in the direction of loading ($a > 0$ and $\theta_a \approx \pi/2$),

θ should be lower than 90° in the $q_{tri} - p_{tri}{}'$ diagram ($\theta_{tri} < 90°$). The stress deviator in the triaxial test and the hydrostatic component of the stress tensor are defined as $q_{tri} = \sigma_1 - \sigma_3$ and $p_{tri}{}' = (\sigma_1 + 2\sigma_3)/3$ respectively. Furthermore, an undrained sample presenting an initial degree of contact normal anisotropy oriented perpendicular to the direction of loading ($a > 0$ and $\theta_a \approx 0$), θ should be greater than 90° in the stress path diagram ($\theta_{tri} < 90°$).

Specimen	θ
A	76°
B	87.5°
C	110°

Table 6.1: Initial angle of stress paths with angles measured counterclockwise from the p' axis.

Table 6.1 shows the measured initial angles in Figure 6.7. In general, the measured data agrees well with the predictions of Yimsiri and Soga [104].

6.4 Evolution of Fabric Descriptors

The most direct way to quantify the microscopic evolution of the granular structure is to trace the development of the coordination number and anisotropy in both contacts and interparticle forces. Knowledge of parameters γ and a, a_n, a_t, provides both qualitative and quantitative information that reflects the ability of the system to withstand the directional variation of the contacts and the forces carried by them.

The evolution of these parameters for tests A, B and C, has been collected in Figures 6.8, 6.9 and 6.10 respectively. Graph (a) in these figures shows the evolution of contact anisotropy parameters a, a_n, and a_t, and the second of the plots, (b), shows the evolution of the average coordination number γ. The third plot, (c), presents the evolution of the average contact normal force $\bar{f}_n^o$. The principal stress difference q has also been included in this plot for comparison.

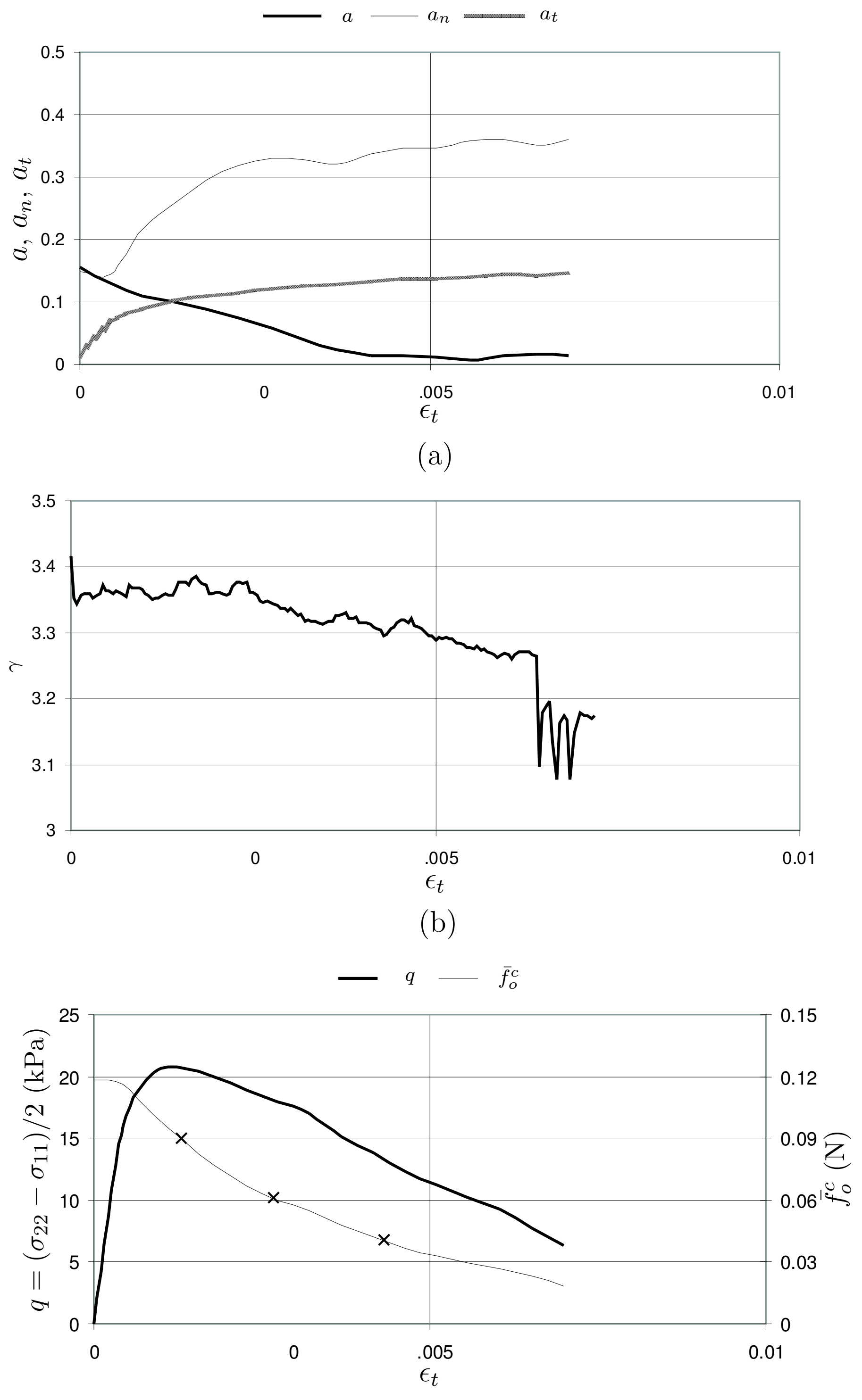

(a)

(b)

(c)

Figure 6.8: Evolution of fabric descriptors for assembly A

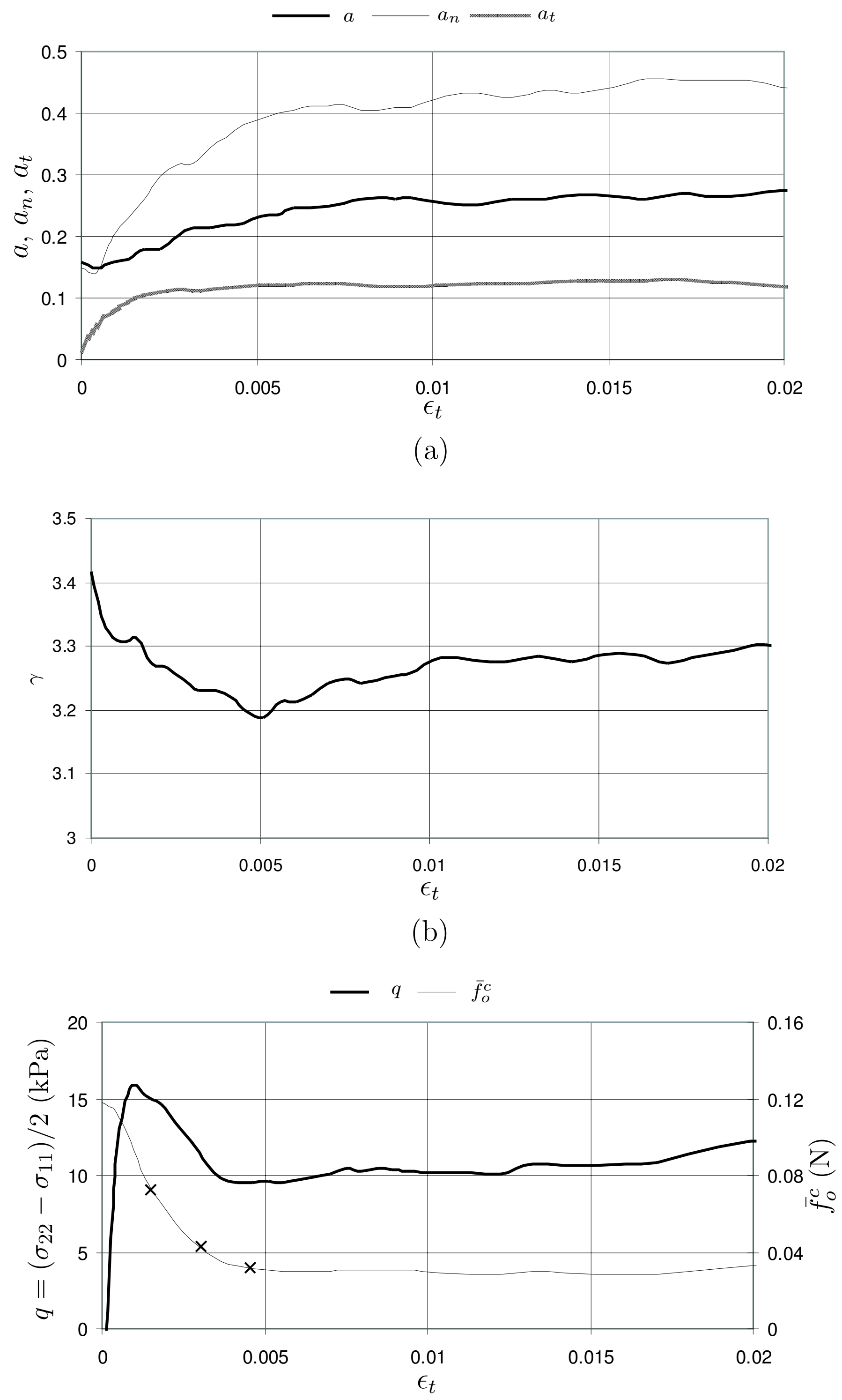

(a)

(b)

(c)

Figure 6.9: Evolution of fabric descriptors for assembly B

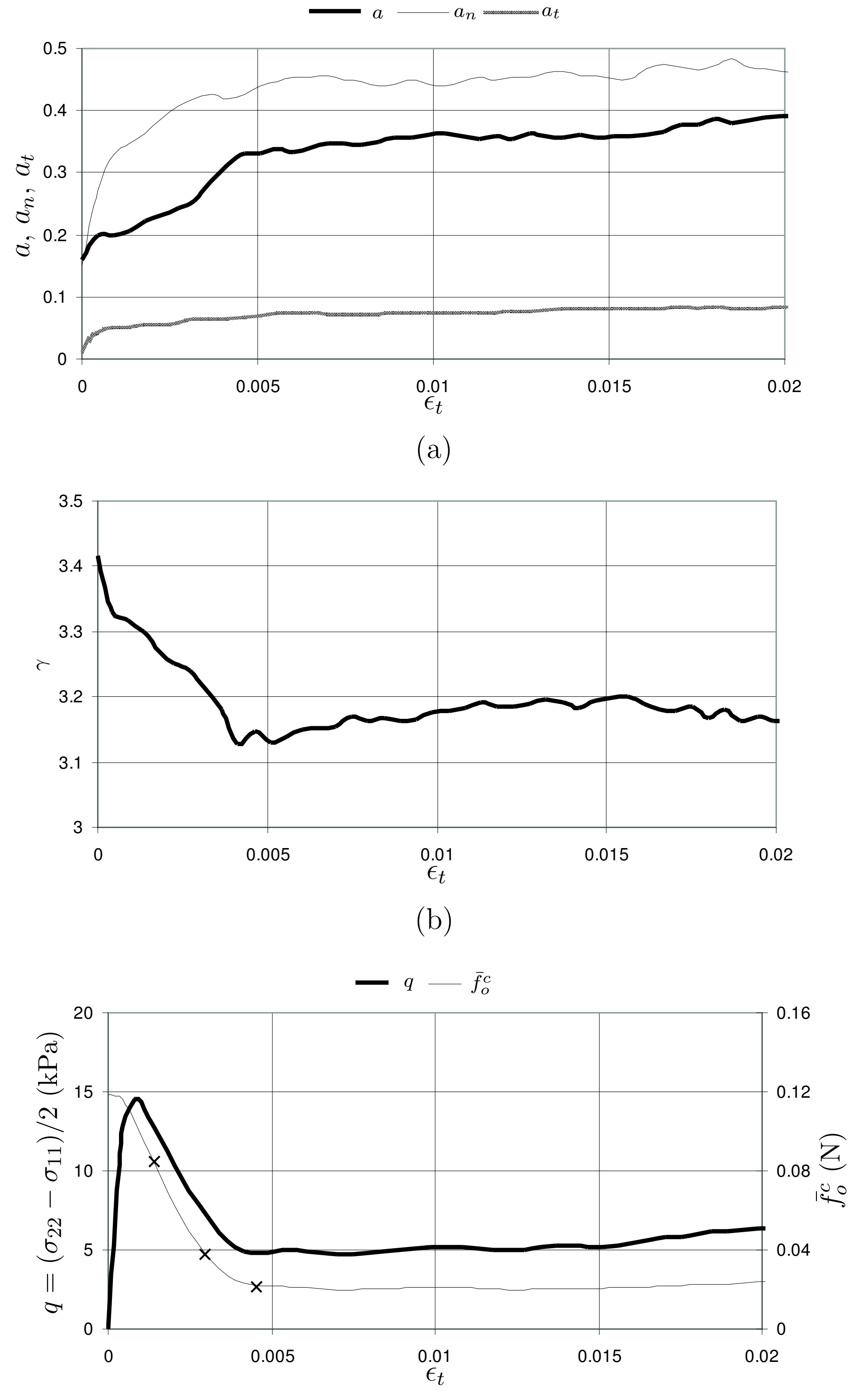

Figure 6.10: Evolution of fabric descriptors for assembly C

6.4.1 Coordination Number

An analysis of the evolution of the average coordination number of specimen A is of special importance for understanding the instabilities detected. The curve presented in Figure 6.8b shows an acute reduction in the number of contacts triggered during the strain softening stage; 94 contacts were lost in a short period, resulting in a change in coordination number from 3.26 to 3.07. Based on the results, it is concluded that the specimen presented unstable behaviour similar to that of sand during liquefaction.

The curves showing the evolution of the coordination number for simulations B and C are given in Figures 6.9b and 6.10b. The number of contacts initially decrease until reaching a minimum value at small strains. The point of minimum coordination number for specimens B and C coincides with the attainment of the minimum stress difference q. After the minimum coordination number is reached, the specimens' response changed from contractive to dilative, and γ increased with further deformation. The average coordination number in assembly C is the lowest among the three assemblies and remains so until the end of the simulation.

6.4.2 Contact Anisotropy Coefficients

The change of the coefficient of contact normal anisotropy with deformation corresponding to test A is presented in Figure 6.8a. The curve shows that anisotropy in contact normals decreases considerably until it becomes almost zero, an indication of contacts evolving from an initially anisotropic state into an isotropic one. The opposite behaviour is observed in the normal force distribution shown in Figure 6.8b. Parameter a_n indicates that anisotropy develops and normal forces concentrate along the loading direction. Additionally, Figure 6.8c shows how parameter $\bar{f}_o^c$ gradually decreases until the end of the test.

The evolution of contact normal anisotropy of assemblies B and C presented in Figures 6.9a and 6.10a shows that a, increased since the beginning of the tests and the rate of growth is maximum during the strain softening stage, indicating that the observed drop in coordination number can be attributed to loss of contacts in the lateral direction. During the strain softening stage the contact force anisotropy coefficients a_n and a_t for tests B and C increase, and parameter $\bar{f}_o^c$ decreases.

With the information thus far analyzed, it becomes possible to study the onset of instability experienced by assembly A.

It has been customary in the literature to characterize the loss of strength or instability onset by tracing the state of stresses in the state diagram [82]. Accordingly, when the stress path reaches a limiting value or a threshold condition pre-established experimentally, instability is expected to be initiated. For this particular case, however, the instability observed in specimen A cannot be attributed to the attainment of a given state of stresses. Figure 6.7 shows in detail that the state of stresses for assemblies A and C at the phase transformation point (the point where instability was initiated) is quite similar. In spite of the similar stress condition, specimen C was able to remain at static equilibrium at all times during deformation.

The presence of a higher number of contacts in the assembly could be associated to the capacity of the assembly to withstand higher loads. However, the observed instability cannot be attributed to the attainment of a minimum coordination number. The data shows that the average number of contacts present in assembly A prior to instability was the lowest throughout the test, $\gamma = 3.26$. Nevertheless, this minimum value was higher than the minimums exhibited by specimens B and C, $\gamma = 3.184$ and $\gamma = 3.126$, respectively. Hence, the unstable characteristics of specimen A can neither be attributed to the attainment of a certain state of stresses nor to a low coordination number.

Developments in Section 2.7 have shown that the coefficient terms a, a_n, and a_t, reflect the ability of the system to rearrange in more stable configurations to respond to imposed loads. Changes in the coefficients of anisotropy are observed to occur in all tests, denoting the gradual destruction of the original configuration. The evolution of the anisotropy parameters is considerably different for the different tests, capturing the strong effects of the initial fabric arrangement in the overall response of the fabric. A complete interpretation of the micromechanical behaviour requires the recognition of all the microstructure descriptors, since the stress tensor is expressed in terms of these coefficients (see relation (2.21b)). The fundamental parameter required to explain the observed instability is the contact normal anisotropy a. Common to all tests is the tendency of contacts to align in the direction of loading while contacts are lost laterally. The particle arrangement of specimen A was such that fewer contacts were available in the direction of loading. As loading is initiated, the additional number of lateral contacts provided additional support for the particles to withstand the imposed load; this is reflected in a higher peak strength when compared with the other two tests. However, as loading continues, contact disruption continues in the lateral direction and parameter a starts to evolve towards an isotropic state, reaching eventually a value of zero. Every increment in the stress deviator is accompanied by lateral contact disruption; thus, parameter a can be envisaged as a measurement of damage inflicted to the structure due to the application of the deviatoric load.

Hence, the contacts in assembly A evolved to a state such that the structure as a whole offered a low resistance to the imposed stresses. Furthermore, the great majority of the particles had their principal axis aligned in the direction of the principal stress, the slenderness of the particles make this configuration the least stable when the lateral support is lost. These particles develop larger moments in their long axis and smaller moments in the perpendicular direction. The moment imbalance and the evolution of the system towards more stable states causes the particles to reorient such that their long axis is perpendicular to the direction of loading. All these mechanisms, combined together, contributed with the instabilities observed in specimen A.

6.4.3 Contact Normal Force Anisotropy

The spatial arrangement of the inter-particle forces for tests A, B and C were extracted at strain levels of ϵ_t= 0.0015, 0.003 and 0.0045, and have been plotted in Figures 6.11, 6.12, and 6.13, respectively. The lines within the assemblies denote the interparticle forces and their orientations, and their thickness represents the force magnitude. The stages at which the distributions were extracted are marked by crosses in Figures 6.8c, 6.9c, and 6.10c. Included in the Figures are the contact normal-force orientation histograms and their approximations calculated using the following truncated Fourier series:

$$\bar{f}_n^c(\theta) = \frac{\bar{f}_o^c}{2\,\pi}\left\{1 + a_n \cos 2(\theta - \theta_{an}) + b_n \cos 4(\theta - \theta_{bn})\right\} \tag{6.4}$$

The approximation is similar to relation (2.7) in page 28 including the fourth order component which becomes necessary to obtain a better fit. Further, the distribution was the property

$$\int_0^{2\pi} \bar{f}_n^c(\theta)\, d\theta = \bar{f}_o^c$$

so the size of the histogram reflects the magnitude of $\bar{f}_o^c$. Additionally, a plot showing the rotation of the principal contact normal force orientation captured by parameter θ_{an} is presented in Figure 6.15.

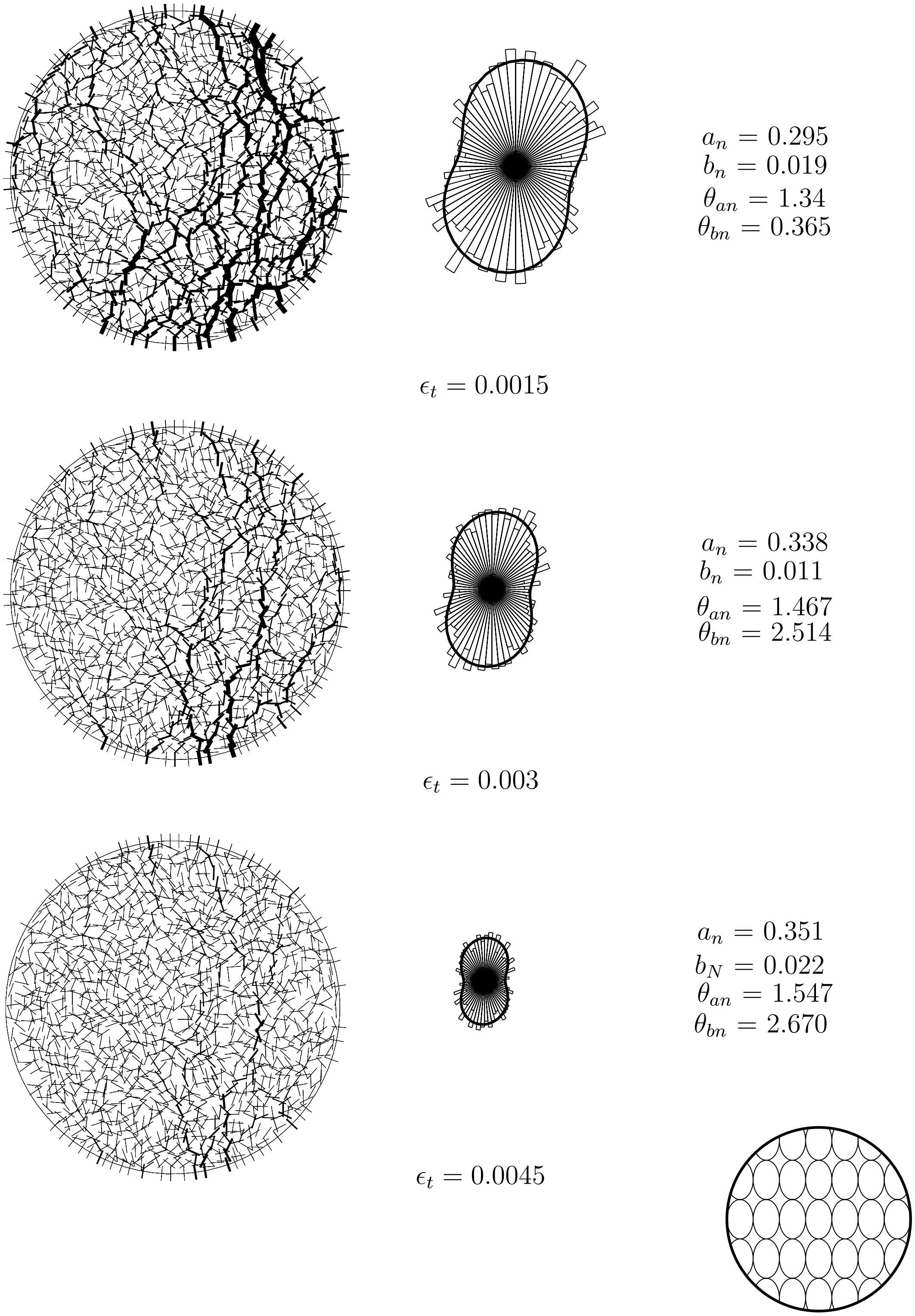

$a_n = 0.295$
$b_n = 0.019$
$\theta_{an} = 1.34$
$\theta_{bn} = 0.365$

$\epsilon_t = 0.0015$

$a_n = 0.338$
$b_n = 0.011$
$\theta_{an} = 1.467$
$\theta_{bn} = 2.514$

$\epsilon_t = 0.003$

$a_n = 0.351$
$b_N = 0.022$
$\theta_{an} = 1.547$
$\theta_{bn} = 2.670$

$\epsilon_t = 0.0045$

Figure 6.11: Force distribution at three levels of strain for test A

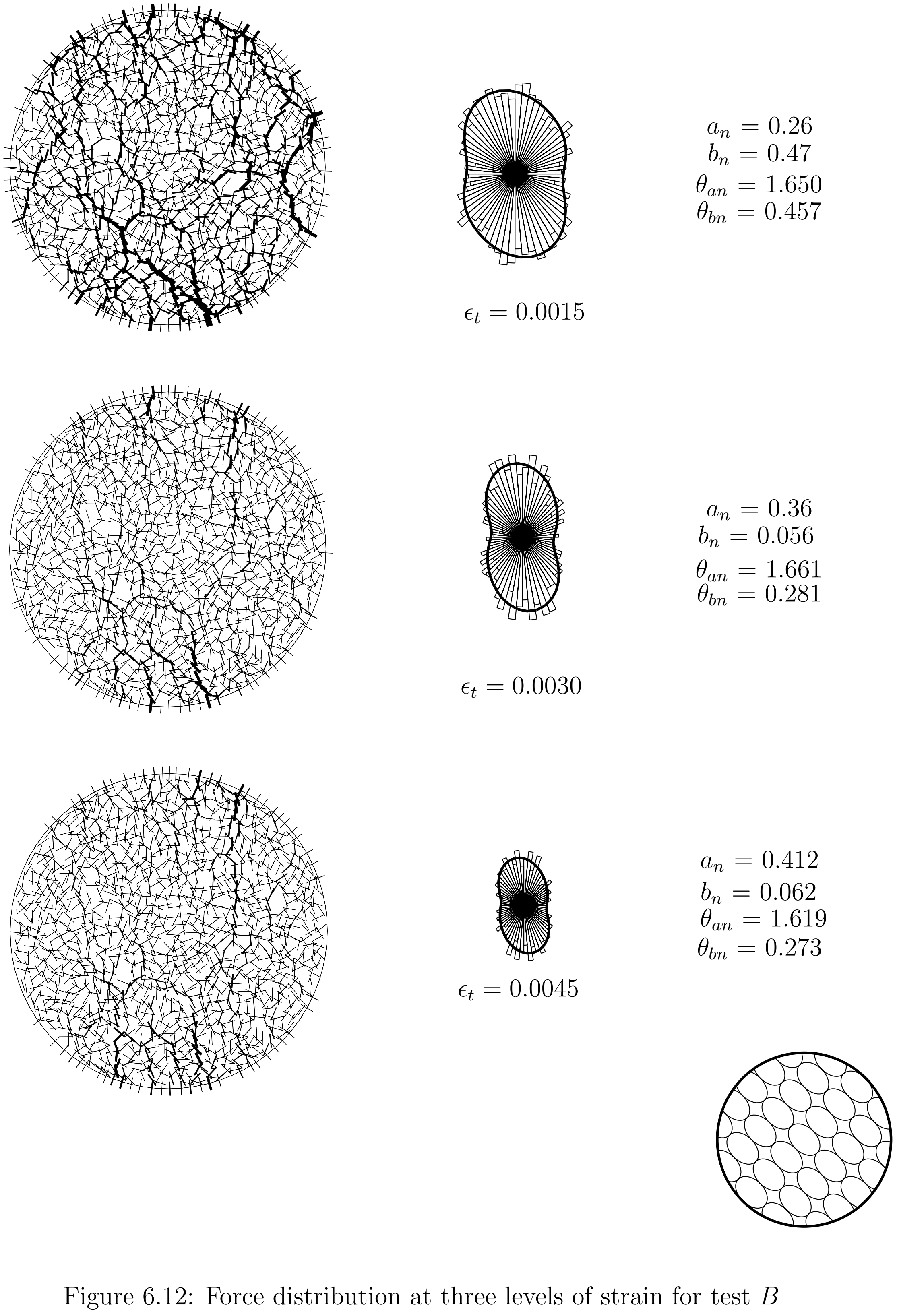

Figure 6.12: Force distribution at three levels of strain for test B

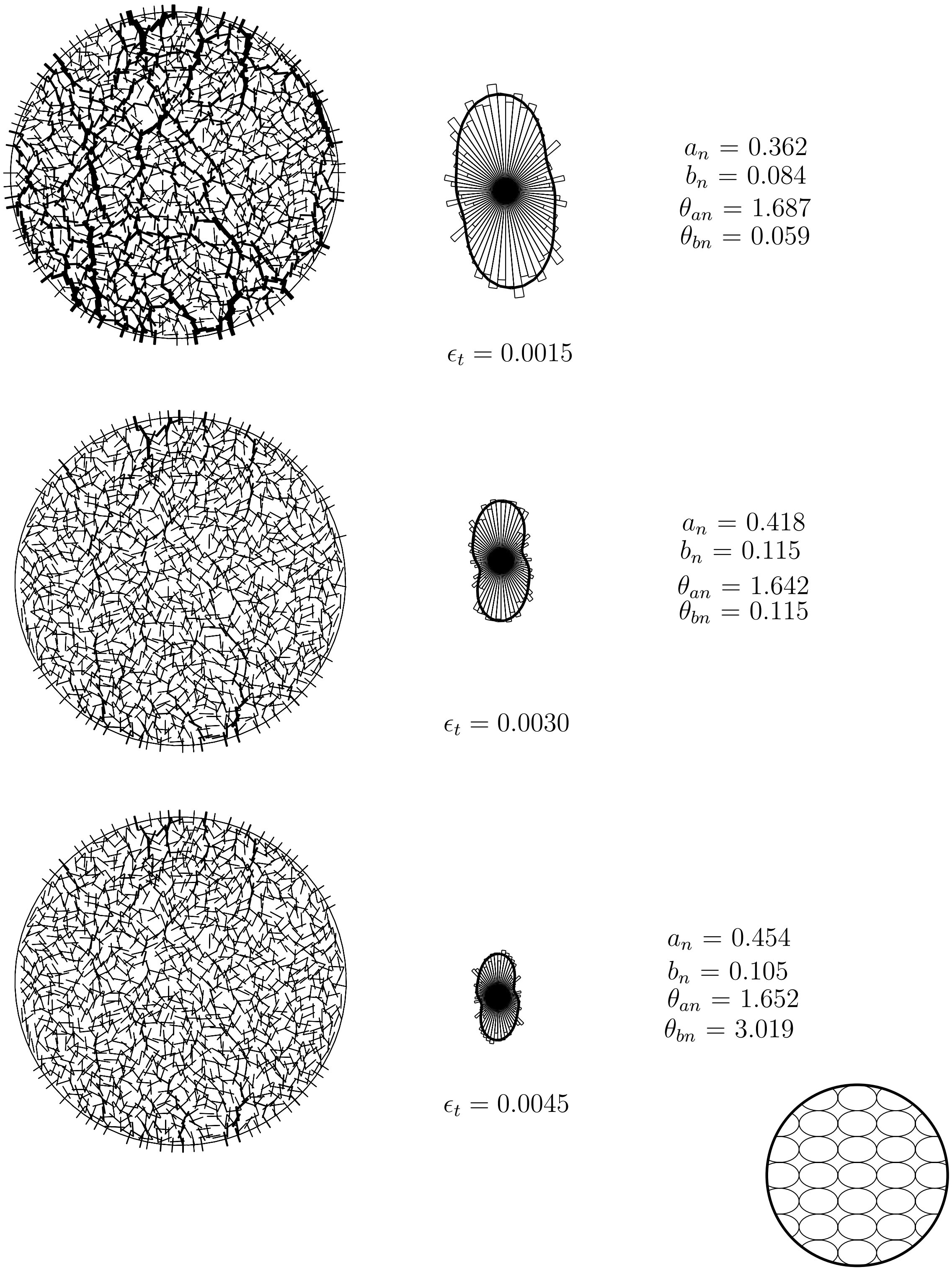

Figure 6.13: Force distribution at three levels of strain for test C

The decreasing size of the histograms capture the progressive reduction in contact forces; this effect can also be visually verified by comparing the thickness (magnitude) of force vectors at the different deformation stages. The data collected in the figures shows a tendency of normal contact forces distribution to align themselves in the direction of loading, which is manifested as a development of chains of contacts carrying higher forces than average. This process is accentuated in the distribution corresponding to Test A, where the principal direction of the contact normal forces appears to evolve from $\theta_{an} = 0°$ to $\theta_{an} = 90°$. It is observed in Figure 6.11 that the rotation of parameter θ_{an} is accompanied by an uneven spatial distribution of stresses, as contact normal forces tend to concentrate towards the right side of the assembly.

The direction of the fabric and contact normal force distributions can be quantified by means of parameters θ_a and θ_{an}. The evolution of these parameters is presented in Figures 6.14 and 6.15 respectively. The data presented in Figure 6.14 shows that the direction of fabric anisotropy is initially determined by the particle orientation, however, as the system is loaded, the principal contact normal direction shifts towards the vertical. The plots in Figure 6.15 show the existing relation of the contact normal orientation and the orientation of contact normal forces, as both parameters in general, follow the same trend. The parameter θ_{an} however, rotates more rapidly than θ_a, since the latter requires physical movement between particles to rotate, whereas the former may change if the contact magnitude and the shear component change, and does not necessarily require particles to move.

Micromechanical concepts introduced in Section 2 demonstrate that the stress tensor measured at the boundary of a system is the result of the contributions of all load carrying contacts. Additionally, stress-force-fabric relationships indicate that the stress tensor and hence the direction of principal stresses is a function of θ_{an}, among other parameters. It is expected then that the direction of major principal stress should be closely related to the direction of contact normal force anisotropy. Figure 6.16 shows a plot of the major principal stress direction θ_σ against the orientation of the contact normal force distribution. It is observed that principal stress direction and normal contact forces are generally coincident in the tests, with a maximum deviation of 20°. Thus, the rotation of the contact normal force anisotropy can be related to the rotation experienced by the major principal stress.

The results of the simulations show that the direction of the major principal stress in Tests A and B is not initially coincident with the loading direction. Although, the

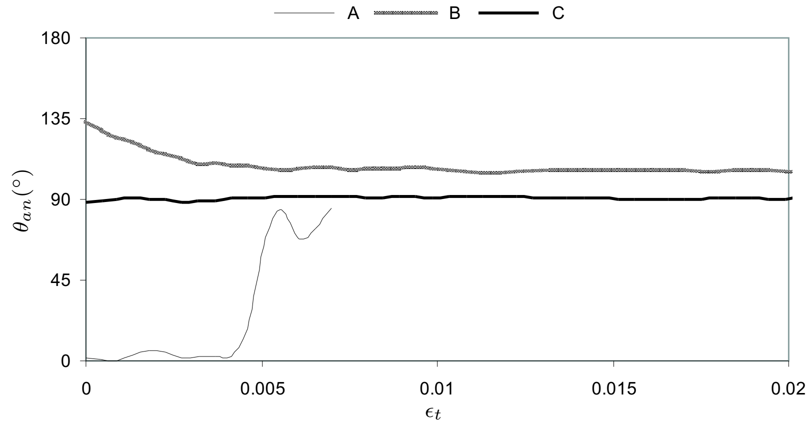

Figure 6.14: Evolution of the contact normal direction (θ_a) for initially anisotropic fabrics

evolution of parameter θ_{an} shows that coaxiality between the major principal stress and the loading direction rapidly re-establishes, the initial difference can be attributed to the initial particle arrangement.

The data collected from the simulations show the complexity of the mechanisms involved in the evolution of forces, and the strong effects imposed by the arrangement of elliptical particles.

6.4.4 Orientation of Particles

The average orientation of the particles's long axis during deformation was quantified by tracing the evolution of parameter a_c in equation (6.1). The change of a_c with strain is shown in Figure 6.17, from where the following observations can be made with respect to the three tests:

1. The small portion of the curve corresponding to test A reveals the initial tendency of particles to evolve towards an isotropic state.

2. The imposed load in assembly B resulted in the gradual rotation of the particles into a more isotropic state.

3. The evolution of parameter a_c in test C shows that particles rotated into a practically perfect anisotropic configuration ($a_c \approx 1$).

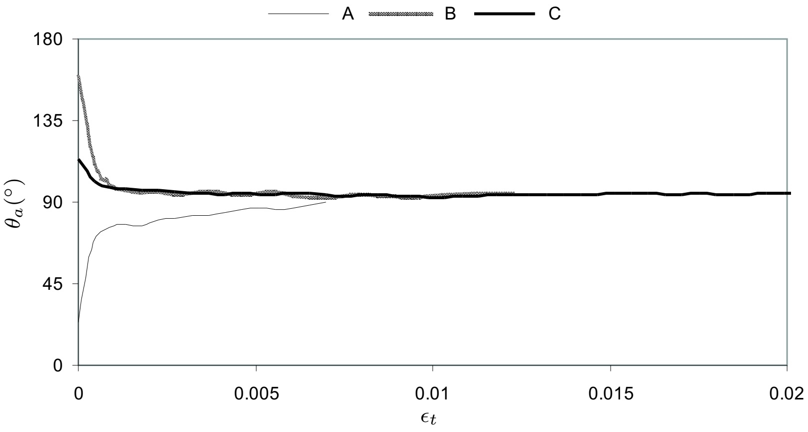

Figure 6.15: Evolution of the contact normal force direction (θ_{an}) for initially anisotropic fabrics

It was previously observed that forces are transmitted along chains and column-like structures that are formed and aligned in the loading direction. In general, more stable configurations are expected to be achieved if particles are aligned with their major axis perpendicular to the major principal stress. The results of the simulations suggest that there exists a tendency of the particles to evolve towards this more stable arrangement. It is expected that at high deformations all of the assemblies will tend to the condition $a_c \approx 1$, since under this arrangement particles are in general more stable. However, particles in specimen A and B have to overcome a greater amount of anisotropy when compared with specimen C, and as a consequence they rotate more. The amount of particle rotation should be associated to the undrained resistance and consequently to the dilatant characteristics of the idealized assemblies.

The amount of particle rotation during deformation can be further quantified by means of parameter $\bar{\Theta}$ defined as follows:

$$\bar{\Theta} = \sqrt{\frac{\displaystyle\sum_{i=1}^{N} \Delta\theta_i^2}{N}} \tag{6.5}$$

where $\Delta\theta_i$ is the difference between the current and the initial angles of particle i. The evolution of the parameter $\bar{\Theta}$ is plotted in Figure 6.18.

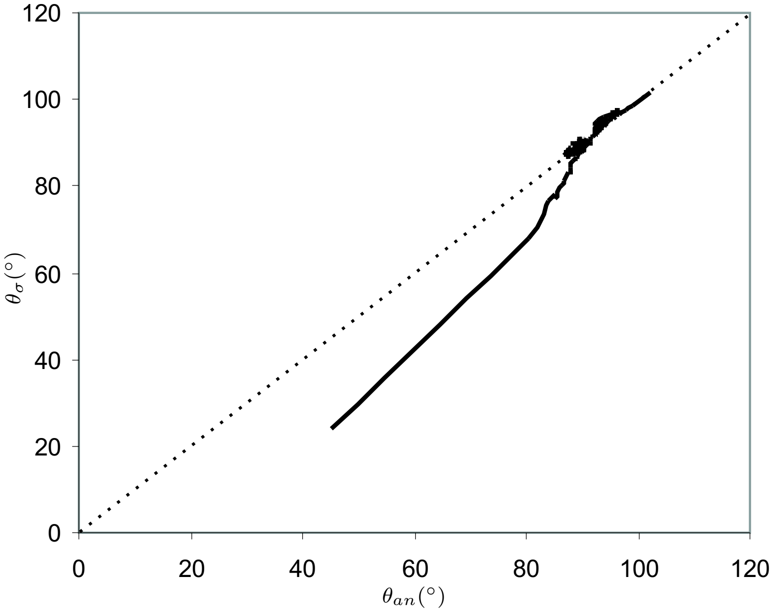

Figure 6.16: Comparison between the principal contact normal force direction (θ_{an}) and the major principal stress direction (θ_{σ})

The information depicted in Figure 6.18 shows that a greater amount of particle rotation takes place in specimen A, followed by assembly B and C. The different average rotations may be associated with the development of macroscopic average pore pressures, mainly, the greater the particle rotation the lower the amount of pore pressure generated and the higher the dilatant characteristics of the granular structure. Therefore, dilatancy is biased by the angle between the bedding plane and the loading direction. Dilatancy effect are globally reflected in the stress-strain curve in Figure 6.5, as specimen B develops less pore pressure (lower dilation) when compared to specimen C.

6.5 Concluding Remarks

The effects of direction of principal stresses on initially anisotropic structures were examined and a great amount of data was collected from the simulations.

The results showed that highly anisotropic fabrics can be constructed using elliptical

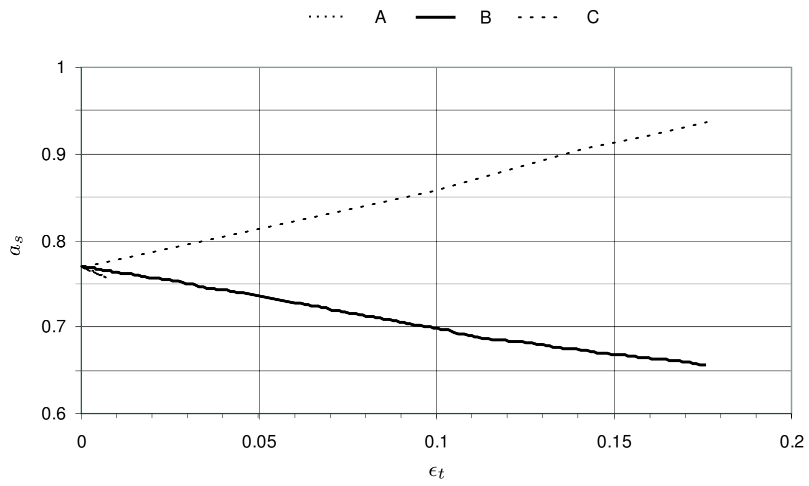

Figure 6.17: Evolution of major axis orientation (a_s)

particles. The degree of anisotropy includes particle orientations, contact arrangement and for this particular case, hydraulic conductivity.

The development of contact normal orientation and conduit arrangement is biased by the orientation of the elliptical particles. This relation is expected to be more pronounced with increasing particle eccentricity. Accordingly, more elongated particles should be able to create higher degrees of anisotropy in the orientation of contacts and conduits.

The adopted approach to simulate fluid flow within the assembly proved to successfully capture some conditions encountered in real soils. For example, it is known that soils deposited in marine environments have particles preferably oriented in the horizontal direction and a higher hydraulic conductivity in the direction parallel to the bedding plane. The flow network of conduits successfully captures this condition, the greater number of conduits oriented in the bedding plane allows the system to transmit more fluid along this direction. Additionally, the orientation and arrangements of the conduits in the system is expected to vary during deformations: as the pores are continuously changing their position and shape, the flow network constantly restructures, creating an anisotropic flow condition.

An analysis of the micromechanical descriptors suggests that the resistance to deformation is greatly enhanced when lateral contacts exists. The reduction in strength during the strain softening stage can be related to the loss of contacts in the direction of maximum

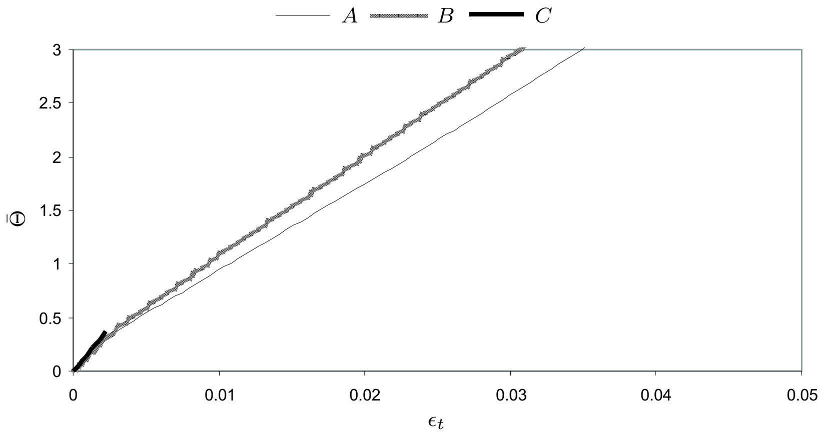

Figure 6.18: Average rotation of the particles

strain.

The results show that the direction of the major principal stress was not coincident with the loading direction for the initial condition where the principal contact normal direction is not coincident with the loading direction. However, after the assembly is slightly deformed, both directions become coincident and remain so with higher deformations.

Finally, the rotation of particles was quantified by means of major axis anisotropy coefficient and the average particle rotation. The higher particle rotation was associated with the development of lower average pore water pressure (lower dilatancy). Therefore, for the initially anisotropic fabric, dilatancy is affected by the angle between the loading direction and the loading plane.

6.6 Introduction to Effects of Conduit Diameter

The hydraulic conductivity (K) is a parameter that characterizes the capacity of a granular medium to transmit water. Liquefaction in the field can be simplified to a problem related to the hydraulic conductivity of the soil. Non-cohesive saturated granular materials may liquefy when pore pressure in localized zones are generated, creating gradients and initiating fluid flow. When the excess pore pressure reaches a value equal to the initial effective stress, liquefaction occurs, and in more severe cases, sand boils develop. The model adopted in the present approach to simulate fluid-flow particle interaction considers that the rate of excess pore pressure increase Δu is the difference between the rate of pore pressure generation Δu^g and the rate of pore pressure dissipation Δu^d (see equation (3.30) in page 64). Experimental data, as well as the results presented in Section 5, have shown that the rate of pore pressure generation is highly dependent on the initial density and the initial confining pressure. Additionally, the rate of pore pressure generation is exclusively a function of the hydraulic conductivity of the soil. Therefore, regardless of the mechanisms that initiate the development of pore pressures, a reduction of the effective stresses can only occur if pore pressures in excess of hydrostatic are not rapidly dissipated (low pore pressure dissipation rate).

A great amount of attention has been given to different factors affecting the mechanisms of pore pressure generation, but little attention has been paid to the relation existing between liquefaction and hydraulic conductivity. Results presented in Section 4.5 demonstrate that the conduit diameter can be related to a hydraulic conductivity representative of the numerical assembly. The ease with which program AQUA can handle different geometries of the flow network motivated the author to examine the effects of the conduit diameter on the the overall behaviour of the assembly.

The following sections address the results of simulated biaxial tests with varying conduit diameters and examines the relationship between conduit diameter and the strength of the idealized systems.

6.7 Test Program and Assembly Characteristics

The results presented in the following sections refer to three biaxial simulations where the conduit diameters were equal to 15, 30, and 50 μm. The assembly was initially confined and brought to equilibrium under an initial confining pressure $\sigma_o^{'} = 50$ kPa. The characteristics of the particles and the flow network are those presented in Tables 5.4 and 5.2, with the exception of the parameters presented in Table 6.2.

Tests	d	$\dot{\epsilon}_{22}$	ω
A	15 μm	0.0005	15
B	30 μm	0.0005	10
C	50 μm	0.0005	10

Table 6.2: Parameters used in the computations

The initial average coordination number and void ratio were $\gamma_o = 4.02$ and $e = 0.209$, the rationale for choosing this density being twofold. First, results of tests presented in the previous sections have shown that coordination numbers of around 4 have both compressive and dilatant characteristics when loaded. This characteristic allows study of the effects of pore pressure forces during the strain softening as well as the strain hardening stages. Second, greater coordination numbers provide a higher particle stability. A number of trial runs were conducted in order to chose optimum parameters for the simulations. It was found that reducing the conduit diameter may considerably increase the magnitude of the transient pore pressure forces acting on the particles, resulting in greater unbalanced forces; thus, choosing a relatively high coordination number helped to maintain static equilibrium at acceptable levels.

6.8 Simulation Results

Figure 6.19 illustrates the variation of strength q with deviatoric strain ϵ_t. The curves show that the strength was noticeably enhanced by the reduction of the conduit diameter. Accordingly, the assembly with the lowest conduit diameter showed, in general, a higher resistance to deformation, captured by the higher peak and pots-peak strengths, a tendency also observed in the stress-strain curves and that becomes more evident at higher deformations. The measured peak strengths and minimum post-peak strengths are presented in Table 6.3, showing that the peak strength of assembly A, was about 7 per cent higher than that of assembly C.

Tests	Peak strength (kPa)	Minimum strength (kPa)
A	16.06	9.61
B	14.95	4.81
C	14.93	4.51

Table 6.3: Measured peak and minimum strengths for varying conduit diameters

It is interesting to note that both specimens B and C showed similar strength characteristics, with both stress-strain curves practically overlapping each other, suggesting that the mechanical response is not considerably affected when high conduit diameters are considered.

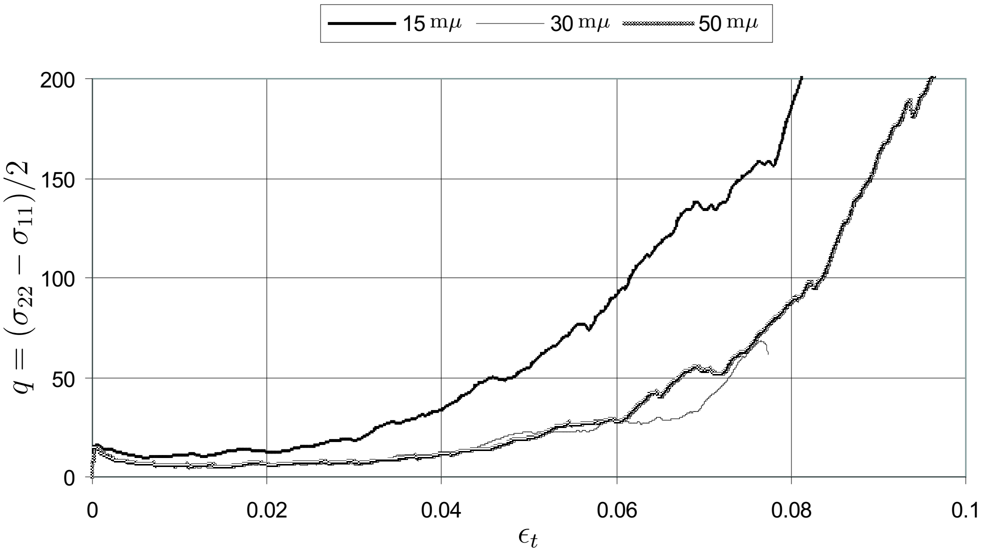

Figure 6.19: Stress-strain curves for varying conduit diameters

The results show in general that the strength of the assembly is enhanced when using lower conduit diameters. An intuitive analysis would suggest that reducing the conduit diameter decreases the ability of the flow network to transmit fluid, and that greater variations in microscopic pressures must develop resulting in higher pore pressure forces acting on the particles. Hence the observed increase in shear resistance would appear to be associated with the development of higher microscopic pressures in the individual pores. This observation was further examined by quantifying the distribution of micro-pressures during deformations, and the spatial arrangement of the pore pressure force-vector at a given time.

An analysis of the microscopic aspects at the particle level and the characteristics of microscopic pore pressures during deformation follows.

6.8.1 Evolution of Micromechanical Parameters

The change of the average coordination number with deformation of the three specimens is shown in Figure 6.20. It is observed that the coordination number decreases considerably at the beginning of the tests, reaching a value near 3.4. Additional strains result in a slight increase in γ reaching a value near 3.5 at the end of the tests. The evolution

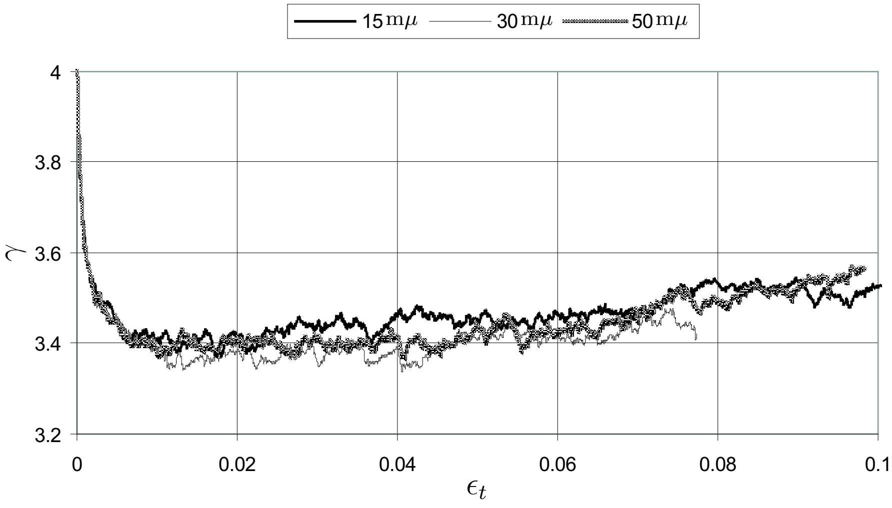

Figure 6.20: Evolution of coordination number for varying conduit diameters

of anisotropy coefficients is presented in Figure 6.21, showing a considerable increase in anisotropy during a short period. The combined reduction in coordination number and the increase in contact normal anisotropy indicate that the majority of contacts are lost in the direction of maximum extensional strain, that is, the lateral direction.

The sudden increase in parameter a_n shows that contact normal forces align in the direction of the major principal stress, when deformation is initiated. However, as deformation continues, a_n remains practically constant and fluctuates around a value of about 0.4. The same observation is applicable to parameter a_t; it initially increases and then stabilizes at a value of about 0.1. For this particular case, the evolution of coefficients a_n and a_t appears to be little affected by the different conduit diameters.

6.8.2 Evolution of Pore Pressures

The evolution of the macroscopic pore pressure normalized with respect to the initial effective confining pressure has been plotted in Figure 6.22. It is observed that the shape of the normalized pore pressure curves is closely related to the stress-strain behaviour. Pore pressures are generated rapidly during the initial stage of deformation, reaching a plateau at a stage where the assemblies exhibit the minimum post-peak strength. As expected, the higher strength exhibited by assembly A is related to the development of

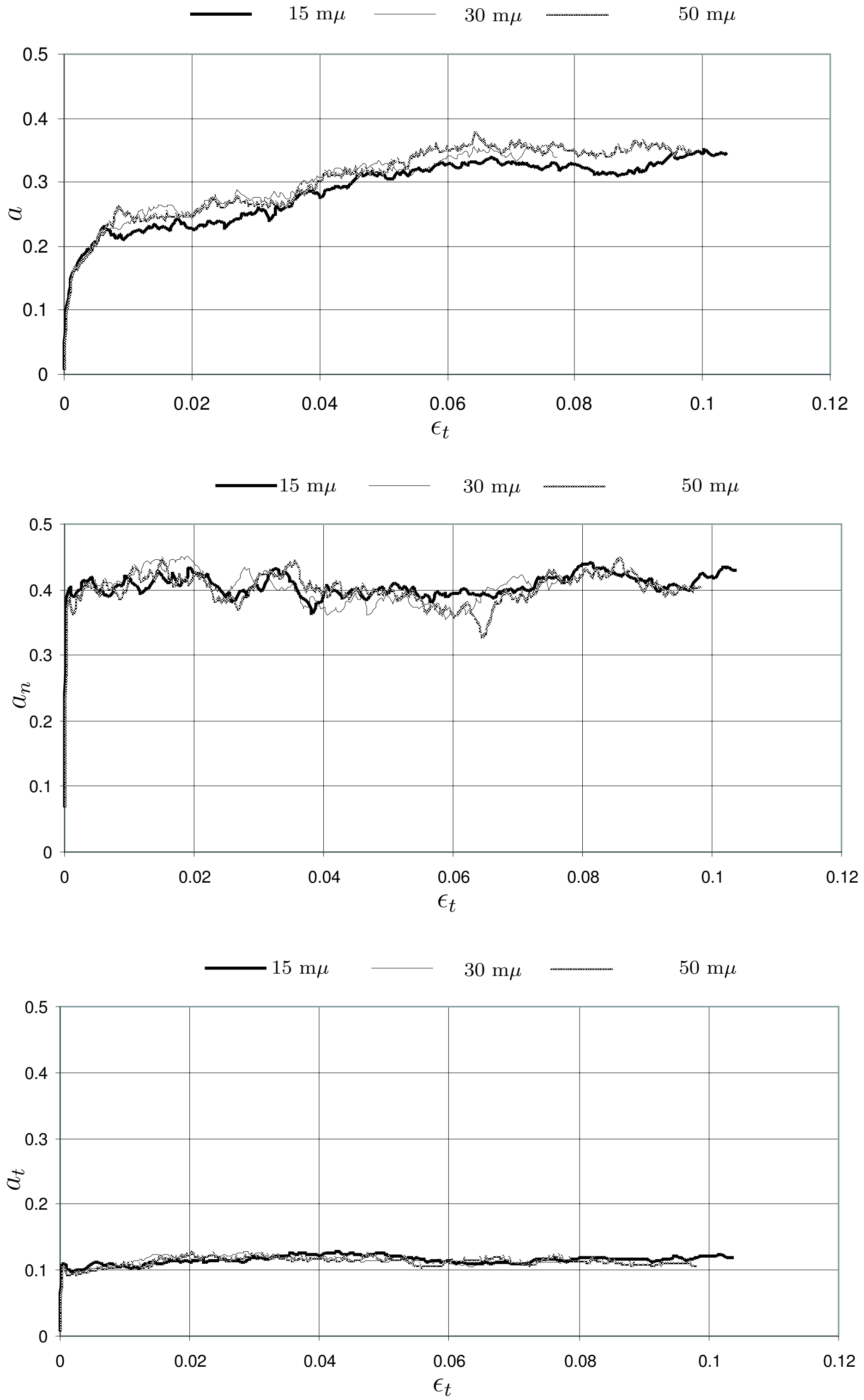

Figure 6.21: Evolution of anisotropy coefficients for varying conduit diameters

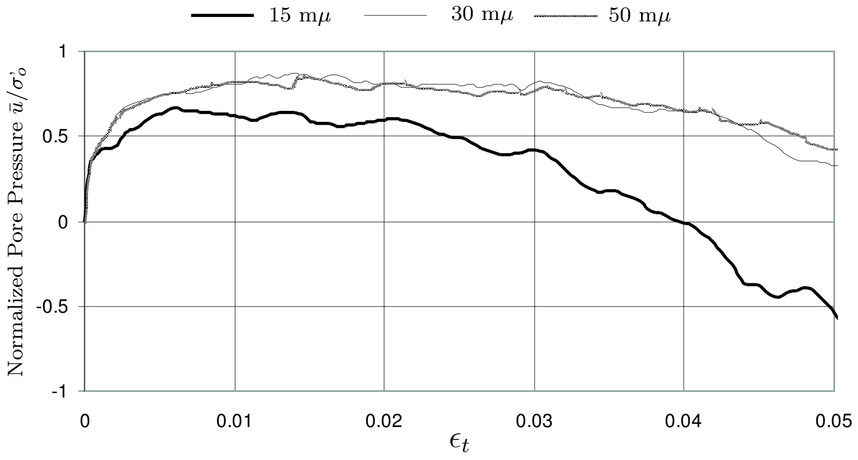

Figure 6.22: Evolution of the normalized pore pressures $\bar{u}/\sigma'_o$, for varying conduit diameters

lower average pore pressures. In general, the evolution of parameter $\bar{u}$ with respect to the stress-strain behaviour of the assembly is in agreement with previous observations made in the laboratory (see Figure 2.2).

The deviation of the microscopic pressures from a mean value can be better understood by evaluating the standard deviation, which provides information on the magnitude of the dispersion, permitting an assessment of how distant the individual pore pressures are from reaching equilibrium. Measurements of pore micro-pressures were taken at different deformation stages, and the standard deviation ($\bar{s}$) of the pressures was computed. The variation of $\bar{s}$ with the deviatoric strain is presented in Figure 6.23.

It is observed that the standard deviation increases with decreasing conduit diameter. The deviations during the range where the specimens presented their lowest strength are considerably greater; this is manifested by spikes in the curves during deformation ranges between $\epsilon_t = 0.01$ and 0.03. The presence of spikes can be seen more clearly in assemblies having diameters of 30 and 50 mμ. The increase in standard deviations during the minimum strength stage indicates that some pores were constantly straining and coalescing with their neighbours, generating micro-pressures that were different than the average value $\bar{u}$. Further, as can be observed in Figure 6.22, the dispersion in micro-pressures is such that the average is maintained constant. This data suggests that two simultaneous processes take place during the transition to more stable states - mainly the creation and disintegration

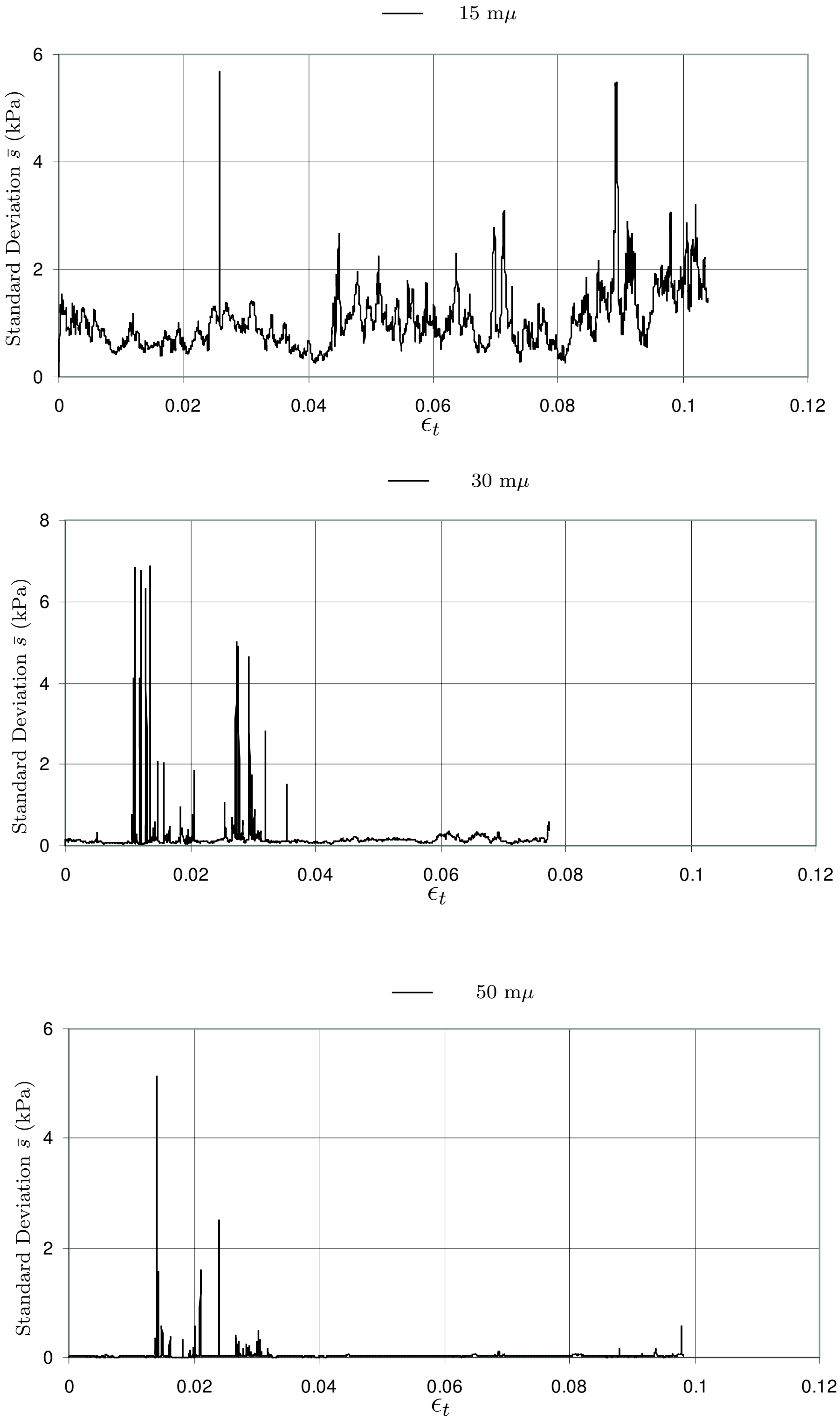

Figure 6.23: Evolution of the standard deviation for varying conduit diameters

of contacts.

The process of contact disintegration would be reflected in a reduction of the coordination number; nevertheless, Figure 6.20 shows that γ does not change considerably during the range where the standard deviations increased, suggesting that when contacts are lost, equilibrium is rapidly restored by the creation of new contacts.

As deformation is continued, the characteristics of the assemblies change from contractive to dilative and negative pore pressures begin to develop. This change is accelerated by lower conduit diameters. Accordingly, assembly A starts to regain strength at a deviatoric strain of about $\epsilon_t = 0.015$, whereas assemblies B and C do so at deviatoric strains of about $\epsilon_t = 0.03$. It is observed that the reduction of standard deviation in assemblies B and C is approximately coincident with the point where the specimens begin to regain strength, an indication that the increasing interparticle forces provided additional stability to the system.

Spatial Distribution of Micro-Pressures

Although the standard deviation proves to be a useful measurement of the degree of pressure dispersion around a mean value, it does not provide information on the spatial distribution of pressures within particular zones. To visualize such distribution, contour plots were constructed from information extracted at different levels of deformation.

The contour plots are presented in Figures 6.24, 6.25; they correspond to strain levels of $\epsilon_t = 0.002$ and 0.01. The gray tones in the contours are related to the pressure magnitudes presented in the scales at the side of the plots. The scales are different for each plot, so a direct comparison between tones is not straightforward. Included in the plots are the pressure histograms corresponding to the contours. In most cases the pressures present a Gaussian type of distribution.

Under the proposed modified DEM scheme, pressures are generated by considering the straining of the pores. The contour plots show that greater pressures tend to concentrate at the centre of the assemblies, where it becomes evident that, in general, greater relative displacements between particles occur. The relative displacements of the particles can be conceived as being the sum of slip and rotation motion. The principal mechanism responsible for the development of higher relative deformations is the biaxial shear mode, which applies compressional axial and extensional lateral loads.

The presence of zones with pressures higher than average results in the development

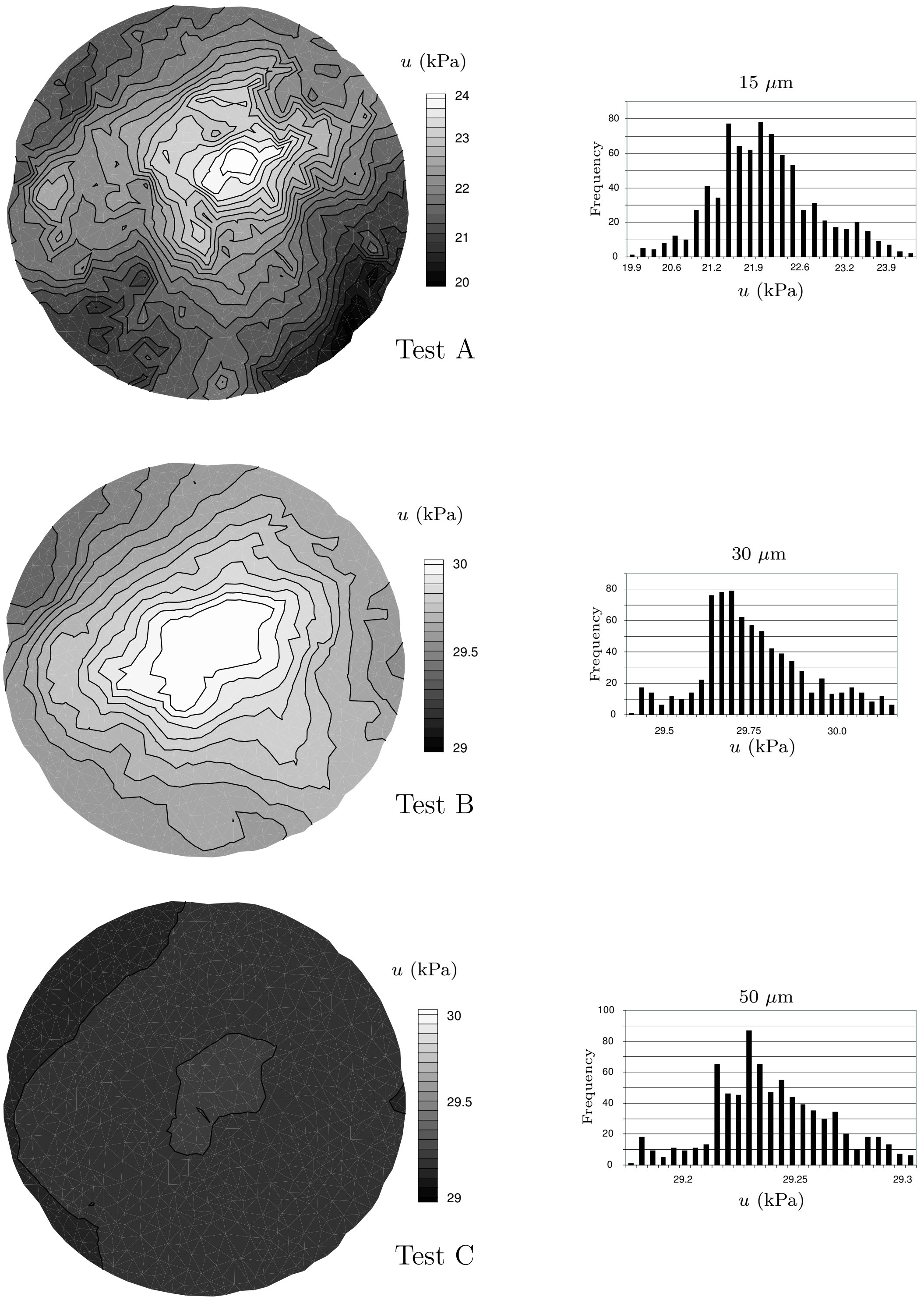

Figure 6.24: Contour showing the distribution of pore pressures at a deviatoric strain of ϵ = 0.002, for varying conduit diameters

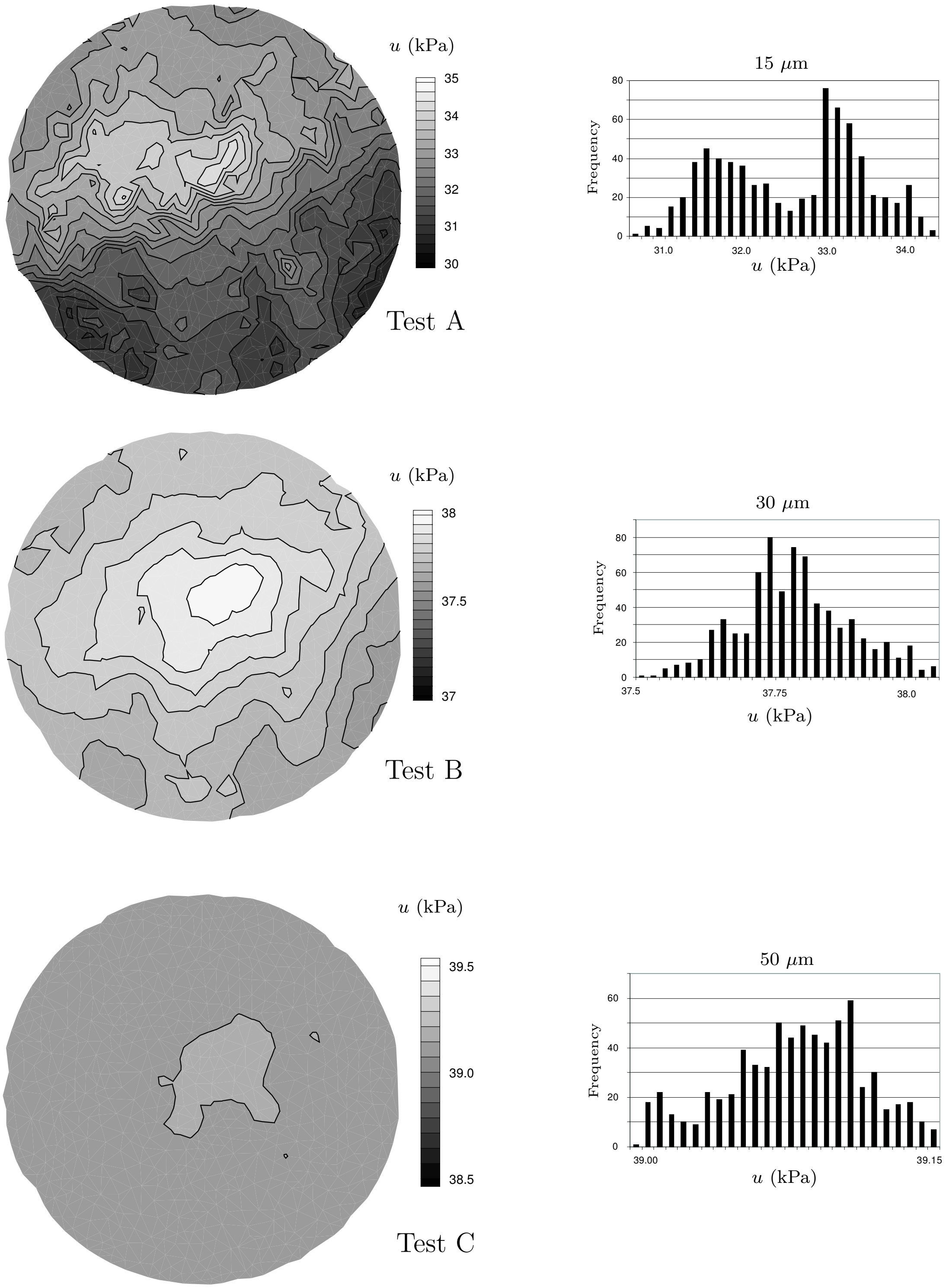

Figure 6.25: Contour showing the distribution of pore pressures at a deviatoric strain of ϵ = 0.01, for varying conduit diameters

of gradients that drive fluid flow from the centre of the assembly towards the boundary. Generally, higher gradients result in higher pore pressure forces on the particles. The results suggest that the additional pore pressure forces create a stiffening effect on the system, resulting in a higher resistance to deformation.

Spatial Distribution of Pore Pressure Forces

To clearly visualize the distribution of pore pressure forces in the assembly, a pore-pressure-force field was constructed, after integrating microscopic pressures around the particles according to relations (3.31) and (3.32). The resulting force field is presented in Figure 6.26; the magnitude of the force vectors is proportional to the force. The corresponding pore pressure contour plot is also presented in the figure.

The data show a general tendency of pore pressure vectors to align themselves towards the boundary. As expected, the direction of the vectors is normal to the contour lines.

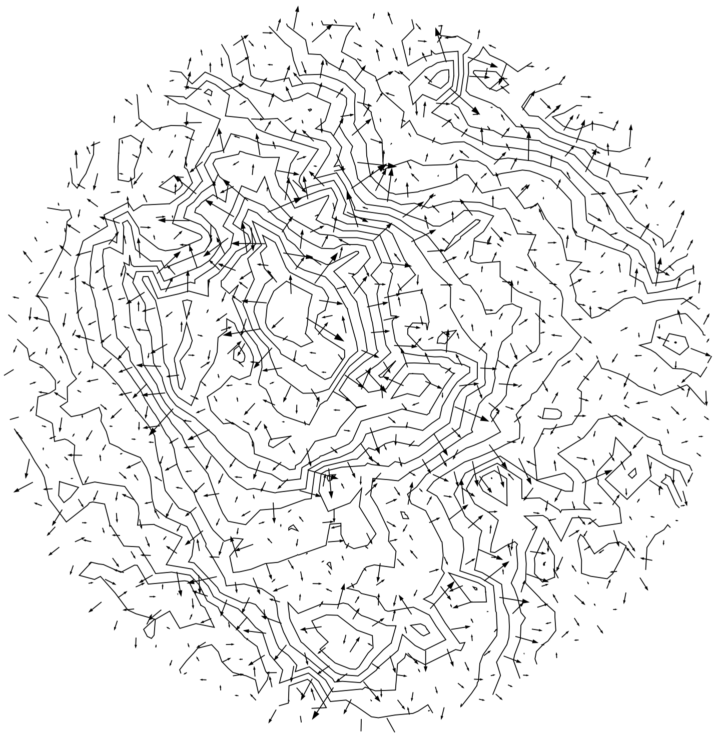

Figure 6.26: Pressure contours and pore pressure force vectors

The information analyzed so far indicates that the higher resistance to deformation observed in the experiments can be attributed to an internal stiffening of the assembly, imposed by the pore pressures concentrated in the centre of the sample.

6.9 Comments

One of the intentions of conducting numerical simulations is to improve knowledge on how real systems behave. In this sense, reducing the diameter of the conduits in the idealized system may be interpreted as decreasing the hydraulic conductivity of a granular soil. It is desirable to find a link between the results obtained from numerical simulations and those obtained from experimental studies. However, a direct comparison between both approaches is not feasible because decreasing the hydraulic conductivity of a soil without altering its fabric represents a hypothetical condition not possible to duplicate in real soils. Nevertheless, information obtained from specialized laboratory tests can be used to asses indirectly the relationship between strength and hydraulic conductivity. At least two laboratory methods can be used to evaluate this relationship:

1. The effects of non-plastic fine particles on liquefaction susceptibility have been evaluated by Yamamuro and Lade [102]. It is well known that fine particles decrease the ability of soil to transmit water. The results obtained from this type of test are not adequate to study the possible effects of the hydraulic conductivity on the global response because the presence of fine particles not only decreases the capacity of the soil to dissipate pore pressures, but also affects its mechanical response. Additionally, the presence of fine particles may considerably alter the packing density because the pore spaces that particles can occupy during deformations become filled by fine particles, producing a more stable structure and reducing the ability of the system to generate pore pressures.

2. The effects of the loading rate on the undrained response of granular soils have been evaluated by Yamamuro and Lade [100]; some of their results are summarized in Figure 2.7. Increasing the loading rate does not affect the hydraulic conductivity of the soil, but it reduces the time in which pore pressures can dissipate. The loading rate however, is known to affect the response of viscous materials such as clays, and to a lower extend the response of sands. Nevertheless, this type of test may be an

adequate point of reference to evaluate the possible effects of hydraulic conductivity on the shear strength.

The results presented by Yamamuro and Lade on tests conducted on Nevada sand showed that increasing the strain rate significantly increases the undrained resistance of the samples. This behaviour has also been reported for undrained tests at high pressures by Yamamuro and Lade [101]. If these type of tests are considered to be representative of the possible effects of the hydraulic conductivity on the undrained strength, the results of the numerical simulations then agree with those obtained from experimentation.

Chapter 7

Conclusions and Recommendations

7.1 General

The objective of this study was to formulate and develop a fluid-flow coupled discrete element model capable of simulating undrained tests. The employed pore pressure generation scheme is essentially the same as reported by Hakuno *et al.* [36] and Hakuno [35]. The fluid flow within the assembly has been simulated by solving a system of differential equations that effectively captures the transient nature of the problem. The proposed technique considers the interactions between fluid and solid particles by converting pore pressure into discrete forces acting on the particle. Different aspects of the code were independently verified. Undrained simulations have proven to realistically mimic the behaviour commonly observed in undrained laboratory experiments.

The results reported in this dissertation should be regarded as the first step in an effort to better understand the mechanisms involved in the process of liquefaction from a micromechanical frame of reference. The solution of the programmed algorithms requires intensive calculations, limiting the number of particles that can be considered. With the advancement of technology, it will be possible to expand this technique to study a number of problems with a greater number of particles loaded under different boundary and initial conditions. It is expected that in the next years, this approach will be widely used to simulate liquefaction problems.

The next section summarizes the adopted approach to the problem and highlights the major conclusions drawn from the undrained simulations of two-dimensional assemblies of idealized granular systems. Section 7.2 presents some recommendations for future research.

7.2 Conclusions

7.2.1 Development of the Fluid-Flow coupled DEM

A fluid-flow coupled DEM programm was developed and used to conduct a number of numerical simulations. The reported results were obtained from undrained tests conducted in an assembly composed of 1000 elliptical particles. The assembly is three-dimensional in principle, although movement of particles is restricted to the plane. The particles interact with each other at contact points; contact forces were calculated using a non-linear contact law, invoking the theory developed by Hertz for three-dimensional solids.

The pores of the assembly were filled by a fluid with elastic properties. Using the individual deformations of the pores and the elastic properties of the fluid, discrete pore pressures were calculated at the pore level. An adequate description of the macroscopic pore pressure present in the assembly is computed using a weighted averaging procedure. Identification of the pores in the assembly was successfully made using the subroutine MAKEPOLYGONS; it constructs polygons that join the centres of particles enclosing the assembly's pores.

Fluid flow between contiguous pores was assumed to take place through conduits of circular cross section. Under this approach, the assembly can be envisaged as a system of reservoirs interconnected by pipes or conduits. The resulting network of conduits was termed the flow network, and transient flow through it has been described by a system of differential equations that is solved in an alternate manner with the force-displacement equations.

The effects of pore water forces acting on the particles have been incorporated in the program. Discrete pore pressures are decomposed into three force components that are subsequently applied to the centroid of each particle. These forces, resulting from pore fluid pressures acting on the particles, have been included in the force-displacement solution.

7.2.2 Verification and Parametric Study

The most fundamental subroutines employed in the simulations have been verified in Chapter 4, obtaining satisfactory results. The major conclusions from the numerical experiments are:

1. The non-linear contact law was first verified by monitoring the relationship between normal and tangential forces during the simulation. The results show that slippage is correctly initiated according to Coulomb's principle. Inter-particle forces were then verified by disturbing one particle from its equilibrium state and monitoring the force-displacement response at one contact. The forces reached a state that was a function of the amount of rotation experienced by the particles. It was demonstrated that the non-linear contact law for the case of elliptical particles produces forces at equilibrium that are a function of the curvature of the ellipses at the point of contact, an effect that is not observed in disc-shaped particles.

2. The results of the pore pressure computations were corroborated with measurements of volumetric strains measured using the boundary displacements. The existing relation between macro pore pressure increments and the volumetric strain measured at the boundary of the assembly,

   $$\Delta\epsilon_v = \frac{B_f}{n}\Delta\bar{u}, \tag{7.1}$$

   was employed for this purpose. The numerical simulation provided results that compare favorably with the values computed using relation (7.1). The equation further demonstrates that a given increment of pore pressure is always accompanied by a macroscopic deformation which is directly proportional to the porosity of the specimen and inversely proportional to the bulk modulus of the fluid.

3. The flow-network approach to simulate the combined effects of pore pressure generation and dissipation has proven to be effective. Qualitative comparisons were made with Terzaghi's one dimensional theory of consolidation to validate the pressure dissipation scheme. The results have shown that the model is capable of simulating two-dimensional pressure dissipation problems under a number of initial and boundary conditions.

After verification of the principal routines, simulations were conducted to study the effect of different parameters on the macroscopic response of the system of 1000 elliptical particles. The following conclusions are made from the results:

1. The results from simulations showed that varying the conduit diameter influences the macroscopic response of the planar assembly of elliptical particles. In general, reducing the conduit diameter increases the macroscopic strength of the sample. The reasons for this behaviour were examined using the distribution of discrete pore pressures within the sample and the resulting pore pressure forces acting on the particles. Zones of higher pressure concentrated in the centre of the assembly, where higher relative displacements occur as a result of the characteristics of the deformation field. The higher relative displacements at the centre of the assembly resulted in flow gradients directed from the centre towards the boundary. The direction of pore pressure force vectors coincides with that of the pressure gradients, producing stiffening effect on the sample. The spatial deviation of discrete pressures from the macroscopic average was measured by computing the standard deviation. The evolution of this parameter clearly shows the presence of peaks when the specimen is deforming at its lowest strength. During this deformation stage, the average coordination number remains practically constant while contact anisotropy develops. This result suggest that the rates of contact creation and disintegration should be approximately the same.

2. The conduit diameter required to match the macroscopic permeability of the assembly was such that pressure equalization occurred almost instantaneously during the simulations, reducing the effect of pore pressure forces acting on the particles.

3. The effect of fluid compressibility was evaluated in the last part of Chapter 4. The compressibility of the fluid was varied in an attempt to simulate the effect of different degrees of saturation. It was found that the void ratio remained practically constant during the experiment when the assembly was assumed to be 100 % saturated.

7.2.3 Results of Undrained Simulations

Simulations of undrained biaxial tests in idealized assemblies of elliptical particles have been successfully conducted. The boundary was controlled by a servo mechanism to simulate undrained biaxial compression tests. Accordingly, an axial constant strain rate was used while maintaining the lateral total stress constant. Conclusions drawn from analysis of the results are presented below:

1. The initial confining pressure was found to have an effect on the peak strength of the specimens. For a fixed initial void ratio, increasing the confining pressure results in higher peak strengths.

2. Numerical results showed that the initial density greatly influences the macroscopic stress-strain response. The denser assemblies presented a post-peak strain-hardening response, whereas the loosest assemblies presented a strain-softening and, finally, an unstable behaviour. In general, for a fixed initial confining pressure, increasing the density results in higher peak strengths.

3. A fundamental parameter that quantifies the average number of contacts per particle is the average coordination number (γ). Common to all numerical experiments is the initial reduction in average coordination number upon shearing. The evolution of contact anisotropy shows that most of the contacts are lost in the lateral direction, as the servo mechanism tries to maintain the total horizontal effective stress constant. Depending on the initial coordination number, the process of contact disintegration can be such that the assembly reaches the minimum value of γ required to maintain equilibrium ($\gamma \approx 3.1$), resulting in an imminent failure or collapse.

4. The results of numerical simulations showed that the evolution of anisotropy coefficients a, a_n, and a_t were very similar for assemblies presenting the same initial coordination number. These results suggest that, for these particular cases, the initial confining pressure does not have a considerable effect in the evolution of the anisotropy coefficients. The results can serve as an aid to develop micromechanical-based constitutive models like the one proposed by Wan and Guo [98].

5. A strong correlation between the strength of the specimen (q) and the normal contact force average ($\bar{f}^o$) was observed in all numerical experiments. The latter is a direct measurement of the effective state of stress present in the sample. The results show that in general, at a certain deformation stage, the characteristics of the assembly changes from contractive to dilative. This tendency is globally reflected in the stress-strain curve, as it changes its behaviour from strain-softening to strain-hardening, as well as in the development of negative pore pressures. Since the assembly is compelled to remain at a constant volume, the volume reduction tendency leads to the

development of elastic interparticle deformations and consequently higher interparticle forces.

6. Developments presented in Chapter 2 showed that the stress tensor could be approximated by an expression containing averages of contact normal vectors, contact vectors, and force vectors over groups of similar orientation. Assuming coaxiality of the functions describing the contact information, the following expression was derived:
$$q = \frac{\sigma_{22} - \sigma_{11}}{2} \approx \frac{m_v \, \bar{l}^o \, \bar{f}^o}{4} \left\{ \frac{a + a_n + a_t}{2} \right\} \tag{7.2}$$
Results of numerical simulations showed this expression satisfactorily predicts the observed strength.

7. The macroscopic stress-strain behaviour of numerical assemblies was observed to be dependent on the magnitude of the values assigned to the coefficient of interparticle friction μ. The results show that in general the tests with higher μ were stiffer and exhibit higher shear strength. It was found that the post peak stress-strain behaviour changed from strain-softening to strain-hardening when μ was varied from 0.55 to 0.95. It was found that dilatancy is increased by higher interparticle friction coefficients. A relation between the increment of pore pressure and dilatancy was then presented and it was concluded that the observed increase in undrained resistance could be attributed to the enhancement of dilatancy by higher values of μ.The previous experimental findings have a practical value, since they suggest that liquefaction of sands may be inhibited by slightly increasing the friction between grains.

8. A quantitative comparison between volume-controlled simulations and tests using the proposed fluid-flow scheme was presented. Both approaches provided similar results. However, results presented in Section 6.6 suggest that different results are expected to be obtained when lower conduit diameters are considered. Accordingly, by reducing the diameter of the flow-network conduits, the interaction between the pore fluid and the mechanical response of the particles is increased, and the overall response of the system is considerably altered.

7.2.4 On Principal Stress Rotation

One of the objectives of the study was to utilize the code to highlight the response of an initial anisotropic assembly under rotation of the principal stresses. Section 6 contains the results of samples sheared by rotating the principal stresses with respect to the bedding plane. The following conclusions have been drawn.

1. The results of simulations on initially anisotropic samples of elliptical particles have shown that the direction of the principal stress with respect to the bedding plane has an important effect on the stress-strain characteristics of the assembly.

2. An analysis of the interparticle force distribution showed that boundary loads are internally transmitted through chains of contacts that align with the direction of the principal stress.

3. In general, the idealized assembly behaved in a stiffer fashion when the direction of major principal stress was coincident with the bedding plane. The greater number of contacts available in the direction perpendicular to the major stress initially provide a higher stability. However, as lateral contacts are lost with subsequent deformation, internal instabilities are generated, leading to an internal failure of the structure.

4. It has been shown that the state of stresses and coordination number are not sufficient descriptors of the deformation mechanisms. A complete micromechanical description requires consideration of parameters of anisotropy a, a_n, a_t and average contact forces.

5. The distribution of the long axes of the particles was approximated by a truncated Fourier series. Particles initially having vertical or sub-vertical long-axis orientation developed larger moments in their long axis and smaller moments in the perpendicular direction. The moment imbalance and the evolution of the system towards more stable states causes the particles to rotate to a position were the long axis is perpendicular to the loading direction. A tendency of particles to rotate mobilized higher strengths, reflected in the stress-strain behaviour of the assembly.

7.2.5 Permeability Effects

Numerical simulations using the fluid-flow coupled DEM method offer the possibility to examine the micromechanical behaviour of idealized assemblies of elliptical particles in great detail. Of special interest to the mechanisms of undrained deformation is the development and subsequent evolution of microscopic fluid pressures at the pore level. A number of simulations have been conducted to study the effect of varying conduit diameters on the response of the assemblies and the characteristics of the micro-pressures within the system. Some of the results and observations are summarized as follows:

1. The results show that decreasing the diameters of the conduits results in the development of higher resistance to deformation, as captured by the stress-strain curves. An analysis of the pore pressure distributions revealed that a zone where pore pressures are higher than the average develops at the centre of the assembly. The localized pressures resulted in higher gradients that drove fluid flow from the centre of the assembly towards the boundary, increasing the pore pressure forces on the particles, and, in general, enhancing the strength of the assembly.

2. The dispersion of micro-pressures with respect to the mean macroscopic value was examined using the standard deviation. The evolution of the standard deviation revealed the development of higher dispersions at the stage where the assemblies presented their lowest post-peak strength. It was further observed that the pressure dispersion decreases as the assemblies gradually regain strength with deformation. This behaviour was attributed to the creating of more stable structures resulting from higher interparticle forces.

3. An analysis of the direction of the pore pressure forces was conducted using a force vector plot. The plot showed that force vectors are in general perpendicular to the pressure contours and directed towards the boundary, producing a stiffening effect in the system. These behaviour is probably related to non-linear effects resulting from the type of contact law used in the simulations.

7.3 Applicability and Recommendations

The following comments list some recommendations for future research and the applicability of the developments presented in this dissertation.

- Efforts should be directed at improving computational efficiency. The adaptive dynamic relaxation technique (ADR) proposed by Bardet and Proubet [5] is an attractive method; it may improve particle stability and reduce the computational time by selecting optimum values for the damping coefficients and producing faster convergence rates. Implementing this method may eliminate the trial and error procedure required in the selecting suitable damping coefficients.

- The coupling of the fluid with the mechanical system was successfully achieved by considering the transient nature of the problem. It was shown that the fluid flow network by itself adequately simulates classical transient problems encountered in geotechnical engineering (*i.e.*, consolidation phenomena). The method could be further expanded to study the mechanisms of consolidation.

- A different kind of constitutive relation for the bulk modulus of the fluid is needed. The present implementation assumes that the fluid has the same elastic properties both in compression and tension. This assumption is obviously incorrect, as the fluid is capable of taking an infinite amount of tension. Thus the effects of cavitation should be further examined.

- The effect of different degrees of saturation could be simulated considering two-phase fluid flow. Additionally, the effective forces provided by the menisci could be incorporated assuming a bounding forces at the contacts.

- In real materials, plastic deformations at the contacts can be generated at low confining stresses. A non linear elasto-plastic contact law can be incorporated in the program with minor modifications, and the effects of such type of contact law on the overall stress-strain response may be further examined.

- Experimental results shows that dense sands tested undrained in the triaxial test exhibit a strain-hardening response and eventually reach a *steady state* at large deformations [40]. Such steady state was never reached in the assemblies tested. The combined effects of grain crushing, elasto-plastic contact law and fluid cavitation may be responsible for the steady state of deformation observed in real sands. These mechanisms should be incorporated in the model to define a steady state line for the assemblies of elliptical particles. The steady state concepts can further be examined using micromechanical descriptors. The void ratio in the state diagram should be replaced by the coordination number, leading to a more comprehensive understanding of residual strength at large deformations. Such approach has already been adopted in drained simulations leading to satisfactory results [72].

Bibliography

[1] F. S Acton. *Numerical Methods That Work*. Mathematical Association of America, corrected edition edition, 1990.

[2] A. Alarcón-Guzmán. *Cyclic stress-strain and liquefaction characteristics of sands.* PhD thesis, Purdue University, August 1986.

[3] A. Alarcón-Guzmán and G. A. Leonards. Discussion of *L*iquefaction evaluation procedure, by S. J. Poulos, G. Castro and J. W. France. *Journal of Geotechnical Engineering*, 114(2):232–236, 1988.

[4] A. Alarcón-Guzmán, G. A. Leonards, and J. L. Chameau. Undrained monotonic and cyclic strength of sands. *Journal of the Geotechnical Engineering Division, ASCE*, 114(10):1089–1109, 1988.

[5] J. P. Bardet and J. Proubet. Adaptative dynamic relaxation for statics of granular materials. *Computers and Structures*, 39(3/4):221–229, 1991.

[6] R. Bathurst. *A study of stress and anisotropy in idealized granular assemblies.* PhD thesis, University of Waterloo, Waterloo, Ontario, 1985.

[7] K. Been and M. G. Jefferies. A state parameter for sands. *Géotechnique*, 35(2):99–112, 1985.

[8] K. Been, M. G. Jefferies, and J. Hachey. The critical state of sand. *Géotechnique*, 41(3):365–381, 1991.

[9] J. M. Bolton, D. S. Dunford, and W. A. Charlie. One dimensional shock and quasi-static liquefaction of silt and sand. *Journal of Geotechnical Engineering*, 120(10):1874–1889, 1994.

[10] R. W. Brankin, I. Gladwell, and L. F. Shampine. Rksuite: a suite of runge-kutta codes for the individual value problem of odes. Softreport 91-1, Math. Dept., Southern Methodist University, Dallas, Texas, U.S.A., 1991.

[11] A. Casagrande. Liquefaction and cyclic deformation of sands, a critical review. *Proceeding of the 5th International Conference on Soil Mechanics and Foundation Engineering*, 5:79–133. Buenos Aires, Argentina.

[12] A. Casagrande. Characteristics of cohesionless soils affecting the stability of earth fills. In *Contributions to soil mechanics 1925-1940*, pages 257–276. Boston Society of Civil Engineers, 1936.

[13] G. Castro. *Liquefaction of Sands*. PhD thesis, Harvard University, Cambridge, Mass., January 1969.

[14] G. Castro. Liquefaction and cyclic mobility of saturated sands. *Journal of the Geotechnical Engineering Division, ASCE*, 101(GT6):551–569, 1975.

[15] G. Castro, J. L. Enos, J. W. France, and S. J. Poulos. Liquefaction induced by cyclic loading. Technical Report No. NSF/CEE-82018, Report to National Science Foundation, Washington, DC, 1982.

[16] G. Castro and S. J. Poulos. Factors affecting liquefaction and cyclic mobility. *Journal of the Geotechnical Engineering Division, ASCE*, 103(GT6):501–516, 1977.

[17] C. S. Chang and J. Gao. Kinematic and static hypotheses for constitutive modelling of granulates particle rotation. *Acta Mechanica*, 115:213–229, 1996.

[18] C. S. Chang and C. L. Liao. Estimates of elastic modulus for media of randomly packed granules. *Applied Mechanics Review*, 47(1):S197–S206, 1994. Part 2.

[19] K. Chantawarangul. *Numerical Simulations of Three-Dimensional Granular Assemblies*. PhD thesis, University of Waterloo, Waterloo, Ontario, 1993.

[20] J. Christoffersen, M. M. Mehrabadi, and S. Nemat-Nasser. A micromechanical description of granular material behaviour. *Journal of Applied Mechanics*, 48:339–344, 1981.

[21] P. A. Cundall. Computer simulations of dense sphere assemblies. In M. Satake and J. T. Jenkins, editors, *Proc. US/Japan Seminar on the Micromechanics of Granular Material*, pages 113–123, Amsterda, 1987. North-Holland, Amsterdam.

[22] P. A. Cundall. Computer simulations of dense sphere assemblies. In M. Satake and J. T. Jenkins, editors, *Proceedings of the U.S./Japan Seminar on the Micromechanics of Granular Materials*, pages 113–123, North-Holland, Amsterdam, 1987.

[23] P. A. Cundall and O. D. L. Strack. A discrete numerical model for granular assemblies. *Géotechnique*, 29(1):47–65, 1979.

[24] P. Dantu. Contribution á l'étude mécanique et géometriquedes milieux pulvérulents. In *Proceedings of the 4th International Conference on Soil Mechanics and Foundation Engineering*, volume 1, page 144, London, 1957.

[25] B. M. Das. *Advanced Soil Mechanics.* Taylor and Francis, 1983.

[26] G. De Josselin de Jong and A. Verruijit. Etude photo-élastique d'un empilement de disquetes. *Cah. Grpe fr. Etu. Rhéol*, 2:73–86, 1969.

[27] J. Desrues, R. Chambon, Mokni M., and F. Mazerolle. Void ratio evolution inside shear bands in triaxial sand specimens studied by computed tomography. *Géotechnique*, 46(3):529–546, 1996.

[28] A. Mohamad R. Dobry, R. Vasquez-Herrera and M. Vuvetic. Liquefaction flow failure os silty sand by torsional cyclic tests. In *Advances in the art of testing soils under cyclic conditions*, pages 29–50. ASCE, 1985.

[29] P. Dubujet and F. Dedecker. Micro-mechanical analysis and modelling of granular materials loaded at constant volume. *Granular Matter*, 1:129–136, 1998.

[30] F. A. L. Dullien. *Porous media : fluid transport and pore structure.* Academic Press, New York : Toronto, 2nd edition, 1991.

[31] A. Džiugys and B. Peters. A new approach to detect the contact of two-dimensional elliptical particles. *Int. J. Numer. Anal. Meth. Geomech.*, 25:1487–1500, 2001.

[32] R. J. Finno, W. W. Harris, M. A. Mooney, and G. Viggiani. Strain localization and undrained steady state of sand. *Journal of Geotechnical Engineering*, 122(6):462–473, 1996.

[33] J. A. Franklin and M. B. Dusseault. *Rock Engineering*. Mc Graw Hill, 1989.

[34] R. A. Freeze and J. A. Cherry. *Ground Water*. Englewood Cliffs, Prentice Hall, NJ, USA, 1979.

[35] M. Hakuno. Simulation of the dynamic liquefaction of sand. In Ishihara, editor, *Earthquake Geotechnical Engineering*, pages 857–862, Rotterdam, 1995. Balkema.

[36] M. Hakuno and Y. Tarumi. Sand liquefaction analysis by granular assembly simulation. In *Proceedings of Ninth World Conference on Earthquake Engineering*, volume 8, pages 231–236, Tokyo, Japan, August 1988.

[37] A. Hazen. Hydraulic-fill dams. *ASCE Transaction*, 83:1713–1745, 1920.

[38] A. B. Huang, H. H. Hsu, and J. W. Chang. The behavior of a compressible silty fine sand. *Canadian Geotechnical Journal*, 36(1):88–101, 1999.

[39] M. A. Ioannidis and I. Chatzis. Network modelling of pore structure and transport properties of porous media. *Chemical Engineering Science*, 48(5):951–972, 1993.

[40] K. Ishihara. Liquefaction and flow failure during earthquakes. *Géotechnique*, 43(3):351–415, 1993.

[41] K. Ishihara, F. Tatsuoka, and S. Yasuda. Undrained deformation and liquefaction of sand under cyclic stresses. *Soils and Foundations*, 15(1):29–44, 1975.

[42] K. Ishihara and I. Towhata. Sand response to cyclic rotation of principal stress directions as induced by wave loads. *Soils and Foundations*, 23(4):11–26, 1983.

[43] E. Juárez Badillo and A. Rico Rodriguez. *Mecánica de Suelos*, volume 1. Limusa, third edition, 1996.

[44] Y. Kishino. Quasi-static simulation of liquefaction phenomena in granular materials. In S. Ishisaka, editor, *Second International Symposium for Science on Form*, pages 157–174, Tokyo, 1990. KYK Scientific Publishers.

[45] J.M. Konrad. Sand state from cone penetration tests: a framework considering grain crushing stress. *Géotechnique*, 48(2):201–215, 1998.

[46] P. V. Lade and D. Pradel. Instability and plastic flow of soils. i: Experimental observations. *Journal of Engineering Mechanics*, 116(11):2532–2550, 1990.

[47] K. T. Law, Cao L., and N. G. He. An energy approach for assessing seismic liquefaction potential. *Canadian Geotechnical Journal*, 27:320–329, 1990.

[48] J. Lindenberg and H. L. Koning. Critical density of sand. *Géotechnique*, 31(2):231–245, 1981.

[49] G. R. Martin, W. D. L. Finn, and H. B. Seed. Fundamentals of liquefaction under cyclic loading. Technical report.

[50] K. Meguro and N. Ravichandran. 3-dimensional distinct element simulation of liquefaction phenomena. *Bulletin of Earthquake Resistant Structure Research Center*, (34):99–106, 2001.

[51] R. Mohamad and R. Drobry. Undrained monotonic and cyclic strength of sand. *Journal of the Geotechnical Engineering Division, ASCE*, GT10(112):941–958, 1986.

[52] J. P. Mulilis, C. K. Chan, and H. B. Seed. The effects of method of sample preparation on the cyclic stress-strain behaviour of sands. Report EERC 75-18, University of California, Berkeley, July 1975.

[53] H. Nakase, T. Takeda, and M. Oda. A simulation study on liquefaction using DEM. In Sêco e Pinto, editor, *Earthquake Geotechnical Engineering*, pages 637–642, Rotterdam, 1999. Balkema.

[54] D. Negussey, W. K. D. Wijewickreme, and Y. P. Vaid. Constant-volume friction angle for granular materials. *Canadian Geotechnical Journal*, 25:50–55, 1988.

[55] T. T. Ng and N. Dobry. A non-linear numerical model for soil mechanics. *International Journal for Numerical and Analytical Methods in Geomechanics*, 16:247–263, 1992.

[56] T. T. Ng and N. Dobry. Numerical simulations of monotonic and cyclic loading of granular soil. *International Journal for Numerical and Analytical Methods in Geomechanics*, 120(2):388–403, 1994.

[57] K. Nubel. Particle shape effect in stress-force-fabric relationship for granular media. Master's thesis, University of Waterloo, 1996.

[58] K. Nübel and L. Rothenburg. Particle shape effect in stress-force-fabric relationship for granular media. *Journal of the Mechanical Behavior of Materials*, 7(3):219–233, 1996.

[59] M. Oda. Deformation mechanism of sand in triaxial compression test. *Soils and Foundations*, 12(4):45–63, 1972.

[60] M. Oda and K. Iwashita. *Mechanics of Granular Materials, An Introduction.* A. A. Balkema, 1999.

[61] M Oda and H. Kazama. Microstructure of shear bands and its relation to the mechanisms of dilatancy and failure of dense granular soils. *Géotechnique*, 48(4):465–481, 1998.

[62] M. Oda, I. Koishikawa, and T. Higuchi. Experimental study of anisotropic shear strain of sand by plane strain test. *Soils and Foundations*, 18(1):25–38, 1978.

[63] H. Ouadfel. *Numerical simulations of granular assemblies with three-dimensional ellipsoid-shaped particles.* PhD thesis, University of Waterloo, Waterloo, Ontario, Canada, 1998.

[64] S. J. Poulos. Steady state of deformation. *Journal of the Geotechnical Engineering Division, ASCE*, 107(GT5):553–562, 1981.

[65] J. H. Prevost. A simple plasticity theory for frictional cohesionless soils. *Soil Dynamics and Earthquake Engineering*, 4(1):9–17, 1985.

[66] P. K. Robertson and Wride C. E. Evaluating cyclic liquefaction potential using the cone penetration test. *Canadian Geotechnical Journal*, 35:442–459, 1998.

[67] K. H. Roscoe and H. B. Pooroshasb. A fundamental principle in similarity in model tests for earth pressure problems. In *Proceedings, 2nd Asian Regional Conference on Soil Mechanics*, volume 1, pages 134–140, Tokyo, 1963.

[68] L. Rothenburg. *Micromechanics of idealized granular systems.* PhD thesis, Carleton University, Ottawa, Ontario, Canada, 1980.

[69] L. Rothenburg and R. J. Bathurst. Numerical simulation of idealized granular assemblies with plane elliptical particles. *Computers and Geotechnics*, 11:315–329, 1991.

[70] L. Rothenburg and R. J. Bathurst. Micromechanical features of granular assemblies with planar elliptical particles. *Géotechnique*, 42(1):79–95, 1992.

[71] L. Rothenburg and R. J. Bathurst. Influence of particle eccentricity on micromechanical behavior of granular materials. *Mechanics of Materials*, 16:141–152, 1993.

[72] L. Rothenburg and N. P. Kruyt. Micromechanical study of critical state in granular materials. In K. Bagi, editor, *Proceedings of the QuaDPM workshop*, pages 203–212, Budapest, Hungary, 2003.

[73] L. Rothenburg, E. L. Matyas, and S. Z. Ambrus. Statistical aspects of flow in a random network of channels. *Stochastic Hydrology and Hydraulics*, 1(3):217–240, 1987.

[74] P. W. Rowe, L. Barden, and K. Lee. Energy components during the triaxial cell and direct shear tests. *Géotechnique*, 14(3):245–261, 1964.

[75] A. D. Saada, G. Fries, and C.-C. Ker. An evaluation of laboratory testing techniques in soil mechanics. *Soils and Foundations*, 23(2):98–112, 1983.

[76] C. Santamarina, K. Klein, and M. Fam. *Soils and Waves.* Wiley, 2001.

[77] M. Satake. Constitution of mechanics of granular materials through the graph theory. In *U.S.-Japan Seminar on Continuum-Mechanics and Statistical Approaches in the Mechanics of Granular Materials*, pages 47–62S, Tokyo, 1978.

[78] M. A. Schofiel and C. P. Wroth. *Critical state soil mechanics.* McGraw-Hill Book Co., New York, N. Y., 1968.

[79] E. T. Selig and C. S. Chang. Soil failure modes in undrained cyclic loading. *Journal of the Geotechnical Engineering Division, ASCE*, GT5(?):539–551, 1981.

[80] S. Sivathayalan and Y. P. Vaid. Influence of generalized initial state and principal stress rotation on the undrained response of sands. *Canadian Geotechnical Journal*, (39):63–76, 2002.

[81] A. E. Skinner. A note on the influence of interparticle friction on the shearing strength of a random assembly of spherical particles. *Géotechnique*, 19:150–157, 1969.

[82] J. A. Sladen, R. D. D'Hollander, and J. Krahn. The liquefaction of sands, a collapse surface approach. *Canadian Geotechnical Journal*, (22):564–578, 1985.

[83] M. R. Spiegel. *Applied Differential Equations.* Prentice-Hall, third edition, 1981.

[84] O. D. L Strack and P. A. Cundall. The distinct element method as a tool for research in granular media. Report ENG 76-20711, National Science Foundation, Dept. Civil and Mining Eng., University of Minnesota, 1978.

[85] M. J. P. R. Symes, A. Gens, and D. W Hight. Undrained anisotropy and principal stress rotation in saturated sand. *Géotechnique*, 34(1):11–27, 1984.

[86] D. W. Taylor. *Fundamentals of soil mechanics.* Wiley and Sons, 1948.

[87] K. Terzaghi and R.B. Peck. *Soil Mechanics in Engineering Practice.* John Wiley & Sons, 1948.

[88] S. Thallak. *Numerical simulation of hydraulic fracturing in granular media.* PhD thesis, University of Waterloo, 1991.

[89] C. Thornton. Micromechanics of elastic sphere assemblies during 3d shear. In *Workshop on Mechanics and Statistical Physics of Particulate Materials, Institute for Mechanics and Materials Report*, number 94-9, pages 64–67. University of California, San Diego, 1994.

[90] C. Thornton and W. C. Randall. Applications of theoretical contact mechanics to solid particle system simulation. In M. Satake and J. T. Jenkins, editors, *Proceedings of the U.S./Japan Seminar on the Micromechanics of Granular Materials*, pages 133–142, North-Holland, Amsterdam, 1988.

[91] J. M. Ting, M. Khwaja, L. Meachum, and J. D. Rowell. An ellipse-based discrete element model for granular materials. *International Journal for Numerical and Analytical Methods in Geomechanics*, 17:603–623, 1993.

[92] M. Uthayakumar and V. P. Vaid. Static liquefaction of sand under multiaxial loading. *Canadian Geotechnical Journal*, 35:273–283, 1998.

[93] and Sivathayalan S. Vaid, Y. P. Fundamental factors affecting liquefaction susceptibility of sands. *Canadian Geotechnical Journal*, 37:592–606, 2000.

[94] Y. P. Vaid and J. C. Chern. Effect of static shear on resistance to liquefaction. *Soils and Foundations*, 23(1):47–60, 1983.

[95] Y. P. Vaid and J. C. Chern. Cyclic and monotonic undrained response of saturated sands. In *Advances in the art of testing soils under cyclic conditions*, pages 120–147. ASCE, 1985.

[96] R. Verdugo. *Characterization of sandy soil behavior under large deformation.* PhD thesis, University of Tokyo, 1992.

[97] R. Verdugo and K. Ishihara. The steady state of sandy soils. *Soils and Foundations*, 36(2):81–91, 1996.

[98] R. G. Wan and P. J. Guo. Effects of microstructure on undrained behaviour of sands. *Canadian Geotechnical Journal*, 38:16–28, 2001.

[99] H. Xia and T. Hu. Effects of saturation and back pressure on sand liquefaction. *Journal of Geotechnical Engineering*, 117(9):1347–1362, 1991.

[100] Y. Yamada and K. Ishihara. Undrained deformation characteristics of sand in multi-directional shear. *Soils and Foundations*, 23(1):61–79, 1983.

[101] J. A. Yamamuro and P. V. Lade. Effects of strain rate on instability of granular soils. *Geotechnical Testing Journal*, 16(3):304–313, 1993.

[102] J. A. Yamamuro and P. V. Lade. Effects of non-plastic fines on static liquefaction of very loose sand. *Canadian Geotechnical Journal*, 34:918–928, 1997.

[103] J. A. Yamamuro and P. V. Lade. Steady-state concepts and static liquefaction of silty sands. *Journal of Geotechnical and Geoenvironmental Engineering, ASCE*, 124(9):868–877, 1998.

[104] S. Yimsiri and K. Soga. Application of micromechanics model to study anisotropy of soils at small strains. *Géotechnique*, 42(5):15–26, 2002.

[105] M. Yoshimine and Ishihara. Flow potential of sand during liquefaction. *Soils and Foundations*, 38(3):189–198, 1998.

[106] M. Yoshimine and W. Ishihara, K.and Vargas. Effects of principal stress direction and intermediate principal stress on undrained shear behavior of sand. *Soils and Foundations*, 38(3):179–188, 1998.

[107] T. L. Youd, I. M. Idriss, and *et al.* . Liquefaction resistance of soils: Summary report from the 1996 nceer and 1998 nceer/nsf workshops on evaluation of liquefaction resistance of soils. *Journal of Geotechnical and Geoenvironmental Engineering*, 127(10):817–833, 2001.

Nomenclature

$(\boldsymbol{F}_i)_N$	translational force acting at the particle's centroid
$(D_n)_N$	normal contact damping force component
$(D_s)_N$	tangential contact damping force component
$(M)_N$	rotational force
α	angle between the ellipse's major axis and a contact vector
α	damping coefficient of proportionality
$\bar{\mu}$	viscosity
$\bar{\Theta}$	average particle rotation
$\bar{D}$	average diameter of an elliptical particle
$\bar{f}_n^c(\theta)$	distribution of average normal contact force
$\bar{f}_t^c(\theta)$	distribution of tangential contact force anisotropy
$\bar{f}_o^c$	average contact normal force
$\bar{l}_j^c$	average contact vector
$\bar{R}$	average radius of an elliptical particle
$\bar{s}$	standard deviation
$\bar{u}$	macroscopic pore pressure

$\ddot{\boldsymbol{x}}_i$	translational acceleration of a particle
$\boldsymbol{D}_i$	contact damping force component
$\boldsymbol{e}^\beta$	unit vector normal to S^β
$\boldsymbol{f}^c$	contact force vector
$\boldsymbol{l}^c$	contact vector
$\boldsymbol{z}^c$	branch vector
$\ddot{\theta}$	angular acceleration of a particle
Δt	time step
ΔV_e	elastic volumetric change
ΔV_p	plastic volumetric change
δ_{ij}	Kronecker's delta
ϵ_n	volumetric strain
ϵ_t	shear strain
ϵ_ω	rigid body rotation
ϵ_{ij}	strain tensor
γ	coordination number
γ_o	initial coordination number
γ_w	volumetric weight of water
γ_{lim}	minimum coordination number required for equilibrium
μ	interparticle friction coefficient ($\tan\phi_\mu$)
∇u	gradient
ν	Poisson's ratio

ω	rotational damping coefficient
ϕ_μ	interparticle friction angle
ϕ_{cv}	angle of friction at critical state
$\phi_{\max}$	peak angle of friction
ϕ_{mob}	mobilized friction angle ($\sigma_{22} - \sigma_{11}$ / $\sigma_{22} + \sigma_{11}$)
ψ	state parameter
ρ	density
$\sigma^{'}_{o}$	effective confining pressure
σ_{ij}	total stress tensor
σ^{β}_{ij}	boundary stress tensor
$\sigma^{'}_{ij}$	effective stress tensor
$\mathbf{T}^{\beta}$	boundary traction
θ	principal axis orientation of an elliptical particle
θ_a	second-order principal direction of contact normal anisotropy
θ_b	fourth-order principal direction of contact normal force anisotropy
θ_n	second-order principal direction of contact normal force anisotropy
θ_t	principal direction of tangential force anisotropy
θ_σ	major principal stress orientation
θ_{ap}	second-order principal direction of conduit anisotropy
θ_{as}	principal orientation of major axis anisotropy
θ_{bp}	fourth-order principal direction of conduit anisotropy
A	area

a	major axis of an elliptical particle
a	second-order coefficient of contact normal anisotropy
A_n	normalized area of a region in an ellipse
a_p	second-order coefficient of conduit anisotropy
a_s	coefficient of major axis anisotropy
a_t	coefficient of tangential force anisotropy
b	fourth-order coefficient of contact normal anisotropy
b	minor axis of an elliptical particle
B_a	bulk modulus of air
B_f	bulk modulus of the fluid
b_p	fourth-order coefficient of conduit anisotropy
B_w	bulk modulus of water
c_n	normal contact damping coefficient
c_s	tangential contact damping coefficient
C_v	coefficient of consolidation
D	dilatancy rate
E	Young's modulus
e	void ratio
$E(\Omega)$	contact normal distribution
e_c	eccentricity
F	number of faces (polygons) in a graph
G	shear modulus

I	polar moment of inertia
I_1	first stress invariant
k_n	normal stiffness
k_s	tangential stiffness
L	conduit length
m	particle mass
M_L	slope of the failure envelope in the stress-state diagram
m_v	contact density
N	number of particles
n	porosity
N_p	number of pores in an assembly
n_p	number of pores surrounding a particle
$P(\theta)$	conduit distribution
p'	effective mean confining stress
q	stress difference $(\sigma_{11} - \sigma_{22}/2)$
S	degree of saturation
S^β	vector connecting boundary particles
T_v	time factor
u_n	Compliance of two elastic bodies in contact
V	volume
V^c	contact overlapping volume
V^p	volume of a pore

z	relative distance between centres of curvature
CSR	critical stress ratio
CVR	critical void ratio
DEM	distinct element method
QSS	quasi-steady state
SSL	steady state line